

The Dynamics in the Upper Atmospheres of Mars and Titan

by
Jared M. Bell

A dissertation submitted in partial fulfillment
of the requirements for the degree of
Doctor of Philosophy
(Atmospheric, Oceanic and Space Sciences)
in The University of Michigan
2008

Doctoral Committee:

Doctor Stephen W. Bougher, Chair
Associate Professor Aaron Ridley
Doctor J. Hunter Waite
Doctor Gregory Tarle
Doctor August Evrard

In Memory of W.T. and Barbara Clay Gullette.

ACKNOWLEDGEMENTS

Thanks to my wife Anna for not killing me(yet). Also thanks to my son for being a little Flirt.

TABLE OF CONTENTS

DEDICATION	ii
ACKNOWLEDGEMENTS	iii
LIST OF FIGURES	vi
LIST OF TABLES	x
LIST OF APPENDICES	xii
CHAPTER	
I. Introduction	1
1.1 Atmospheres in the Solar System	1
1.2 The Structure of an Atmosphere	4
1.3 Transport in Atmospheres	7
1.4 The Upper Atmosphere	23
1.5 Investigating Two Planetary Bodies: Mars and Titan	28
1.6 The Remainder of the Thesis: An Brief Outline of What is to Come	38
II. The Navier-Stokes Fluid Equations	40
2.1 Introduction	40
2.2 Phase Space Distribution Function	40
2.3 Time Evolution of the Phase Space Distribution: Boltzmann Equation	43
2.4 From Boltzmann to the Generalized Transport Equations	44
2.5 Collisions: Maxwell-Boltzmann Distribution	48
III. Numerical Planetary Models	52
3.1 Introduction	52
3.2 A Brief History of Upper Atmospheric Modeling	53
3.3 The Mars Thermosphere General Circulation Model (MTGCM)	57
3.4 The Titan Global Ionosphere-Thermosphere Model (T-GITM)	69
3.5 Fundamental Fluid Equations	73
3.6 Numerical Method	83
3.7 Key Takeaways from GITM	85
IV. Vertical Dust Mixing and the Interannual Variability of Mars' Upper Atmosphere	87
4.1 Abstract	87
4.2 Introduction and Motivation	88

4.3	The Coupled Model (MGCM-MTGCM)	95
4.4	Specifying Lower Atmospheric Dust in the MTGCM-MGCM: Two Approaches	97
4.5	Sensitivity of the MTGCM Lower Thermosphere to Vertical Dust Mixing . .	101
4.6	Interannual Variations in the Mars Lower Thermosphere	112
4.7	Response of the MTGCM to Variations in the Lower Boundary Forcing from the MGCM	124
4.8	Discussion	129
4.9	Future Work	133
V. Exploring Titan through T-GITM		136
5.1	Introduction	136
5.2	Previous Theoretical Work in Titan’s Upper Atmosphere	137
5.3	The Titan Global Ionosphere-Thermosphere Model	143
5.4	The Titan-Specific Driving Terms for T-GITM	144
5.5	Boundary Conditions, Initial Conditions, and Key Parameter Settings . . .	149
5.6	Benchmarking T-GITM: A Comparison with Cassini INMS TA Flyby Data .	161
5.7	Solar Cycle Variations and T-GITM	186
5.8	Seasonal Variations and T-GITM	197
5.9	Key Takeaways and Final Thoughts	202
VI. Comparing T-GITM to Cassini Data		205
6.1	Flyby Comparisons	205
6.2	Comparing the T-GITM against 15 flybys: T5 - T40	205
6.3	The State of Titan’s Thermosphere During T5 - T40	218
6.4	Changing the Super-Rotation Speed at 500 km	218
VII. Conclusions and Discussion		234
APPENDICES		235
B.1	HCN Rotational Cooling: Formalism	239
B.2	HCN’s Rotational Lines	239
B.3	Line Profiles	242
B.4	Radiative Transfer and HCN Cooling	248
B.5	Numerical Methods for the HCN Cooling Routine	257
B.6	Cooling to Space	259

LIST OF FIGURES

Figure

1.1	Venus, Mars, and Titan	2
1.2	Atmospheric Layers of Earth	6
1.3	BlackBody Functions for the Sun and Earth	10
1.4	Cartoon of Incident Solar Radiation on an Atmosphere	11
1.5	Absorption as a Function of Altitude and χ	13
1.6	Mars and Earth Unit Optical Depth	14
1.7	EddyMixing	20
1.8	Earth's Ionospheric Layers and Diurnal Variations	25
1.9	Mars	29
1.10	Mars Neutral Thermosphere	30
1.11	Mars Ionospheric Composition	31
1.12	Mars Winter Polar Warming	33
1.13	Titan's Hazes	34
1.14	Titan Neutral Composition	35
1.15	Vervack	36
1.16	INMS Densities of N_2 and CH_4	37
1.17	INMS Temperatures	38
4.1	Thermal Emission Spectrometer (TES) lower atmospheric dust variations for 3 years	91
4.2	Sample vertical Conrath profiles, for three mixing levels: low, medium, and high	98
4.3	Zonal average temperatures for the dust mixing study	104
4.4	Zonal average neutral densities for the dust mixing study	107

4.5	Zonal Average MTGCM Temperatures at $L_S = 270$ and $\tau = 1.0$	110
4.6	Zonal average MTGCM temperatures at $L_S = 90$ and 270 for three TES years . .	115
4.7	Zonal average MTGCM adiabatic heating and cooling function at $L_S = 90$ and 270 for three TES years	119
4.8	Line plots for neutral densities at 120 km for three TES years at $L_S = 090$ and 270.123	
4.9	Three MTGCM lower boundary comparisons	127
5.1	Titan Heating Efficiency as a function of altitude	145
5.2	Chemical Pathways of T-GITM	148
5.3	Electron Temperature adopted at Titan	151
5.4	Initial N_2 and CH_4 Densities	152
5.5	Initial Temperatures in T-GITM	153
5.6	Line Plot of Latitude Temperature Variations	155
5.7	Latitude vs. Longitude plot of lower boundary temperatures at 500 km	155
5.8	Line plot of latitude zonal wind variations	157
5.9	Latitude vs. Longitude plot of lower boundary zonal winds at 500 km	157
5.10	Latitude vs. Longitude plot of lower boundary \log_{10} neutral densities at 500 km .	158
5.11	Vertical profiles of nominal eddy diffusion and molecular diffusion profiles	160
5.12	Model to data comparisons of N_2 and CH_4 densities for the TA flyby	162
5.13	Comparing T-GITM atmospheric mass density, ρ , and mean major mass, \bar{m} , with Cassini INMS TA flyby data	163
5.14	Model to data comparisons of Argon mixing ratio between T-GITM and INMS measurements	165
5.15	Model to data comparisons of $^{15}N - ^{14}N$ densities	166
5.16	Model to data comparisons of Argon mixing ratio between T-GITM and INMS measurements	167
5.17	T-GITM global and zonally averaged thermal structures during the TA flyby . . .	170
5.18	T-GITM Global Average N_2 and CH_4 Densities	171
5.19	T-GITM zonally averaged neutral N_2 and CH_4 densities for the TA Flyby	173
5.20	T-GITM global and zonally averaged Argon mixing ratios during the TA flyby . .	174

5.21	T-GITM global and zonally averaged HCN mixing ratios during the TA flyby	175
5.22	T-GITM zonally averaged northward and eastward velocity components during the TA flyby	177
5.23	T-GITM zonally averaged bulk radial (vertical) velocity component during the TA flyby	178
5.24	T-GITM global average energy balance terms	181
5.25	Global average energy balances in two regions: 500 - 1000 km and 1000 - 1500 km.	182
5.26	T-GITM global average energy balance terms, focusing on the first order terms	183
5.27	Global average energy balances in two regions: 500 - 1000 km and 1000 - 1500 km.	184
5.28	Global average and diurnal temperature variations over the solar cycle	187
5.29	Global average N_2 , CH_4 , Ar, and HCN profiles over the solar cycle	188
5.30	Zonal average temperatures and N_2 neutral densities over the solar cycles.	189
5.31	Zonal average CH_4 neutral densities and u_ϕ over the solar cycles.	190
5.32	Zonal average u_θ and u_r over the solar cycle.	194
5.33	Neutral temperatures over the solar cycle at the exobase and homopause.	195
5.34	Zonal average temperature and u_ϕ over the seasons.	199
5.35	Zonal average u_θ over the seasons.	200
5.36	Exobase and homopause temperature over the seasons.	201
6.1	T-GITM and INMS N_2 and CH_4 density comparisons for T5 - T26.	206
6.2	T-GITM and INMS N_2 and CH_4 density comparisons for T28 - T40.	207
6.3	T-GITM and INMS \bar{m} comparisons for T5 - T26.	208
6.4	T-GITM and INMS \bar{m} comparisons for T28 - T40.	209
6.5	T-GITM and INMS ρ comparisons for T5 - T26.	213
6.6	T-GITM and INMS ρ comparisons for T28 - T40.	214
6.7	T-GITM and INMS Argon mixing ratio comparisons for T16 - T28.	215
6.8	T-GITM and INMS Argon mixing ratio comparisons for T29 - T40.	216
6.9	T-GITM and INMS $^{14}N/^{15}N$ comparisons for T5 - T26.	219
6.10	T-GITM and INMS $^{14}N/^{15}N$ comparisons for T28 - T40.	220

6.11	T-GITM and INMS $^{12}\text{C}/^{13}\text{C}$ comparisons for T5 - T26.	221
6.12	T-GITM and INMS $^{12}\text{C}/^{13}\text{C}$ comparisons for T28 - T40.	222
6.13	T-GITM and INMS Ar mixing ratio Scatter Plot	223
6.14	T-GITM and INMS $^{12}\text{C}/^{13}\text{C}$ Scatter Plot.	224
6.15	T-GITM and INMS $^{14}\text{N}/^{15}\text{N}$ scatter plot comparisons.	225
6.16	Zonal average fields for the T5-T40 flyby simulation.	226
6.17	Additional zonal average fields for the T5-T40 flyby simulation.	227
6.18	Altitude slices of temperature and mass density, ρ at the exobase and homopause for the T5-T40 flyby simulation.	228
6.19	T-GITM and INMS N_2 and CH_4 density comparisons for T5 - T26 (Non Super-Rotating).	229
6.20	T-GITM and INMS N_2 and CH_4 density comparisons for T28 - T40 (Non Super-Rotating).	230
6.21	T-GITM and INMS N_2 and CH_4 density comparisons for T5 - T26 (Strongly Super-Rotating).	231
6.22	T-GITM and INMS N_2 and CH_4 density comparisons for T28 - T40 (Strongly Super-Rotating).	232
6.23	Zonal average temperatures and u_ϕ for the three lower boundary cases.	233

LIST OF TABLES

Table

1.1	Selected Planetary Parameters for Earth, Mars, and Titan.	28
3.1	Difference between GITM and Other GCMs	70
3.2	Neutral and Ionic Species Breakdown in TGITM	72
3.3	Selected Binary Diffusion Coefficients, $D_{qs} = \frac{A_{qs} T^b}{N}$ in cm^2/s	82
4.1	Polar Warming Features in Kelvin for Sensitivity Study	102
4.2	Polar Warming Features in Kelvin for Interannual Study	117
4.3	Winter Polar Neutral Densities for Interannual Study	121
5.1	Photochemical Reactions in T-GITM	149
5.2	Intermolecular Chemical Reactions and Associated Rates in T-GITM [<i>De La Haye, 2005; Wilson, 2002a; Wilson and Atreya, 2004</i>].	150
5.3	T-GITM Comparisons with INMS Data	169
5.4	Temperatures at the Exobase (1500 km) over the Solar Cycle	191
5.5	Temperatures at the Homopause (850 km) over the Solar Cycle	191
5.6	Zonal average variations in T-GITM temperatures for solar minimum, solar moderate, and solar maximum conditions at three key altitudes and three key latitudes. .	192
5.7	Zonal average variations in T-GITM N_2 densities for solar minimum, solar moderate, and solar maximum conditions at three key altitudes and three key latitudes. .	193
5.8	Zonal average variations in T-GITM CH_4 densities for solar minimum, solar moderate, and solar maximum conditions at three key altitudes and three key latitudes. .	193
6.1	Normalized Root Mean Squared Error (NRMSE) between T-GITM and Cassini INMS data for T5 - T40 flybys	212
6.2	Correlation Coefficient (r) between T-GITM and Cassini INMS data for T5 - T40 flybys	217
6.3	Total NRMSE and Correlation Coefficient for the Non Super-Rotating and Strongly Super-Rotating Lower Boundaries for the T5 - T40 flybys	218

A.1	N ₂ Photoabsorption Cross-Sections and Quantum Yields	237
A.2	CH ₄ Photoabsorption Cross-Sections and Quantum Yields	238

LIST OF APPENDICES

Appendix

A. Photoabsorption Cross-Sections	236
B. Hydrogen Cyanide (HCN) Radiative Transfer Model	239

CHAPTER I

Introduction

The most beautiful experience we can have is the mysterious.

*It is the fundamental emotion which stands at the cradle of
true art and true science.*

– *Albert Einstein*

1.1 Atmospheres in the Solar System

1.1.1 What is an Atmosphere?

As in *Strobel* [2002], I define an atmosphere as a “gaseous envelope bound to a gravitating body.” This broad definition covers the most familiar case of a terrestrial planet or moon (e.g. Venus, Earth, Mars, Titan, and Triton) where a fluid atmosphere overlies a solid planetary body, while also applying to the gas giant outer planets (e.g. Jupiter, Saturn, Uranus, and Neptune). In the latter case, distinguishing the atmosphere from the gravitating body becomes more difficult. However, this definition precludes the inclusion of evanescent gaseous envelopes that form around comets, termed comas, and it excludes out-gassing emissions that become temporarily trapped by smaller bodies, such as Jupiter’s moon Io. Lastly, the adopted definition also removes from consideration surface exospheres, such as on Mercury and Earth’s moon.



Figure 1.1: Pictured above (not to scale) from left to right: Venus, Mars (prior to a dust storm), Mars(during a dust storm), and Titan. This is just a small sampling of the dynamic planetary atmospheres that exist in our solar system. Courtesy NASA Public Image Database.

However, despite its usefulness, this simple description fails to capture the complexities that occur in our solar system's planetary atmospheres. From the impenetrable hazes of Venus and Titan, to the planet-encircling dust storms of Mars, all manner of unexplained phenomena occur. Thus, although an atmosphere may be simply defined, it remains a complex physical and chemical system that can defy our best attempts at comprehension. Finally, though the multiplicity of phenomena occurring in planetary atmospheres cannot possibly be catalogued here, Figure 1.1 contains a small sampling of the menagerie that is our solar system.

1.1.2 Why Study Planetary Atmospheres?

Ever since humans first looked to the heavens and observed the planets' motion in the night sky, we have pondered the nature of their existence. This deeply ingrained urge to comprehend the unknown and the mysterious partially explains our enduring desire to understand our sister planets. However, a more practical reason to study planetary atmospheres is that, by studying these diverse systems in our solar system, we simultaneously reach a greater understanding of Earth's atmosphere. In fact, each planetary atmosphere represents a new laboratory within which to explore the interplay between the various physical and chemical processes common to them all.

And, by comparing and contrasting what we learn from each planetary atmosphere, we reach a greater understanding of how these systems function in general.

For instance, Titan, possessing an atmosphere rich in complex hydrocarbons and nitrogen, resembles Earth at a time before the biota, or biological life forms, began to alter our planet's atmosphere [*Clarke and Ferris, 1997; Sagan and Thompson, 1984; Yung et al., 1984*]. Could Titan represent an epoch of Earth's history long lost to time? Does Titan represent an opportunity for humans to explore our planet's past by studying the physical and chemical processes in this Saturnian satellite's atmosphere? Similarly, Venus, with its thick shield of greenhouse gases, might resemble a potential future state of Earth, should greenhouse gases in our own atmosphere reach unsustainable levels [*Kasting, 1988*]. Could our sister planet serve as a warning to humans about the potential impact of aerosols in our own atmosphere? Could we be seeing a potentially devastating future epoch of our own world?

Finally Mars, possessing tantalizing hints of previous oceans, rivers, and lakes, entices us to question where the water went [*Malin et al., 2006*]. Did Mars at one time resemble Earth? Did rivers flow? Did oceans exist? If so, then how did it come to its present state? Why did Mars fail to remain as it did? Finally, what fundamental physical and chemical processes drove its evolution to its current state, and could these play a role at Earth?

All of these questions and more emerge as we gaze out at our sister planets. Ultimately, the answers to them may always elude humankind; however, by studying and better understanding the physical and chemical forces at play in other planetary atmospheres, we may simultaneously come closer to understanding our own world.

1.1.3 Comparative Planetary Aeronomy: The Focus of this Thesis

The discipline of studying atmospheres segregates itself primarily into two camps: meteorology and aeronomy. The separation between the two disciplines remains nebulous at best, but, for historical reasons, meteorology deals primarily with the lower atmosphere, while aeronomy encompasses the physics and chemistry of the upper atmosphere [*Schunk and Nagy*, 2000]. Furthermore, planetary aeronomy extends the study of upper atmospheres to other planetary bodies, exploring the physics and chemistry dominating these systems.

Keeping with these historical definitions, this thesis relegates its subject matter to the field of planetary aeronomy, focusing on the physical and chemical processes at high altitudes in the atmospheres of both Mars and Titan. In particular, this thesis deals with the dynamical processes at work in the upper atmospheres of these two terrestrial bodies, using three dimensional numerical/theoretical models. However, before discussing the specific scientific questions addressed by this thesis' research, one must first understand the processes and structures common to most atmospheres in the solar system.

1.2 The Structure of an Atmosphere

At the most fundamental level, the coupled, non-linear Navier-Stokes fluid equations of chapter 2 govern the physics of atmospheres. However, to a large degree, the balance between upward (radially outward) pressure forces and downward (radially inward) gravitational forces define the structure of atmospheres, giving rise to the hydrostatic equation:

$$(1.1) \quad \nabla P = -\rho g.$$

Here, P is the pressure (Pa), ρ is the mass density (kg/m^{-3}), and g is gravitational acceleration (positive quantity, m/s^2). Assuming an ideal gas and introducing the definition of mass density, one arrives at:

$$P = nkT,$$

$$\rho = \bar{m}n.$$

Where \bar{m} represents the mean atmospheric mass (kg), n is the atmospheric number density (m^{-3}), T is the atmospheric temperature (K), and finally k is Boltzmann's constant (J/K). Next, substituting the expressions for ρ and P back into equation 1.1 above, dividing the resulting equation by nkT , and assuming that only the vertical gradient matters, one derives the following:

$$(1.2) \quad \frac{1}{nT} \frac{\partial(nT)}{\partial r} = -\frac{\bar{m}g}{kT}.$$

This can be integrated immediately by inspection to give:

$$\begin{aligned} \ln[n(r)T(r)] - \ln[n(r_0)T(r_0)] &= - \int_{r'=r_0}^{r'=r} \frac{\bar{m}g}{kT} dr', \\ \Rightarrow n(r)T(r) &= n(r_0)T(r_0) \exp\left[- \int_{r'=r_0}^{r'=r} \frac{\bar{m}g}{kT} dr'\right], \\ \Rightarrow n(r) &= n(r_0) \frac{T(r_0)}{T(r)} \exp\left[- \int_{r'=r_0}^{r'=r} \frac{\bar{m}g}{kT} dr'\right]. \end{aligned} \tag{1.3}$$

This is the famous barometric equation. If one makes some further simplifications, such as assuming T , g , and \bar{m} remain roughly constant over the domain of interest, then a more familiar form of the barometric equation emerges:

$$(1.4) \quad n(r) = n(r_0) \exp\left[-\frac{(r - r_0)}{H}\right].$$

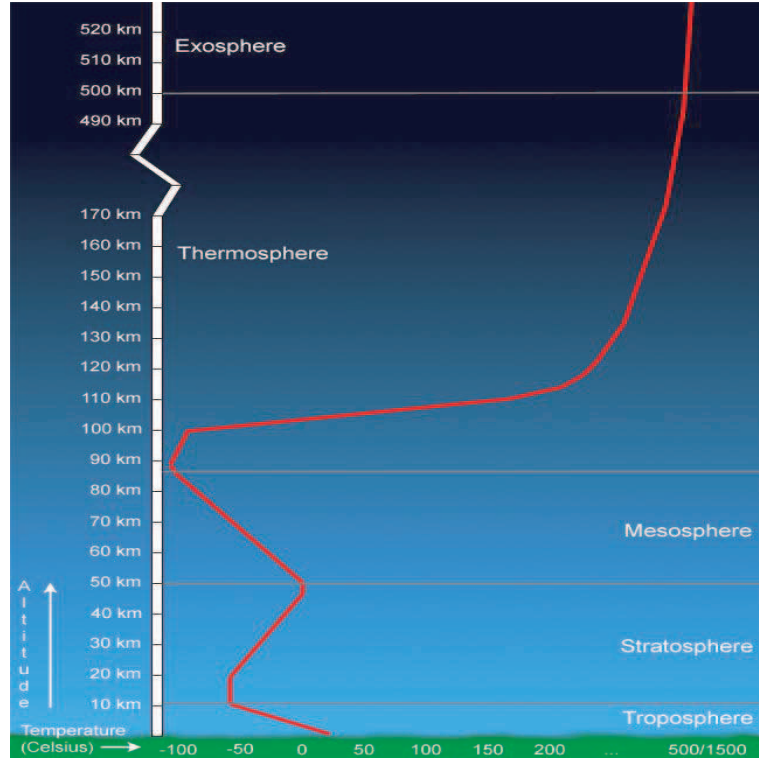


Figure 1.2: A diagram of the vertical structure of Earth's atmosphere. The structures illustrated above typically have analogues at other planetary atmospheres. Thus, this vertical structure serves as a template for most planetary atmospheres in our solar system. Source: The source of this material is Windows to the Universe, at <http://www.windows.ucar.edu/> at the University Corporation for Atmospheric Research (UCAR). 1995-1999, 2000 The Regents of the University of Michigan; 2000-05 University Corporation for Atmospheric Research. All Rights Reserved

Equation 1.4 introduces the mean atmospheric scale height, H , which is defined as:

$$(1.5) \quad H = \frac{kT}{\overline{mg}}.$$

Despite the restrictive assumptions applied during its derivation, an important relationship emerges from equation 1.4: atmospheres vary exponentially with altitude and these vertical variations dominate over horizontal variations. Because of this, physicists organize atmospheric regions according to altitude, as shown in Figure 1.2. The atmospheric levels of this figure actually represent concentric spherical shells centered on the planet's gravitational core. Moreover, the dominant physical and chemical processes of atmospheres vary drastically with altitude. Thus, the var-

ious atmospheric regions in Figure 1.2 also represent different physical and chemical regimes. Despite their vertical stratification, atmospheres ultimately remain completely continuous fluid systems whose fundamental processes are detailed in the following section.

1.3 Transport in Atmospheres

At the most general level, atmospheres all perform the same basic function: to redistribute energy from external (or internal) sources in order to establish an energetic equilibrium. Because an atmosphere is a coupled fluid-chemical system, it can accomplish this redistribution of energy in a multitude of ways. Despite their inherent complexities, atmospheres may transport energy primarily through one of four fundamental processes: (1) Conduction, (2) Radiation, (3) Advective convection, or (4) Diffusive convection [*De Pater and Lissauer, 2001*]. Additionally, atmospheres may redistribute energy through the chemical reactions among its constituents. Thus, a plethora of physical and chemical phenomenon can manifest themselves in planetary atmospheres that all serve to balance the energetics of these large-scale systems.

1.3.1 Conduction

Conduction represents the transport of energy through collisions between constituent particles, and it plays a major role in the tenuous upper atmosphere. Ignoring external temperature sources, thermal diffusion in an atmosphere is governed by the following simple formulation :

$$(1.6) \quad \rho c_V \frac{\partial T}{\partial t} = -\nabla \cdot \mathbf{q}.$$

This expression contains, c_V , the specific heat capacity at a constant volume ($J/K/kg$), and \mathbf{q} , the heat conduction vector (W/m^2) given by Fourier's law of conduction:

$$(1.7) \quad \mathbf{q} = -\kappa_T \nabla T.$$

Here, κ_T represents the molecular thermal diffusion coefficient ($W/m/K$), derived from the following micro-physical relationship:

$$(1.8) \quad \kappa_T = \frac{5}{3}(N_l + 2) \frac{k p_s}{m_s z_{ss} \nu_{ss}}.$$

Here, N_l represents the conducting particles' internal degrees of freedom. Furthermore, this equation also contains k as Boltzmann's constant (J/K), p_s as the pressure (Pa), m_s as the mass of species "s" (kg), z_{ss} as a geometrical factor (no units), and finally ν_{ss} as the self-collision frequency (Hz).

In planetary upper atmospheres, the collision frequency between particles decreases because of the exponential decrease in the number density. This drop in density implies that fewer inter-particle collisions can occur, resulting in molecular conduction becoming a very important thermal transport process at high altitudes. Physically, this drop in collision frequency also represents an increase in the average distance traveled by particles between collisions, which defines a new parameter: λ_{mfp} , the mean free path. Thus in the upper atmosphere, the particles travel farther between collisions, subsequently transporting their energy over larger distances. Over time, this results in vertical layers of the atmosphere reaching a temperature equilibrium that closely resembles its neighbors both above and below. Hence, when conduction dominates, temperature perturbations tend to equilibrate or "smear out" vertically.

This "smearing out" effect emerges more clearly after substituting equation 1.7 into equation 1.6, arriving at the canonical expression for conduction in planetary

atmospheres:

$$(1.9) \quad \rho c_V \frac{\partial T}{\partial t} = \nabla \cdot (\kappa_T \nabla T).$$

Equation 1.9 describes simple diffusion, which tends to spread out perturbations. In other words, conduction transports energy from areas of high concentration (i.e. hot zones) to areas of lower concentration (i.e. cooler zones).

1.3.2 Radiation

Radiation emerges as another key energy redistribution mechanism at work in planetary upper atmospheres. In this context, radiative processes consist of absorbing and re-emitting electromagnetic energy. This process dominates in regions of the atmosphere where the optical depth, or optical thickness, of the radiation is greatest. Because electromagnetic energy attenuates as it passes through an absorbing medium, such as an atmosphere, its impact on the energy budget becomes a complex function of atmospheric density, radiation wavelength, angle of incidence, and altitude. Finally, radiative processes remain a key component of the energy budget at all atmospheric altitudes [*Schunk and Nagy, 2000; Gombosi, 1999*].

For the majority of terrestrial planetary atmospheres in the solar system, the sun's radiation is the single largest external source of energy. Essentially, the sun approximates a black body source, radiating at a peak frequency of 480 nm in the visible spectrum. Planetary atmospheres typically absorb the sun's shortwave radiation, while re-radiating at longer wavelengths, as shown in Figure 1.3. Although most planetary atmospheres behave this way radiatively, solar absorption becomes less and less important in the outer solar system. However, even in the outer solar system, the sun's radiation is an important driver for dynamics and chemistry, especially in the upper atmosphere [*Atreya, 1986*].

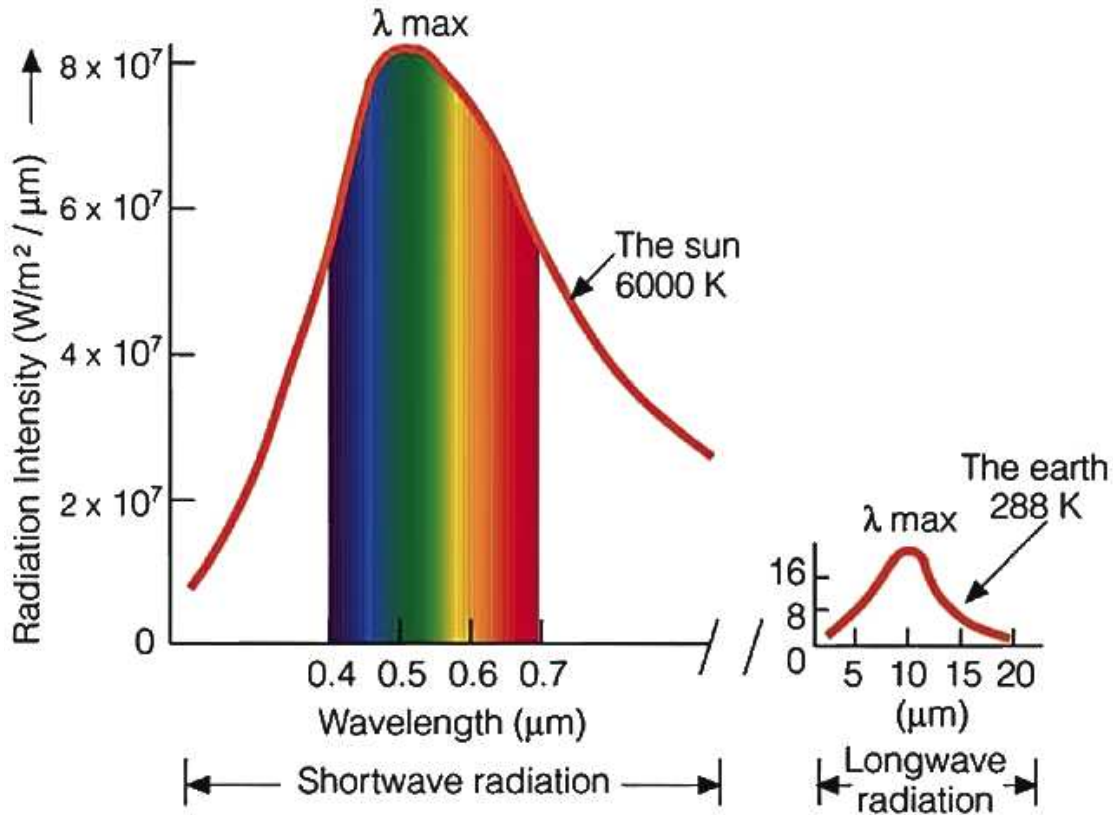


Figure 1.3: Pictured above are both the black body radiation functions for both the sun (shortwave radiation) and the Earth (longwave radiation). This diagram illustrates how our sun emits at energetic short-wavelengths, while, in general, planets re-emit radiation at long-wavelengths. Also, the sun's intensity remains far greater than those of the intensity of planetary radiation. Adapted from Thomson Higher Education (2007).

The Sun's Extreme Ultraviolet (EUV) radiation represents a key contributor to the thermal and chemical processes in planetary upper atmospheres. In this region, solar EUV radiation causes: (1) Heating of the neutral atmosphere, (2) Photoionization of neutral constituents, and (3) Photodissociation of molecular constituents. Figure 1.4 depicts a cartoon idealization of incident radiation on the topside of an atmosphere. In this figure, the solar radiation, denoted by the rays labeled $h\nu$, at the frequency ν passes through the absorbing atmosphere, being attenuated along its path. This figure defines an incidence angle, denoted as χ , relative to the zenith and, thus, this angle is termed the solar zenith angle (SZA) of the incident radiation. Also,

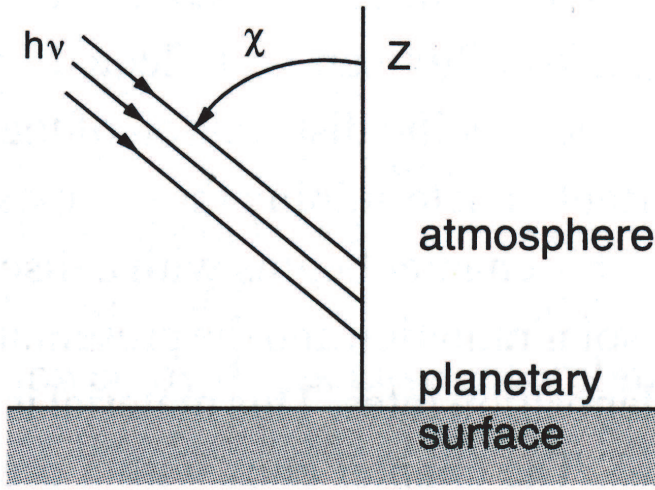


Figure 1.4: How incident radiation from the sun travels through a planetary atmosphere is depicted above. χ is the solar zenith angle (SZA), while Z is the altitude above the planetary surface. $h\nu$ is the incident solar radiation at frequency ν . Adapted from *Schunk and Nagy* [2000]

this figure denotes the altitude coordinate as Z along the vertical axis. However, not shown clearly on this cartoon, the behavior of radiation in an atmosphere remains intimately coupled to its frequency and the path-length traveled by the radiation through the atmosphere.

Figure 1.4 also provides a rough visual guide to developing the mathematical description of radiative absorption in the upper atmosphere, as done in *Schunk and Nagy* [2000]; *Gombosi* [1999]. First, for each incremental step, denoted by ds_λ , traversed through an absorbing medium by a beam of electromagnetic radiation, its intensity will decrease by a proportional amount, labeled $dI(s_\lambda)$. If one ignores scattering in the upper atmosphere, a reduced form of the radiative transfer equation relates these two quantities:

$$(1.10) \quad dI(s_\lambda) = -I(s_\lambda)n(z)\sigma_\lambda^a ds_\lambda.$$

In this equation, $I(s_\lambda)$ represents the radiation's intensity ($photons/m^2$), $n(z)$

is the neutral density (m^{-3}), σ_λ^a is the photon absorption cross-section (m^{-2}) for a given wavelength, and finally ds_λ is the pathlength of the radiation (m). As a first approximation, atmospheres remain roughly vertically stratified into parallel planes that are uniform horizontally. This assumption comprises the “plane-parallel” approximation, which is typically employed in most radiative transfer techniques. Finally, if this plane-parallel assumption applies, then, as depicted in Figure 1.4, a simple geometrical relationship exists between dz and ds_λ :

$$(1.11) \quad ds_\lambda = -\sec(\chi)dz.$$

Next, after substituting the expression in equation 1.11 for ds_λ into equation 1.10 and dividing both sides by $I(s_\lambda)$, a new expression for intensity attenuation emerges:

$$(1.12) \quad \frac{dI(z, \chi, \lambda)}{I(z, \chi, \lambda)} = n(z)\sigma_\lambda^a \sec(\chi)dz.$$

In equation 1.12, the intensity now possess an explicit variation with altitude, solar zenith angle, and wavelength. Next, if the barometric equation 1.4 replaces $n(z)$ in equation 1.12, then this last expression can be integrated from z to ∞ to give:

$$(1.13) \quad \int_{I'=I_{z,\chi,\lambda}}^{I'=I_\infty} \frac{dI'(z, \chi, \lambda)}{I'(z, \chi, \lambda)} = \int_{z'=z}^{z'=\infty} \left[n(z_0)e^{-\frac{(z'-z_0)}{H}} \right] \sigma_\lambda^a \sec(\chi)dz'.$$

Here, the definition of ∞ remains ambiguous, but one may assume that it approximates a location sufficiently far outside the atmosphere so that I_∞ represents the incident radiation before any attenuation occurs. Also, from this definition, the neutral density becomes negligibly small, $n(\infty) = 0.0$. Given this definition of ∞ , equation 1.13 integrates readily to:

$$(1.14) \quad \ln(I_\infty) - \ln(I(z, \chi, \lambda)) = n(z_0)\sigma_\lambda^a \sec(\chi) \int_{z'=z}^{z'=\infty} e^{-\frac{(z'-z_0)}{H}} dz'.$$

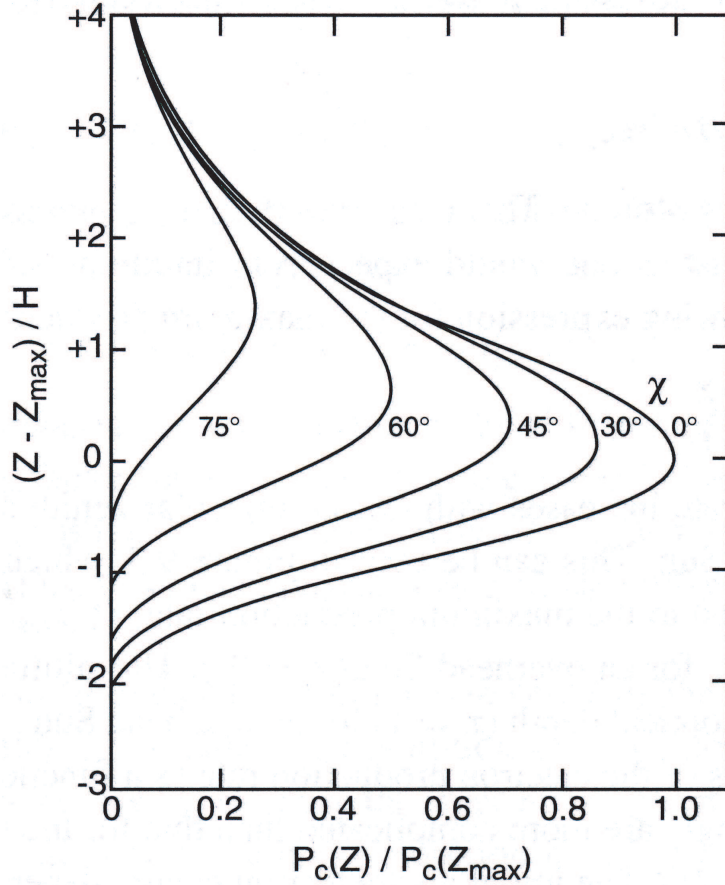


Figure 1.5: The curves above illustrate how solar radiation is absorbed in planetary atmospheres as a function of normalized altitude (a scaled measure of distance above or below a reference altitude, Z_{max}) and solar zenith angle, χ . It's important to note that, for a specific χ value, a maximum solar absorption occurs in the atmosphere, corresponding to the peak in the production function. Similarly, at a given altitude, as χ approaches 0° (that is, the angle directly "below" the sun), the absorption increases. *Schunk and Nagy* [2000]

Further, this simplifies to:

$$(1.15) \quad \ln(I_\infty) - \ln(I(z, \chi, \lambda)) = -H \left[n(z_0) e^{-\frac{(z' - z_0)}{H}} \right] \sigma_\lambda^a \sec(\chi).$$

With further re-arranging and a look to equation 1.4, this finally simplifies to the following:

$$(1.16) \quad I(z, \chi, \lambda) = I_\infty \exp(-Hn(z)\sigma_\lambda^a \sec(\chi)).$$

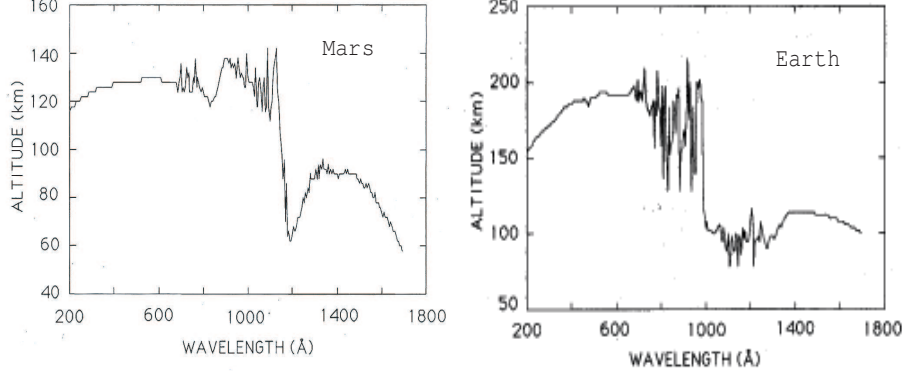


Figure 1.6: The altitude of the peak atmospheric absorption $\tau = 1.0$ as a function of wavelength λ for Mars (left panel) and Earth (right panel), taken from *Paxton and Anderson [1992]*. At Mars, the primary absorber is CO_2 , while at Earth, both N_2 and O_2 participate in absorption.

Equation 1.16 represents a very simplified formulation for how incoming radiation intensity attenuates in a strictly absorbing atmosphere. However, even this simple formulation poses a challenge to one's intuition. Figure 1.5 illustrates how the intensity of radiation at a single wavelength varies as a function of altitude and solar zenith angle. Importantly, this figure illustrates that radiation of any wavelength finds a peak absorption at some altitude given a fixed solar zenith angle. Furthermore, for a given altitude, the absorption of radiation increases with decreasing solar zenith angle. In other words, the peak absorption of solar radiation occurs at the subsolar point, which represents local noon.

The argument of the exponent in equation 1.16 represents a simplified version of optical path, or optical depth, $\tau(z, \chi, \lambda)$. More generally, a radiation's optical path length remains an integral equation given by:

$$(1.17) \quad \tau(z, \chi, \lambda) = \int_{z'=z}^{z'=\infty} n(z) \sigma_{\lambda}^a \sec(\chi) dz'.$$

Optical depth essentially describes the amount of atmosphere, for a given wavelength, λ , that must be traversed by the radiation from the source at ∞ to the point

of interest at height z and solar zenith angle χ . The altitude where $\tau(z, \chi, \lambda)$ is equal to 1.0 correlates with the peak atmospheric absorption of this radiation.

Figure 1.6 illustrates how the atmospheres of Earth and Mars absorb incoming solar radiation from the sun. In this figure, the altitude of unit optical depth varies as a function of absorbed wavelength between $200 - 1800 \text{ \AA}$ [Paxton and Anderson, 1992]. This figure illustrates a general trend in planetary atmospheres: shorter wavelengths are absorbed at higher altitudes, while longer wavelengths are absorbed at lower altitudes. Also, due to the difference in atmospheric composition, that the altitudes of the $\tau = 1.0$ peaks for a given wavelength vary significantly on both planets. Ultimately, this variation in radiation absorption represents a key component in the energy balance in all planetary atmospheres.

1.3.3 Convection I: Advection of Matter and Energy

Convection remains the final major transport process to consider in planetary atmospheres. This mechanism differs from both thermal conduction and radiation because it redistributes both energy and matter. Advection and Diffusion represent the principle components comprising convection. Advection transports both energy and material through fluid flow. These winds result from the variegated forces at play in planetary atmospheres, but remain primarily induced through density and temperature gradients.

Adiabatic buoyancy driven convection serves as a simple, yet famous, example of an advection/convection process [De Pater and Lissauer, 2001]. First, one considers a parcel of air at a specific altitude. Next, suppose that this parcel possesses the same density as its surroundings, but instantaneously experiences an increase in temperature, imposing a pressure greater than the ambient atmosphere. In order to re-establish pressure equilibrium with its surroundings without exchanging heat

(adiabatic process), the parcel must expand in order to decrease its density and temperature.

However, as its density decreases below that of its surroundings, the parcel experiences an upward buoyancy force, moving it to a higher atmospheric altitude. As the parcel moves higher, however, the ambient pressure continually decreases with altitude. Thus, the small parcel must continuously expand and cool, as it attempts to establish a pressure equilibrium with the ambient atmosphere. If the background atmosphere's temperature profile also cools sufficiently quickly, then the parcel will continue to rise, transporting its elevated temperature upward into the atmosphere.

This ultimately results in a net transport of heat from lower altitudes to higher altitudes. Simultaneously, the opposite process, whereby a cooler parcel of air descends through the atmosphere, results in a net cooling effect for lower altitudes. However, in order for this buoyant convection mechanism to play a major role in atmospheric dynamics, the temperature must decrease with altitude. That is, the temperature must decrease with decreasing pressure [*De Pater and Lissauer, 2001*]. This simple example remains just one possible mechanism to transport both energy and material through advection.

When convection dominates, the thermal profile typically follows an adiabatic lapse rate, which can be derived from thermodynamics and the hydrostatic relationship found in equation 1.1. From the first law of thermodynamics, we have:

$$(1.18) \quad dQ = dU + PdV.$$

Here, dQ is the amount of energy absorbed by the system from its surroundings, dU is the change in the system's total internal energy (sum of potential and kinetic), and PdV is the work done by system on the surroundings. Assuming that no energy exchange occurs between a hypothetical convecting fluid parcel and its surroundings,

then the first law of thermodynamics becomes:

$$(1.19) \quad dQ = 0 = dU + PdV.$$

Thus, the convecting parcel's internal energy, dU , changes by an incremental amount given by

$$(1.20) \quad dU = -PdV.$$

Next, two critical thermodynamic quantities, the thermal heat capacities, need introduction using the following formulation:

$$(1.21) \quad C_V = \left(\frac{\partial Q}{\partial T} \right)_V,$$

and

$$(1.22) \quad C_P = \left(\frac{\partial Q}{\partial T} \right)_P.$$

These thermal heat capacities represent the amount of heat required to elevate the temperature of one mole of atmospheric material by 1 K without changing the pressure (C_P) or volume (C_V). After substituting in equation 1.18 for dQ , these definitions lead to the following expression for C_V and C_P for an adiabatic process:

$$(1.23) \quad C_V = \left(\frac{\partial U}{\partial T} \right)_V,$$

and

$$(1.24) \quad C_P = \left(\frac{\partial U}{\partial T} \right)_P + P \left(\frac{\partial V}{\partial T} \right)_P.$$

Next, the ideal gas law applies to the convecting air parcel under consideration and it may be used to evaluate the term $\left(\frac{\partial V}{\partial T} \right)_P$ in equation 1.24. However, first, a more convenient form of the ideal gas law emerges by recalling that $n(z) = N/V$

where n represents the number density, N represents the number of particles, and V represents the volume. Using these new variables, the ideal gas law becomes:

$$(1.25) \quad PV = NkT.$$

Using this new ideal gas law, the differential volume element reduces to:

$$(1.26) \quad dV = \frac{Nk}{P} dT - \frac{NkT}{P^2} dP,$$

$$(1.27) \quad \left(\frac{\partial V}{\partial T} \right)_P = \frac{Nk}{P}.$$

Finally, after substituting equation 1.27 and equation 1.20 back into expression 1.24, C_P becomes :

$$\begin{aligned} C_P &= -PdV + P \left(\frac{Nk}{P} \right), \\ \Rightarrow C_P &= -P \left(\frac{Nk}{P} - \frac{NkT}{P^2} \frac{dP}{dT} \right) + P \left(\frac{Nk}{P} \right), \\ \Rightarrow C_P &= \left(-Nk + \frac{NkT}{P} \frac{dP}{dT} \right) + Nk, \\ (1.28) \quad \Rightarrow C_P &= \left(\frac{NkT}{P} \right) \frac{dP}{dT} = V \frac{dP}{dT}. \end{aligned}$$

From this last form, one may multiply both sides by $\frac{dT}{dz}$ and introduce a new term, $\overline{m}N c_p = C_P$. Here, c_p represents the specific heat capacity at a constant pressure (J/kg/K). Using these two manipulations, dividing both sides by V , and recalling that $\rho = \overline{m}N/V = \overline{m}n$ one arrives finally at:

$$(1.29) \quad \rho c_p \frac{dT}{dz} = \frac{dP}{dz}.$$

And, using the pressure gradient formulation of equation 1.1, a new expression emerges:

$$(1.30) \quad \rho c_p \frac{dT}{dz} = -\rho g,$$

which can be further simplified to:

$$(1.31) \quad \frac{dT}{dz} = -\frac{g}{c_p} = \Gamma_d.$$

Γ_d (K/m) represents the *dry* adiabatic lapse rate of an atmosphere. Convection in an atmosphere is extremely efficient when the actual temperature gradient is superadiabatic. That is, convection dominates whenever the actual temperature decreases faster than the dry adiabatic lapse rate. In fact, a superadiabatic temperature gradient in a real atmosphere exists only when other forces drastically inhibit convection. Although this section began by considering only the simple example of buoyancy-driven convection, all advective processes, such as global winds, waves, and tides, play a significant role in redistributing energy and matter in planetary atmospheres.

1.3.4 Convection II: Diffusive Processes

Although advective processes remain critical for matter and energy transport, diffusion of particles through the background atmosphere represents another major convective mechanism. Diffusion describes the net transport of material and energy through the micro-physical brownian motion of particles and the subsequent inter-particle collisions. Planetary atmospheres remain macro-physical systems, so accounting for all of these micro-physical interactions becomes theoretically and computationally prohibitive. However, the net effect of these collisions on the mass and energy budget of a planetary atmosphere can be summarized by two semi-empirical formulations: eddy (turbulent) diffusion and molecular diffusion.

Micro-physical turbulence or eddy diffusion presents planetary aeronomers with a problem, because it seeks to sum over all of the small-scale turbulent motions in an atmosphere that, by definition, cannot be accounted for explicitly. Thus, eddy diffusion takes on a semi-heurisitc formulation: if it works, then it is most

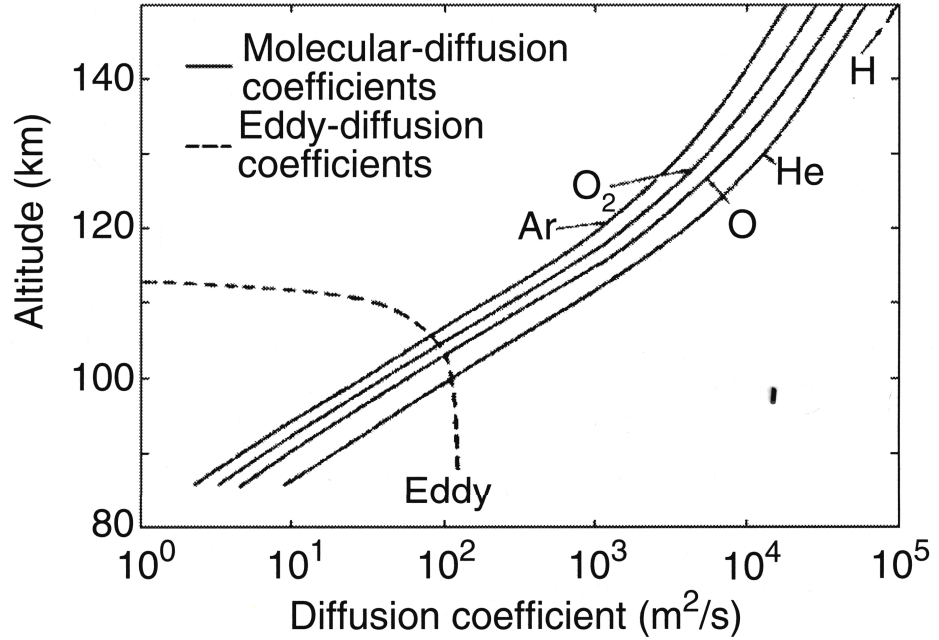


Figure 1.7:

This figure depicts the model interplay between the opposing forces of turbulent (eddy) diffusion and molecular diffusion. The region where the eddy diffusion curve and the molecular diffusion curve overlaps is nominally termed the homopause or the turbopause. Below the turbopause, eddy processes clearly dominate, while, above the homopause, molecular diffusion dominates. Taken from *Gombosi* [1999]

likely correct. While this approach leaves much to be desired from a theoretical perspective, most aeronomers generally agree on the net result of turbulent processes: maintaining constant mixing ratios in an atmosphere. That is, microphysical turbulent processes tend to mix the atmosphere into a uniform composition. Keeping with this semi-empirical implementation of eddy diffusion, a macro-scale turbulent diffusion coefficient, denoted as K_E , can be prescribed according to [Atreya, 1986]:

$$(1.32) \quad K_E(z) = K_E(0) \sqrt{\frac{n(0)}{n(z)}}.$$

In this formulation $K_E(0)$ and $n(0)$ are the eddy diffusion coefficient (m^2/s) and neutral density (m^{-3}) at a reference altitude.

In addition to transporting material, turbulent processes may also transport en-

ergy. According to *Gombosi* [1999] and *Richmond* [1983], eddy processes result in a net energy flux given by:

$$(1.33) \quad \mathbf{q}_{eddy} = -\rho c_p K_E [\nabla T + \Gamma_d].$$

Here, the eddy heat flux, \mathbf{q}_{eddy} , transports energy downward to the lower atmosphere, resulting in a net cooling effect on the upper atmosphere. Additionally, the term $\rho c_p K_E$ (W/K/m) functions as a turbulent heat conduction coefficient, analogous to κ_T in the formulation for thermal conduction. However, some, including *Hunten* [1974], contend that eddy fluxes contribute nothing to either heating or cooling, netting to zero. Conversely, *Roble et al.* [1988] includes eddy conduction as an integral component of the upper atmosphere's energetics. Furthermore, *Thomas* [1981] illustrates that eddy heat fluxes remain essential for properly characterizing the dynamics and energetics of the middle atmosphere. Thus, although eddy diffusion processes remain of paramount importance in planetary upper atmospheres, a great deal of debate surrounds their usage in theoretical models [*Hunten*, 1974; *Roble et al.*, 1988; *Thomas*, 1981].

The opposite process, that of separating constituents from one another, is governed by molecular diffusion. Molecular diffusion describes how individual fluid species diffuse through one another, termed binary diffusion, and varies inversely with their collision frequency. Mathematically, one can define a molecular diffusion coefficient as follows [*Gombosi*, 1999; *Schunk and Nagy*, 2000]:

$$(1.34) \quad D_s(z) = \frac{1}{\sum_t \nu_{st}} \frac{kT}{m_s}.$$

Here, ν_{st} is the bi-molecular collision frequency (Hz) between species “*s*” and species “*t*”. Binary molecular diffusion coefficients can be measured empirically and typically

follow the formulation of *Banks and Kockarts* [1973]:

$$(1.35) \quad D_s(z) = \frac{A_s T^b}{n(z)}.$$

In this expression, A_s and b represent experimentally determined parameters, and this represents the formulation employed by most theoretical calculations of planetary atmospheres. However, some aeronomers, such as *Boqueho and Bnelly* [2005], employ a more elegant formulation for the binary-diffusion coefficient, utilizing calculations of collisional integrals in their approach.

Finally, comparing equation 1.35 to that of 1.32, one sees that the eddy turbulence increases with altitude as $\frac{1}{\sqrt{n}}$, while the molecular diffusion increases at the faster rate of $\frac{1}{n}$. Thus, given these functional behaviors, at a sufficiently high altitude molecular diffusion overtakes micro-scale turbulence as the dominant diffusive process. This interplay between turbulence and molecular diffusion gives rise to another separation of the atmosphere.

Figure 1.7 depicts the typical behavior of eddy and molecular diffusion as functions of altitude. As shown in this figure, micro-scale turbulent processes dominate over molecular diffusion at low altitudes in a planetary atmosphere. Meanwhile, higher in the atmosphere, molecular diffusion overtakes and dominates eddy processes. Aeronomers denote the region where turbulence dominates as the homosphere, since atmospheric constituents mix homogeneously throughout the region. On the other hand, scientists dub the region where molecular diffusion dominates as the heterosphere, since atmospheric constituents in this region form a heterogeneous mixture, separating out according to their molecular weights. The transition region, where the eddy diffusion and molecular diffusion coefficients are nearly equivalent, is termed the homopause or the turbopause, which may span several atmospheric scale heights.

Ultimately, the antipodal processes of turbulence and of molecular diffusion play an important part in the transport of atmospheric constituents. Because of this, they can determine the local atmospheric composition, which itself plays an integral role in determining the thermal and dynamical structure.

1.4 The Upper Atmosphere

This thesis' research focuses almost exclusively on the thermosphere and ionosphere. In addition to these regions, it addresses, albeit to a minimal degree, the mesosphere and exosphere. Sections 1.4.1 – 1.4.4 outline the defining characteristics of each region, highlighting the physical processes and characteristics most important in the context of the present research.

1.4.1 The Mesosphere

The mesosphere resides below the thermosphere, as shown in Figure 1.2. At Earth, this region possesses a negative temperature gradient throughout its domain. Many complex chemical and aeronomical processes, such as airglow, occur in Earth's mesosphere. This region also remains the least understood by Earth atmospheric science, primarily due to its distance from both Earth's surface and satellites' orbits [*Schunk and Nagy, 2000; Gombosi, 1999*].

Planetary mesospheres distinguish themselves by the temperature minimum that usually occurs in these regions, as in Figure 1.2. In fact, this temperature minimum, which is termed the mesopause, serves as one of the mesosphere's defining characteristics. In the context of the current research, the mesosphere functions as a natural lower boundary because heat exchange between the thermosphere and mesosphere remains minimal [*Müller-Wodarg et al., 2000; Müller-Wodarg and Yelle, 2002*].

1.4.2 The Thermosphere

The thermosphere, depicted in Figure 1.2, is typically characterized by a positive temperature gradient and by an asymptotic temperature maximum at the highest altitudes. However, this generalization fails to hold on some planetary bodies, such as Venus and Titan. At Earth, this region represents a balance between solar extreme ultraviolet (EUV) absorption, radiative cooling, and molecular conduction. Thermospheric particles absorb solar shortwave EUV and x-ray radiation, heating the upper atmosphere. The efficiency with which an atmosphere converts absorbed solar radiation into thermal energy is termed the atmospheric heating efficiency [*Gombosi, 1999; Schunk and Nagy, 2000*].

Radiative cooling mechanisms almost always exist to balance the thermosphere's absorption of solar radiation, re-emitting longwave radiation outward into space. Although the specific constituents responsible for radiative cooling differ, this process has analogues in most of the known planetary atmospheres. Locally, radiative heating and cooling do not always balance one another, and, in such instances, molecular thermal conduction plays a major role in the upper atmosphere. The long path-lengths available to particles in the rarified upper atmosphere provide a natural conduit for molecular thermal conduction to transporting energy between atmospheric regions [*Schunk and Nagy, 2000*].

Finally, dynamics also plays an important role in the energy budget of planetary thermospheres. Dynamics typically provides a global, planetary-scale redistribution, rather than a localized transport of energy. In most instances, winds convect energy from warmer zones, such as the dayside or summer hemisphere, to cooler zones, such as the night side or winter hemisphere. The resulting global temperature structures can be quite counter-intuitive, such as a warmer-than-expected winter polar atmo-

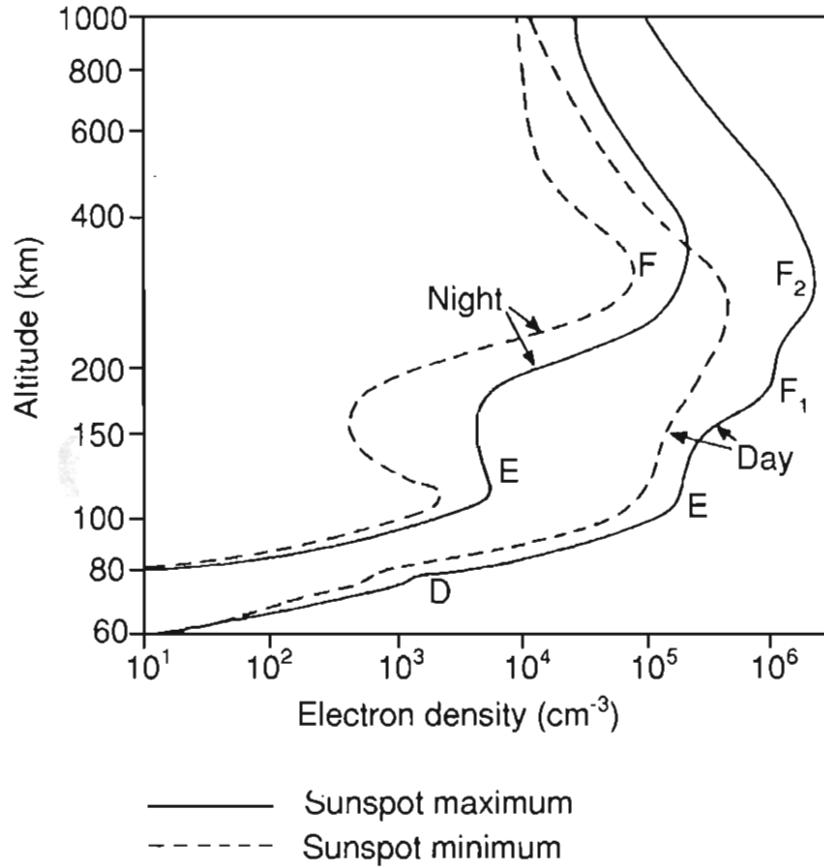


Figure 1.8: Pictured above is a schematic of the Earth's ionosphere as a template for all planetary ionospheres. The different regions are pictured above: D, E, F₁, and F₂. Also, the diurnal (day-night) variation of the different layers are pictured [Gombosi, 1999].

sphere. In summary, several key processes impact the thermosphere's structure, and investigating these physical drivers remains the primary focus of this thesis.

1.4.3 The Ionosphere

The ionosphere co-exists spatially with the thermosphere. However, unlike the neutral thermosphere, the ionosphere represents the upper atmosphere's ionized component. Because of this, ionospheres behave like weakly ionized plasmas in their dynamics [Gombosi, 1999; Schunk and Nagy, 2000]. This fact remains particularly important for magnetized planets, such as Earth. To a lesser degree, the ionospheric

dynamics possess importance even for the atmospheres of unmagnetized bodies, such as Venus, Mars, or Titan.

In general, solar EUV and x-ray radiation photoionize the neutral thermospheric particles, producing the planetary ionospheres. These ionospheres can also be populated by transported ions from other atmospheric regions, by incoming charged particles from space, or by chemical reactions between ions and neutrals. This thesis relegates itself to considering photoionization, chemical, and energetic particle impact mechanisms.

At Earth, several regions comprise the ionosphere. These are the D, E, F1, and F2 regions, shown in Figure 1.4.3. These regions differ in their chemical and physical properties, although it should be noted that these regions may or may not have analogues in other planetary ionospheres. The Earth's ionospheric layers, serving as a template, can be described as in *Schunk and Nagy* [2000] and *Chamberlain and Hunten* [1987]:

1. D-Region (60 – 90 km): Created due to x-ray and lyman- α ionization and disappears at night due to molecular collisions.
2. E-Region (90 – 150 km): Created due to solar EUV ionization and coincides with the vertical photoionization peak. Composed primarily of molecular ions (NO^+ at Earth).
3. F1-Region (150 – 200 km): This represents a photochemical production peak.
4. F2-Region (> 200 km): Represents a balance between photochemistry and vertical transport, where photochemical and diffusion time scales are comparable. Composed of primarily atomic ions (O^+ at Earth).

Ultimately, this thesis focuses on the dynamics of the thermosphere, downplaying

detailed considerations of the ionosphere. However, ionospheric feedbacks can become important to the neutral atmosphere's energetics and dynamics, making it a critical component of thermospheric modeling.

1.4.4 The Exosphere

The exosphere comprises an atmosphere's topside interface with interplanetary space, where the particles transition to a collisionless regime. This transition occurs when the atmospheric particle's mean free path, λ_{mfp} , equals its scale height. At this point, termed the exobase, the particles no longer experience collisions over a characteristic scale length of the atmosphere. The population of particles in an exosphere can be broken down into five primary groups [*Gombosi*, 1999; *Schunk and Nagy*, 2000]:

1. Ballistic particles that emerge from the exobase and fall back to the planetary upper atmosphere along elliptical orbits.
2. Trapped particles in bound orbits. These are created by collisions in the exosphere.
3. Escaping particles, coming up from the exobase along hyperbolic orbits.
4. Interplanetary neutral particles crossing the exobase.
5. Interplanetary neutral particles passing through the exosphere (not the exobase).

For the purposes of this thesis, the exobase functions as a natural upper boundary. Furthermore, the current research does not explicitly attempt to capture the complex exospheric physics self-consistently. Instead, only population (3), the escaping particles upward from the thermosphere into the exosphere, is considered.

Table 1.1: Selected Planetary Parameters for Earth, Mars, and Titan.

Planet Property	Earth	Mars	Titan
Mean Radius (km)	6,371.0	3,389.9	2,575.0
Mass ($\times 10^{23}$ kg)	59.736	6.4185	1.3455
Equatorial Gravity(m^2/s)	9.78	3.69	1.35
Mean Solar Day (Earth Days)	1.00	1.027	15.945

1.5 Investigating Two Planetary Bodies: Mars and Titan

Having explored in detail the general characteristics and physical processes that most planetary atmospheres share in common, one may now turn to the physics and chemistry in the upper atmospheres of two terrestrial bodies: Mars and Titan. At Mars, this thesis illustrates how the phenomenon of winter polar warming, which was observed by Mars Odyssey and Mars Global Surveyor, can be explained through a global circulation, encompassing the entire Mars atmosphere from the surface to the exosphere. At Titan, this research explores the fundamental physical processes that produce the structures observed by the Ion-Neutral Mass Spectrometer (INMS) experiment onboard the Cassini spacecraft. In both cases, this thesis employs computational three-dimensional global circulation models to explore the physics and chemistry of these upper atmospheres.

1.5.1 Mars

Mars, named after the Roman god of war, is the fourth planet from the sun, appearing prominently in Earth's night sky. Table 1.1 contains selected parameters for Mars. Mars remains roughly 1/2 Earth's size with a similar rotational period of 24h 36m 22.65s. However, it possesses a highly eccentric orbit relative to Earth, with a perihelion of 1.381 AU and an aphelion of 1.666 AU, resulting in more extreme differences between its solstice periods. At its surface, Mars' upper atmosphere is composed primarily of CO₂ (95.3 %), N₂ (2.7 %), Ar (1.6 %), O₂ (0.13 %), and H₂O

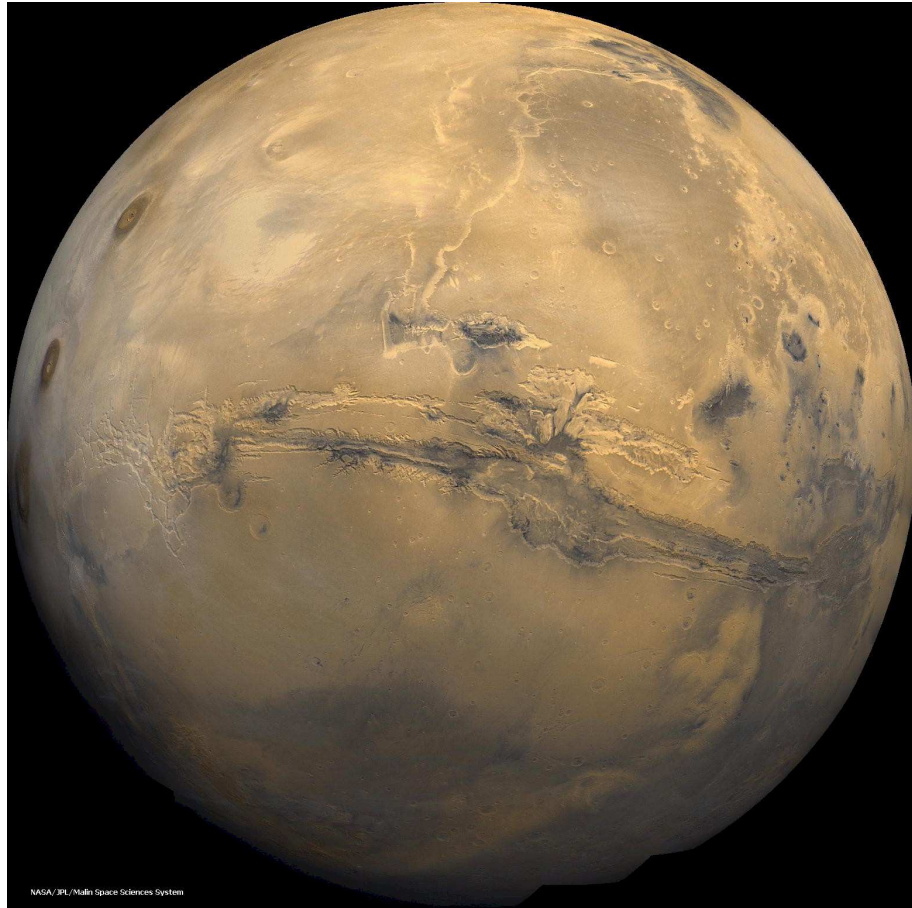


Figure 1.9: A close-up picture of Mars' surface with no polar ice caps visible. The surface of mars is clearly visible in this picture, but can be almost completely occluded by global dust storms that originate in the lowlands to the South. Courtesy NASA Public Image Database.

(0.03 %), possessing a surface pressure of roughly 6 milibars, which is approximately 1 % of Earth's surface pressure. Figure 1.10 depicts the red planet's primary neutral thermospheric constituents as a function of altitude, while Figure 1.11 similarly contains its primary ionospheric constituents as a function of altitude.

Although recorded Mars observations by humans began with the Pharaonic Egyptians, modern Martian science began with the first *in situ* measurements by the Mariner 4 spacecraft in 1965. Since Mariner 4, many scientific missions departed for Mars; however, perhaps the most elucidating observations have been made by the long-term orbiting satellites Mars Global Surveyor (MGS), Mars Odyssey (ODY),

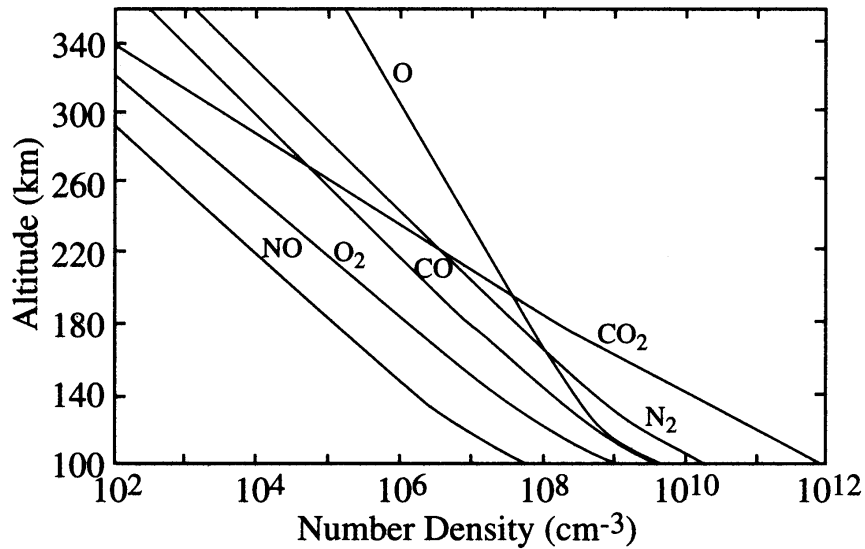


Figure 1.10: Vertical composition of Mars' thermosphere, illustrating the major neutral constituents above 100 km. Adapted from Schunk and Nagy [2000]

Mars Reconnaissance Orbiter (MRO), and the newly arrived Mars Express (MEX). MGS and ODY have provided a plethora of both remote and *in situ* measurements, cataloguing the variations in Mars atmosphere over time [Liu *et al.*, 2003; Keating *et al.*, 1998]. Despite the pure scientific value of these experiments, what has been the ultimate impetus for studying our sister planet so closely?

Why Study Mars?

In 1996, the wildly successful Mars Pathfinder project brought images of the planet's surface directly to a new generation of Americans, ushering in a renewed fascination with solar system exploration not felt since the NASA moon landings of the late 1960's and early 1970's. Additionally, the combined experiments onboard the orbiting satellites MGS and ODY, along with the ground-based observations of the Mars Expedition Rovers "Opportunity" and "Spirit," indicated geological traces of past and present water. This incredible discovery has tasked planetary scientists to explain where this water went and where it may currently be located. Moreover,

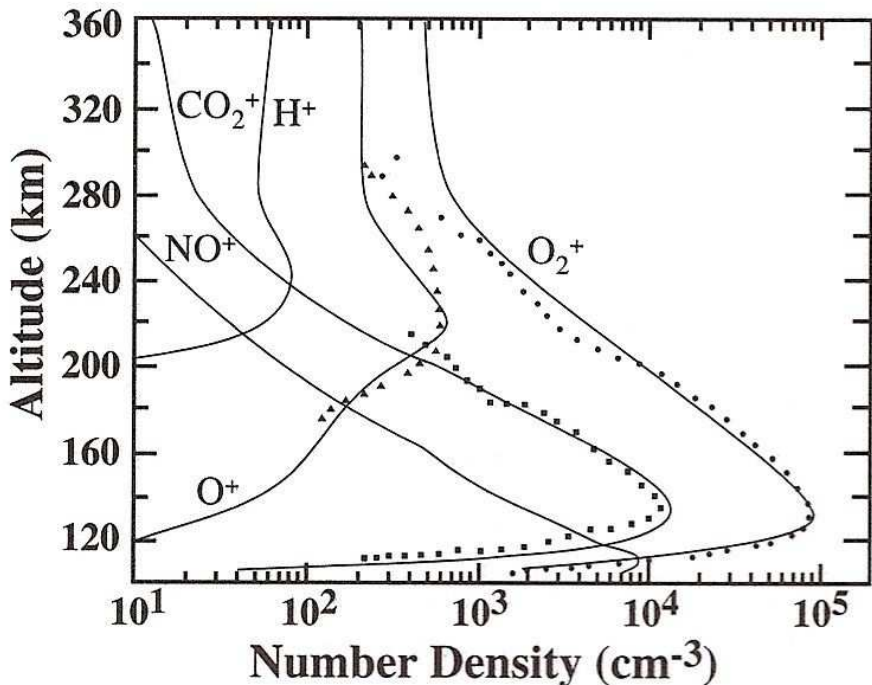


Figure 1.11: Vertical composition of Mars' Ionosphere, illustrating the major ion constituents above 100 km. Adapted from *Schunk and Nagy* [2000]

these discoveries have led many to posit that Mars, early in its history, may have resembled an early Earth, replete with rivers, oceans, and lakes of liquid water. These exciting revelations, combined with a renewed emphasis by NASA to achieve a manned space flight to Mars in the next half century, has forced modern scientists to ask, “Where did the water go?”

In order to better address this question, planetary scientists have begun to investigate how the Martian atmosphere evolved over its lifetime. The planetary community has attacked this question on two fronts: (1) from the geological record of Mars [Carr, 2006; Carr and Head, 2003; Jakosky *et al.*, 1997, 2005], and (2) from the atmospheric escape of constituents from Mars [Chaufray *et al.*, 2007; Chassefière *et al.*, 2007; Leblanc and Johnson, 2002]. In the latter case, many planetary aeronomers have begun to identify the various loss processes from the Martian upper atmosphere

to space. In particular, the scientific community has endeavored to create a paleoclimatological model that might better explain how Mars existed during past epochs and how it evolved to its current state.

A Newly Discovered Problem: Winter Polar Warming

However, in order to realistically explore the paleo-climate of Mars, one must first be capable of explaining the current state of the Martian atmosphere. Ironically, the satellites MGS and ODY that have elicited so much interest in Martian water sources and losses, have uncovered another major scientific conundrum: thermospheric winter polar warming [*Keating et al.*, 1998, 2003]. The data depicting winter polar warming appear in Figure 1.12, which contains the temperatures inferred from both MGS and ODY aerobraking data at 120 km. In this figure, thermospheric temperatures rise significantly from mid-latitudes into the winter polar regions, resulting in a counter-intuitive thermal structure for which no explanation existed.

However, *Bouger et al.* [2006] and *Bell et al.* [2007] posited a dynamical solution to this scientific puzzle, using theoretical/numerical modeling tools. These authors suspected that the enormous reservoir of lower atmospheric dust could dominate the circulation in the upper atmosphere, leading to the formation of these anomalous temperature structures in the winter polar thermosphere. Indeed, by utilizing realistic dust loading in the lower atmosphere, *Bouger et al.* [2006] illustrated that the coupled Mars General Circulation Model – Mars Thermosphere General Circulation Model (MGCM-MTGCM) reproduced winter polar thermosphere temperatures consistent with measurements. Expanding upon this work, *Bell et al.* [2007] found that winter polar warming occurs due to the presence of an integrated atmospheric response to dust forcing in the lower atmosphere. They found that the entire atmosphere of Mars responds with a global interhemispheric Hadley circulation, extending

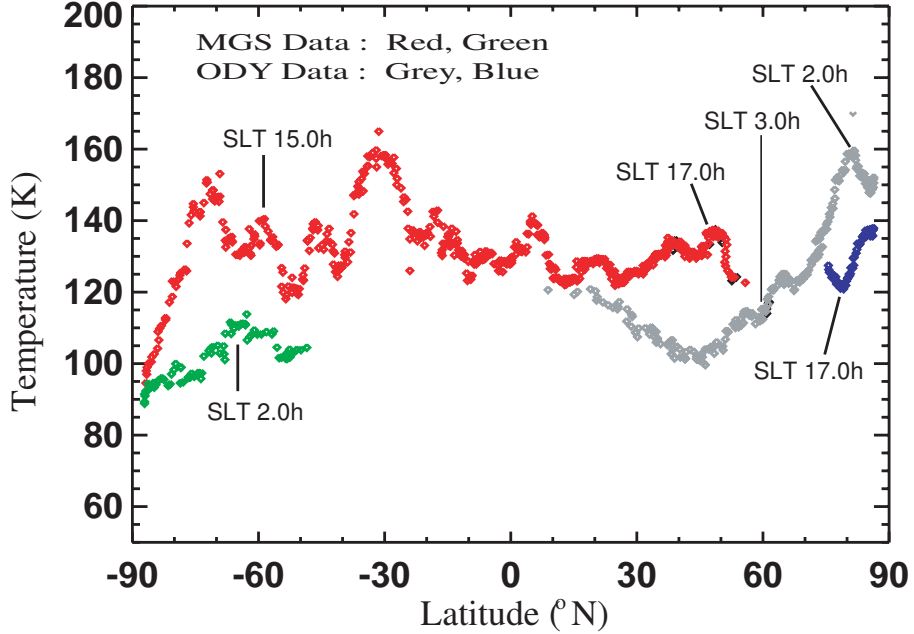


Figure 1.12: This plot represents a composite over many flybys of aerobraking inferred temperatures from the MGS (red and green data) and ODY (gray and blue data) Missions. The solar local time (SLT) for the data are indicated by the labels. MGS aerobraking occurred over the southern winter hemisphere, while ODY aerobraking occurred over the northern winter pole. All data values were at the same altitude of 120 km. Adapted from *Bouger et al.* [2006]

from the surface to the exobase, to produce the measured winter polar temperatures.

These researchers further found that, in order to model the Martian atmosphere, a self-consistent treatment of the lower and upper atmospheres must be employed.

Chapter 4 contains the details of this research by *Bell et al.* [2007]. Ultimately, the greatest contribution of this particular work resides in its qualitative and quantitative illustrations of how intimately coupled the Mars atmospheric system remains. Additionally, these anomalous structures emerge as dynamically driven, as opposed to radiatively driven, meaning that, on a global scale, dynamics dominates the Martian upper atmosphere.



Figure 1.13: A close up picture of Titan's hazy atmosphere, along with detached high altitude haze layers (purple hazes on the edge of the planet). These hazes can impact the chemical and radiative character of the atmospheric layers within which they reside. Courtesy NASA Public Image Database.

1.5.2 Titan

Titan, the second largest moon in the solar system and the largest of the Saturnian system, derives its name from the Grecian elder gods. Titan's surface, until recently, has been shrouded from view by thick hydrocarbon hazes that permeate the atmosphere, as shown in Figure 1.13. Its atmosphere at the surface consists primarily of N_2 (98.4 %) and CH_4 (1%), making Titan and Earth the only two nitrogen-rich planetary atmospheres in our solar system. H_2 , H , complex organic hydrocarbons, and nitriles comprise the remainder of Titan's atmosphere. Furthermore, Titan pos-

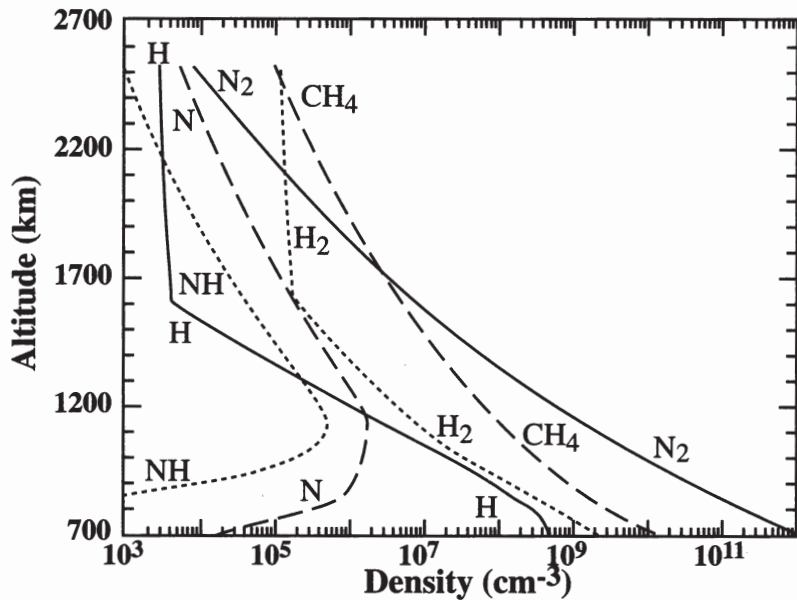


Figure 1.14: Vertical composition of Titan’s thermosphere, illustrating the major constituents and some key minor constituents. Adapted from *Schunk and Nagy* [2000]

seses a surface pressure of roughly 1.5 bars – 50 % larger than Earth’s atmospheric pressure at sea-level. Figure 1.14, adapted from *Schunk and Nagy* [2000], depicts the thermospheric neutral composition of Titan as a function of altitude above 700 km.

Scientific Motivation for Studying Titan

Unlike Mars, Titan’s discovery did not occur until 1655, when it was observed by Christian Huygen’s. Nearly 300 years later, *Kuiper* [1944] detected Methane on Titan in the visible spectrum at 6190 Å. *Jaffe et al.* [1980] re-measured the methane abundance on Titan and concluded that the moon most likely possessed a surface temperature 87.6 K, for which the model of *Hunten* [1978] predicted a surface pressure of 1 bar. Furthermore, Earth-based observations of Titan found evidence of heavy organics, C_2H_4 , C_3H_8 , C_2H_6 , and C_2H_2 , in Titan’s atmosphere [Gillett et al., 1973; Gillett, 1975; Danielson et al., 1973] , making this celestial object, like Earth, ultimately one of the most unique in the solar system. However, the main

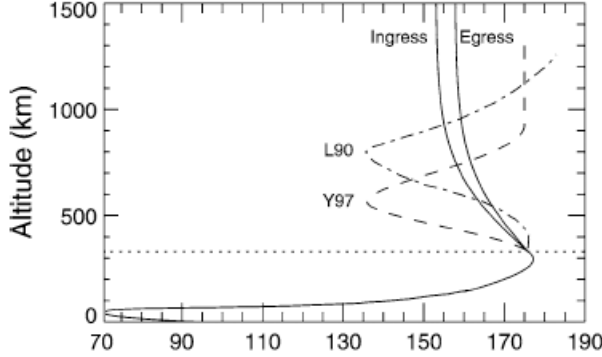


Figure 1.15: Reanalysis of neutral temperatures by *Vervack et al.* [2004]. This reanalysis radically differed from accepted temperature profiles at the time, shown in this figure as the *Yelle et al.* [1997] (Y97) and *Lellouch* [1990] (L90) temperature profiles.

atmospheric gas remained elusive, but was suspected to be one of Ne, Ar, or N_2 .

On November 12, 1980 Voyager 1 made a close encounter with Titan, measuring N_2 as the most abundant gas and putting to rest the mystery of Titan's composition. In the upper atmosphere, N_2 , CH_4 , and C_2H_2 were measured by the Voyager ultraviolet spectrometer in a solar occultation experiment [*Broadfoot et al.*, 1981], providing scale heights and temperatures. These measurements implied a thermospheric exobase temperature of roughly 186 ± 20 K [*Broadfoot et al.*, 1981; *Smith et al.*, 1982]. In the lower atmosphere, *Samuelson et al.* [1981] and *Hunten et al.* [1984] derived a mean surface temperature of roughly 95 K. This inspired others to speculate that Titan could serve as a cryogenic version of a pre-biotic Earth, as discussed in *Sagan and Thompson* [1984] and *Clarke and Ferris* [1997].

Despite these discoveries, a great deal of mystery still surrounded Titan. Using Earth-based observations, *Hubbard et al.* [1993] detected differential super-rotating winds in Titan's stratosphere. In sharp contrast to previous analysis, *Vervack et al.* [2004] reanalyzed the Voyager 1 data, resulting in a new temperature profile shown in Figure 1.15. In this figure, the newly derived temperature by *Vervack et al.* [2004] was overlain with the previously accepted temperature profiles of *Yelle et al.* [1997]

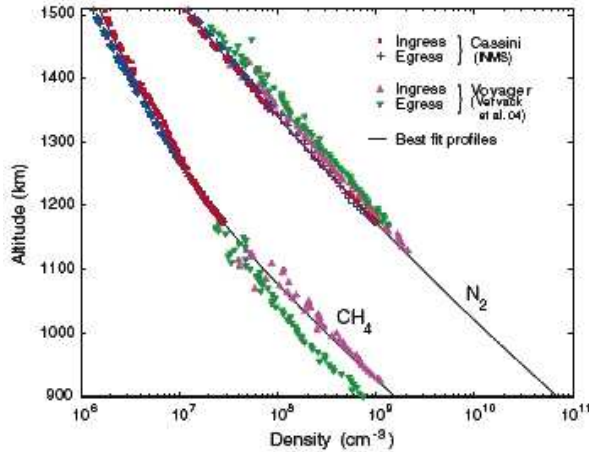


Figure 1.16: Vertical profiles of the N_2 and CH_4 densities from the Cassini INMS measurements [Waite *et al.*, 2005, 2004].

and *Lellouch* [1990], which were based upon the previous analysis of the Voyager 1 flyby datasets. Finally, in 1998 the Cassini-Huygen's spacecraft was launched and the first dedicated Titan mission got underway.

In October, 2004, Cassini arrived at Titan for the first time and a plethora of new data flooded the planetary community. In particular, the Cassini Ion-Neutral Mass Spectrometer (INMS) shed new light on the upper atmospheric composition by *in situ* measurements of the major and minor constituent densities with unprecedented resolution [Waite *et al.*, 2004, 2005]. Figure 1.16 contains the densities measured by INMS. Furthermore, the derived temperature structure contains wave-like variations, shown in Figure 1.17. These temperature perturbations possess a vertical wavelength of nearly 100 km with a 10 K amplitude. The sources for the waves have remained a mystery and illustrate the fascinating structures that remain unexplained in the atmosphere of this distant world.

Amidst this renewed era of discovery and excitement surrounding Titan, numerical and theoretical modeling is simultaneously emerging as a mature field in its own right. The convergence of improved theoretical tools and the influx of new discoveries

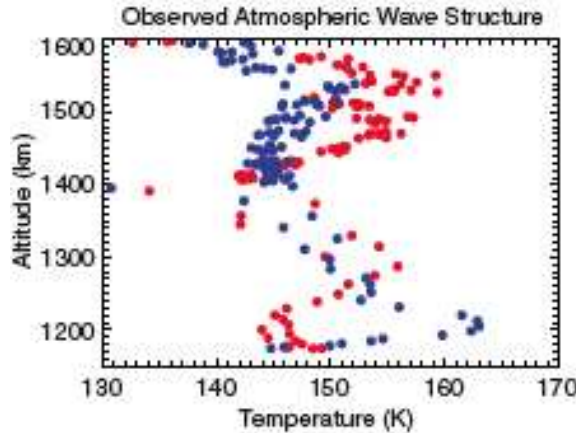


Figure 1.17: Fascinating wave structures occur in the temperature profile of Titan's upper atmosphere [Waite *et al.*, 2005]. Although many mechanisms could possibly cause this structure, its true nature has yet to be explained fully.

fortuitously places this thesis at a fulcrum point, where the computational and theoretical capabilities now enable the construction of complex three dimensional models that are reliable enough to explore the dynamics of planetary atmospheres. Thus, this thesis introduces a new theoretical framework for Titan's upper atmosphere, the Titan Global Ionosphere-thermosphere Model, which derives itself from state of the art numerical frameworks developed at the University of Michigan [Ridley *et al.*, 2006; Tóth *et al.*, 2005]. Utilizing this theoretical tool, the physical processes producing the measured structures by INMS are analyzed. To this end, this thesis aims for two primary goals: (1) to benchmark the model against Cassini INMS data and (2) to analyze and discuss the physics producing the observed structures. Through this process, this research attempts to reach a greater understanding of the physics governing Titan's upper atmosphere and atmospheric systems in general.

1.6 The Remainder of the Thesis: An Brief Outline of What is to Come

The remainder of the thesis focuses on the detailed physics and chemistry of the Thermosphere-Ionosphere systems of both Mars and Titan. To that end, chapter 2

derives the theoretical underpinnings of planetary aeronomy, the Navier-Stokes equations. Chapter 3 explores the theoretical/numerical frameworks that are used in this thesis. Chapter 4 explores the phenomenon of winter polar warming in Mars upper atmosphere, which emerges as a whole-atmosphere dynamical response of the Martian atmosphere. Chapter 5 explores the primary physical and chemical processes in Titan’s thermosphere-ionosphere. In this chapter, we also explore to what extent the various dynamical, radiative, and chemical forcing terms dominate in this moon’s upper atmosphere. Finally, chapter 6 compares the Titan theoretical model’s calculations with Cassini INMS (ion-neutral mass spectrometer) *in situ* measurements of neutral density and temperature. This section serves as a benchmark for the validity of the model. Finally, Chapter 7 distills the lessons learned about the dynamics of both Mars and Titan into lessons that can be applied to all planetary atmospheres, both within and without our solar system.

CHAPTER II

The Navier-Stokes Fluid Equations

Mathematics is the language with which God has written the universe.

– Galileo Galilei

2.1 Introduction

Before exploring the physics and chemistry of Mars and Titan, one must first delve into the mathematical physics of fluids. This chapter begins with the most fundamental transport equation, the Boltzmann Equation, and subsequently builds up to the Navier-Stokes equations, which form the theoretical framework for the research in Chapters 4 – 6 [Schunk and Nagy, 2000; Gombosi, 1999].

2.2 Phase Space Distribution Function

The 7-dimensional phase space distribution function, f_s , represents the core mathematical description of multi-component fluids. This function describes the spatial and temporal evolution of the atmospheric particles of species “s.” In this 7-dimensional phase space, the 3-component position vector, \mathbf{r} , 3-component velocity vector, \mathbf{v} , and time, t , act as 7 independent variables. In a coordinate-independent form, the vector quantities \mathbf{r} and \mathbf{v} become:

$$(2.1) \quad \mathbf{r} = x_1 \hat{x}_1 + x_2 \hat{x}_2 + x_3 \hat{x}_3,$$

$$(2.2) \quad \mathbf{v} = \frac{d\mathbf{r}}{dt} = \frac{dx_1}{dt}\hat{x}_1 + \frac{dx_2}{dt}\hat{x}_2 + \frac{dx_3}{dt}\hat{x}_3.$$

Mathematically, $f_s(\mathbf{r}, \mathbf{v}, t)$ represents the number of fluid particles of species “s” at a specific time t , located between \mathbf{r} and $\mathbf{r} + d\mathbf{r}$ and possessing a velocity between \mathbf{v} and $\mathbf{v} + d\mathbf{v}$. Physically measurable fluid properties arise by taking velocity moments of the phase-space distribution function. For instance, the number density, n_s , arises from integrating f_s over all velocity space:

$$(2.3) \quad n_s(\mathbf{r}, t) = \iiint_{-\infty}^{+\infty} f_s(\mathbf{r}, \mathbf{v}, t) d^3\mathbf{v}.$$

$n_s(\mathbf{r}, t)$ represents the total number density of species “s” (m^{-3}) located between positions \mathbf{r} and $\mathbf{r} + d\mathbf{r}$ at a time t . By taking higher order velocity moments of f_s , more fluid properties emerge. One derives the average flow velocity for species “s”, $\mathbf{u}_s(\mathbf{r}, t)$, by taking the first velocity moment of the phase space distribution:

$$(2.4) \quad n_s(\mathbf{r}, t) \mathbf{u}_s(\mathbf{r}, t) = \iiint_{-\infty}^{+\infty} \mathbf{v}_s f_s(\mathbf{r}, \mathbf{v}, t) d^3\mathbf{v}.$$

Dividing both sides by $n_s(\mathbf{r}, t)$, one obtains another expression for the average (bulk) velocity:

$$(2.5) \quad \mathbf{u}_s(\mathbf{r}, t) = \frac{1}{n_s(\mathbf{r}, t)} \iiint_{-\infty}^{+\infty} \mathbf{v}_s f_s(\mathbf{r}, \mathbf{v}, t) d^3\mathbf{v},$$

or, alternatively in integral form:

$$(2.6) \quad \mathbf{u}_s(\mathbf{r}, t) = \frac{\iiint_{-\infty}^{+\infty} \mathbf{v}_s f_s(\mathbf{r}, \mathbf{v}, t) d^3\mathbf{v}}{\iiint_{-\infty}^{+\infty} f_s(\mathbf{r}, \mathbf{v}, t) d^3\mathbf{v}}.$$

This last expression closely resembles the expectation value, $\langle \rangle$, of a probability distribution. Using this analogy, one derives the expectation value for any measurable physical quantity, $\zeta_s(\mathbf{r}, \mathbf{v}, t)$, from the following integral equation:

$$(2.7) \quad \langle \zeta_s(\mathbf{r}, \mathbf{v}, t) \rangle = \frac{\iiint_{-\infty}^{+\infty} \zeta_s(\mathbf{r}, \mathbf{v}, t) f_s(\mathbf{r}, \mathbf{v}, t) d^3\mathbf{v}}{\iiint_{-\infty}^{+\infty} f_s(\mathbf{r}, \mathbf{v}, t) d^3\mathbf{v}} = \frac{1}{n_s(\mathbf{r}, t)} \iiint_{-\infty}^{+\infty} \zeta_s(\mathbf{r}, \mathbf{v}, t) f_s(\mathbf{r}, \mathbf{v}, t) d^3\mathbf{v}.$$

Hence, the bulk velocity, $\mathbf{u}_s(\mathbf{r}, t)$, can be re-defined as:

$$(2.8) \quad \mathbf{u}_s(\mathbf{r}, t) = \langle \mathbf{v}_s \rangle = \frac{1}{n_s(\mathbf{r}, t)} \iiint_{-\infty}^{+\infty} \mathbf{v}_s f_s(\mathbf{r}, \mathbf{v}, t) d^3 \mathbf{v}.$$

Using this mean velocity, the species' thermal velocity, \mathbf{c}_s , emerges as:

$$(2.9) \quad \mathbf{c}_s = \mathbf{v}_s - \mathbf{u}_s.$$

Using this definition, the scalar pressure, p_s , arises from:

$$(2.10) \quad \frac{1}{\gamma - 1} p_s = \frac{1}{\gamma - 1} n_s k T_s = \frac{1}{2} n_s m_s \langle \mathbf{c}_s \cdot \mathbf{c}_s \rangle = \frac{m_s}{2} \iiint_{-\infty}^{+\infty} f_s(\mathbf{r}, \mathbf{v}, t) (\mathbf{v}_s - \mathbf{u}_s) \cdot (\mathbf{v}_s - \mathbf{u}_s) d^3 \mathbf{v},$$

where γ represents the specific heat ratio for the fluid, $\gamma = c_p/c_v$. Equation (2.10) generalizes readily, producing a second-order pressure tensor given by:

$$(2.11) \quad \mathbf{P}_s = n_s m_s \langle \mathbf{c}_s \mathbf{c}_s \rangle = m_s \iiint_{-\infty}^{+\infty} f_s(\mathbf{r}, \mathbf{v}, t) (\mathbf{v}_s - \mathbf{u}_s) (\mathbf{v}_s - \mathbf{u}_s) d^3 \mathbf{v}.$$

In this last equation, $\langle \mathbf{c}_s \mathbf{c}_s \rangle$ represents the direct product of \mathbf{c}_s with itself, forming a rank-two tensor. This pressure tensor decomposes as follows:

$$(2.12) \quad \mathbf{P}_s = \mathbf{I} p_s + \boldsymbol{\tau}_s.$$

Here, \mathbf{I} is the unit tensor, p_s is the scalar pressure, and $\boldsymbol{\tau}_s$ is a traceless rank two tensor that measures the fluid's deviation from isotropic character.

With this elegant mathematical machinery, one can continue taking moments of the distribution function *ad infinitum*, producing an entire suite of variables, such as higher-order heat flux vectors or stress tensors. However, the time evolution of the phase-space distribution ultimately contains the most important physics for fluid dynamics, leading inexorably to the Boltzmann equation.

2.3 Time Evolution of the Phase Space Distribution: Boltzmann Equation

The time-derivative of the phase-space distribution function arises directly from a straightforward application of multivariate vector calculus:

$$(2.13) \quad \frac{df_s(\mathbf{r}, \mathbf{v}, t)}{dt} = \lim_{\Delta t \rightarrow 0} \frac{f_s(\mathbf{r} + \Delta\mathbf{r}, \mathbf{v} + \Delta\mathbf{v}, t + \Delta t) - f_s(\mathbf{r}, \mathbf{v}, t)}{\Delta t}.$$

In complete analogy to single variable calculus, one may perform a Taylor expansion in terms of the vector quantities \mathbf{r} and \mathbf{v} , giving:

$$(2.14) \quad \frac{df_s(\mathbf{r}, \mathbf{v}, t)}{dt} = \lim_{\Delta t \rightarrow 0} \frac{1}{\Delta t} \left[f_s(\mathbf{r}, \mathbf{v}, t) + \frac{\partial f_s}{\partial t} \Delta t + \Delta\mathbf{r} \cdot \nabla f_s + \Delta\mathbf{v}_s \cdot \nabla_v f_s + \dots - f_s(\mathbf{r}, \mathbf{v}, t) \right].$$

Retaining only the first-order terms, which is appropriate for most atmospheric considerations, a simplified version of the total time derivative arises as:

$$(2.15) \quad \frac{\delta f_s(\mathbf{r}, \mathbf{v}, t)}{\delta t} = \lim_{\Delta t \rightarrow 0} \left[\frac{\partial f_s}{\partial t} + \frac{\Delta\mathbf{r}}{\Delta t} \cdot \nabla f_s + \frac{\Delta\mathbf{v}_s}{\Delta t} \cdot \nabla_v f_s \right].$$

As Δt approaches 0, the vector differences in the previous equation become familiar vector derivatives, with velocity defined as:

$$(2.16) \quad \mathbf{v}_s = \lim_{\Delta t \rightarrow 0} \frac{\Delta\mathbf{r}}{\Delta t},$$

and acceleration defined as: \mathbf{a}_s :

$$(2.17) \quad \mathbf{a}_s = \lim_{\Delta t \rightarrow 0} \frac{\Delta\mathbf{v}_s}{\Delta t}.$$

Thus, the phase space distribution's time derivative becomes:

$$(2.18) \quad \frac{\delta f_s(\mathbf{r}, \mathbf{v}, t)}{\delta t} = \frac{\partial f_s}{\partial t} + \mathbf{v}_s \cdot \nabla f_s + \mathbf{a}_s \cdot \nabla_v f_s.$$

Equation (2.18) is the famous Boltzmann equation, which describes the fluid's evolution in space and time. In this expression, $\frac{\delta f_s(\mathbf{r}, \mathbf{v}, t)}{\delta t}$ denotes that the time derivative equation is not exact, but instead represents a relaxation f_s due to collisional

processes. In planetary atmospheres, the acceleration term, \mathbf{a}_s , is composed of gravitational, lorentz, coriolis, and centripetal forces:

$$(2.19) \quad \mathbf{a}_s = -\mathbf{G} + \frac{q_s}{m_s}(\mathbf{E} + \mathbf{v}_s \times \mathbf{B}) + 2\boldsymbol{\Omega}_r \times \mathbf{v}_s + \boldsymbol{\Omega}_r \times (\boldsymbol{\Omega}_r \times \mathbf{r}).$$

Where $\boldsymbol{\Omega}_r$ represents the planetary rotation rate, \mathbf{G} is the gravitational acceleration, $\mathbf{E} = \mathbf{E}(\mathbf{r}, t)$ is an externally imposed electric field, and $\mathbf{B} = \mathbf{B}(\mathbf{r}, t)$ is an external magnetic field.

2.4 From Boltzmann to the Generalized Transport Equations

The Boltzmann equation describes the fluid phase space distribution's evolution. However, in order to obtain information about measurable, physical quantities, one must take velocity moments of Equation (2.18). First, a few vector identities must be reviewed:

$$(2.20) \quad \nabla \cdot (f_s \mathbf{v}_s) = \mathbf{v}_s \cdot (\nabla f_s) + f_s (\nabla \cdot \mathbf{v}_s).$$

However, because \mathbf{v}_s and \mathbf{r} represent independent variables in the context of the fluid's 7-dimensional phase space, Equation (2.20) becomes:

$$(2.21) \quad \nabla \cdot (f_s \mathbf{v}_s) = \mathbf{v}_s \cdot (\nabla f_s).$$

In a way analogous to Equations (2.20) and (2.21) for the spatial derivative, similar simplifications exist for the velocity gradient, ∇_v :

$$(2.22) \quad \nabla_v \cdot (f_s \mathbf{a}_s) = \mathbf{a}_s \cdot (\nabla_v f_s) + f_s (\nabla_v \cdot \mathbf{a}_s).$$

If one considers the acceleration term of Equation (2.19), only two terms depend explicitly upon velocity: $2\boldsymbol{\Omega}_r \times \mathbf{v}_s$, and $\mathbf{v}_s \times \mathbf{B}$. In order to evaluate their velocity divergence, one must recall the following relationship for any two arbitrary vector

quantities, \mathbf{A} and \mathbf{C} :

$$(2.23) \quad \nabla \cdot (\mathbf{A} \times \mathbf{C}) = \mathbf{C} \cdot (\nabla \times \mathbf{A}) - \mathbf{A} \cdot (\nabla \times \mathbf{C})$$

Substituting in for the two velocity-dependent terms, one derives the following:

$$(2.24) \quad \nabla_v \cdot (\boldsymbol{\Omega}_r \times \mathbf{v}_s) = \mathbf{v}_s \cdot (\nabla_v \times \boldsymbol{\Omega}_r) - \boldsymbol{\Omega}_r \cdot (\nabla_v \times \mathbf{v}_s) = -\boldsymbol{\Omega}_r \cdot (\nabla_v \times \mathbf{v}_s)$$

$$(2.25) \quad \nabla_v \cdot (\mathbf{v}_s \times \mathbf{B}) = \mathbf{B} \cdot (\nabla_v \times \mathbf{v}_s) - \mathbf{v}_s \cdot (\nabla_v \times \mathbf{B}) = \mathbf{B} \cdot (\nabla_v \times \mathbf{v}_s)$$

However, the term $\nabla_v \times \mathbf{v}_s$ remains identically zero, in complete analogy to $\nabla \times \mathbf{r} = \mathbf{0}$.

Thus, both terms possess zero velocity space divergence, resulting in Equation (2.22) simplifying to:

$$(2.26) \quad \nabla_v \cdot (f_s \mathbf{a}_s) = \mathbf{a}_s \cdot (\nabla_v f_s).$$

Using expressions (2.21) and (2.26), the Boltzmann equation immediately becomes:

$$(2.27) \quad \frac{\delta f_s(\mathbf{r}, \mathbf{v}, t)}{\delta t} = \frac{\partial f_s}{\partial t} + \nabla \cdot (\mathbf{v}_s f_s) + \nabla_v \cdot (\mathbf{a}_s f_s).$$

Equation (2.27) describes the Boltzmann equation in conservative form, since the total time evolution of the phase space distribution, $\frac{\delta f_s(\mathbf{r}, \mathbf{v}, t)}{\delta t}$, depends only on $\frac{\partial f_s}{\partial t}$ and the generalized fluxes $(\mathbf{v}_s f_s)$ and $(\mathbf{a}_s f_s)$. Using Equation (2.27), one may derive the Navier-Stokes fluid transport equations by taking appropriate velocity moments, as was done earlier with the phase-space distribution.

2.4.1 Continuity Equation

In order to derive the Navier-Stokes equations, one begins with the zeroth velocity moment of Equation (2.27) by integrating over all velocity space:

$$(2.28) \quad \iiint_{-\infty}^{+\infty} \frac{\delta f_s(\mathbf{r}, \mathbf{v}, t)}{\delta t} d^3 \mathbf{v} = \iiint_{-\infty}^{+\infty} \left[\frac{\partial f_s}{\partial t} + \nabla \cdot (\mathbf{v}_s f_s) + \nabla_v \cdot (\mathbf{a}_s f_s) \right] d^3 \mathbf{v}.$$

The right-hand side of this integral equation can be broken down and re-written term-wise. The first term on the right-hand side becomes:

$$(2.29) \quad \iiint_{-\infty}^{+\infty} \frac{\partial f_s}{\partial t} d^3\mathbf{v} = \frac{\partial}{\partial t} \iiint_{-\infty}^{+\infty} f_s d^3\mathbf{v} = \frac{\partial n_s(\mathbf{r}, t)}{\partial t}.$$

In this integral, one recalls that time and \mathbf{v}_s represent independent variables in the fluid phase space, enabling the time derivative to be moved outside the velocity space integral. Additionally, this last equation utilizes the definition for $n_s(\mathbf{r}, t)$ derived in Equation (2.3).

In the second term on the right-hand side of (2.27), the spatial divergence, ∇ , may be taken outside of the velocity-space integral, since \mathbf{r} and \mathbf{v}_s represent independent variables:

$$(2.30) \quad \iiint_{-\infty}^{+\infty} \nabla \cdot (\mathbf{v}_s f_s) d^3\mathbf{v} = \nabla \cdot \iiint_{-\infty}^{+\infty} (\mathbf{v}_s f_s) d^3\mathbf{v} = \nabla \cdot (n_s(\mathbf{r}, t) \mathbf{u}_s(\mathbf{r}, t)).$$

This last expression utilizes Equation 2.4. Finally, with the last term on the right-hand side of Equation (2.27), one may apply Gauss' law to the volume integral. Gauss's law in this context applies to any generalized vector, \mathbf{V} , in velocity space:

$$(2.31) \quad \iiint_{-\infty}^{+\infty} \nabla_v \cdot \mathbf{V} d^3\mathbf{v} = \iint_{-\infty}^{+\infty} \mathbf{V} \cdot d\mathbf{A}_v.$$

In this expression, the velocity volume integral becomes a velocity surface integral. Furthermore, because the choice of Gaussian surface remains arbitrary, represented by $d\mathbf{A}_v$, one may choose it to be a spherical velocity surface with a radius, $|\mathbf{v}|$, such that $|\mathbf{v}| \rightarrow \infty$. However, because no particles may physically exist with an infinite velocity, then the phase-space distribution necessarily evaluates to zero along the entire Gaussian spherical surface. Thus, the surface integral in Gauss's law must also become identically zero, resulting in:

$$(2.32) \quad \iiint_{-\infty}^{+\infty} \nabla_v \cdot (\mathbf{a}_s f_s) d^3\mathbf{v} = \iint_{-\infty}^{+\infty} (\mathbf{a}_s f_s) \cdot d\mathbf{A}_v = 0.$$

Finally, the left-hand side of Equation (2.27) may be dealt with. If one integrates over the phase space distribution's collisional time derivative, then it produces:

$$(2.33) \quad \iiint_{-\infty}^{+\infty} \frac{\delta f_s(\mathbf{r}, \mathbf{v}, t)}{\delta t} d^3 \mathbf{v} = \frac{\delta n_s}{\delta t}.$$

Here, $\frac{\delta n_s}{\delta t}$ represents the neutral density's total time evolution due to collisional relaxation. Thus, the *neutral density continuity equation* finally emerges by re-writing Equation (2.28) as:

$$(2.34) \quad \frac{\delta n_s}{\delta t} = \frac{\partial n_s}{\partial t} + \nabla \cdot (\mathbf{u}_s n_s).$$

2.4.2 Momentum Equation

The Navier-Stokes momentum equation, which mathematically describes fluid's response to the forces that it experiences, arises from taking the first velocity moment of Equation (2.27). In this instance, however, it proves more useful to multiply Equation (2.27) by the fluid species' random momentum, $m_s \mathbf{c}_s = m_s(\mathbf{v}_s - \mathbf{u}_s)$, and then to integrate over all velocity space:

$$(2.35) \quad \iiint_{-\infty}^{+\infty} m_s \mathbf{c}_s \frac{\delta f_s(\mathbf{r}, \mathbf{v}, t)}{\delta t} d^3 \mathbf{v} = \iiint_{-\infty}^{+\infty} m_s \mathbf{c}_s \left[\frac{\partial f_s}{\partial t} + \nabla \cdot (\mathbf{v}_s f_s) + \nabla_v \cdot (\mathbf{a}_s f_s) \right] d^3 \mathbf{v}.$$

After a great deal of algebra, which Appendix A contains, one arrives at the following elegant expression for the *species' momentum equation*:

$$(2.36) \quad \frac{\delta \mathbf{M}_s}{\delta t} = \rho_s \left(\frac{\partial \mathbf{u}_s}{\partial t} + \mathbf{u}_s \cdot \nabla \mathbf{u}_s \right) + \nabla \cdot \mathbf{P}_s + \rho_s \mathbf{a}_s.$$

Where \mathbf{P}_s is the pressure tensor, \mathbf{a}_s is the acceleration vector given by Equation (2.19), and $\frac{\delta \mathbf{M}_s}{\delta t}$ is the collisional forces contributing to the species' momentum evolution over time. Furthermore, the derivatives for \mathbf{u}_s may be combined into a total convective derivative operator, $\frac{D}{Dt}$, given by:

$$(2.37) \quad \frac{D}{Dt} = \left(\frac{\partial}{\partial t} + \mathbf{u}_s \cdot \nabla \right).$$

Finally, using this convective derivative, the momentum equation takes on a more succinct form given by:

$$(2.38) \quad \frac{\delta \mathbf{M}_s}{\delta t} = \rho_s \frac{D \mathbf{u}_s}{Dt} + \nabla \cdot \mathbf{P}_s + \rho_s \mathbf{a}_s.$$

2.4.3 Energy Equation

The Navier-Stokes energy equation mathematically describes the time evolution of a fluid's total internal energy. It emerges by multiplying Equation (2.27) by the thermal kinetic energy, $\frac{1}{2}m_s c_s^2$, and integrating over all velocity space, giving the following expression.

$$(2.39) \quad \iiint_{-\infty}^{+\infty} \left(\frac{1}{2}m_s c_s^2 \right) \frac{\delta f_s(\mathbf{r}, \mathbf{v}, t)}{\delta t} d^3 \mathbf{v} = \iiint_{-\infty}^{+\infty} \frac{1}{2}m_s c_s^2 \left[\frac{\partial f_s}{\partial t} + \nabla \cdot (\mathbf{v}_s f_s) + \nabla_v \cdot (\mathbf{a}_s f_s) \right] d^3 \mathbf{v}.$$

As done for both the continuity and the momentum equations, this last equation can be evaluated term-wise. This process incurs a significant amount of vector algebra, detailed in Appendix A, resulting in the following mathematically succinct version of the Navier-Stokes *Energy Equation*:

$$(2.40) \quad \frac{\delta E_s}{\delta t} = \frac{D}{Dt} \left(\frac{1}{\gamma - 1} p_s \right) + \left(\frac{\gamma}{\gamma - 1} p_s \right) \nabla \cdot \mathbf{u}_s + \nabla \cdot \mathbf{q} + \mathbf{P}_s : \nabla \mathbf{u}_s.$$

Here, $\frac{\delta E_s}{\delta t}$ represents the collisional time evolution of the fluid's energy, p_s represents the scalar pressure, γ once again represents the specific heat ratio, \mathbf{q} represents the heat flux vector, and the term $\mathbf{P}_s : \nabla \mathbf{u}_s = P^{\alpha\beta} \nabla_\alpha u_\beta$ represents a double contraction between these two second-order tensors in dyadic notation.

2.5 Collisions: Maxwell-Boltzmann Distribution

Although three fundamental transport equations have been derived, the temporal evolution terms $\frac{\delta n_s}{\delta t}$, $\frac{\delta \mathbf{M}_s}{\delta t}$, and $\frac{\delta E_s}{\delta t}$ require further discussion. Furthermore, in the

context of the Navier-Stokes equations, some closure assumptions and simplifications are needed in order to specify the proper forms for both \mathbf{q} and \mathbf{P}_s .

2.5.1 Maxwell-Boltzmann Velocity Distribution

In planetary upper atmospheres, the fluid particles exhibit a near-Maxwellian behavior, meaning that they possess a phase-space distribution function given by the Maxwell-Boltzmann distribution:

$$(2.41) \quad f_s(\mathbf{r}, \mathbf{v}_s, t) = n_s(\mathbf{r}, t) \left[\frac{m_s}{2\pi k T_s(\mathbf{r}, t)} \right]^{3/2} \exp \left[-m_s \frac{(\mathbf{v}_s - \mathbf{u}_s)^2}{2k T_s(\mathbf{r}, t)} \right].$$

In this expression, f_s , peaks at the bulk velocity, \mathbf{u}_s and falls off as a Gaussian away from \mathbf{u}_s with a half-width given by $\sigma = \sqrt{\frac{2kT}{m_s}}$. In order for this distribution function to truly represent the fluid particles in a planetary atmosphere, inter-species collisions must dominate, which is a reasonable approximation below the exobase. However, in regions where collisions are inhibited, the atmospheric particles' velocity distribution can deviate significantly from the formulation in Equation (2.41). For the purposes of this work, the Maxwell-Boltzmann distribution is assumed to apply throughout the domain of interest.

2.5.2 Collisions

Given the phase-space distribution of Equation (2.41), one may now determine the collisional terms in Equations (2.34), (2.38), and (2.40): $\frac{\delta n_s}{\delta t}$, $\frac{\delta \mathbf{M}_s}{\delta t}$, and $\frac{\delta \mathbf{E}_s}{\delta t}$. Strictly speaking, in order to determine these collisional relaxation derivatives, one must use the Maxwell-Boltzmann distribution to determine a series of inter-species collision integrals. Although these calculations remain beyond the scope of this thesis, *Schunk and Nagy* [2000] and *Gombosi* [1999] provide an excellent derivation of these collisional integrals in the specific case of a Maxwellian velocity distribution, resulting in

the following expressions:

$$(2.42) \quad \frac{\delta n_s}{\delta t} = 0,$$

$$(2.43) \quad \frac{\delta \mathbf{M}_s}{\delta t} = - \sum_t n_s m_s \nu_{st} (\mathbf{u}_s - \mathbf{u}_t),$$

$$(2.44) \quad \frac{\delta \mathbf{E}_s}{\delta t} = - \sum_t \frac{n_s m_s}{m_s + m_t} [3k(T_t - T_s) + m_t(\mathbf{u}_s - \mathbf{u}_t)^2].$$

In these expressions, collisions do not impact the total neutral densities, resulting in $\frac{\delta n_s}{\delta t} = 0$. The second term, $\frac{\delta \mathbf{M}_s}{\delta t} = - \sum_t n_s m_s \nu_{st} (\mathbf{u}_s - \mathbf{u}_t)$ represents inter-species momentum exchange through collisions, where ν_{st} is the collision frequency between species “t” and species “s”. Essentially, as collisions increase, the velocity profiles of all the species will converge to a single value, the bulk velocity. Finally, the energy time evolution is governed by two processes. First the temperature difference between species produces a net heat exchange through the term proportional to $3k(T_t - T_s)$. Furthermore, differences in the species’ kinetic energies also results in frictional heat exchange, expressed by the term proportional to $(\mathbf{u}_s - \mathbf{u}_t)^2$.

2.5.3 Closure Approximations

Lastly, some closure relations must exist for both the heat flux vector, \mathbf{q} , and the pressure tensor, \mathbf{P}_s . Although these variables can be directly derived through higher-order velocity moments of the phase-space distribution, they are typically approximated in upper atmospheric science as follows:

$$(2.45) \quad \mathbf{q} = -\kappa_T \nabla T,$$

$$(2.46) \quad \mathbf{P}_s = \mathbf{I} p_s + \boldsymbol{\tau}_s.$$

Here, Fourier’s law of conduction provides the closure expression for the heat flux vector. Finally, the pressure tensor closure relation simply states that the pressure

can be separated into an isotropic component, $\mathbf{I}p_s$ where p_s is the scalar pressure, and an anisotropic stress tensor, τ_s which is given by:

$$(2.47) \quad \tau_s = \eta_s \left[\nabla \mathbf{u}_s + (\nabla \mathbf{u}_s)^T - \frac{2}{3} (\nabla \cdot \mathbf{u}_s) \mathbf{I} \right],$$

where, η_s represents the viscosity coefficient.

2.5.4 Navier-Stokes Equations

Finally, after gathering all of the equations of the previous sections together, the Navier-Stokes equations applicable to planetary atmospheres emerge:

$$(2.48) \quad \frac{\partial n}{\partial t} + \nabla \cdot (\mathbf{u}_s n_s) = 0,$$

$$(2.49) \quad \rho_s \frac{D \mathbf{u}_s}{Dt} + \nabla \cdot \mathbf{P}_s + \rho_s \mathbf{a}_s = - \sum_t n_s m_s \nu_{st} (\mathbf{u}_s - \mathbf{u}_t),$$

$$(2.50) \quad \frac{D}{Dt} \left(\frac{p_s}{\gamma - 1} \right) + \left(\frac{\gamma p_s}{\gamma - 1} \right) \nabla \cdot \mathbf{u}_s + \nabla \cdot \mathbf{q} + \mathbf{P}_s : \nabla \mathbf{u}_s = - \sum_t \frac{n_s m_s}{m_s + m_t} [3k(T_t - T_s) + m_t(\mathbf{u}_s - \mathbf{u}_t)^2].$$

CHAPTER III

Numerical Planetary Models

What I cannot create, I do not understand.

—Richard Feynman

3.1 Introduction

The Navier-Stokes fluid equations, Equations (2.48) – (2.50), represent coupled, non-linear partial differential equations for which no analytical solution exists, except in the simplest of circumstances that fail to apply to real atmospheres. Faced with these challenges, aeronomers turn to numerical modeling in order to understand the physics governing atmospheric systems. In what follows, a brief historical development of upper atmospheric modeling over the past half century is presented, following the excellent review by *Wang* [1998]. Then, the numerical modeling frameworks used in this thesis to explore the upper Atmospheres of Mars and Titan are introduced, focusing on the general aspects of the modeling frameworks themselves and leaving planet-specific physical processes for later chapters.

3.2 A Brief History of Upper Atmospheric Modeling

3.2.1 From One-Dimensional to Three-Dimensional Neutral Atmosphere Models: Earth

Numerical modeling of planetary upper atmospheres has enjoyed a long heritage, extending back to the 1960's when theoreticians first began modeling Earth's upper atmosphere. The primary constraints at this time were: computer memory size, computer processing speed, availability of computer time, and accessibility of numerical outputs. Thus, in the earliest stages, one-dimensional (1-D) thermosphere-ionosphere numerical codes were developed by neglecting horizontal advection, chemical reactions, and high latitude energy and momentum inputs. The heat conduction model of *Harris and Priester* [1962, 1965] represented a canonical example of these 1-D models. However, these early numerical frameworks failed to account for the diurnal variation in the Earth's neutral density and temperature variations, motivating aeronomers to develop more complex numerical tools.

Later in that decade, two-dimensional (2-D) models were introduced to describe the horizontal advection of the neutral atmosphere, using empirical prescriptions of global neutral temperature and density [*Geisler*, 1967; *Kohl and King*, 1967]. These 2-D frameworks employed greatly simplified electron density calculations, ignored high latitude sources of momentum and energy, and eliminated the nonlinear terms from the fluid equations. Thus, the winds generated from these 2-D models were driven primarily by pressure gradients alone. Shortly afterward, more sophisticated two-dimensional theoretical tools were developed, such as that of *Fedder and Banks* [1972], which accounted for high-latitude ion-neutral drag effect on the mean circulation and the ion-neutral frictional heating on the mean temperature. Additionally, the 2-D models of [*Dickinson et al.*, 1975, 1977] and *Roble et al.* [1977] addressed the seasonal variations of the meridional circulation and neutral tempera-

ture. Meanwhile *Richmond and Matsushita* [1975] used their 2-D framework to study the thermospheric response to a geomagnetic storm and to investigate gravity wave propagation/dissipation in the thermosphere [*Richmond*, 1979]. Finally, spectral methods were employed by *Mikkelsen et al.* [1981] and *Mikkelsen and Larsen* [1983] to study the neutral wind response to plasma convection momentum sources. Despite their limitations however, these pioneering works greatly improved our understanding of thermospheric energetics and dynamics, while simultaneously advancing our mathematical and computational approaches.

The beginning of the 1980's marked a watershed epoch upper atmospheric modeling. *Fuller-Rowell and Rees* [1980b] introduced a three-dimensional (3-D) self-consistent approach to solving simultaneously the momentum, thermodynamic, and continuity equations in a time-dependent framework, accounting also for non-linear terms in the coupled fluid equations. This 3-D model, the University College at London Thermosphere General Circulation Model (UCL-TGCM), possessed a global grid of 2° in latitude by 18° longitude, while the vertical grid consisted of 15 pressure levels that spanned the altitude range between 80 - 450 km. Contemporaneously, *Dickinson et al.* [1981] unveiled the National Center for Atmospheric Research - Thermospheric General Circulation Model (NCAR-TGCM), which solved the same set of coupled fluid equations on a uniform $5^{\circ} \times 5^{\circ}$ on 25 vertical pressure levels, spanning the 97 - 500 km altitude regime. Both numerical codes were extensively benchmarked and validated against satellite and *in situ* observations (e.g. *Killeen and Roble* [1984]; *Killeen et al.* [1987]; *McCormac et al.* [1988]). However these models did not account for the intimate coupling between the thermosphere and the co-located ionosphere.

3.2.2 Ionosphere Modeling: Earth

At Earth, the ionospheric community took a different path than that taken for the neutral atmosphere. Regional models were developed that focused on the electrodynamics of the equatorial [Anderson, 1973, 1981], mid-latitude [Stubbe, 1970; Schunk and Walker, 1973], and high-latitude F-regions [Knudsen, 1974; Knudsen *et al.*, 1977; Sojka *et al.*, 1981]. These theoretical tools included the time-dependent 1-D and 3-D coupled ion continuity equations locally. Sojka and Schunk [1985] introduced the first global time-dependent ionospheric model (TDIM) that simultaneously solved the ion continuity, ion transport, and ion energy equations. Later, the electron energy equation was added in order to evaluate electron temperatures [Schunk *et al.*, 1986; Schunk, 1988]. These Ionosphere models utilized empirical specifications for the background thermosphere, taken from the Mass Spectrometer/Incoherent Scatter (MSIS) series of models: MSIS-83, 86, MSISE-90 [Hedin, 1983, 1987, 1991].

3.2.3 Three-Dimensional Coupled Thermosphere-Ionosphere Models: Earth

In 1987, Fuller-Rowell *et al.* [1987] unveiled a global model of the thermosphere coupled with a polar ionosphere, addressing the dynamical and chemical interactions between the neutral and ionized components of the polar upper atmosphere. This coupled model incorporated the ionospheric model of Quegan *et al.* [1982] with that of Fuller-Rowell and Rees [1980b] through interpolation at each time-step. Simultaneously, the NCAR-TGCM was upgraded [Roble *et al.*, 1988] to include a self-consistent, coupled aeronomic scheme for the thermosphere and the ionosphere, using the chemical scheme developed by Roble *et al.* [1987] and the auroral ionospheric scheme developed in Roble and Ridley [1987]. This newly developed framework was dubbed the NCAR Thermosphere-Ionosphere General Circulation Model (NCAR-

TIGCM). This numerical tool also utilized a parameterization for the impact of semi-diurnal tides on the thermosphere, adopting the method of *Fesen et al.* [1986]. Later, the NCAR-TIGCM was further upgraded to include electrodynamical interactions between the thermosphere and ionosphere, including the dynamo effects of the thermospheric winds at low and mid-latitudes. This newer model was dubbed the NCAR Thermosphere-Ionosphere-Electrodynamics General Circulation Model (NCAR-TIEGCM) [*Richmond et al.*, 1992]. Most recently, the NCAR-TIEGCM was extended downward to the stratosphere, incorporating the chemical and physical processes appropriate for the mesosphere. This created the NCAR Thermosphere-Ionosphere-Mesosphere-Electrodynamics General Circulation Model (NCAR-TIME-GCM) of *Roble and Ridley* [1994].

Later, in the 1990's, advancements in upper atmospheric modeling continued to accelerate. The CTIM model [*Fuller-Rowell and Rees*, 1980b] was updated to include plasmasphere physics, dubbing the new framework the Coupled Thermosphere-Ionosphere-Plasmasphere (CTIP) model. Furthermore, the Coupled Middle Atmosphere-Thermosphere (CMAT) code of *Harris et al.* [2002] was coupled to the CTIM model, extending it to the mesosphere. At the same time, the Thermosphere-Ionosphere Nested Grid (TING) framework of *Wang et al.* [1999] was incorporated into the NCAR TIEGCM, allowing for higher resolution in the high-latitude ionosphere and thermosphere. The Global Assimilation of Ionospheric Measurements (GAIM) model by *Schunk* [2004] represented a physics-based data assimilation model of Earth's ionosphere and plasmasphere. Finally, in 2006, *Ridley et al.* [2006] unveiled the Global Ionosphere-Thermosphere Model (GITM), which represented a significant departure from previous theoretical frameworks.

First, GITM possesses adjustable resolution in the horizontal direction, while

also allowing for user-specified non-uniform grid spacing in latitude and altitude. Next, this new framework does not assume hydrostatic solutions, instead it directly solves the non-hydrostatic Navier-Stokes equations. GITM also employs explicit numerical solvers for both advection and chemistry, while also calculating vertical transport directly. Finally, this new framework provides the ability to incorporate user-specified magnetic field configurations into the model, allowing for an investigation into ionosphere-thermosphere-magnetosphere coupling. Thus, due to these many capabilities, this model serves as the numerical framework for the Titan upper atmospheric model of this thesis.

3.3 The Mars Thermosphere General Circulation Model (MTGCM)

3.3.1 Introduction to the MTGCM and its heritage

The Mars Thermosphere General Circulation Model (MTGCM) is a modified version of the National Center for Atmospheric Research (NCAR) Thermosphere-Ionosphere-Electrodynamics General Circulation Model (TIEGCM) framework. This NCAR-TIEGCM is modified from its Earth-based roots to function in Mars' chemical and physical environment. The details of this modification are found in *Bouger et al.* [1988b]; *Bouger and Dickinson* [1988]; *Bouger et al.* [1988a, 1990] and *Bouger et al.* [2000]. The model itself is a primitive equation model that self-consistently solves for the neutral temperatures, neutral-ion densities, and the three-component neutral winds around the globe. More details on the model can be found in Chapter 4, where the MTGCM is used to investigate the phenomenon of winter polar warming. Currently, the Thermospheric MTGCM is coupled with its lower atmosphere analogue, the NASA Ames Mars General Circulation Model (MGCM), detailed in *Haberle et al.* [1999] and *Pollack et al.* [1990]. The next few sections walk through the numerical framework that makes up the core of the MTGCM.

3.3.2 Pressure Coordinates, Hydrostatics, and the NCAR Formulation

The core fluid solvers in the MTGCM assume that hydrostatic equilibrium applies at all altitudes in the Martian upper atmosphere, by enforcing:

$$(3.1) \quad \frac{\partial P}{\partial r} = -\rho(r)g(r).$$

However, the underlying NCAR numerical framework utilizes a quasi-Cartesian vertical coordinate, resulting in a new formulation for the hydrostatic equation:

$$(3.2) \quad \frac{\partial P}{\partial z} = -\rho(z)g(z).$$

This step, in going from r to z , is significant because it eliminates from consideration the geometrical curvature terms inherent to spherical geometry in the vertical direction. Moreover instead of utilizing the standard Cartesian vertical coordinate, the MTGCM adopts a logarithmic pressure-based system, resulting in the new vertical coordinate, Z , given by

$$(3.3) \quad Z = \ln\left(\frac{P_0}{P}\right),$$

where P_0 is a planet-specific reference pressure. At Mars, this reference pressure is $1.2 \times 10^{-3} \mu b$, which represents the F1 ionospheric peak.

Given this definition of the vertical coordinate, one can immediately evaluate how it behaves at different pressure levels. First, one finds that $Z = 0$ at the reference pressure level, P_0 . At higher altitudes, where $P < P_0$, then one finds that $Z > 0$. Conversely, at lower altitudes, where $P > P_0$, then one has $Z < 0$. Thus, this pressure-level coordinate Z does in fact represent a normalized vertical coordinate relative to the reference pressure. In the MTGCM, because Z acts as the independent altitude coordinate, the modeling framework solves the above equation for P as a

function of Z by inspection:

$$(3.4) \quad P = P_0 e^{-Z}.$$

Next, in order to illustrate the core fluid equations of the MTGCM, one must consider the coordinate transform from the Cartesian altitude coordinate z to the pressure coordinate Z for any arbitrary fluid quantity, η :

$$(3.5) \quad \frac{\partial \eta}{\partial z} = \frac{\partial Z}{\partial z} \frac{\partial \eta}{\partial Z}.$$

Next the form of $\frac{\partial Z}{\partial z}$ must be considered. Using the definition of the logarithmic derivative, one gets:

$$(3.6) \quad \frac{\partial Z}{\partial z} = -\frac{1}{\left(\frac{P_0}{P}\right)} \frac{\partial\left(\frac{P_0}{P}\right)}{\partial z} = -\frac{1}{P} \frac{\partial P}{\partial z} = -\frac{e^Z}{P_0} \frac{\partial P}{\partial z}.$$

This can be further rewritten by employing the hydrostatic assumption in equation 3.2, which gives:

$$(3.7) \quad \frac{\partial Z}{\partial z} = -\frac{e^Z}{P_0} \frac{\partial P}{\partial z} = \frac{e^Z \rho g}{P_0}.$$

This last expression may be re-cast in terms of the atmospheric scale height, H , using the ideal gas equation:

$$(3.8) \quad \frac{\partial Z}{\partial z} = \frac{e^Z \rho g}{P_0} = \frac{\rho g}{P} = \frac{\rho g}{n k T} = \frac{\overline{m} n g}{n k T} = \frac{\overline{m} g}{k T} = \frac{1}{H}.$$

Thus, the proper derivative transformation needed to convert from the Navier-Stokes equations to the formulation in the NCAR MTGCM framework is as follows:

$$(3.9) \quad \frac{\partial \eta}{\partial z} = \frac{\partial Z}{\partial z} \frac{\partial \eta}{\partial Z} = \frac{e^Z \rho g}{P_0} \frac{\partial \eta}{\partial Z} = \frac{1}{H} \frac{\partial \eta}{\partial Z}.$$

Using this pressure-coordinate formulation, the Navier-Stokes fluid equations take on a new form discussed in the following sections.

3.3.3 Continuity Equation

The MTGCM does not solve the Navier-Stokes continuity equation directly. Instead, the NCAR framework solves for mass mixing ratios, Ψ for the major and minor species. Because of the inherent complexities, the transformation from the fundamental Navier-Stokes expression, Equation 2.48 to the formulation of the MTGCM framework is not attempted here. Instead, the following section highlights how the Mars model calculates atmospheric composition in this re-casted formulation.

The mass mixing ratio Ψ for a species “i” is given by:

$$(3.10) \quad \Psi_i = n_i m_i \left(\sum_{j=1}^N n_j m_j \right)^{-1},$$

where N represents the total number of major species. Moreover, using this definition, the atmospheric mean major mass is given by:

$$(3.11) \quad \bar{m} = \left(\sum_{i=1}^N \frac{\Psi_i}{m_i} \right)^{-1}$$

The MTGCM separates the solution for major and minor species mixing ratios, utilizing the matrix solvers given in *Roble et al.* [1988] and *Dickinson et al.* [1984].

Major Species

The major species at Mars consist of CO_2 , CO , O and N_2 . The mixing ratios Ψ_{CO} and Ψ_O are solved for directly, Ψ_{N_2} is specified empirically, while the mixing ratio for CO_2 is derived from the following equation:

$$(3.12) \quad \Psi_{CO_2} = 1.0 - \Psi_{CO} - \Psi_O - \Psi_{N_2}.$$

In order to solve coupled continuity equations for Ψ_{CO} and Ψ_O , a vector, $\hat{\Psi}$ is defined such that $\hat{\Psi} = (\Psi_{CO}, \Psi_O)$. Finally, the vector equation coupling the major species

chemistry in the MTGCM is given by:

$$(3.13) \quad \frac{\partial \hat{\Psi}}{\partial t} = -\frac{e^Z}{\tau} \frac{\partial}{\partial Z} \left[\frac{\bar{m}}{m_{CO_2}} \left(\frac{T_{00}}{T} \right)^{0.25} \hat{\alpha}^{-1} L \hat{\Psi} \right] + S - R + e^Z \frac{\partial}{\partial Z} \left[K(Z) e^{-Z} \frac{\partial}{\partial Z} \left(1 + \frac{1}{\bar{m}} \frac{\partial m}{\partial Z} \right) \hat{\Psi} \right] - \left(\mathbf{V} \cdot \nabla \hat{\Psi} + w \frac{\partial \hat{\Psi}}{\partial Z} \right).$$

In this extensive vector equation, T_{00} represents a reference temperature that is planet specific, m_{CO_2} is the molecular mass of Carbon Dioxide, and τ is the diffusive time scale in the Martian atmosphere. The terms on the right-hand side of the last equation are, respectively: (1) Molecular Diffusion, (2) Chemical Sources (S) and Losses (R), (3) Eddy Diffusion, and finally (4) Non-Linear Advection. The matrix $\hat{\alpha}^{-1}$ represents the inverse of a matrix operator, $\hat{\alpha}$ which is defined element-wise by the following:

$$(3.14) \quad \begin{aligned} \alpha_{11} &= -[\phi_{13} + (\phi_{12} - \phi_{13}) \Psi_O] \\ \alpha_{22} &= -[\phi_{23} + (\phi_{21} - \phi_{23}) \Psi_{CO}] \\ \alpha_{12} &= (\phi_{12} - \phi_{13}) \Psi_{CO} \\ \alpha_{21} &= (\phi_{21} - \phi_{23}) \Psi_O. \end{aligned}$$

In this formulation, the subscripts stands for the species as follows: 1 stands for CO , 2 stands for O , and 3 stands for CO_2 . The ϕ_{ij} terms represent normalized molecular diffusion coefficients, given by:

$$(3.15) \quad \phi_{ij} = \frac{D}{D_{ij}} \frac{m_{CO_2}}{m_j},$$

where D_{ij} denotes the binary diffusion coefficient for gases “i” and “j.” These values are obtained from *Banks and Kockarts* [1973] and *Colegrove et al.* [1966]. Finally, L_{ii} denotes a matrix operator given by:

$$(3.16) \quad L_{ii} = \frac{\partial}{\partial Z} - \left(1 - \frac{m_i}{\bar{m}} - \frac{1}{\bar{m}} \frac{\partial \bar{m}}{\partial Z} \right).$$

Ultimately, these matrix equations enable the MTGCM to make implicit time stepping, which results in faster computations while maintaining numerical stability. Thus, although the transition from the Navier-Stokes continuity equation, Equation (2.48), to these matrix equations utilized in the NCAR formulation involves a considerable amount of effort, this transformation produces robust, fast computations of the Martian upper atmospheric composition.

Minor Species

The Minor species in the MTGCM (Ar , He , NO , $N(^4S)$, and O_2) possess their own unique composition solver, detailed in *Roble et al.* [1988]. The solvers for the minor species parallels that for the major species, given by:

$$(3.17) \quad \frac{\partial \hat{\Psi}}{\partial t} = -e^Z \frac{\partial}{\partial Z} \left[\hat{A} \left(\frac{\partial}{\partial Z} - \hat{E} \right) \hat{\Psi} \right] + \hat{S} - \hat{R} - \left(\mathbf{V} \cdot \nabla \hat{\Psi} + w \frac{\partial \hat{\Psi}}{\partial Z} \right) + e^Z \left[e^{-Z} K_E(Z) \left(\frac{\partial}{\partial Z} + \frac{1}{\bar{m}} \frac{\partial \bar{m}}{\partial Z} \right) \hat{\Psi} \right],$$

where

$$(3.18) \quad \hat{E} = \left(1 - \frac{\hat{m}}{\bar{m}} - \frac{1}{\bar{m}} \frac{\partial \bar{m}}{\partial Z} \right) - \hat{\alpha} \frac{1}{T} \frac{\partial T}{\partial Z} + \hat{F} \hat{\Psi}.$$

Here, \hat{A} represents the vertical molecular diffusion coefficient, while \hat{S} and \hat{R} represent the chemical sources and losses, respectively. \hat{E} comprises the effects of gravity, thermal diffusion, and the frictional interactions between the minor constituents and the majors, given by \hat{F} . $\hat{\alpha}$ represents the thermal diffusion coefficient. Thus, one finds that the minor species, although treated differently than the majors, possess the same fundamental drivers for their composition.

3.3.4 Momentum Equations

The Navier-Stokes momentum equation, Equation (2.49), represents the fluid's response to the forces that it experiences. The MTGCM framework does not explic-

itly calculate vertical transport, instead, it derives vertical winds by first calculating the horizontal winds, u (eastward) and v (northward), and then demanding that the divergence of the total velocity vanishes, $\nabla \cdot \mathbf{u} = 0$, where \mathbf{u} represents the full wind vector $\mathbf{u} = (u, v, w)$. In what follows, the MTGCM momentum equations for the vertical, zonal, and meridional directions are discussed.

Although the NCAR continuity formulation of the previous section departed significantly from that chapter 2, the horizontal momentum equations represent almost a direct application of the Navier-Stokes formulation. First, the the inter-species collisional term in Equation 2.49 is not considered, leaving:

$$(3.19) \quad \rho_s \frac{D\mathbf{u}_s}{Dt} + \nabla \cdot \mathbf{P}_s + \rho_s \mathbf{a}_s = 0$$

Next, after expanding the pressure tensor into components, $\mathbf{P}_s = \mathbf{I}p_s + \boldsymbol{\tau}_s$, and expanding the convective derivative, one obtains:

$$(3.20) \quad \rho_s \frac{\partial \mathbf{u}_s}{\partial t} + \rho_s \mathbf{u}_s \cdot \nabla \mathbf{u}_s + \nabla p_s + \nabla \cdot \boldsymbol{\tau}_s + \rho_s \mathbf{a}_s = 0.$$

The NCAR Framework assumes that all species move with one bulk velocity, resulting in a single momentum equation:

$$(3.21) \quad \rho \frac{\partial \mathbf{u}}{\partial t} + \rho \mathbf{u} \cdot \nabla \mathbf{u} + \nabla p + \nabla \cdot \boldsymbol{\tau} + \rho \mathbf{a} = 0.$$

Moreover, the MTGCM considers only the following subset of external forces (accelerations):

$$(3.22) \quad \mathbf{a} = \mathbf{g} + \mathbf{C} + \hat{\mathbf{F}},$$

where \mathbf{g} is the gravitational acceleration, \mathbf{C} represents both spherical geometry correction terms and Coriolis forces, and finally $\hat{\mathbf{F}}$ represents ion-drag forces. The last of these forces is not considered at Mars. Thus, one finally arrives at the following

simplified formulation for the MTGCM:

$$(3.23) \quad \rho \frac{\partial \mathbf{u}}{\partial t} + \rho \mathbf{u} \cdot \nabla \mathbf{u} + \nabla p + \nabla \cdot \tau + \rho (\mathbf{g} + \mathbf{C}) = 0.$$

In the following sections, this reduced momentum equation set is expanded in terms native to the NCAR numerical framework.

Vertical Momentum

The MTGCM vertical velocity is determined by solving the equivalent of $\nabla \cdot \mathbf{u} = 0$ for all three components, resulting in:

$$(3.24) \quad \frac{1}{r \cos \phi} \frac{\partial}{\partial \phi} (v \cos \phi) + \frac{1}{r \cos \phi} \frac{\partial u}{\partial \lambda} + e^Z \frac{\partial}{\partial Z} (e^{-Z} w) = 0.$$

This vertical wind, w , represents a unitless velocity. In order to calculate the vertical transport speed in units m/s , one must multiply by the atmospheric scale height, H . Thus, the vertical winds are not directly calculated and, instead, are treated as a secondary derivation from this continuity equation.

Zonal (Eastward) Momentum and Meridional (Northward) Momentum

The zonal momentum equation is given by the following expression:

$$(3.25) \quad \frac{\partial u}{\partial t} = \frac{ge^Z}{P_0} \frac{\partial}{\partial Z} \left(\frac{K_M}{H} \frac{\partial u}{\partial Z} \right) + \frac{uv}{r} \tan \phi + fv - \left[\mathbf{V} \cdot \nabla u + w \frac{\partial u}{\partial Z} \right] - \frac{1}{r \cos \phi} \frac{\partial \Phi}{\partial \lambda}.$$

Likewise, the meridional momentum equation arises as:

$$(3.26) \quad \frac{\partial v}{\partial t} = \frac{ge^Z}{P_0} \frac{\partial}{\partial Z} \left(\frac{K_M}{H} \frac{\partial v}{\partial Z} \right) + \frac{u^2}{r} \tan \phi - fu - \left[\mathbf{V} \cdot \nabla v + w \frac{\partial v}{\partial Z} \right] - \frac{1}{r} \frac{\partial \Phi}{\partial \phi}.$$

Both of the previous equations make use of the geopotential height, Φ , that is used to enforce hydrostatic balance and is given by

$$(3.27) \quad \frac{\partial \Phi}{\partial Z} = \frac{RT}{\overline{m}}$$

Furthermore, in the horizontal momentum equations, K_M represents the molecular viscosity coefficient, f is the Coriolis parameter $2\Omega \sin \phi$, ϕ is the longitude, λ is the latitude, and H is the pressure scale height. The right-hand side of both equations express the forces acting in the upper atmosphere of Mars: (1) the first term is vertical shear of horizontal velocity, (2) is the curvature forces for horizontal velocity components, (3) is the Coriolis force, (4) is the non-linear advection of horizontal winds, and (5) is the pressure gradient. Interestingly enough, the horizontal winds do possess curvature terms consistent with spherical geometry. However, the MTGCM does not include vertical curvature terms in its formulation.

Lastly, to make advection stable, several horizontal diffusion terms are added to eliminate non-linear computational instability caused by aliasing. These horizontal diffusion terms are given by:

$$(3.28) \quad F_\lambda = \frac{1}{r \cos \phi} \frac{\partial}{\partial \lambda} (\rho K_{MH} D_T) + \frac{1}{r} \frac{\partial}{\partial \phi} (\rho K_{MH} D_S),$$

$$(3.29) \quad F_\phi = \frac{1}{r \cos \phi} \frac{\partial}{\partial \lambda} (\rho K_{MH} D_S) + \frac{1}{r} \frac{\partial}{\partial \phi} (\rho K_{MH} D_T).$$

In this equation, D_T and D_S are given by:

$$(3.30) \quad D_T = \frac{1}{r \cos \phi} \left[\frac{\partial u}{\partial \lambda} - \frac{\partial}{\partial \phi} (v \cos \phi) \right],$$

$$(3.31) \quad D_S = \frac{1}{r \cos \phi} \left[\frac{\partial v}{\partial \lambda} - \frac{\partial}{\partial \phi} (u \cos \phi) \right].$$

(3.32)

Here, K_{MH} represents the horizontal eddy viscosity, given by:

$$(3.33) \quad K_{MH} = 2 k_0^2 l^2 \sqrt{(D_T^2 + D_S^2)},$$

where l is the characteristic horizontal grid cell size and k_0 is an heuristically determined constant that produces stable results. Ultimately, with this numerical machinery, the MTGCM can produce robust horizontal winds through the use of these

momentum equations and the stabilizing diffusive terms that eliminate non-linear computational instabilities.

3.3.5 Thermodynamic Equation

Finally, the Navier-Stokes Energy equation, given in Equation (2.50), gives rise to the thermodynamic equation, after a set of assumptions consistent with the MT-GCM framework are made. First, the NCAR numerical framework assumes that the energy equation may be solved for all species simultaneously. This means that only bulk quantities are treated in Equation (2.50), resulting in dropping the “s” from variables. Second, one assumes that the ideal gas law holds, meaning that $p = nkT$. Furthermore, in the NCAR formulation, one assumes that $\nabla \cdot \mathbf{u} = 0$ holds, while dropping the second order contraction $\mathbf{P}_s : \nabla \mathbf{u}$. Additionally, the MTGCM ignores the collisional contributions to energy evolution. Thus, Equation (2.50) reduces to:

$$(3.34) \quad \frac{D}{Dt} \left(\frac{nkT}{\gamma - 1} \right) + \nabla \cdot \mathbf{q} = Q_{external}.$$

In this equation, $Q_{external}$ represents the radiative heating and cooling contributions to the energy budget of the atmosphere. Expanding this last expression, and assuming that k and γ remain roughly constant over the scales of the derivatives, one arrives at:

$$(3.35) \quad \frac{k}{\gamma - 1} \frac{\partial (nT)}{\partial t} + \frac{k}{\gamma - 1} \mathbf{u} \cdot \nabla (nT) + \nabla \cdot \mathbf{q} = Q_{external}.$$

Making a substitution of $C_p = \frac{1}{\gamma-1} \frac{k}{m}$ into the above equation, one obtains:

$$(3.36) \quad C_p \bar{m} \frac{\partial (nT)}{\partial t} + C_p \bar{m} \mathbf{u} \cdot \nabla (nT) + \nabla \cdot \mathbf{q} = Q_{external}.$$

Next, assuming that \bar{m} does not vary significantly over the scales considered, the last expression may be re-written in terms of $\rho = \bar{m}n$:

$$(3.37) \quad C_p \frac{\partial (\rho T)}{\partial t} + C_p \mathbf{u} \cdot \nabla (\rho T) + \nabla \cdot \mathbf{q} = Q_{external}.$$

Next, separating the density and temperature terms results in the following expanded form:

$$(3.38) \quad C_p T \left[\frac{\partial \rho}{\partial t} + \mathbf{u} \cdot \nabla \rho \right] + C_p \rho \left[\frac{\partial T}{\partial t} + \mathbf{u} \cdot \nabla T \right] + \nabla \cdot \mathbf{q} = Q_{external}.$$

However, according to the continuity equation, when summed over all species, one realizes that mass is neither created nor destroyed by chemical reactions, leading to the following for the continuity equation for the total mass density:

$$(3.39) \quad \frac{\partial \rho}{\partial t} + \mathbf{u} \cdot \nabla \rho = 0.$$

Finally one arrives at the following:

$$(3.40) \quad C_p \rho \left[\frac{\partial T}{\partial t} + \mathbf{u} \cdot \nabla T \right] + \nabla \cdot \mathbf{q} = Q_{external}.$$

Finally, if one decomposes $\mathbf{u} = \mathbf{V} + w \hat{Z}$, allows $\mathbf{q} = -K_T [\nabla T] - K_{T,E} [\nabla T + \Gamma_d]$, then the neutral temperature in the MTGCM arises from the following equation:

$$(3.41) \quad \frac{\partial T}{\partial t} = \frac{e^Z g}{P_0 C_p} \frac{\partial}{\partial Z} \left[\frac{K_T}{H} \frac{\partial T}{\partial Z} + K_E C_p \rho \left(\frac{g}{C_p} + \frac{1}{H} \frac{\partial T}{\partial Z} \right) \right] - \mathbf{V} \cdot \nabla T - w H \left(\frac{g}{C_p} + \frac{1}{H} \frac{\partial T}{\partial Z} \right) + \frac{Q - L}{\rho C_p}.$$

Here T is the temperature in K, t is time, g is gravitational acceleration, C_p is the specific heat at a constant pressure per unit mass, K_T is the molecular thermal conductivity, H is the pressure scale height, K_E is the eddy diffusion coefficient which is assumed to be the same as the eddy thermal conductivity, ρ is the atmospheric mass density, \mathbf{V} is the horizontal velocity, and Q and L are the heating and cooling rates due to radiative processes. Finally, w is the TIEGCM vertical velocity. Also, note that an additional term $w H (\Gamma_d) = w H \left(\frac{g}{C_p} \right)$ appears. This accounts for adiabatic cooling (heating) that occurs when a fluid parcel travels upward (downward).

The Eddy Diffusion coefficient, K_E follows a common aeronomic formulation *Atreya* [1986], given by

$$K_E = K_t \sqrt{\frac{P_0}{P}}$$

for $P > P_0$ and $K_E = K_t$ for all $P < P_0$. Thus, the eddy diffusion coefficient is capped at high altitudes to the value of K_t , which typically lies between $1 - 5 \times 10^3 m^2/s$.

Additionally, the molecular conduction coefficient used in the thermal equation represents a number density-weighted mean of the major constituent's molecular conductivities:

$$K_T = \frac{\sum_i k_{T,i} n_i}{\sum_i n_i}.$$

Here i is one of the major atmospheric constituents on Mars (i.e. CO_2, CO, O, N_2). Furthermore, n_i are the number densities and the $k_{T,i}$ are the species' molecular thermal conductivities. Finally, C_p is given by a similar number density-weighted average of the major species' specific heats:

$$C_p = \frac{\sum_i C_{p,i} n_i}{\sum_i n_i}.$$

3.3.6 Key Takeaways

Although this section contains a great deal of numerical formulations unique to the NCAR MTGCM framework, a few key points should be emphasized here. First, the MTGCM, deriving itself from the NCAR TIE-GCM, represents the culmination of over twenty years of numerical model development and testing. This alone commands enough respect to merit an exploration into the underlying mechanics of this framework. Additionally, the MTGCM forms the basis for the research on the Martian upper atmosphere in Chapter 4, making it imperative to understand the model's strengths and its weaknesses.

The MTGCM possesses a robust, implicit solver for all the primary equations with stabilizing diffusive terms to add another level of computational stability. This means that the Mars model can take large time-steps, while producing stable results. Furthermore, the core assumption of the MTGCM, which is hydrostatic equilibrium, remains a very reasonable approximation over much of Mars' upper atmosphere. However, the Mars model's inability to directly calculate vertical transport from the Navier-Stokes equation represents a potential weakness. Furthermore, possessing only a bulk momentum formulation becomes another possible shortcoming. However, despite these limitations, the MTGCM emerges as an extremely useful and well-tested numerical tool with which to study the aeronomy of the Martian thermosphere.

3.4 The Titan Global Ionosphere-Thermosphere Model (T-GITM)

The T-GITM is based upon an already extant Earth Global Ionosphere-Thermosphere Model (GITM), developed at the University of Michigan and detailed in *Ridley et al.* [2006]. This numerical framework possesses several key characteristics, summarized in Table 3.1, that distinguish it from pre-existing general circulation models (GCMs). First, the GITM framework utilizes spherical polar coordinates to solve the Navier-Stokes system of equations [*Schunk and Nagy*, 2000; *Gombosi*, 1999]. Thus, the radial distance from the planetary center, r , serves as the "vertical" coordinate, instead of using pressure levels as in previous GCMs. This formulation allows the planetary gravitational acceleration to vary explicitly with altitude, instead of either approximating a constant gravitational acceleration, as in *Roble et al.* [1988]; *Roble and Ridley* [1994], or mapping it to a function of pressure, as in *Müller-Wodarg et al.* [2000]; *Müller-Wodarg and Yelle* [2002].

Secondly, GITM does not *a priori* enforce a hydrostatic equilibrium at all points

Table 3.1: Difference between GITM and Other GCMs

Point of Difference	GITM	Other GCMs
1). Vertical Coordinate	r	Pressure
2). Gravity	$g(r)$	constant, or a function of pressure
3). Hydrostatic Balance $\frac{dP}{dz} = -\rho g$	not enforced	enforced at all points
4). Vertical Transport	calculated	derived from $\nabla \cdot \mathbf{u}$

in the atmosphere. In practice, pressure gradients balance gravitational forces over much of the numerical domain. However, differences between these two forces can become significant, appreciably modifying the thermosphere's dynamics, especially where intense localized heating occurs. Thirdly, GITM explicitly calculates vertical transport. By contrast, in previous modeling frameworks (e.g. *Roble et al.* [1988]; *Roble and Ridley* [1994]; *Fuller-Rowell and Rees* [1980a, 1983]), the horizontal velocities, u_θ, u_ϕ , are first calculated, then vertical velocities are derived by demanding that $\nabla \cdot \mathbf{u} = 0$ at all points in the calculation domain.

However, due to the exponential nature of planetary atmospheres along the radial coordinate, calculating vertical transport represents a very difficult task. In order to address this inherent difficulty, GITM separates the solution of the coupled Navier-Stokes' equations into two regimes: (1) a vertical solver (radial direction, r) and (2) a horizontal solver (for latitude, θ , and longitude, ϕ). In the vertical solver, logarithms of number densities are employed in the continuity, momentum, and thermal equations. The application of logarithms allows reduces the exponential variation of the atmosphere to a form tractable by finite-difference techniques. In the horizontal direction, the familiar (i.e. non-logarithmic) gradients of densities are utilized.

3.4.1 Components of TGITM specific to Titan

Although the Titan GITM inherits its numerical fluid solvers directly from its Earth predecessor, it differs greatly in the specific components that constitute it.

The Titan Global Ionosphere-Thermosphere Modeling framework is comprised of 15 neutral species, 5 ionic species, and an electron population equal to the total ion density. Table 3.2 summarizes how TGITM treats the various neutral and ionic species. As shown in this table, TGITM separates the neutrals into two classes. The first class of neutral constituents consists of 7 primary species that each possess their own continuity and momentum equations (N_2 , CH_4 , Ar , HCN , H_2 , $^{13}\text{CH}_4$, and $^{15}\text{N}-^{14}\text{N}$). These class 1 species represent constituents that function as: (1) key radiatively active neutrals (HCN), (2) major atmospheric constituents by number mixing ratio (N_2 , CH_4 , H_2), or (3) independent constraints to the dynamics of Titan (Ar , $^{13}\text{CH}_4$, and $^{15}\text{N}-^{14}\text{N}$).

The 8 remaining neutral species ($^3\text{CH}_2$, $^1\text{CH}_2$, CH_3 , CH , $\text{N}(^4\text{S})$, H , C_2H_4 , and H_2CN) comprise the class 2 neutral species. These species possess individual continuity equations, but advect with the mean atmospheric flow. The mean atmospheric flow is defined as the mass-weighted average of the class 1 species' velocities. These class 2 neutral species function primarily as components to the chemical scheme currently employed in the model. Ultimately, we employ this classification of neutral species only to conserve computational resources. Theoretically, TGITM can treat all species as class 1 species, but this requires a significant reduction in computational efficiency.

As with the class 2 neutral species, the 5 ionic species in TGITM (N_2^+ , N^+ , H_2CN^+ , CH_3^+ , and C_2H_5^+) possess individual continuity equations, but advect with the mean atmospheric winds. However, GITM has the ability to calculate each ion's individual velocity, including the effects of electrodynamic forcing terms in the Navier-Stokes momentum equation [*Ridley et al.*, 2006; *Schunk and Nagy*, 2000; *Gombosi*, 1999]. However, in this work we concern ourselves primarily with the neutral dynamics, and

Table 3.2: Neutral and Ionic Species Breakdown in TGITM

Classes	Species	Properties
Class 1 Neutrals	N_2 , CH_4 , HCN , H_2 , Ar , $^{13}\text{CH}_4$, ^{15}N - ^{14}N	Individual Species Continuity and Momentum Equations
Class 2 Neutrals	$^3\text{CH}_2$, $^1\text{CH}_2$, CH_3 , CH $\text{N}(^4\text{S})$, H , C_2H_4 , and H_2CN	Individual Species Continuity but Advect with the Mean Winds
Ions	N_2^+ , N^+ , H_2CN^+ , CH_3^+ , C_2H_5^+ ,	Individual Species Continuity but Advect with the Mean Winds

we defer a complete ion treatment to future research. Finally, the electrons simply provide neutrality to the ionosphere and there is currently no separate calculation for electron temperature, velocities, or densities enabled. Again, however, GITM can separately calculate a unique thermal, dynamical, and compositional structure for electrons and ions.

Running TGITM

Currently, T-GITM runs with an uniform horizontal resolution of 2.5° in latitude and 5° in longitude, since the variations of key prognostic variables (\mathbf{u} , T , and n) were found to be much greater in latitude than in longitude. However, the GITM framework remains very flexible and can accommodate any desired resolution in latitude, longitude, and altitude. In the radial direction, TGITM spans the altitude range from 500 km – 1500 km and possesses a uniform 12.5 km grid cell spacing, representing a resolution of roughly 0.25 scale heights at 600 km and roughly .125 scale heights at 1500 km. The modeling framework can also accommodate non-uniform grid-cells in latitude and altitude, providing even more customization of the numerical domain. However, for the purposes of this work, the resolutions in the horizontal and radial dimensions remain uniform.

TGITM remains an explicit time-stepping model, resulting in very small time-

steps that are limited to roughly 1 second. This time-stepping, in turn, requires long integration times for a fully converged simulation on Titan, which typically takes between 7 and 10 Titan simulation days (roughly 3.5 – 5 Earth simulation months). However, TGITM possesses a fully parallel block-based two-dimensional domain decomposition with latitudinal and longitudinal ghost cells bordering the blocks [Oehmke, 2004; Oehmke and Stout, 2001]. This structure allows for parallel computation over the entire Titan domain, exchanging information only between computational iterations. Additionally, TGITM uses the Message Passing Interface (MPI) standard, providing for platform independence. As a concrete example, a typical integration to steady-state on 108 processors, at the resolution stated previously, requires roughly two weeks of computational wall clock time. (NOTE TO SELF: Mention Type of Processors on Columbia and estimate a wall time in hours).

3.5 Fundamental Fluid Equations

The following section delineates the fundamental equations solved by the Titan GITM. In practice, the Titan framework separates the solvers for the coupled Navier-Stokes equations into horizontal and vertical dynamical cores, each possessing a specific set of assumptions. Thus, the discussion below parallels this separation, focusing on the neutral atmospheric dynamics. An in-depth discussion of the planet-specific source terms, such as chemistry, thermal conduction, and radiative balance, until the next section.

3.5.1 Horizontal Neutral Dynamics

The GITM momentum equations represent almost a direct application of Equations (2.48) - (2.50) with some simplifying assumptions. First, in the horizontal direction, the framework assumes that all neutral species move with the same mean

horizontal velocities. Hence, only a single momentum equation exists for the horizontal dimensions. Furthermore, because of this assumption, this single momentum equation deals exclusively with the bulk quantities of ρ , \mathbf{u} , and N that are defined as follows:

$$(3.42) \quad \rho = \sum_s m_s n_s,$$

$$(3.43) \quad N = \sum_s n_s,$$

$$(3.44) \quad \mathbf{u} = \frac{\sum \mathbf{u}_s m_s n_s}{\rho},$$

where \mathbf{u}_s , m_s , and n_s are the individual species' velocity (m/s), mass (kg), and number density (m^{-3}) respectively.

Horizontal Continuity

Using these definitions for ρ , \mathbf{u} , and N , GITM solves the continuity, momentum, and thermal balance equations in the horizontal direction. First, the horizontal continuity equation for each species in this formulation is given by:

$$(3.45) \quad \frac{\partial n_s}{\partial t} + n_s \nabla \cdot \mathbf{u} + \mathbf{u} \cdot \nabla n_s = 0.$$

Note that the above equation represents an exact application of Equation (2.48) in the horizontal dimensions. In this last expression, note that each species has an individual continuity equation, but GITM employs bulk velocities to advect the material. Furthermore, In spherical polar coordinates, this continuity equation may be expanded to:

$$(3.46) \quad \frac{\partial n_s}{\partial t} + n_s \left(\frac{1}{r} \frac{\partial u_\theta}{\partial \theta} + \frac{1}{r \cos \theta} \frac{\partial u_\phi}{\partial \phi} - \frac{u_\theta \tan \theta}{r} \right) + \frac{u_\theta}{r} \frac{\partial n_s}{\partial \theta} + \frac{u_\phi}{r \cos \theta} \frac{\partial n_s}{\partial \phi} = 0.$$

In the above expression, θ is north latitude, ϕ is east longitude, u_θ and u_ϕ are the northward and eastward components of the mean neutral velocity, and Ω is the planetary rotation rate ($\Omega = 4.56 \times 10^{-6} \text{ rad/s}$). The term, $\frac{u_\theta \tan \theta}{r}$, represents a spherical geometry correction (curvature) term.

Horizontal Momentum

The GITM horizontal momentum equations represent an almost direct application of Equation (2.49). However, as with its continuity equation, the vector form for the Titan model's horizontal momentum equation deals exclusively with bulk quantities, giving:

$$(3.47) \quad \frac{\partial \mathbf{u}}{\partial t} + \mathbf{u} \cdot \nabla \mathbf{u} + \frac{\nabla p}{\rho} + \frac{\nabla \cdot \tau}{\rho} + \mathbf{a}_s = \left(\frac{\delta \mathbf{u}}{\delta t} \right)^{ion-drag},$$

where $\left(\frac{\delta \mathbf{u}}{\delta t} \right)^{ion-drag}$ represents the contribution due to horizontal ion-neutral drag, $\frac{\nabla \cdot \tau}{\rho}$ represents the horizontal viscosity shear forces, \mathbf{a}_s represents accelerations due to Coriolis and curvature forces, and p represents the scalar atmospheric pressure and can be expressed with the ideal gas law as:

$$(3.48) \quad p = Nk_b T.$$

Here, T represents the neutral temperature and k_b is boltzmann's constant ($1.381 \times 10^{-23} \text{ J/K}$). Similar to the continuity equation's expansion into spherical coordinates, the horizontal momentum equation decomposes into two primary equations. First, the eastward (zonal) momentum equation is given by:

$$(3.49) \quad \frac{\partial u_\phi}{\partial t} + u_r \frac{\partial u_\phi}{\partial r} + \frac{u_\theta}{r} \frac{\partial u_\phi}{\partial \theta} + \frac{u_\phi}{r \cos \theta} \frac{\partial u_\phi}{\partial \phi} + \frac{1}{r \cos \theta} \frac{\partial p}{\partial \phi} = \frac{F_\phi}{\rho} + \frac{u_\phi u_\theta \tan \theta}{r} - \frac{u_r u_\phi}{r} + 2\Omega u_\theta \sin \theta - 2\Omega u_r \cos \theta,$$

where the terms, $\frac{u_\phi u_\theta \tan \theta}{r}$ and $\frac{u_r u_\phi}{r}$, represent spherical curvature corrections and the terms, $2\Omega u_\theta \sin \theta$ and $2\Omega u_r \cos \theta$, represent the zonal component of the Coriolis force.

Finally, the term, $\frac{F_\phi}{\rho}$, contains the ion-neutral drag and the viscosity contributions (detailed in Equation).

Similarly, the northward (meridional) momentum equation is as follows:

$$(3.50) \quad \frac{\partial u_\theta}{\partial t} + u_r \frac{\partial u_\theta}{\partial r} + \frac{u_\theta}{r} \frac{\partial u_\theta}{\partial \theta} + \frac{u_\phi}{r \cos \theta} \frac{\partial u_\theta}{\partial \phi} + \frac{1}{r} \frac{\partial p}{\partial \theta} = \frac{F_\theta}{\rho} - \frac{u_\phi^2 \tan \theta}{r} - \frac{u_r u_\theta}{r} - \Omega^2 r \cos \theta \sin \theta - 2\Omega u_\phi \sin \theta,$$

where the terms, $\frac{u_\phi^2 \tan \theta}{r}$ and $\frac{u_r u_\theta}{r}$, represent spherical curvature corrections and the terms, $\Omega^2 r \cos \theta \sin \theta$ and $2\Omega u_\phi \sin \theta$, represent the meridional component of the Coriolis force. Finally, the term, $\frac{F_\theta}{\rho}$, contains the ion-neutral drag and the viscosity contributions (detailed in Equation).

F_θ and F_ϕ , which comprise the ion-drag and viscosity forcing terms in the meridional and zonal directions respectively, are given by:

$$(3.51) \quad F_\theta = \rho_i \nu_{in} (v_\theta - u_\theta) + \frac{\partial}{\partial r} \eta \frac{\partial u_\theta}{\partial r}$$

$$F_\phi = \rho_i \nu_{in} (v_\phi - u_\phi) + \frac{\partial}{\partial r} \eta \frac{\partial u_\phi}{\partial r},$$

where ρ_i is the ion mass density (kg/m^3), ν_{in} is the total ion-neutral collision frequency, v_θ and v_ϕ are the ions' meridional and zonal velocities, and η is the dynamic viscosity ($\text{kg}/\text{m}/\text{s}$). As shown above, TGITM currently only accounts for radial shear of the horizontal velocity components. Furthermore, the ion-drag component is identically zero, since the ions are currently constrained to flow with the bulk velocity. More specifically, currently we set $v_\theta = u_\theta$ and $v_\phi = u_\phi$.

Horizontal Energy

The GITM horizontal energy equation deviates slightly from the formulation given by Equation (2.50). First, as with its continuity and momentum equations, the Titan model utilizes only a single, average temperature in the horizontal dimensions.

Furthermore, the Navier-Stokes energy equation is re-cast slightly. First, one expands $p = Nk_bT$ in Equation (2.50), while assuming that $\frac{1}{\gamma-1}$ and k_b remain constant over the scale of the derivatives considered. Finally, the framework formulation drops the second-order tensor contraction $\nabla\mathbf{P} : \nabla\mathbf{u}$, treating it as second order. These assumptions reduce the Navier-Stokes Energy equation to:

$$(3.52) \quad \frac{k_b T}{\gamma - 1} \left[\frac{\partial N}{\partial t} + \mathbf{u} \cdot \nabla N \right] + \frac{k_b N}{\gamma - 1} \left[\frac{\partial T}{\partial t} + \mathbf{u} \cdot \nabla T \right] + \frac{\gamma k_b}{\gamma - 1} N T \nabla \cdot \mathbf{u} = Q^{horiz}.$$

Here, Q^{horiz} represents the horizontal energy sources. Next, one defines a specific heat at a constant volume, $c_v = \frac{1}{\gamma-1} \frac{k_b}{m}$, (J/K/kg) giving now:

$$(3.53) \quad c_v T \bar{m} \left[\frac{\partial N}{\partial t} + \mathbf{u} \cdot \nabla N \right] + c_v N \bar{m} \left[\frac{\partial T}{\partial t} + \mathbf{u} \cdot \nabla T \right] + \gamma c_v \bar{m} N T \nabla \cdot \mathbf{u} = Q^{horiz}.$$

Furthermore, assuming that \bar{m} does not vary significantly over the scales of the derivatives in this equation and recalling that by definition $\rho = \bar{m}N$, one obtains:

$$(3.54) \quad c_v T \left[\frac{\partial \rho}{\partial t} + \mathbf{u} \cdot \nabla \rho \right] + c_v \rho \left[\frac{\partial T}{\partial t} + \mathbf{u} \cdot \nabla T \right] + \gamma c_v \rho T \nabla \cdot \mathbf{u} = Q^{horiz}.$$

However, after multiplying the GITM continuity equation by \bar{m} , one also obtains:

$$(3.55) \quad \left[\frac{\partial \rho}{\partial t} + \mathbf{u} \cdot \nabla \rho \right] = -\rho (\nabla \cdot \mathbf{u}).$$

Substituting this last expression into the Energy equation, it becomes:

$$(3.56) \quad c_v T [-\nabla \cdot \mathbf{u}] + c_v \rho \left[\frac{\partial T}{\partial t} + \mathbf{u} \cdot \nabla T \right] + \gamma c_v \rho T \nabla \cdot \mathbf{u} = Q^{horiz}.$$

Finally, the GITM horizontal energy equation emerges in the following succinct form:

$$(3.57) \quad \frac{\partial T}{\partial t} + \mathbf{u} \cdot \nabla T + (\gamma - 1) T \nabla \cdot \mathbf{u} = \frac{Q^{horiz}}{\rho c_v}.$$

The thermal balance equation may be expanded in spherical polar coordinates to:

$$(3.58) \quad \frac{\partial T}{\partial t} + \frac{u_\theta}{r} \frac{\partial T}{\partial \theta} + \frac{u_\phi}{r \cos \theta} \frac{\partial T}{\partial \phi} + (\gamma - 1) T \left(\frac{1}{r} \frac{\partial u_\theta}{\partial \theta} + \frac{1}{r \cos \theta} \frac{\partial u_\phi}{\partial \phi} - \frac{u_\theta \tan \theta}{r} \right) = \frac{Q^{horiz}}{\rho c_v}.$$

In conclusion, the equations of the previous sections form the core solvers for the horizontal composition, winds, and thermal structure in T-GITM. The external sources for these equations are described in detail in later sections..

3.5.2 Vertical Fluid Equations

Unlike the horizontal fluid solvers in the Titan GITM, the vertical (radial) solver allows each species to have a unique velocity. These velocities are coupled through neutral-neutral species bi-molecular friction coupling taken after *Colegrove et al.* [1966]. The radial set of fluid equations compensate for the exponential nature of the atmosphere by numerically solving for the logarithm of densities, rather than the neutral densities themselves. We define the natural logarithm of the neutral densities as \mathcal{N}_s as follows:

$$(3.59) \quad \mathcal{N}_s = \ln(n_s)$$

$$(3.60) \quad \frac{\partial \mathcal{N}_s}{\partial t} + \frac{\partial u_{r,s}}{\partial r} + \frac{2u_{r,s}}{r} + u_{r,s} \frac{\partial \mathcal{N}_s}{\partial r} = \frac{1}{n_s} S_s,$$

Where \mathcal{N}_s is the natural logarithm of neutral density, $u_{r,s}$ is the species' velocity in the radial direction, and S_s is the species-specific chemical source function given by

$$(3.61) \quad S_s = P_s - L_s,$$

where P_s is the chemical source term and L_s the chemical loss term.

In rotating spherical polar coordinates, the individual species' momentum equations are given as:

$$(3.62) \quad \frac{\partial u_{r,s}}{\partial t} + u_{r,s} \frac{\partial u_{r,s}}{\partial r} + \frac{u_\theta}{r} \frac{\partial u_{r,s}}{\partial \theta} + \frac{u_\phi}{r \cos \theta} \frac{\partial u_{r,s}}{\partial \phi} + \frac{k_b}{m_s} \frac{\partial T}{\partial r} + T \frac{k_b}{m_s} \frac{\partial \mathcal{N}_s}{\partial r} = g + \mathcal{F}_s + \frac{F^{turb}}{\rho} + \frac{u_\theta^2 + u_\phi^2}{r} + r\Omega^2 \cos^2 \theta + 2\Omega u_\phi \cos \theta$$

Where θ is north latitude, ϕ is east longitude, u_θ and u_ϕ are the northward and eastward components of the mean neutral velocity. Ω is the planetary rotation rate, g is the gravitational acceleration. The term, \mathcal{F}_s , contains the vertical ion-neutral friction force and a modified version of the neutral-neutral momentum coupling term of *Colegrove et al.* [1966]; *Schunk and Nagy* [2000]; *Gombosi* [1999]:

$$(3.63) \quad \mathcal{F}_s = \frac{\rho_i}{\rho} \nu_{in} (v_{i,r} - u_{s,r}) + \frac{k_b T}{m_s} \frac{1}{n - n_s} \sum_{q \neq s} \frac{n_q}{\tilde{D}_{qs} + K} (u_{r,q} - u_{r,s}).$$

In this equation, \tilde{D}_{qs} represents the binary molecular diffusion coefficient between neutral species q and s , as formulated by *De La Haye* [2005]; *De La Haye et al.* [2007b, a] and *Yelle et al.* [2006]: Meanwhile, the contribution due to turbulence represents a break from previous 3-D coupled modeling frameworks. First, note above that turbulent processes have been incorporated into the neutral-neutral friction term explicitly with the inclusion of the Eddy Diffusion coefficient, K , following the method of *Boqueho and Blelly* [2005]. This formulation of neutral-neutral momentum coupling allows for a smooth transition between the turbulent-dominated regime of the trubosphere to the diffusion-dominated heterosphere [*Boqueho and Blelly*, 2005]. Further, we incorporate an explicit mixing force, $\frac{F^{turb}}{\rho}$, that represents the effect of turbulence in forcing minor constituents to follow the mean atmosphere scale height. This force represents a modified version of the formulation in [*Boqueho and Blelly*, 2005] and is given by:

$$(3.64) \quad F^{turb} = \frac{k_b T}{m_s} \frac{1}{n - n_s} \sum_{q \neq s} \frac{n_q}{\tilde{D}_{qs} + K} \left[K \left(\frac{m_s g}{k_b T} - \frac{\overline{m} g}{k_b T} \right) \right].$$

Finally, the thermal conduction equation is given by:

$$(3.65) \quad \frac{\partial T}{\partial t} + u_r \frac{\partial T}{\partial r} + (\gamma - 1) \left(2 \frac{u_r}{r} + \frac{\partial u_r}{\partial r} \right) = \frac{Q_{tot}}{\rho c_v}$$

$$(3.66) \quad Q_{tot} = Q_{EUV} - Q_{HCN} + Q_{Magneto} + \frac{\partial}{\partial r} \left[\kappa_m \frac{\partial T}{\partial r} + \kappa_t \left(\frac{\partial T}{\partial r} + \Gamma_d \right) \right]$$

Here, Q_{tot} is the total source function, which is comprised of Solar EUV forcing (Q_{EUV}), HCN rotational line cooling (Q_{HCN}), Magnetospheric inputs (Q_{Magnet}), and finally thermal conduction. Γ_d represents the mean atmosphere dry adiabatic lapse rate, given by *Kundu and Cohen* [2004] as:

$$(3.67) \quad \Gamma_d = -\frac{\gamma - 1}{\gamma} \frac{T}{p} \frac{\partial p}{\partial r}.$$

It should be noted that the above expression for Γ_d reduces the more familiar form of $\Gamma_d = -\frac{g}{c_p}$ when one makes a hydrostatic assumption.

3.5.3 Key Physical Parameters: Viscosity, Thermal Conductivity, Turbulence, and Others

In this section, we provide details for the physical parameters used in the Navier-Stokes equations of the previous section.

Specific Heat at a Constant Volume

Furthermore, we employ a number density-weighted mean of the N_2 and CH_4 as follows:

$$(3.68) \quad c_v = \left(\frac{n_{N_2}}{N} \right) c_{v,N_2} + \left(\frac{n_{CH_4}}{N} \right) c_{v,CH_4}.$$

Here, we adopt the values of $c_{v,N_2} = \frac{5}{2} \frac{k_b}{m_{N_2}}$ and $c_{v,CH_4} = \frac{6.5374}{2} \frac{k_b}{m_{CH_4}}$ (J/K/kg) [Serway, 1996].

Viscosity

We adopt the dynamic viscosity coefficient, η , from a mass-weighted mean of N_2 and CH_4 viscosities:

$$(3.69) \quad \eta = \left(\frac{\rho_{N_2}}{\rho} \right) \eta_{N_2} + \left(\frac{\rho_{CH_4}}{\rho} \right) \eta_{CH_4}.$$

In order to calculate η_{N_2} , we adopt the Sutherland formula for η_{N_2} [De La Haye, 2005; Crane, 1988; Weast, 1984], which is given by:

$$(3.70) \quad \eta_{N_2} = \eta_{0,N_2} \frac{T_{0,N_2} + C_{N_2}}{T + C_{N_2}} \left(\frac{T}{T_{0,N_2}} \right)^{\frac{3}{2}}.$$

Here, $T_{0,N_2} = 300.55$ K and $\eta_{0,N_2} = 0.01781$ centipoise [Weast, 1984], are the reference temperature and associated viscosity for Nitrogen. $C_{N_2} = 111$ K is the Sutherland constant for nitrogen [Crane, 1988]. For Methane, we utilize the empirical expression from Yaws [1995], valid between 95 – 850 K, given by:

$$(3.71) \quad \eta_{CH_4} = (3.8435 + 4.0112 \times 10^{-1}T - 1.4303 \times 10^{-4}T^2) \times 10^{-4}.$$

The η_{CH_4} above also possess units of centipoise.

Thermal Conductivity

The molecular conductivity used in TGITM represents a combination of both N_2 and CH_4 molecular conductivities. For N_2 , we use the formulation by Yaws [1997, 1995]:

(3.72)

$$78K \leq T \leq 1500K \quad \kappa_{N_2}(T) = 0.00309 + 7.593 \times 10^{-5}T - 1.1014 \times 10^{-8}T^2,$$

(3.73)

$$97K \leq T \leq 1400K \quad \kappa_{CH_4}(T) = -0.00935 + 1.4028 \times 10^{-4}T + 3.318 \times 10^{-8}T^2,$$

Because CH_4 is non-negligible in Titan's upper atmosphere, we must employ a mixture conductivity, which for polyatomic gases is given by Mason and Saxena [1958]:

$$(3.74) \quad \kappa_{mix} = \sum_i \kappa_i \left(1 + \sum_{j \neq i} G_{ij} \frac{x_i}{x_j} \right)^{-1},$$

where x_i is the mole fraction of the i th species and where G_{ij} is given by:

$$(3.75) \quad G_{ij} = \frac{1.065}{2\sqrt{2}} \left(1 + \frac{m_i}{m_j} \right)^{-\frac{1}{2}} \left[1 + \left(\frac{\kappa_i^0}{\kappa_j^0} \right)^{\frac{1}{2}} \left(\frac{m_i}{m_j} \right)^{\frac{1}{4}} \right]^2.$$

Table 3.3: Selected Binary Diffusion Coefficients, $D_{qs} = \frac{A_{qs} T^b}{N}$ in cm^2/s

Interacting Species	A_{qs}	b	Reference
$N_2 - N_2$	5.09×10^{16}	0.810	Massman [1998]
$CH_4 - CH_4$	5.73×10^{16}	0.765	Wilson [2002a]; Reid <i>et al.</i> [1987]
$N_2 - CH_4$	7.34×10^{16}	0.750	Massman [1998]
$N_2 - H_2$	1.88×10^{17}	0.820	Banks and Kockarts [1973]
$CH_4 - H_2$	2.30×10^{17}	0.765	Mason and Marrero [1970]

Here, κ_i is the i th species' individual thermal conductivity and κ_i^0 represents the frozen thermal conductivity of species. The ratio of the κ_i^0 's can be expressed as in *Mason and Saxena* [1958]:

$$(3.76) \quad \frac{\kappa_i^0}{\kappa_j^0} = \frac{\eta_i m_j}{\eta_j m_i}$$

Molecular Diffusion and Eddy Diffusion

In this equation, \tilde{D}_{qs} represents the binary molecular diffusion coefficient between neutral species q and s , as formulated by *De La Haye* [2005]; *De La Haye et al.* [2007b, a] and *Yelle et al.* [2006]:

$$(3.77) \quad \tilde{D}_{qs} = \frac{D_{qs}}{1 - \frac{n_s}{N} \left(1 - \frac{m_s}{m_{\neq s}} \right)},$$

where m_s is the molecular mass of species, s , and $m_{\neq s}$, is the gas mixture's mean mass excluding species s . D_{qs} is the familiar neutral-neutral binary molecular diffusion coefficient as given in *Banks and Kockarts* [1973]. Here D_{qs} is given by the following empirical relationship:

$$(3.78) \quad D_{qs} = \frac{A_{qs} T^b}{N}.$$

In TGITM, the values for the most significant A_{qs} coefficients are given in Table 3.3. Most values for these binary diffusion coefficients are available in the literature (c.f. *Banks and Kockarts* [1973], *Mason and Marrero* [1970], and *Massman* [1998])

for the species included in the Titan GITM model. However, where binary diffusion coefficients could not be obtained directly, we employ the analytical approximation given by *De La Haye* [2005]; *Wilson and Atreya* [2004]:

$$(3.79) \quad \text{if } m_q < m_s \rightarrow D_{qs} = D_{qq} \sqrt{\frac{1/m_s + 1/m_q}{2/m_q}}$$

$$(3.80) \quad \text{if } m_q \geq m_s \rightarrow D_{qs} = D_{qq} \sqrt{\frac{m_q}{m_s}}$$

The eddy diffusion coefficient, K , varies according to the formulation put forth in *Atreya* [1986]:

$$(3.81) \quad K = K_0 \sqrt{\frac{N_0}{N(r)}}, \quad K \leq K_{max}.$$

In this expression, K_0 and K_{max} represent the lower boundary eddy diffusion and the maximum eddy diffusion allowed in the atmosphere respectively.

3.6 Numerical Method

In this section, we put forth the numerical techniques used to solve the horizontal and vertical Navier-Stokes' equations delineated above, following the discussion in *Ridley et al.* [2006] closely.

Spatial Discretization for Advection

In what follows, let U represent a generalized primitive variable being advected. The spatial gradients are obtained by finite differencing the face values:

$$(3.82) \quad \nabla U_j = \frac{U_{j+1/2} - U_{j-1/2}}{\Delta x_j},$$

where the index, $j + 1/2$, represents the cell interface between grid cells indexed by j and $j + 1$ in the direction of the gradient and Δx_j is the cell size. The face values

are taken as the average of the *left* and *right* face values, U^L and U^R :

$$(3.83) \quad U_{j+1/2} = \frac{U_{j+1/2}^L + U_{j+1/2}^R}{2}.$$

Furthermore, GITM employs limited reconstruction [*van Leer, 1979*] in obtaining the face values:

$$(3.84) \quad \begin{aligned} U_{j+1/2}^L &= U_j + \frac{1}{2}\bar{\Delta}U_j \\ U_{j+1/2}^R &= U_{j+1} - \frac{1}{2}\bar{\Delta}U_j. \end{aligned}$$

Here, $\bar{\Delta}U_j$ represents the limited slope of the primitive variable. In order to obtain this limited slope, we utilize a modified monotized central limiter. If the left and right slopes, $\Delta U_{j-1/2} = U_j - U_{j-1}$ and $\Delta U_{j+1/2} = U_{j+1} - U_j$, have opposite signs, then the monotized slope becomes zero. Otherwise, GITM takes the following:

$$(3.85) \quad \bar{\Delta}U_j = \text{sign}(\Delta U_{j+1/2}) \min \left(\beta |\Delta U_{j-1/2}|, \beta |\Delta U_{j+1/2}|, \frac{1}{2} |U_{j+1} - U_{j-1}| \right),$$

where *sign* is the sign function, and $1 \leq \beta \leq 2$ is an adjustable parameter. At Titan, $\beta = 1.6$ produces stable and accurate results.

In order to add stability, and to provide upwind bias, the framework adds a second-order Lax-Friedrichs numerical flux to the variable updates. For example, in the vertical advection routines, it adds the gradient of the flux

$$(3.86) \quad F_{j+1/2} = \frac{1}{2} \max(c_{j-1/2}, c_{j+1/2})(U_{j+1/2}^R - U_{j+1/2}^L),$$

where $c = |u| + c_s$ is the maximum wave speed calculated from the bulk speed, u , and the local sound speed, $c_s = \sqrt{\frac{\gamma p}{\rho}}$. This diffusive flux remains second-order for regions with smooth gradients; however, in regions of sharp gradients, this flux becomes first-order and produces a stable and oscillation-free solution.

Viscosity, Neutral Friction, and Conduction

Viscosity, neutral-neutral bi-molecular friction, and thermal conduction all represent numerically stiff source terms. Thus, instead of using the fluid solvers of the previous section, we utilize a tri-diagonal implicit solver for these. Since these terms are applied in the vertical direction only (i.e. only vertical gradients are considered), the resulting linear systems of equations require the inversion of simple tri-diagonal matrices, using a direct solver to obtain the solution. Furthermore, in a parallel run, only horizontal information is distributed across processors, making the data in these linear systems local information.

Chemistry

GITM solves for chemistry using a subcycling technique. Furthermore, this method does not *a priori* assume photochemical equilibrium and is implemented on a grid-point by grid-point basis. For each iteration in the subcycle (chemical time-step), all sources and losses for all constituents are calculated. GITM determines the chemical time-step by demanding that each species can only be changed by 25% in a single step. Thus, multiple chemical time-steps may be taken during a single advective time-step. This can cause chemistry, depending on the local conditions, to comprise a significant amount of the overall run-time.

3.7 Key Takeaways from GITM

Ultimately, this framework represents a significant break from previous 3-D upper atmosphere models. The equations and formulations of the last sections cement this fact. Titan GITM's greatest strength lies in its ability to calculate vertical transport explicitly in spherical polar coordinates without assuming hydrostatic equilibrium. In Chapters 5 and 6, the capabilities of GITM are utilized to explore the coupled

chemistry, dynamics, and energetics of Titan's upper atmosphere.

CHAPTER IV

Vertical Dust Mixing and the Interannual Variability of Mars' Upper Atmosphere

The worthwhile problems are the ones you can really solve or help solve, the ones you can really contribute something to.

—Richard Feynman

4.1 Abstract

Mars winter polar warming is a phenomenon of the lower thermosphere temperatures and densities that is well documented by *in situ* accelerometer data taken during spacecraft aerobraking maneuvers [Keating *et al.*, 2003]. Previous work by Bouger *et al.* [2006] simulates two specific time periods, corresponding to existing aerobraking datasets, and confirms the existence of winter polar warming structures in the Martian upper atmosphere, using the coupled Mars General Circulation Model-Mars Thermosphere General Circulation Model (MGCM-MTGCM). The present work investigates the underlying mechanisms that drive winter polar warming in three major studies: (1) a systematic analysis of vertical dust mixing in the lower atmosphere and its impact upon the dynamics of the lower thermosphere (100 – 130 km), (2) an interannual investigation utilizing three years of lower atmosphere infrared (IR) dust optical depth data acquired by the Thermal Emission Spectrome-

ter (TES) instrument on board Mars Global Surveyor (MGS), and finally (3) a brief study of the MTGCM's response to variations in upward propagating waves and tides from the lower atmosphere.

From the first study, we find that the vertical dust mixing greatly modifies the simulated winter polar warming features in the MTGCM's thermosphere at both solstice seasons. Furthermore, this sensitivity study confirms that an interhemispheric Hadley circulation and the concomitant adiabatic heating rates are the primary causes for these winter polar warming structures. From the second study, we find that, as revealed in the lower atmosphere by *Liu et al.* [2003], the polar lower thermosphere exhibits a high degree of variability at $L_S = 270$, with reduced yet significant variability at $L_S = 090$. Finally, the third numerical experiment indicates, as was found in the lower atmosphere by *Wilson* [1997], that upward propagating waves and tides allow meridional flows to access the thermosphere's winter polar latitudes. This last investigation also indicates that the Hadley circulation responsible for thermospheric winter polar warming originates in the lower atmosphere and extends high into the upper atmosphere. In summary, these new efforts establish a baseline numerical study upon which more comprehensive model-to-data comparisons may be conducted for the Martian thermosphere.

4.2 Introduction and Motivation

Previous work by *Bougher et al.* [2006] indicated that the highly coupled nature of the Martian upper and lower atmospheres remains critical to understanding winter polar warming in the lower thermosphere. In particular, they suggested that lower atmospheric dust functions as the dominant driver for the simulated temperature structures. Furthermore, they posited that lower atmospheric dust varia-

tions modify a vertically extended interhemispheric Hadley circulation that cools the summer polar thermosphere temperatures while simultaneously warming the winter polar thermosphere temperatures. The simulated thermospheric temperature structures matched the trends found in Mars Odyssey (ODY) and Mars Global Surveyor (MGS) aerobraking data sets. From these simulations, *Bougher et al.* [2006] hypothesized that a dust driven, summer-to-winter Hadley circulation, resulting from the tight coupling between the upper and lower atmospheres, combines with an *in situ* Extreme Ultraviolet (EUV) heating driven circulation to produce the observed temperature structures in aerobraking data. However, this previous work focused solely upon reproducing winter polar warming at times that matched available *in situ* accelerometer data, and it did not attempt a more systematic exploration of the impacts of lower atmospheric dust upon the thermosphere.

In this work, we characterize the dynamical impact of lower atmospheric dust upon the thermosphere of the coupled Mars General Circulation Model – Mars Thermosphere General Circulation Model (MGCM - MTGCM) through a series of numerical experiments: a dust sensitivity study, an interannual study, and a wave-impact analysis study. In the sensitivity investigation, we focus primarily upon the solstice period of $L_S = 090$ and quantify the response of the lower thermosphere's temperature, density, and dynamical structures to variations in lower atmospheric vertical dust mixing altitudes. The interannual study includes both solstice periods ($L_S = 090$ and $L_S = 270$) for three Mars years (24- 27) that overlap with three MGS Thermal Emission Spectrometer (TES) mapping years. We utilize the TES database because it provides a nearly continuous lower atmosphere dust climatological database that serves as a natural foundation for modeling a suite of interannual variations in the thermosphere. In the final numerical experiment, we examine the

thermosphere's response to variations in its lower boundary coupling with the lower atmosphere at the $1.32\text{-}\mu\text{bar}$ pressure level. In essence, this last study measures the variability of the MTGCM's circulation to fluctuations in the amplitude of upward propagating waves and tides transmitted from the lower atmosphere MGCM.

Throughout this work, we highlight the impacts upon the lower thermosphere, spanning the $100 - 130$ km altitude range, which most directly impacts aerobraking missions. Furthermore, it is this altitude range where the winter polar warming features appear most prominently in accelerometer datasets [Keating *et al.*, 1998, 2002, 2003]. To simplify the analysis, we focus on the 120 km altitude level, which exhibits the average dynamical, thermal, and density variations expected in the lower thermosphere. Also, we specify solar moderate fluxes ($F_{10.7\text{-}cm} = 130$) for all simulations, in order to remove any perturbations in solar heating not directly related to the lower atmospheric dust. Although, at 120 km altitude, the solar EUV heating rates in the MTGCM remain of limited importance relative to the dominant dynamics. Taken together, these limitations remove the possibility of directly comparing simulation results with *in situ* data. However, these constraints lay the foundation for a detailed theoretical exploration of the fundamental drivers causing the phenomenon of winter polar warming.

4.2.1 Interannual and Seasonal Variations: Previous work

Although this paper addresses interannual variations in the thermosphere, it builds upon a rich body of literature for both the Martian upper and lower atmospheres [e.g. *Angelats i Coll et al.* [2004]; *Bougher et al.* [2004, 2006]; *Deming et al.* [1986]; *Forbes et al.* [2002]; *Forget et al.* [1996, 1999]; *Keating et al.* [2002]; *Santee and Crisp* [1993]; *Theodore et al.* [1993]; *Wilson* [2002b, 1997]; *Withers et al.* [2003]]. *Liu et al.* [2003] provides an exhaustive treatment of seasonal and interan-

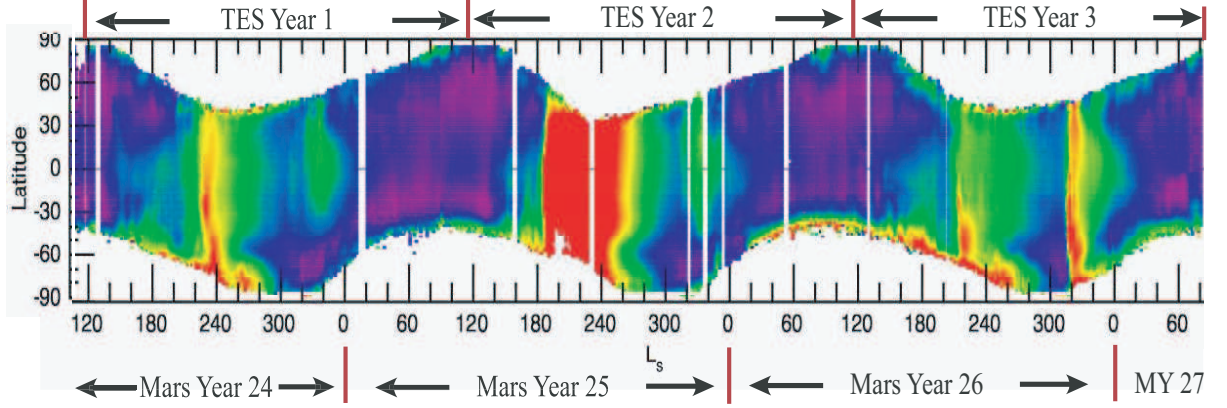


Figure 4.1: Martian lower atmosphere dust opacities (unitless) as a function of latitude for three consecutive TES years. Note that TES years do not overlap directly with conventional Mars Years, which are shown below the panel. All opacities are zonally averaged quantities. By convention the purple is $\tau = 0.0$ while the red is $\tau = 0.5$. This figure was adapted from *Smith [2006]*

nual variations in the lower atmosphere. They find, by analyzing MGS TES, Viking Lander, and Mariner 9 datasets, that the northern spring and summer ($L_S = 000 - 140$) temperatures remain highly repeatable from year to year. Even after globe-encircling dust storms during the preceding southern summer, the lower atmosphere returns to a nominal state relatively quickly, exhibiting temperature variations of only 1 K on the nightside and 6 K on the dayside. Conversely, *Liu et al. [2003]* find that the opposite seasons, southern spring through southern summer (roughly $L_S = 140 - 360$), show a relatively high degree of local variability. These short-term variations arise mostly due to large scale dust-storms, which are observed to occur more frequently during this season. From their work, *Liu et al. [2003]* maintain that the Martian atmosphere does not possess a significant memory of past events. Instead, the atmosphere displays coherent sequences of repeating dynamical configurations, with departures primarily due to variations in local solar insolation, dust forcing, and water-ice interactions.

4.2.2 Mars Global Surveyor and Mars Odyssey

The two satellites, MGS and ODY, have provided a plethora of both *in situ* and remote data from which to build a climatological database for the Martian lower thermosphere (100 – 130 km). Other valuable data sources were available, such as the Viking Landers 1 and 2 (VL1 and VL2) and Mariner 9; however, in this study we focused on the data provided by the MGS and ODY satellites. Both satellites participated in aerobraking maneuvers; the details of these orbital procedures are given in *Withers et al.* [2003] and *Withers* [2006] and *Keating et al.* [1998, 2002, 2003]. The analysis of these datasets indicated a strong coupling between the Martian lower and upper atmosphere with three primary components: (1) seasonal and dust driven inflation/contraction of the lower and upper atmospheres, (2) upward propagating migrating and non-migrating tides, and (3) a strong inter-hemispheric Hadley circulation during solstice conditions in the upper atmosphere.

Significant seasonal variations were discovered during the analysis of both MGS and ODY aerobraking datasets. During MGS Phase 2 aerobraking, lasting from September 1998 to February 1999, accelerometer sampling occurred during the approach to southern winter solstice, $L_S = 030 - 090$. The satellite possessed a nearly polar orbit with periapsis approaching the southern pole. As the satellite tracked from equatorial to polar latitudes, accelerometer-derived temperatures in the lower thermosphere (altitudes spanning 100 – 130 km) increased from 100 K up to a maximum of 110 K, subsequently declining to polar night values of 90 K – 100 K. Similarly, Odyssey possessed a near-polar orbit with periapsis approaching the northern pole near southern summer solstice, $L_S = 250 - 300$. In this instance, the ODY accelerometer found strong polar warming features, rising from 100 K at mid latitudes and peaking at 160 K at the Northern winter polar night [*Keating et al.*,

2003]. *Bougher et al.* [2006] provides more details on these seasonal variations in these winter polar warming structures in the lower thermosphere.

In short, these two satellites provide a wealth of overlapping data that contribute to a growing climatological database for the Martian lower thermosphere. Despite the usefulness of these data sets, they still possess significant shortcomings, such as: limited local time and latitude sampling, and sporadic sampling throughout the solar cycle. However, the TES lower atmospheric IR opacity represents the single most important data set for the present study. Using these IR opacity maps, derived dust distributions in latitude, longitude, and altitude are generated for use in the lower atmosphere MGCM.

4.2.3 Thermal Emission Spectrometer-TES

The TES instrument on board MGS provides nearly continuous IR optical depth measurements, yielding maps for over three consecutive years [*Liu et al.*, 2003; *Christensen et al.*, 2001; *Smith*, 2004]. These maps span most of the Martian globe. However, the winter polar regions pose a problem, due to their low luminosity at IR wavelengths. Further, this longwave radiation represents a good proxy for mixing ratio variations of micron-size dust particles ($1 - 10 \mu\text{m}$).

By cataloguing the data collected by TES over its lifetime, a suspended dust climatological database emerges that provides comprehensive spatial and temporal coverage for three consecutive Martian years. Figure 4.1 illustrates column-integrated dust opacity distributions (zonally averaged) as a function of latitude and season over three Martian years. In this work, we utilize the TES observed opacities to specify the spatial distribution of suspended dust in the lower atmosphere MGCM, and evaluate their impacts on the global circulation and structure of the upper atmosphere MTGCM.

At polar latitudes, where surface temperatures are less than 220 K and TES IR opacity maps are not readily available, we extrapolated the available IR opacity data in the lower atmospheric MGCM to ensure non-zero dust opacities over the entire Martian globe. To accomplish this, we simply reduced the TES opacity at the highest available latitude by a factor of 0.80 for each latitude grid cell in the MGCM poleward of the data. For instance, if the last available (i.e. highest latitude) TES opacity data point possessed a value of $\tau = 1.0$ at 50° N, then the extrapolated dust opacity in the adjacent grid cell at 55° N would be $\tau = 0.80$. Further, the grid cell at 60° N would have $\tau = 0.64$ and so on to the pole. This method allowed us to generate continuous lower atmospheric dust opacities over the entire Martian globe during all of our TES Year simulations.

In the context of this work, two measures of time remained important. First, the TES Year time stamp was keyed to the beginning of the MGS mapping phase, which began in March, 1999. This first TES mapping year, dubbed TES Year 1, began at $L_S = 104$ of Mars Year 24 and data collection continued until the end of its mapping mission, which was approximately $L_S = 081$ during Mars Year 27. Although $L_S = 081$ marks the end of the TES mapping phase as it is defined in this paper, the instrument still provided data intermittently from that date until $L_S = 160$.

Figure 4.1 illustrates the relationship between the Mars Years and TES Mapping Years. It should be noted that some controversy surrounds the assignment of Mars Years [Šuráň, 1997; *Gangale and Dudley-Rowley, 2005*]. In this paper, we adopt the timekeeping standard put forth by *Clancy et al. [2000]* and *Smith [2004]*, which designates $L_S = 000$ of Mars Year 0 on April 11th, 1955. These lower atmospheric dust distributions are incorporated into the lower atmosphere MGCM, where ther-

mal structures, dynamics, and chemistry are self-consistently calculated. Then, key outputs—Temperature (T), Zonal Winds (U), Meridional Winds (V), and Geopotential Height (Φ)— are produced at each 2-minute time step at the $1.32\text{-}\mu\text{bar}$ level. These outputs are then interpolated to the Mars Thermosphere General Circulation Model (MTGCM) grid at each time step. In the next section, the details of both models are discussed.

4.3 The Coupled Model (MGCM-MTGCM)

The MTGCM itself is a finite difference primitive equation model that self-consistently solves for time-dependent neutral temperatures, neutral-ion densities, and three component neutral winds over the globe [Bougher *et al.*, 1999b, a, 2000, 2004, 2006]. Prognostic equations for the major neutral species (CO_2 , CO, N_2 , and O), selected minor neutral species (Ar, He, NO, $\text{N}^{(4)\text{S}}$, and O_2), and several photochemically produced ions (e.g. O_2^+ , CO_2^+ , O^+ , and NO^+ below 180 km) are included. All fields are calculated on 33 pressure levels above $1.32\text{-}\mu\text{bar}$, corresponding to altitudes from roughly 70 to 300 km (at solar maximum conditions), with a 5° resolution in latitude and longitude. The vertical coordinate is log pressure, with a vertical spacing of 0.5 scale heights. Key adjustable parameters which can be varied for individual MTGCM cases include the $\text{F}_{10.7\text{-}cm}$ index (solar EUV/UV flux variation), the heliocentric distance and solar declination corresponding to Mars seasons. The MTGCM is a modified version of the National Center for Atmospheric Research (NCAR) Thermospheric-Ionospheric-Energetics General Circulation Model (TIE-GCM) [Roble *et al.*, 1988]. Detailed discussion of this modification is given in Bougher *et al.* [2000]. Currently, a fast non-Local Thermodynamic Equilibrium (NLTE) 15-micron cooling scheme is implemented in the MTGCM, along with corre-

sponding near-IR heating rates *Bougher et al.* [2006]. These improvements are based upon recent detailed one dimensional (1-D) NLTE model calculations for the Mars upper atmosphere, (e.g. *López-Valverde et al.* [1998]).

The MTGCM is currently driven from below by the NASA Ames Mars General Circulation Model (MGCM) code [*Haberle et al.*, 1999] at the $1.32\text{-}\mu\text{bar}$ level (near 60-80 km). This coupling allows both the migrating and non-migrating tides to cross the MTGCM lower boundary and the effects of the expansion and contraction of the Mars lower atmosphere to extend to the thermosphere. The entire atmospheric response to simulated dust storms can also be monitored using these coupled models. Key prognostic variables are passed upward from the MGCM to the MTGCM at the $1.32\text{-}\mu\text{bar}$ level at every MTGCM grid point: Temperature (T), zonal (U) and meridional (V) winds, and geopotential height (Z). The continuity equation is solved to provide consistent vertical velocities (W) across this $1.32\text{-}\mu\text{bar}$ lower boundary. Two dimensional (2-D) interpolation is applied to construct MGCM fields at the $1.32\text{-}\mu\text{bar}$ level to match the $5^\circ \times 5^\circ$ MTGCM grid. These two climate models are each run with a 2-minute time step, with the MGCM exchanging fields with the MTGCM at this frequency. Eight Sol (the Martian Day) runs are conducted for various Mars seasonal and solar cycle conditions. This coupled configuration has been previously validated using an assortment of spacecraft observations, including MGS Phase 1 and 2 and ODY aerobraking data sets [*Bougher et al.*, 1999a, 2000, 2004, 2006]. Additionally, no downward coupling is presently activated between the MGCM and the MTGCM. However, the impacts of the lower atmosphere's dynamics upon the upper atmosphere remain the dominant concern of this paper.

At present, a simple photochemical ionosphere is formulated for the MTGCM including e.g. O_2^+ , CO_2^+ , O^+ , and NO^+ below 180 km. Key ion-neutral reactions and

rates are taken from Fox and Sung [2004]; empirical electron and ion temperatures are adapted from the Viking mission. The ionization rates required for the production rates are calculated self-consistently, making use of specified solar EUV fluxes. Photoelectron contributions to these ionization rates are parameterized within the MTGCM code.

The NASA Ames MGCM is a primitive equation, grid-point numerical model of the Martian atmosphere. It contains a variety of numerical parameterizations for the treatment of such physical processes as radiative transfer (solar absorption and infrared absorption and emission by gaseous CO₂ and suspended dust), atmospheric/surface interactions (transfer of momentum and sensible heat), condensation/sublimation of carbon dioxide (and the concurrent changes in atmospheric mass), and imposed flow deceleration near the model top (for both physical and numerical reasons). The model is thoroughly discussed in *Pollack et al.* [1990] and *Haberle et al.* [1999].

4.4 Specifying Lower Atmospheric Dust in the MTGCM-MGCM: Two Approaches

Previous studies of lower atmospheric dust in Mars atmosphere have focused on reproducing observed dust vertical profiles through numerical and theoretical modeling [*Conrath*, 1975; *Murphy et al.*, 1990, 1993]. These studies explored the effects of particle shape, particle size, and atmospheric circulation patterns on simulated dust vertical mixing profiles and on the physics underlying the dust-atmosphere feedback system.

For the current research, the numerical methods for describing the lower atmospheric dust mixing remained critical. The dust in the lower atmosphere was specified as a function of latitude, longitude, and altitude in the lower atmosphere MGCM.

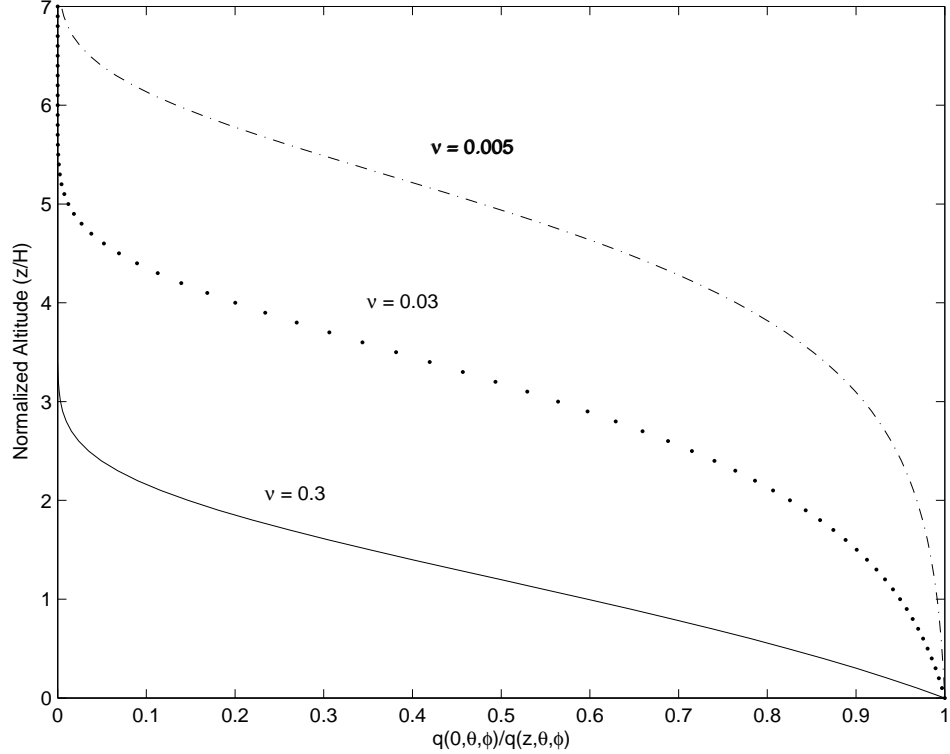


Figure 4.2: Illustration of Conrath vertical dust mixing profiles as a function of altitude above a given reference level. The zero-altitude level in this work is assumed to be the 6.1-mb pressure level. Note the connection between the ν value and the effective dust mixing altitudes.

The total integrated IR dust opacity was specified at the 6.1-mb pressure level. The resulting vertical dust mixing profiles followed directly from the formalism of *Conrath* [1975], which can be summarized by the following:

$$(4.1) \quad \nu = \frac{t_D}{t_s(0)}.$$

Where $t_s(0)$ is the dust particles' characteristic settling time at $z = 0$ and t_D is the vertical diffusion time of the dust given by

$$(4.2) \quad t_D = \frac{H^2}{K}.$$

Here, H is the local atmospheric scale height (roughly 8 – 10 km in the lower

atmosphere) and K is the local eddy diffusion coefficient. Finally, these ν parameters are then used in the following vertical mixing profile:

$$(4.3) \quad q(z, \phi, \theta) = q(0, \phi, \theta) e^{(\nu[1 - e^{(\frac{z}{H})}])}.$$

Sample vertical profiles, corresponding to three ν values, are illustrated in Figure 4.2. In this Figure, the line plots represent the average variation of dust mixing ratio as a function of altitude, and they are meant only as an approximation to the actual dust mixing profiles employed in this study. The Conrath profile describes the vertical dust mixing ratio above a specific point, defined in Figure 4.2 as $q(0, \phi, \theta)$. We define this base level as the 6.1-mb pressure level, below which the lower atmospheric dust is assumed to be well-mixed to the surface, and above which the lower atmosphere dust is assumed to fall off with the exponential character of equation (3).

For clarification on the physical implications of the three Conrath parameters shown in Figure 4.2, the three values of $\nu = 0.3, 0.03$, and 0.005 correspond to uniform local eddy diffusion coefficients of 10^5 , 6×10^5 , and $5 \times 10^6 \text{ cm}^2/\text{s}$, respectively. Furthermore, it should be noted that these eddy diffusion coefficients are less than the values utilized in *Conrath* [1975] because this previous research does not explicitly account for dynamical dust lifting as we do in the current work. Next, the latitudinal and longitudinal variations in the MGCM lower atmospheric dust levels comprise the major distinctions between the first two studies employed in this work and are further discussed below.

4.4.1 Dust profiles for the Sensitivity Study

This numerical experiment seeks to quantify the impacts of the lower atmosphere vertical dust mixing on the MTGCM's temperatures, densities, and circulation. Be-

cause of this, we conduct controlled numerical experiments with the lower atmospheric dust specifications, employing uniform dust distributions at the 6.1-mb pressure level. In other words, the value of $q(0, \phi, \theta)$ of Figure 4.2 is held constant at a preset value, while we vary the ν parameter, which specifies the rate of exponential fall off in the lower atmospheric dust's vertical mixing ratio. This globally symmetric dust distribution isolates the impact of vertical mixing of the dust on the MTGCM lower thermosphere. However, as shown in Figure 4.1, a globally symmetric dust distribution remains inappropriate for most of the Martian year. In order to explore how non-uniform dust distributions impact the MTGCM simulations, we turn to the next phase of the present work.

4.4.2 Dust profiles for the Interannual Study

For the interannual investigation, we derive the lower atmospheric dust distribution, $q(0, \phi, \theta)$, from the TES IR opacity data, which is shown zonally averaged in Figure 4.1 as a function of time. However, for this experiment, the vertical mixing now varies as a function of the lower atmospheric integrated dust opacity. Essentially, the higher the total opacity in the TES data, the more deeply the dust is assumed to mix vertically in Mars' lower atmosphere. For example, the purple regions in Figure 4.1 correspond to a total opacity of near 0.0, which indicates that very little dust existed in the atmosphere and that the dust would not mix to high altitudes. By contrast, the red regions indicate total opacity of 0.5, which results in both a much larger amount of dust in the lower atmosphere and mixing the dust to much higher altitudes. Thus, the ν parameter, which specifies the rate of exponential fall off in the lower atmospheric dust's vertical mixing ratio, varies as a function of θ and ϕ that is derived directly from the TES IR opacity maps in Figure 4.1.

4.5 Sensitivity of the MTGCM Lower Thermosphere to Vertical Dust Mixing

This sensitivity study isolates the impacts of the lower atmospheric dust parameters on the MTGCM lower thermosphere by systematically varying:

- (1) Vertical dust mixing altitudes,
- (2) The total amount of dust in a column or optical depth, τ , between 0.3 and 1.0,
- (3) Seasonal variations at $L_S = 090$ and 270 .

In this experiment, we investigate each variable's impact independent of the others, through a series of tests detailed below.

4.5.1 Varying the Vertical Dust Mixing Profiles

Figures 4.3 – 4.4 illustrate the response of the MTGCM lower thermosphere to variations in the vertical dust mixing height. In both figures, the season, total integrated dust opacity at 6.1-mb, and solar fluxes are held constant at $L_S = 090$, $\tau = 0.3$, and $F_{10.7-cm} = 130.0$ (Solar Moderate) respectively. All plots contain zonal mean quantities, allowing us to integrate over both local time and topographically forced variations. Additionally, we use 120 km altitude, denoted by the horizontal black lines in these figures, as a proxy for the overall response of the lower thermosphere (100 – 130 km).

Response of the MTGCM Temperatures

In Figure 4.3, the temperatures for the low ($\nu = 0.3$), medium ($\nu = 0.03$), and high ($\nu = 0.005$) dust mixing profiles are shown in panels (a), (b), and (c) respectively. Similarly, panels (d), (e), and (f) contain the corresponding adiabatic heating and cooling rates (colored contours) with overlying zonal mean stream functions (black

Table 4.1: Polar Warming Features in Kelvin for Sensitivity Study

Season	Total Opacity	$\nu = 0.3$ (Low)	$\nu = 0.03$ (Medium)	$\nu = 0.005$ (High)
$L_S = 090$	$\tau = 0.3$	$\Delta T = 20$ K	$\Delta T = 30$ K	$\Delta T = 37$ K
$L_S = 090$	$\tau = 1.0$	—	$\Delta T = 40$ K	—
$L_S = 270$	$\tau = 1.0$	—	$\Delta T = 73$ K	—

dotted lines). Moving from panel (a) to panel (c), the lower atmospheric dust is mixed from the lowest altitude to the highest altitude. Furthermore, the maximum meridional velocities at 120 km are indicated in the figure caption for each of the vertical mixing heights in m/s.

Focusing on 120 km altitude in Figure 4.3(a), temperatures near the equator begin at 140 K. Moving towards the southern winter polar region, the temperatures rise to 160 K at 70^0 S and then remain steady into the pole. This results in a minimum-to-maximum polar warming feature of $\Delta T = 20$ K. Panel (b), following the same trajectory, shows a warming from nearly 130 K at the equator to just over 160 K near 80^0 S, corresponding to a $\Delta T = 30$ K. Lastly Figure 4.3(c), at 120 km, depicts a warming from 128 K at the equator to nearly 165 K near 75^0 S latitude, followed by a steep cooling into the pole. This last figure possesses a temperature change of $\Delta T = 37$ K. Thus, in moving from panel (a) to panel (c) the MTGCM temperatures exhibit a systematically larger winter polar warming feature, as illustrated by the ΔT 's found at 120 km. In other words, as the lower atmospheric dust vertical mixing height increases, the winter polar warming feature at 120 km simultaneously increases. The winter polar warming features for each dust mixing height are contained in Table 4.1.

At 120 km altitude in the equatorial and summer latitudes, the lower thermosphere exhibits a net cooling effect, as dust is mixed higher in the lower atmosphere. The equatorial temperatures of Figures 4.3(a), (b), and (c) are 140 K, 130 K, and 128 K

respectively. Similarly, the minimum temperature at 120 km, which occurs near the summer pole, for each panel is likewise 135 K, 120 K, and 117 K. Thus, the summer polar thermosphere exhibits a summer polar cooling that is amplified as the lower atmospheric vertical dust mixing increases. This simultaneous cooling of the summer polar thermosphere while the winter polar thermosphere is warmed indicates that energy is being transported from the summer to the winter hemisphere. We explore this transport mechanism further in the following section.

MTGCM Adiabatic Heating and Cooling Rates

There are five primary drivers for thermal structure in the Mars Thermosphere General Circulation Model (MTGCM): thermal conduction, CO₂ 15- μ m cooling, solar heating, hydrodynamic advection, and adiabatic heating/cooling. Of these five drivers, adiabatic heating (due to convergence of meridional and vertical flows) and cooling (due to divergence of meridional and vertical flows), emerges as the single most significant contributor to the variations in the lower thermosphere structures found in this study. The other source terms possess comparatively smaller amplitudes in the MTGCM at these altitudes. Consequently, we focus the discussion on the adiabatic heating and cooling, which are shown in Figures 4.3(d) – (f).

From these panels, a trend similar to that found in the winter polar temperature structures appears in the adiabatic term as well. First, moving from panel (d) to (f), the adiabatic heating in the winter polar thermosphere intensifies at 120 km as the lower atmospheric vertical dust mixing height is increased. In panel (d), the peak adiabatic heating at 120 km is 400 – 450 K/day whereas in panels (e) and (f) the heating in the lower thermosphere increases to 500 K/day and 600 K/day, respectively. This intensification in the adiabatic heating term parallels the resulting winter polar thermal structures found in Figures 4.3(a) – (c).

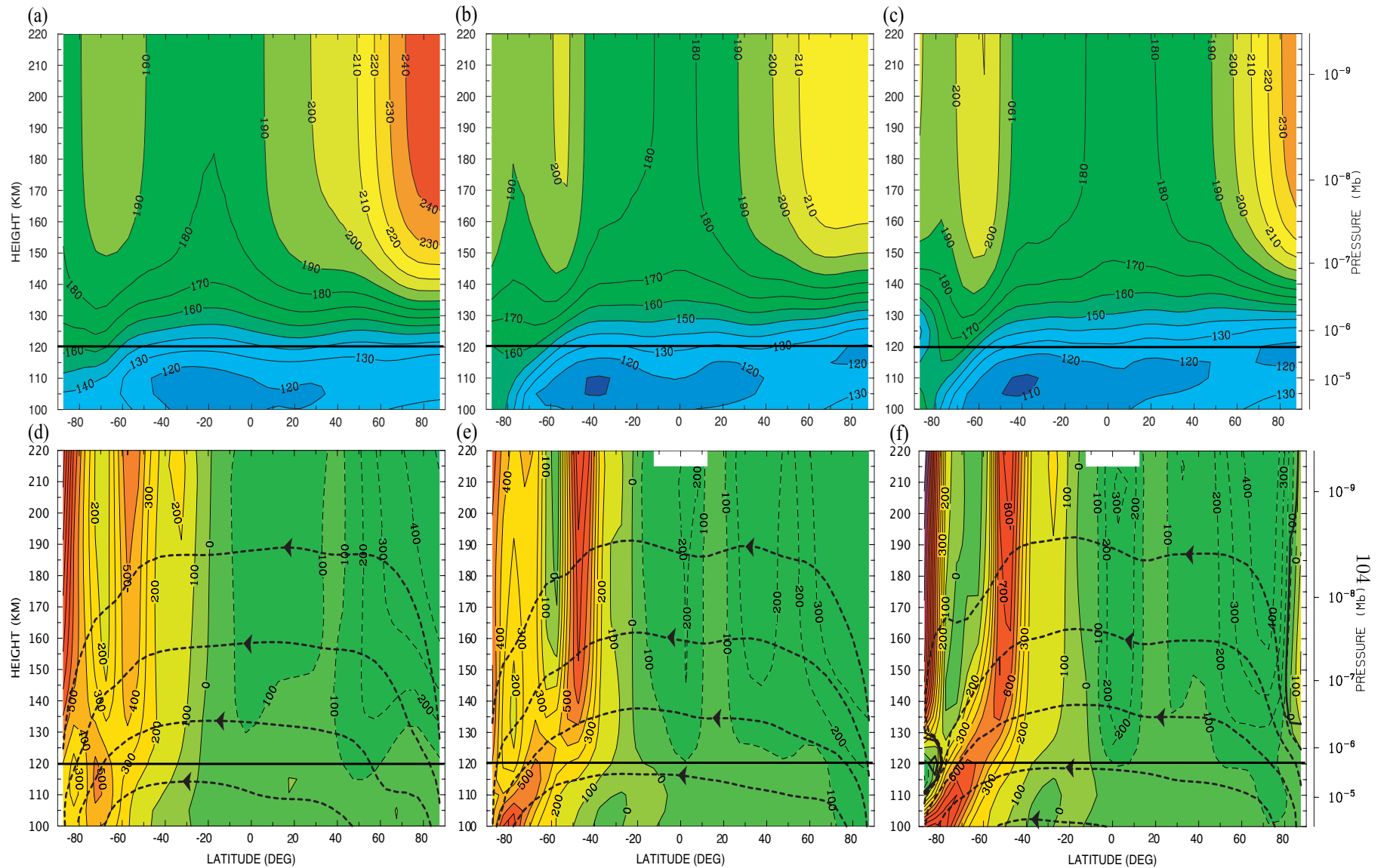


Figure 4.3: Zonal average neutral temperatures are shown in panels (a) – (c) while adiabatic heating (positive contours) and cooling (negative contours) are shown in panels (d) – (f), for the various lower atmospheric vertical dust mixing profiles as a function of both altitude (vertical axis) and latitude (horizontal axis). The season is held constant at $L_S = 090$ for all simulations, as is the total integrated lower atmospheric dust opacity, $\tau = 0.3$, and solar flux at $F_{10.7-cm} = 130$. The black horizontal line in all plots represents 120 km altitude level. Neutral temperatures (in K) are depicted for the various lower atmospheric dust mixing heights: (a) the lowest $\nu = 0.3$, (b) medium $\nu = 0.03$, and (c) highest $\nu = 0.005$. Similarly, the adiabatic heating and cooling contours (in K/day) and the overlaid meridional streamfunctions are depicted for the various lower atmospheric dust mixing heights: (d) the lowest $\nu = 0.3$, (e) medium $\nu = 0.03$, and (f) highest $\nu = 0.005$. The neutral streamfunctions are dimensionless and are indicative of the zonal averaged flow directions. The maximum meridional winds at 120 km are respectively (by convention, negative values are Southward while positive values are Northward): (d) -100 m/s, (e) -120 m/s, and (f) -140 m/s.

In the opposite hemisphere, the northern summer latitudes, adiabatic cooling rates do not systematically intensify as the lower atmospheric dust is mixed to higher altitudes, moving from Figures 4.3(d) to (f). At 120 km, the maximum adiabatic cooling for Figures 4.3(d), (e), and (f) is -100 K/day, -200 K/day, and -150 K/day. This trend in adiabatic cooling contrasts with the noticeably increasing adiabatic heating rates in the winter polar latitudes with an increasing vertical dust mixing height in the lower atmosphere. However, inspection of these same panels suggests an explanation for this difference.

First, Figures 4.3(d) – (f) demonstrate that the adiabatic cooling extends over most, if not all, of the northern hemisphere. Simultaneously, the peak polar warming features of these same plots remain confined to a small subset of winter polar latitudes. Therefore, any increase in the adiabatic cooling of the summer latitudes distributes itself across a larger spatial extent in the northern hemisphere. Thus, the impact of increasing the lower atmosphere vertical dust mixing height should not manifest itself in cooling the summer hemisphere as acutely as it does in warming the winter pole. This asymmetric adiabatic impact reveals itself in the temperature plots of Figures 4.3(a) – (c). However, despite the less intense impact of the adiabatic cooling upon the summer thermosphere, the results suggest that the summer lower thermosphere temperatures do systematically decrease, as the dust is mixed higher in the lower atmosphere.

Although intensifications in the adiabatic heating and cooling rates most likely correlate with winter polar warming and summer hemisphere cooling respectively, the meridional and vertical flows in the thermosphere emerge as the ultimate drivers for this system. In order to illustrate the zonal average circulation and its impact on the thermosphere, stream functions for each lower atmospheric dust mixing level have

been plotted in Figures 4.3(d) – (f). These stream functions, although dimensionless, indicate the direction of the zonally averaged meridional flows in the thermosphere. As can be seen in Figures 4.3(d) – (f), the stream function through all three mixing levels shows a consistently well developed summer-to-winter Hadley circulation that produces the adiabatic heating and cooling structures of the same panels. Further, from the caption of this same figure, note how the maximum meridional circulation velocities at 120 km respond to an increase with the vertical dust mixing height in the lower atmosphere, where they rise from -100 m/s in panel (d) up to -120 m/s in panel (e) and finally -140 m/s in panel (f). Thus, enhancements in the adiabatic heating and cooling rates are most likely the direct result of this interhemispheric Hadley circulation. Furthermore, the resulting heating and cooling rates, in turn, produce the observed temperature variations seen in the lower thermosphere.

Response of the MTGCM Neutral Densities

In a manner similar to Figure 4.3, Figure 4.4 depicts the response of the logarithm of the MTGCM neutral densities to variations in the lower atmosphere vertical dust mixing. Again focusing on 120 km as a proxy for the lower thermosphere, we find that, in general, winter polar densities are enhanced as the lower atmospheric dust vertical mixing is increased. In panel (a), moving from the equator to the winter pole, the densities begin at $5.0 \times 10^{10} \text{ cm}^{-3}$ and remain steady until 70° S , subsequently dropping to $2.0 \times 10^{10} \text{ cm}^{-3}$ in the winter pole. This corresponds to polar densities 40.0 % of the equatorial densities. Similarly, in panel (b) the equatorial densities are nearly $6.3 \times 10^{10} \text{ cm}^{-3}$ and remain steady even into the polar regions, dropping to $5.0 \times 10^{10} \text{ cm}^{-3}$, which results in polar densities 79.4 % of equatorial densities. Finally, in panel (c), the neutral densities at 120 km begin at $1.0 \times 10^{11} \text{ cm}^{-3}$ near the equator and again remain steady, until increasing to $1.3 \times 10^{11} \text{ cm}^{-3}$ at the southern

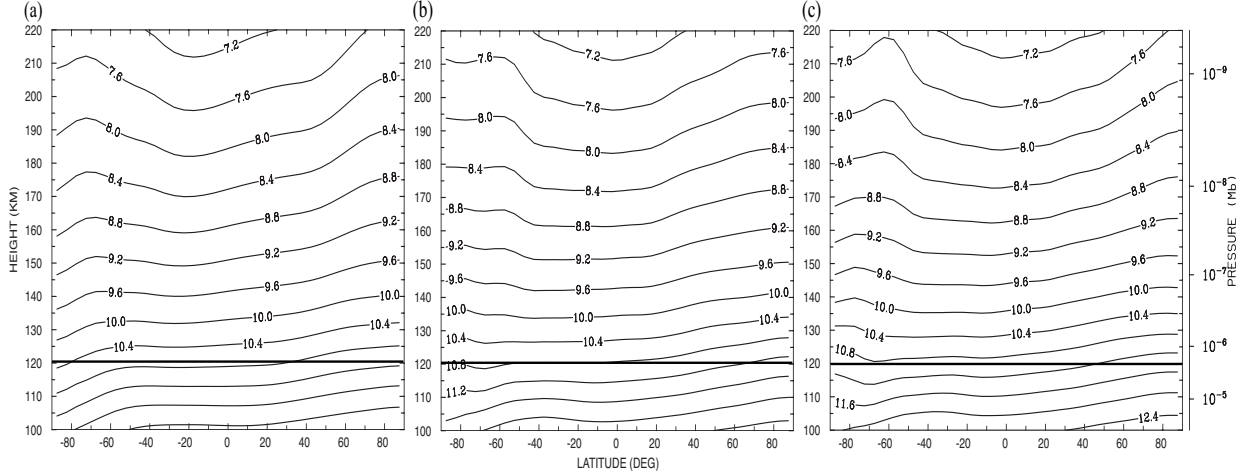


Figure 4.4:

Zonal average $\text{Log}_{10} \text{ cm}^{-3}$ neutral densities (in panels (a) – (c)) for the various lower atmospheric vertical dust mixing profiles as a function of both altitude (vertical axis) and latitude (horizontal axis). The season is held at $L_S = 090$ for all simulations, as is the total integrated dust opacity, $\tau = 0.3$, and solar flux $F_{10.7-cm} = 130$. The black horizontal line in all plots represents 120 km altitude level. Neutral densities (in $\text{Log}_{10} \text{ cm}^{-3}$) are depicted for the various lower atmospheric dust mixing heights: (a) the lowest $\nu = 0.3$, (b) medium $\nu = 0.03$, and (c) highest $\nu = 0.005$.

pole, implying polar densities 130 % of the equatorial densities. Ultimately, as lower atmospheric vertical dust mixing increases, a simultaneous increase in winter polar neutral densities occurs at 120 km.

In order to illustrate the significance of these density enhancements near the winter pole, one can compare these variations with those at the equator. In Figure 4.4, the densities at the equator rise from $5.0 \times 10^{10} \text{ cm}^{-3}$ in panel (a) to $1.0 \times 10^{11} \text{ cm}^{-3}$ in panel (c), corresponding to a low-latitude enhancement of 100% in neutral densities. By contrast, the winter polar neutral densities increase from $2.0 \times 10^{10} \text{ cm}^{-3}$ in panel (a) to $1.3 \times 10^{11} \text{ cm}^{-3}$ in panel (c), corresponding to a increase of 650 %. Thus, as the lower atmospheric dust levels increase from the lowest mixing level to the highest, the winter polar regions are experiencing a neutral density enhancement of roughly 550% more than that experienced at the equator. The equatorial density increases should quantify the impacts of the lower atmosphere's inflation in response to increased

lower atmospheric dust. However, this simple physics cannot explain the significantly higher density perturbations experienced in the thermosphere's winter polar regions. Instead, these simulations suggest that the interhemispherical Hadley circulation dominating the neutral temperatures in the winter polar regions also appears to modify the winter polar thermosphere's neutral density structures significantly.

4.5.2 Response of the MTGCM to Total Integrated Dust Opacities

Next, we illustrate the MTGCM's response to changing the total integrated dust opacity at 6.1-mb from $\tau = 0.3$ to 1.0 , while holding the season constant at $L_S = 090$, $\nu = 0.03$, and $F_{10.7-cm} = 130.0$ (Solar Moderate). The results of this change are illustrated in Figure 4.5(a) and (c). These panels are directly comparable to Figure 4.3(b) and (e). Again picking out the 120 km altitude and moving from the equator to the southern winter polar atmosphere, we find that the temperatures begin at 130 K and achieve a maximum of 170 K at the winter pole ($\Delta T = 40$ K). This change in temperature represents an increase over the corresponding winter polar warming seen in Figure 4.3(b) by 10 K (33 %). Furthermore, the peak temperature has migrated from 80^0 S in the previous figure to the winter pole in Figure 4.5.

Comparing Figure 4.5(c) and Figure 4.3(e), one finds that the adiabatic heating and cooling term is greatly modified. First, adiabatic heating is enhanced in the winter pole at 120 km in Figure 4.5(b) (700 K/day peak heating at 120 km) over the corresponding adiabatic heating found in Figure 4.3(e) (500 K/day peak heating at 120 km). This increase in adiabatic heating is not solely the result of an intensified meridional circulation, since Figures 4.5(b) and 4.3(e) both possess peak meridional winds of -110 to -120 m/s. Rather, Figure 4.5(b) exhibits a much larger vertical wind component of -1.5 m/s (downward) compared with the earlier simulation's vertical wind speed of -1.0 m/s (downward). Thus, we again find that an intensification of

the Hadley circulation, resulting in an increased adiabatic heating in the winter polar thermosphere, ultimately produces the enhanced polar warming features of Figure 4.5(a).

From this comparison, it is evident that an increased integrated dust opacity in the lower atmosphere, while keeping all other variables constant, results in an increase in the polar warming features simulated in the Martian lower atmosphere. Although, only one instance of this is shown for the $L_S = 090$ season, moderate solar fluxes, and at medium vertical dust mixing height ($\nu = 0.03$), this same trend still holds in general for the MTGCM's response to an increase of the total integrated lower atmospheric dust opacity. For brevity, we include only this single case to illustrate this more universal trend.

4.5.3 Response of the MTGCM to Seasonal Variations

Figures 4.5(b) and (d) illustrate the impact of changing seasons from $L_S = 090$ to $L_S = 270$. These panels should be directly compared with panels (a) and (c) of the same figure, as both possess: (1) a uniform dust distribution with total integrated dust opacity ($\tau = 1.0$) at the 6.1-mb pressure level, (2) a medium mixing height ($\nu = 0.03$) and (3) moderate solar fluxes. Thus, the primary difference between these two panels remains the seasonally adjusted orbital distance and subsolar latitude. At $L_S = 270$, Mars is at perihelion, which results in greater solar insolation for a given lower atmospheric dust distribution. Hence, *a priori*, one should anticipate a greater response in the lower thermosphere at $L_S = 270$ than at $L_S = 090$.

As can be seen by comparing panels (b) and (d) with (a) and (c) of Figure 4.5, the seasonally increased solar heating produces a concomitantly larger winter polar warming feature in the winter lower thermosphere (northern latitudes now). Again selecting the 120 km altitude level in panel (b) of Figure 4.5, temperatures begin

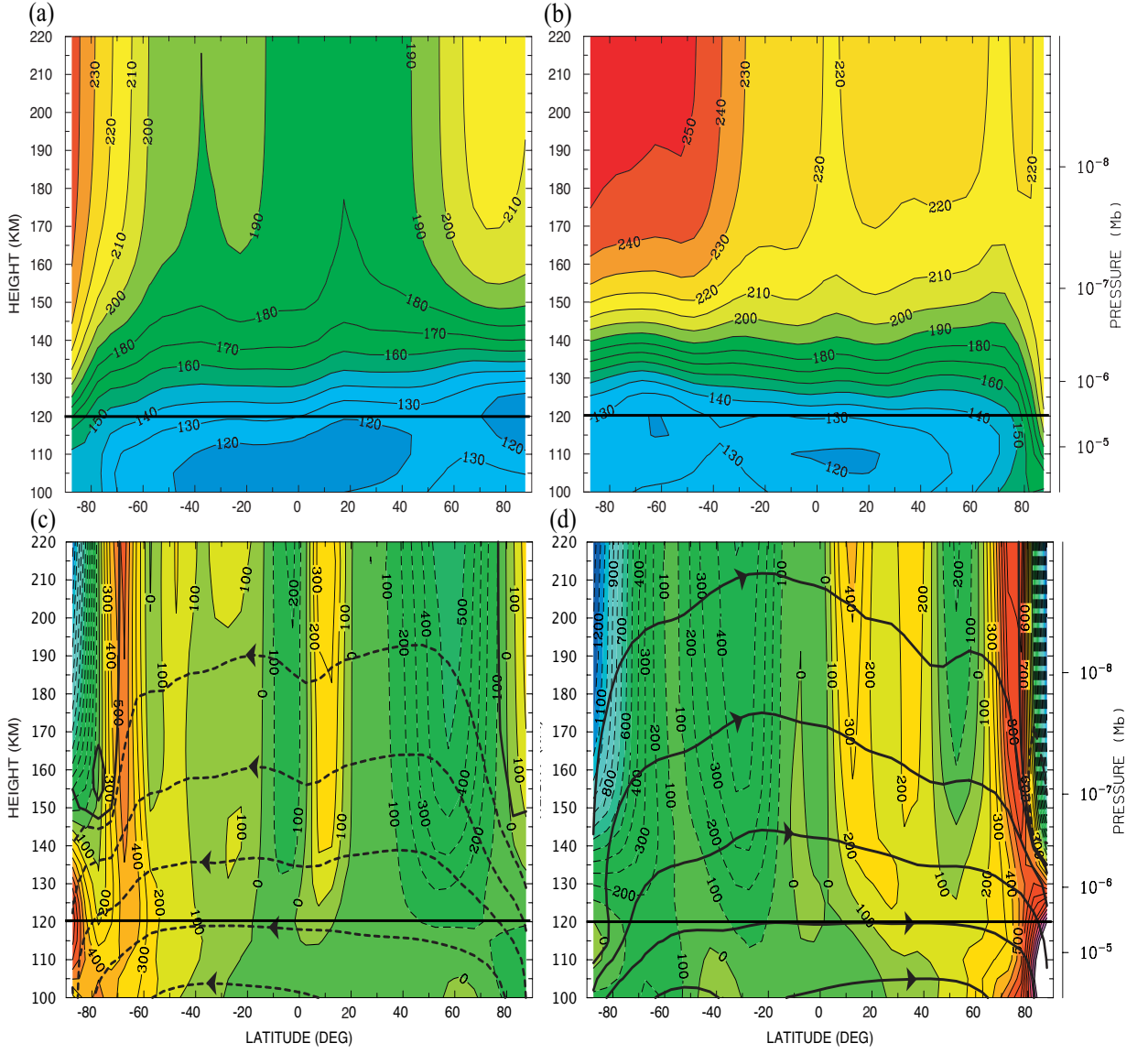


Figure 4.5: Zonal average neutral temperatures (in panels (a) – (b)), and adiabatic cooling (in panels (c) – (d)), for the two solstice seasons, $L_S = 090$ and $L_S = 270$ as a function of both altitude (vertical axis) and latitude (horizontal axis). The vertical dust mixing height parameter, $\nu = 0.03$ is held constant for these simulations, as is the total integrated dust opacity $\tau = 1.0$, and solar flux $F_{10.7-cm} = 130$. The black horizontal line in all plots represents 120 km altitude level. Neutral temperatures (in K) are depicted for the various lower atmospheric dust mixing heights: (a) $L_S = 090$ and (b) $L_S = 270$. Similarly, the adiabatic heating and cooling contours (in K/day) and the overlaid meridional streamfunctions are depicted for the two solstice seasons: (c) $L_S = 090$, and (d) $L_S = 270$. The neutral streamfunctions are dimensionless and are indicative of the zonal averaged flow directions. The maximum zonal averaged meridional winds at 120 km in the lower panels are respectively: (c) -110 m/s and (d) 140 m/s.

at 132 K near the equator. Moving towards the northern winter pole, temperatures slowly rise until 60° N when the temperatures rapidly begin to climb to a polar temperature of 205 K. This represents a polar warming feature of nearly 73 K, in contrast to the winter polar warming feature of 40 K at the opposite season (See Table 4.1). Similarly, adiabatic heating in the thermosphere is greatly enhanced in the winter polar regions in the perihelion season of Figure 4.5(d) (peak heating of 1300 K/day at 120 km) compared with that of the aphelion season of Figure 4.5(c) (peak heating of 700 K/day at 120 km).

The zonal average circulation again explains the intensification of the adiabatic heating term in the polar thermosphere. Figure 4.5(d) possesses meridional winds up to 140 m/s, while Figure 4.5(c) possesses meridional flows of up to -120 m/s. This difference in wind magnitudes again matches the discrepancy in adiabatic heating and cooling between these two simulations. Thus we again find that the interhemispheric Hadley circulation is consistent with the structures seen in the adiabatic heating in the winter polar temperatures. Further, this seasonal enhancement of the winter polar warming during $L_S = 270$ (perihelion) is a general trend found for all variations in lower atmospheric vertical dust mixing height, total lower atmosphere dust opacity, and solar flux. However, again, for the sake of brevity we provide only a single case to illustrate a more universal trend.

4.5.4 Brief Summary of the Vertical Dust Mixing Study

In this section, we establish, through numerical experiments using the coupled MGCM-MTGCM, a causal relationship between the lower atmospheric dust distribution and the thermosphere's response. Specifically, we have shown that the adiabatic heating and cooling rates, resulting from the zonal mean circulation, link the simulated thermospheric temperatures and densities to variations in the lower

atmospheric vertical dust mixing altitude. Furthermore, this circulation is modified by the extent of the vertical dust mixing, the total integrated lower atmospheric dust, and the season. Table 4.1 summarizes the polar warming features produced by the MTGCM as a function of the major variables of this numerical experiment.

Finally, although this study addresses many of the variables that could be encountered in the Martian atmosphere, some key variables are not directly addressed here: solar flux variations, and non-uniform lower atmospheric dust distributions. We acknowledge that solar flux variations are key to approximating the temperatures and densities observed by in-situ measurements. As noted in section 1, solar EUV variations do not significantly impact the energy balance at 120 km. Furthermore, in this study, we are not directly comparing MTGCM outputs with known datasets. Instead, we merely explore the underlying linkage between the upper and lower atmospheres, through this dust-driven interhemispheric Hadley circulation. In the following section, we build upon this dust sensitivity study by investigating the response of the lower thermosphere to non-uniform variations in the lower atmospheric dust distribution in latitude, longitude, and mixing height using TES dust opacity maps.

4.6 Interannual Variations in the Mars Lower Thermosphere

Next, we catalogue the year to year variability of winter polar warming in the MGCM-MTGCM lower thermosphere, using the three available years of TES IR dust opacity data. Beginning with TES mapping year 1 (Mars Year 24-25), we compare the differences between this simulation and the corresponding fields generated from mapping years 2 (Mars Year 25-26) and 3 (Mars Year 26-27). Although we limit ourselves to analyzing only the two solstice seasons, $L_S = 90$ and $L_S = 270$, the simu-

lations should provide lower and upper bounds, respectively, for expected variations in the Martian upper atmosphere. In Figures 4.6 – 4.8, zonal mean quantities are displayed, which allow the discussion to focus on the integrated response of the lower thermosphere, rather than on small but potentially significant topographically-driven perturbations. Furthermore, as in the sensitivity study, we focus our discussion on the variations found at an altitude of 120 km for the same primary reasons: (1) it remains an altitude critical to aerobraking missions in the lower thermosphere, and (2) it represents a relatively good proxy for describing the dynamics of the lower thermosphere (100 – 130 km). Finally, we again restrict ourselves to a solar moderate flux of $F_{10.7-cm} = 130$.

4.6.1 TES Mapping Years 1-3: Neutral Temperatures

Figure 4.6 illustrates zonal mean plots for the MTGCM-MGCM neutral temperature during all three TES Mapping years, during both solstice seasons. On the same figures, the 120 km altitude level has been delimited with a black horizontal line. The zonal mean lower atmospheric dust content for each of the TES Mapping years can be found in Figure 4.1. In the discussions that follow, we emphasize the winter polar warming features, as they remain one of the most prominent structures in the lower thermosphere.

Neutral Temperatures: $L_S = 90$

The MTGCM thermosphere temperatures for $L_S = 090$ at each of the three TES Years are shown in Figures 4.6(a) – (c). Starting with TES Year 1, Figure 4.6(a), we follow the 120 km marker from the equatorial latitudes to the southern winter polar thermosphere. At the equator, temperatures start at 140 K, dropping to a minimum of 137 K near 20° S latitude. Temperatures then warm into the polar thermosphere

up to maximum of 151 K near 63^0 S, subsequently dropping to near 147 K near the pole. This provides a min-to-max deviation of $\Delta T = 14$ K for TES Mapping Year 1.

Figure 4.6(b) illustrates MTGCM thermosphere temperatures at the same season during TES Mapping Year 2. In this figure, at 120 km temperatures begin at 141 K at the equator. Moving toward the winter polar thermosphere, a local temperature minimum of 138 K occurs at 28^0 S latitude. Temperatures then increase into the polar thermosphere to a maximum temperature of 157 K. This produces a min-to-max polar warming of $\Delta T = 19$ K.

In a similar fashion, panel 4.6(c) illustrates MTGCM thermosphere temperatures at the $L_S = 90$ season during TES Mapping Year 3. In this figure, at 120 km temperatures begin at 142 K at the equator. Moving toward the winter polar thermosphere, a local temperature minimum of 138 K occurs at 19^0 S latitude. Temperatures then increase into the polar thermosphere, reaching a maximum temperature of 162 K. This produces a min-to-max polar warming of $\Delta T = 24$ K.

Neutral Temperatures: $L_S = 270$

The MTGCM thermosphere temperatures for the opposite season of $L_S = 270$ at each of the three TES Years are shown in Figures 4.6(d) – (f). Starting with TES Year 1, panel 4.6(d), we again follow the 120 km marker from the equatorial latitudes to the northern winter polar thermosphere. At the equator, temperatures start at 131 K, which is also the local temperature minimum at 120 km. Temperatures then warm into the northern polar thermosphere up to maximum of 163 K near 83^0 N, subsequently dropping to near 160 K near the pole. This provides a min-to-max deviation of $\Delta T = 31$ K for TES Mapping Year 1.

Panel 4.6(e) illustrates MTGCM thermosphere temperatures at the same season during TES Mapping Year 2. In this figure, at 120 km temperatures begin at 130 K at

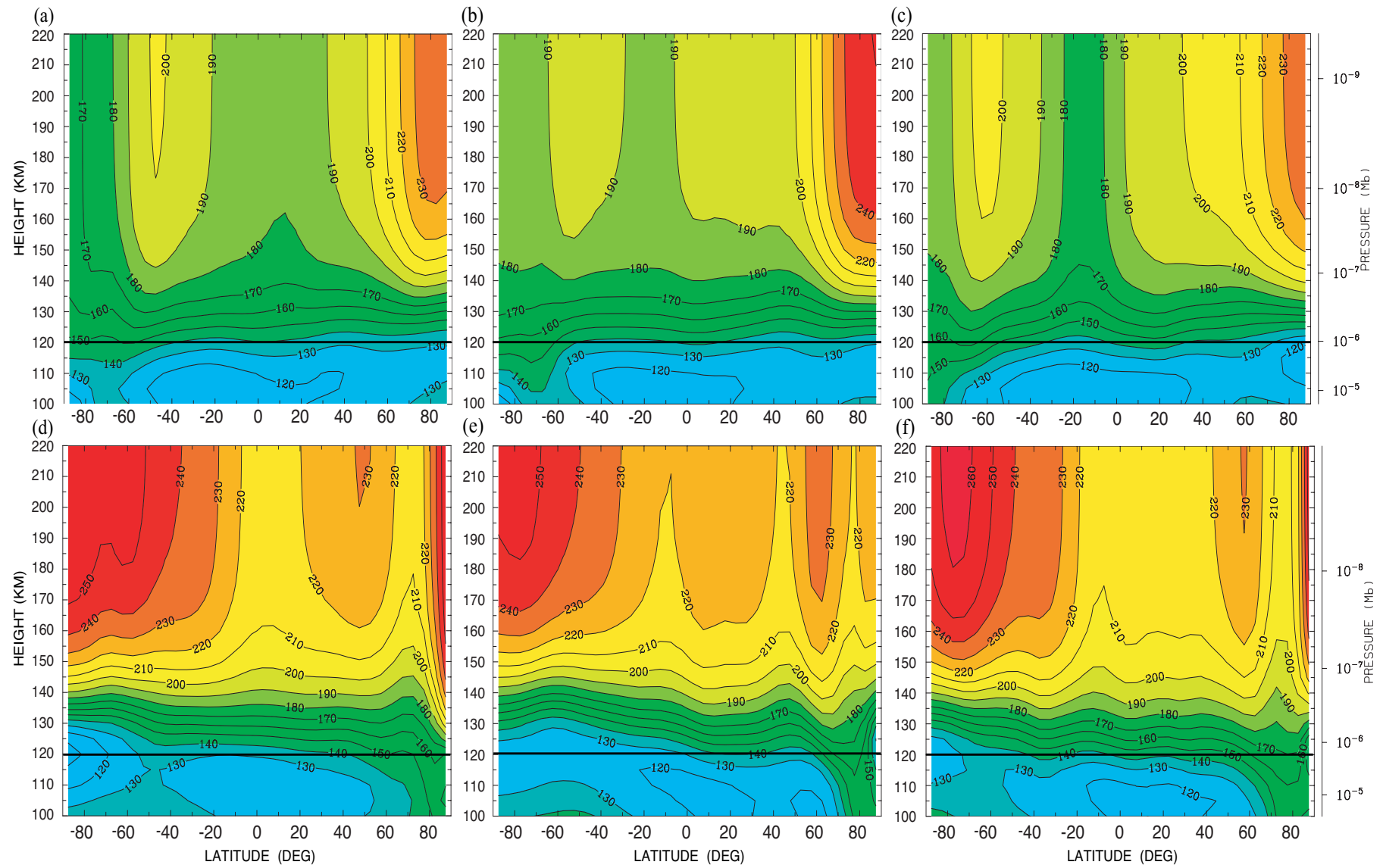


Figure 4.6: Zonal average neutral temperatures, for both solstice seasons at each of the three TES Mapping Years as a function of both altitude (vertical axis) and latitude (horizontal axis). The solar flux is held constant at $F_{10.7-cm} = 130$ for all simulations. The black horizontal line in all plots represents 120 km altitude level. Neutral temperatures (in K) for the northern summer solstice, $L_S = 090$ are depicted for the various lower atmospheric dust (see Figure 4.1) TES Maps: (a) TES Year 1, (b) TES Year 2, and (c) TES Year 3. Similarly, neutral temperatures (in K) for the opposite season of southern summer solstice, $L_S = 270$, are depicted for the various lower atmospheric dust TES Maps: (d) TES Year 1, (e) TES Year 2, and (f) TES Year 3.

the equator, which again represents the local temperature minimum. Temperatures then increase into the northern polar thermosphere to a maximum temperature of 165 K. This produces a min-to-max polar warming of $\Delta T = 35$ K.

In a similar fashion, panel 4.6(f) illustrates MTGCM thermosphere temperatures at the $L_S = 270$ season during TES Mapping Year 3. In this figure, at 120 km temperatures begin at 142 K at the equator. Moving toward the northern winter polar thermosphere, the temperatures reach a local minimum of 140 K at 21^0 N latitude. Temperatures then increase into the polar thermosphere to a maximum temperature of 170 K at 78^0 N latitude. This produces a min-to-max polar warming of $\Delta T = 30$ K.

Temperatures and Dust Levels: A Connection?

Next, having looked at the polar warming features for all three TES Mapping Years at both solstice periods, it proves useful to look at the lower atmospheric dust levels at these same time periods. First, during the $L_S = 090$ seasons of each year, the dust levels in Figure 4.1 appear relatively low. However, $L_S = 090$ during TES Year 1 appears very clear of dust, whereas there exists an enhancement of integrated dust opacity in the southern latitudes during TES Year 2 over the previous year's levels. Finally, although continuous dust opacity data is being lost at this time period, during $L_S = 090$ of TES Year 3, there exist signs of elevated dust opacity, indicated by the green contours, reaching to mid-latitudes. Therefore, in order of increasing lower atmospheric dust content at aphelion, the TES mapping years are sorted as follows: (1) TES Year 1 ($\Delta T = 14$ K), (2) TES Year 2 ($\Delta T = 19$ K), and (3) TES Year 3 ($\Delta T = 24$ K). From this sorting by lower atmospheric dust content, a strong correlation emerges between the lower atmosphere dust opacity and the strength of the winter polar warming feature found in the MTGCM thermal structures at $L_S =$

Table 4.2: Polar Warming Features in Kelvin for Interannual Study

Season	TES Year 1	TES Year 2	TES Year 3
$L_S = 090$	$\Delta T = 14 \text{ K}$	$\Delta T = 19 \text{ K}$	$\Delta T = 24 \text{ K}$
$L_S = 270$	$\Delta T = 31 \text{ K}$	$\Delta T = 35 \text{ K}$	$\Delta T = 30 \text{ K}$

090.

During the opposite season, $L_S = 270$, a similar trend may be established. The summer solstice season of TES Year 1 is found to have a polar warming feature of $\Delta T = 31 \text{ K}$, which remains very close to that of TES Year 3's polar warming of $\Delta T = 30 \text{ K}$. A quick glance at Figure 4.1 implies an explanation. The dust opacities in the lower atmosphere appear to be nominally the same for the southern summer solstice season, $L_S = 270$, of both mapping years. These results again suggest a significant correlation between the lower atmospheric dust levels and the character of the winter polar warming features in the MTGCM lower thermosphere. By contrast, Figure 4.1 shows the lower atmosphere recovering from a global dust storm during TES Year 2 at $L_S = 270$. In this instance, dust opacity levels remain elevated relative to those of TES Years 1 or 3 at perihelion. This enhanced period of lower atmospheric dust content coincides with the strongest winter polar warming feature found at this season in the MTGCM temperature structures, $\Delta T = 35 \text{ K}$. Taken together, the correlation between neutral temperatures at both solstice periods and lower atmospheric dust seems compelling. This connection between interannual variability in winter polar warming and lower atmospheric dust content can be further supported by examining the remaining key diagnostic outputs from the MTGCM for the same time periods of the same mapping years.

4.6.2 TES Mapping Years 1-3: Adiabatic Heating and Cooling Rates

Figure 4.7 contains the adiabatic heating and cooling rates at both the $L_S = 090$ season (panels (a) – (c)) and the $L_S = 270$ season (panels (d) – (f)). In this figure, the first noticeable trend is that the general circulation, as depicted by the stream lines, predominantly flows from the summer hemisphere to the winter hemisphere. Additionally, due to this interhemispheric circulation, the adiabatic term warms the winter polar thermosphere, while concomitantly cooling the summer polar thermosphere. These general observations hold for all TES Mapping years and at both solstice seasons. However, all generalities fail at some level, and we find some structures that do not correspond with this general trend. For instance, panels (b), (c), and (f) all possess some return flow downward into the summer polar thermosphere, which is accompanied by a simultaneous warming of the summer polar thermosphere. These deviations, however, only represent small modifications to a summer-to-winter interhemispheric Hadley circulation that dominates the thermosphere, as shown in the panels of Figure 4.7.

Next, as was done in the temperature structures of Figure 4.6, it is instructive to compare the adiabatic driving terms between the different TES Years in order to expose an underlying correlation with the deviations found earlier in the winter polar warming temperature features contained in Table 4.2. Focusing first on panels 4.7(a),(b), and (c), we find the adiabatic heating and cooling rates for the $L_S = 090$ season for TES Years 1, 2, and 3 respectively. In panel (a), the adiabatic heating term in the winter polar thermosphere is positive and broad, spanning 20^0 S – 90^0 S with a peak heating at 120 km of 400 K/day near the winter polar region.

Similarly, Figure 4.7(b) has a broad warming feature over the same latitudes. However, the regions nearest the winter pole are noticeably enhanced, possessing a

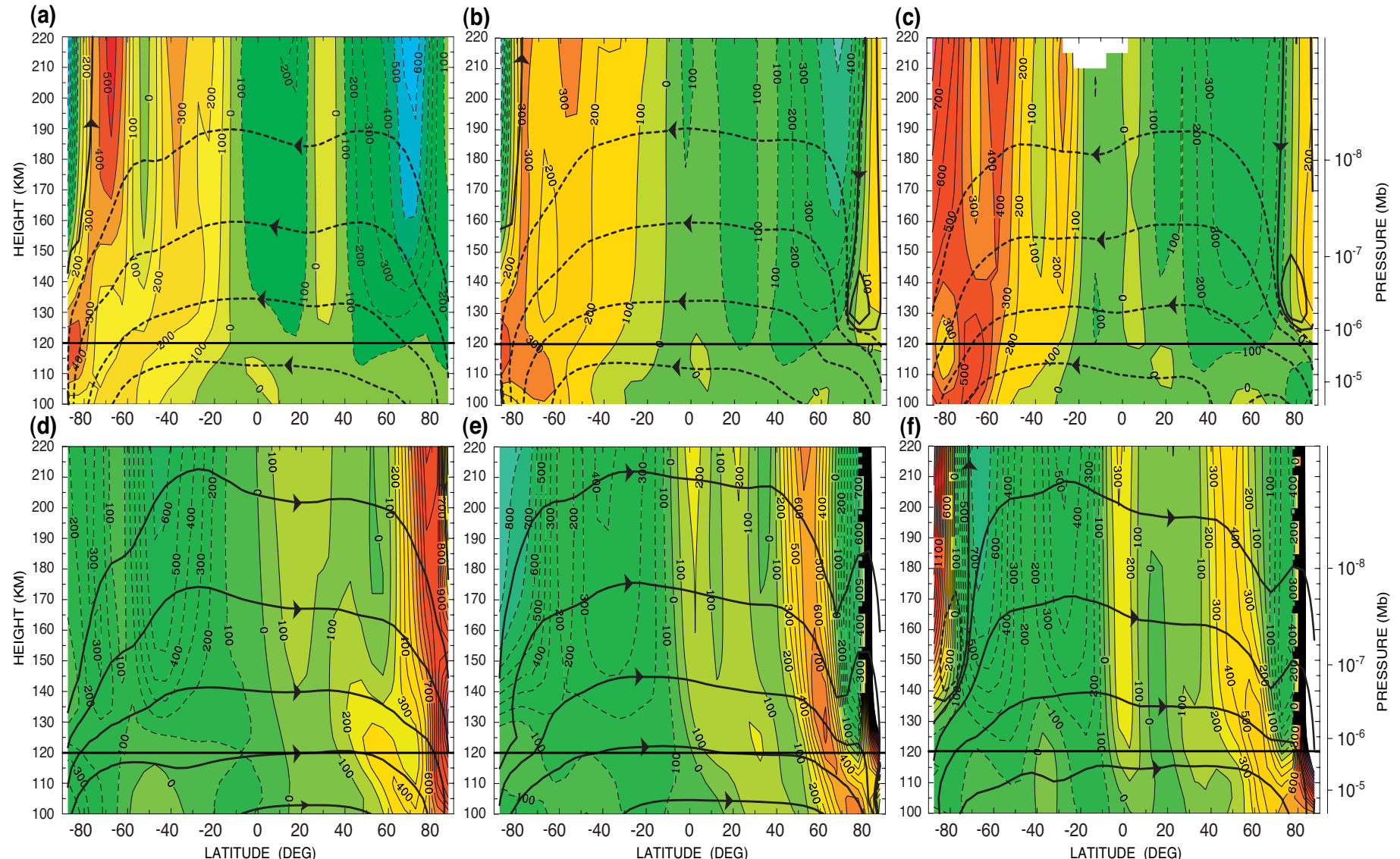


Figure 4.7: Zonal average adiabatic heating and cooling in (colored contours) and zonal mean stream functions (black lines) for both solstice seasons at each of the three TES Mapping Years as a function of both altitude (vertical axis) and latitude (horizontal axis). The solar flux is held constant at $F_{10.7-cm} = 130$ for all simulations. The black horizontal line in all plots represents 120 km altitude level. Adiabatic heating and cooling rates (in K/day) and meridional streamfunctions (black contours with directional arrows) for the northern summer solstice, $L_S = 90$ are depicted for the various lower atmospheric dust (see Figure 4.1) TES Maps: (a) TES Year 1 (maximum meridional wind at 120 km of -100 m/s), (b) TES Year 2 (maximum meridional wind at 120 km of -90 m/s), and (c) TES Year 3 (maximum meridional wind at 120 km of -120 m/s). Similarly, adiabatic heating/cooling (in K/day) and zonal mean streamfunctions for the opposite season of southern summer solstice, $L_S = 270$, are depicted for the various lower atmospheric dust TES Maps: (d) TES Year 1 (maximum meridional wind at 120 km of 130 m/s), (e) TES Year 2 (maximum meridional wind at 120 km of 150 m/s), and (f) TES Year 3 (maximum meridional wind at 120 km of 120 m/s). Note that the neutral streamfunctions are dimensionless and are indicative of the zonal averaged flow directions.

broad contour of 300 K/day warming and peaking at 400 K/day near the winter polar region. As shown in Table 4.2, this region of enhanced warming correlates with the increased polar warming features seen at TES Year 2 relative to TES Year 1 during $L_S = 090$.

Finally, panel (c) of this same figure, contains the zonal mean adiabatic heating and cooling rates for TES Year 3. At 120 km near the winter polar latitudes (South), enhancement of the adiabatic heating term remains evident, possessing a peak warming of up to 500 K/day near 65^0 S latitude. Additionally, the entire region south of 60^0 S latitude contains enhanced warming relative to the other two TES Years at aphelion. Thus, we find that this aphelion season during TES Year 3 possesses the greatest winter polar warming feature in Table 4.2. Thus, it remains evident that the polar warming features simulated for aphelion conditions (Southern winter solstice) for the three available TES mapping years correlate well with the adiabatic heating and cooling rates found in the MGCM-MTGCM.

In an analogous manner for the opposite season of $L_S = 270$, we can compare the adiabatic source term found in 4.7 (d) – (f). In panel (d), the adiabatic warming feature spans latitudes from 50^0 N – 90^0 N with peak adiabatic heating at 120 km of nearly 1200 K/day near the pole. For the next TES Mapping year shown in panel (e), there exist two vertical columns of adiabatic heating. The first column occurs at lower latitudes and possesses a maximum heating of 700 K/day. The second vertical column of adiabatic heating reaches values of 1400 K/day at 120 km. Gradients in the adiabatic heating in the polar region of this figure are strong and positive at the Northern winter pole. This increased heating between panels (d) and (e) correlates with the increased polar warming features seen in the temperatures of Table 4.2. Lastly, panel (f) contains the adiabatic heating and cooling rates for the

Table 4.3: Winter Polar Neutral Densities for Interannual Study

Season	TES Year 1	TES Year 2	TES Year 3
$L_S = 090$	$\rho = 1.6 \times 10^{10} \text{ cm}^{-3}$	$\rho = 1.8 \times 10^{10} \text{ cm}^{-3}$	$\rho = 2.8 \times 10^{10} \text{ cm}^{-3}$
$L_S = 270$	$\rho = 6.3 \times 10^{10} \text{ cm}^{-3}$	$\rho = 1.3 \times 10^{11} \text{ cm}^{-3}$	$\rho = 4.0 \times 10^{10} \text{ cm}^{-3}$

perihelion season for TES Year 3. In this figure, the first, mid-latitude adiabatic warming feature peaks at 500 K/day, while it possesses a global maximum of nearly 1500 K/day near the winter pole. The polar warming structures for this year and season are the weakest for $L_S = 270$. Thus, as was illustrated for $L_S = 090$, a clear correlation between adiabatic heating and the resulting winter polar warming features exists.

4.6.3 TES Years 1-3 Neutral Densities

Figure 4.8 presents the coupled model's neutral densities for the three TES Years in a format different from that of Figure 4.4. In Figure 4.8, the neutral densities at 120 km are illustrated (in $\text{Log}_{10} \text{ cm}^{-3}$ for each TES Mapping Year and each solstice season as a function of latitude. Not surprisingly, the densities follow the general trends established with the corresponding neutral temperatures.

Beginning with Figure 4.8(a), TES Year 1 (the solid black line) densities begin at the equator with a value of $5.0 \times 10^{10} \text{ cm}^{-3}$. These neutral densities rise until reaching a maximum of nearly $6.0 \times 10^{10} \text{ cm}^{-3}$ near 55^0 S latitude (a rise of approximately 20.0%). The densities then decrease into the winter polar latitudes to almost $1.6 \times 10^{10} \text{ cm}^{-3}$. Similarly, focusing on the dashed line in panel (a), neutral densities for $L_S = 090$ season of TES Year 2 also begin with an equatorial value of $5.0 \times 10^{10} \text{ cm}^{-3}$ and reach a local maximum density of nearly $6.6 \times 10^{10} \text{ cm}^{-3}$ at the latitude of 50^0 S . This corresponds to percentage density rise of nearly 32.0% from equatorial values. Similar to the TES Year 1 densities, TES Year 2 densities also drop from

this maximum value to nearly $1.8 \times 10^{10} \text{ cm}^{-3}$ at the northern winter pole.

The final TES Mapping Year for aphelion in panel (a) possesses an equatorial density of $4.0 \times 10^{10} \text{ cm}^{-3}$, which rises to a maximum of nearly $4.5 \times 10^{10} \text{ cm}^{-3}$ at 55^0 S , giving a min-to-max percentage density variation of 12.5%. However, for TES Year 3, the densities do not drop as rapidly into the polar regions, reaching a value of $2.8 \times 10^{10} \text{ cm}^{-3}$ in the southern winter pole. This last case represents an enhancement of winter polar densities over that of TES Years 1 and 2. This same season during TES Year 3 also exhibited the strongest polar warming signature in temperatures, as shown in Table 4.2.

At the opposite perihelion season ($L_S = 270$), Figure 4.8(b), similar trends in the neutral densities are apparent. For TES Year 1 (the solid black line), neutral densities begin at the equator $1.0 \times 10^{11} \text{ cm}^{-3}$ and reach a maximum value of $1.2 \times 10^{11} \text{ cm}^{-3}$ at 55^0 N latitude, corresponding with a density variation of 20.0%. TES Year 2 likewise possesses a minimum density of $1.0 \times 10^{11} \text{ cm}^{-3}$, rising to nearly $1.4 \times 10^{11} \text{ cm}^{-3}$ at 75^0 N latitude. This corresponds to a density variation of nearly 40.0%. Interestingly enough, the densities for this year and season rise into the winter polar regions (reaching $1.3 \times 10^{11} \text{ cm}^{-3}$ at the northern pole), which also possesses the greatest winter polar warming feature in Table 4.2. Finally, the dotted line in panel (b) (TES Year 3) shows densities increasing from an equatorial density of $5.0 \times 10^{10} \text{ cm}^{-3}$ up to nearly $6.7 \times 10^{10} \text{ cm}^{-3}$ near 75^0 N , corresponding to a density variation of 34.0%. This last simulation possesses winter polar neutral densities of $4.0 \times 10^{10} \text{ cm}^{-3}$.

A final examination of Figure 4.8 and Table 4.3 reveals a systematic correlation between variations in winter polar densities and variations in lower atmospheric dust levels. Table 4.2 reveals that the greatest temperature perturbations occur during

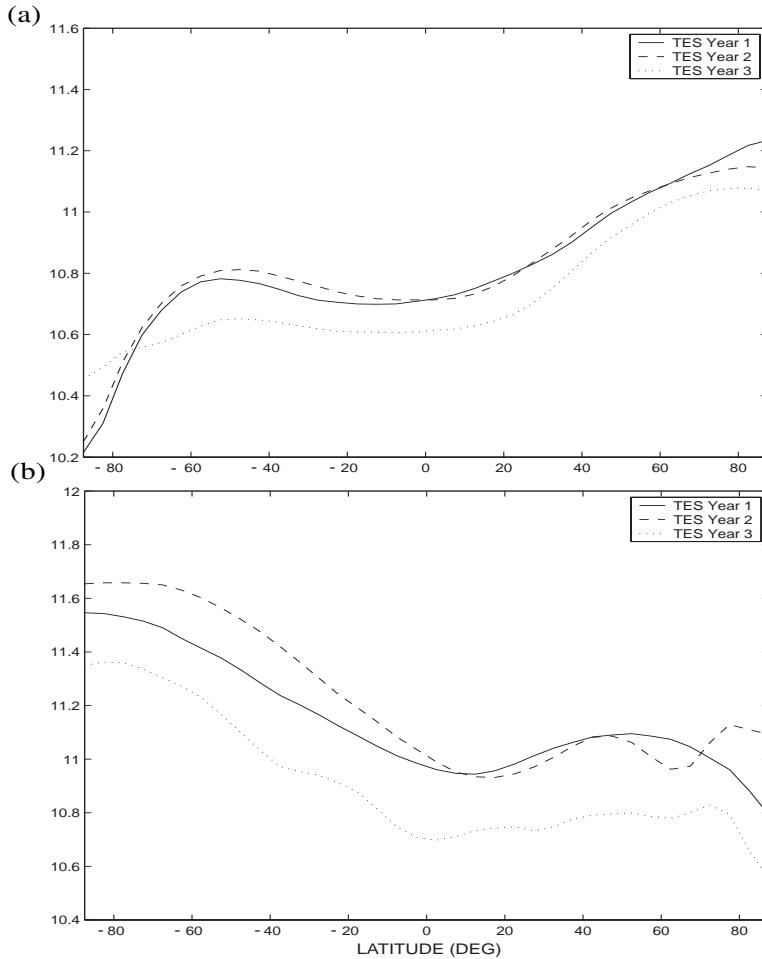


Figure 4.8: Line plots of the zonal averaged $\text{Log}_{10} \text{ cm}^{-3}$ neutral densities at 120 km, for both solstice seasons for each of the three TES Mapping Years as a function of latitude (horizontal axis). The solar flux is held constant at $F_{10.7-cm} = 130$ for all simulations. Panel (a) represents the aphelion season ($L_S = 90$) for each of the TES Mapping years, each represented by a different line style (see legend). Panel (b) is structured identically for the opposite season of perihelion ($L_S = 270$). All neutral densities are depicted in units of $\text{Log}_{10} \text{ cm}^{-3}$. The density trends shown should be compared with lower atmospheric dust variations shown in Figure 4.1.

the $L_S = 090$ season of TES Year 3 and the $L_S = 270$ season of TES Year 2. Similarly, the winter polar densities of Table 4.3 are maximized during these same time periods. Thus, in conjunction with an increased winter polar warming, winter polar densities at 120 km are enhanced as lower atmospheric dust content increases. This indicates that the entire winter polar thermosphere responds to an increase in lower atmospheric dust content with enhanced temperatures and densities. Furthermore, as is established in section 4.1.3, these enhancements in winter polar neutral densities cannot be easily explained by the general inflation and contraction of the lower atmosphere alone. Instead, these enhanced winter polar densities appear strongly correlated with the variations in the strength of the interhemispherical Hadley circulation responsible for winter polar warming.

4.7 Response of the MTGCM to Variations in the Lower Boundary Forcing from the MGCM

4.7.1 Describing the Lower Boundary Forcing Study

In this section, we describe the impact of upward propagating waves and tides from the lower atmosphere on the MTGCM simulated circulation. In order to accomplish this, we employ three different degrees of coupling between the lower and upper atmosphere models. First, we utilize a fully coupled TES Year 3, $L_S = 270$ lower boundary, which passes all key parameters (T, U, V, W , and Φ) at each 2-minute time step of the coupled framework. This coupling scheme, which is identical to that employed in the previous two numerical experiments, allows for a real time upward propagation of migrating and non-migrating tides and planetary waves from the MGCM into the thermosphere of the MTGCM. The resulting temperatures and adiabatic heating/cooling rates from this coupling are illustrated in Figures 4.9(a) and (d) respectively and can be directly compared with Figures 4.6(f) and 4.7(f).

For the second part of this study, we employ a diurnally averaged lower boundary condition from the same mapping year and season (TES Year 3 at $L_S = 270$). By diurnally averaging the lower boundary, we in effect remove the diurnal cycle in the lower atmosphere. Tidal analysis of this diurnally averaged lower boundary indicates that the upward propagating migrating and non-migrating tides are removed from this simulation. However, it is unclear to what degree stationary waves (e.g. Rossby-type wave modes) and low frequency (e.g. baroclinic waves) are impacted by this diurnal averaging process. In all, the primary tidal amplitudes in the thermosphere are drastically reduced by 75 – 80% in the winter polar thermosphere. This, in turn, has a significant effect on the resulting MTGCM simulations, as illustrated in Figures 4.9(b) and (e).

Finally, for the third part of this investigation, we specify all lower boundary fields at the lowest pressure level in the MTGCM (the $1.32\text{-}\mu\text{bar}$ pressure level) with global average values taken from the TES Year 3 lower boundary at $L_S = 270$. We fixed these lower boundary parameters at the lowest pressure level to the following: $T = 150\text{ K}$, $U = 0.0\text{ m/s}$, $V = 0.0\text{ m/s}$, $W = 0.0\text{ m/s}$, and $\Phi = 70\text{ km}$. Tidal analysis of this fixed lower boundary indicates that all upward propagating tides and waves from the lower atmosphere are eliminated. This decoupling from the MGCM at the lower boundary has a pronounced impact on the resulting MTGCM simulations, as illustrated in Figures 4.9(c) and (f).

4.7.2 Results from the Lower Boundary Forcing Study

The six panels of Figure 4.9 summarize the simulated response of the Martian thermosphere to the three variations in the amount of upward propagating tides described above. In this section, we point out the most salient features of this wave-coupling analysis, illustrating the influence that the lower atmosphere has upon the

dynamics of the upper atmosphere.

Figure 4.9(a) contains the temperature structure for the fully coupled TES Year 3 simulation at perihelion. Panel (d) of this same figure contains the adiabatic heating and cooling rates (contours) with the overlying meridional stream function for this same year and season. Because this simulation was discussed in detail in the section on interannual variations, we now point out only the most salient features of the dynamics here. First, as indicated by the meridional streamlines of Figure 4.9(d), the circulation has access to the winter polar latitudes (poleward of 70^0 N). Similarly, the greatest adiabatic heating occurs at the winter pole, with an amplitude in excess of 1600 K/day at 87.5^0 N. This peak of adiabatic heating corresponds to the steep thermal gradient at the northern winter pole seen in Figure 4.9(a).

The thermosphere's responses to a diurnally averaged lower boundary condition are depicted in Figures 4.9(b) and (e). In this simulation, the upward propagating tides are greatly minimized in comparison with those present in the simulations of Figures 4.9(a) and (d). This reduction in the tidal amplitudes results in a circulation that does not penetrate as deeply into the winter polar latitudes, as shown in Figure 4.9(e). Instead, the meridional flow is redirected to lower latitudes, resulting in the adiabatic warming found between 60^0 N and 80^0 N of this same panel. This meridional flow is significantly stronger (maximum speed of 170 m/s) than that of Figure 4.9(d) (maximum speed of 130 m/s). However, the adiabatic heating in Figure 4.9(e) reaches a peak of only 1200 K/day versus the 1600 K/day of Figure 4.9(d). Lower in the thermosphere (below 110 km), adiabatic warming does extend to the winter pole.

The adiabatic heating rates for the diurnally averaged lower boundary mirror the resulting temperature structures found in Figure 4.9(b). In this panel, the peak

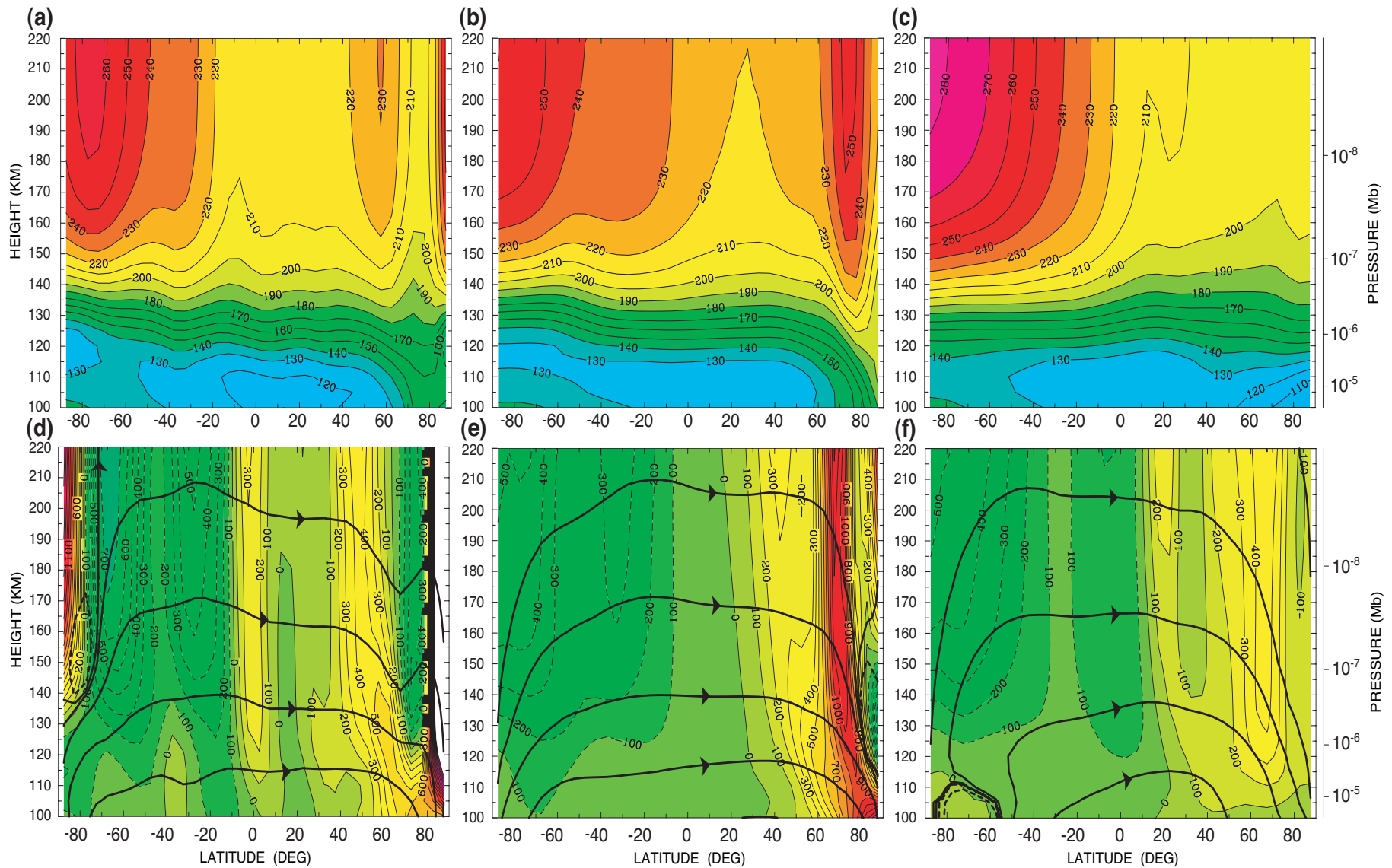


Figure 4.9: Zonal average neutral temperatures are shown in panels (a) – (c) while adiabatic heating (positive contours) and cooling (negative contours) are shown in panels (d) – (f), for the three lower boundary conditions as a function of both altitude (vertical axis) and latitude (horizontal axis). The season is held at $L_S = 270$ for all simulations and solar flux is held at $F_{10.7-cm} = 130$. The black horizontal line in all plots represents 120 km altitude level. Neutral temperatures (in K) are depicted for the various lower boundaries employed: (a) Fully coupled TES Year 3, (b) Diurnally averaged lower boundary, and (c) Global averaged fixed lower boundary. Similarly, the adiabatic heating and cooling contours (in K/day) and the overlaid meridional streamfunctions are depicted for the various lower atmospheric boundary conditions: (d) Fully coupled TES Year 3, (e) Diurnally averaged lower boundary, and (f) Global averaged fixed lower boundary. The neutral streamfunctions are dimensionless and are indicative of the zonal averaged flow directions. The maximum meridional winds at 120 km are respectively: (d) 130 m/s, (e) 170 m/s, and (f) 85 m/s.

temperature high in the thermosphere is displaced equatorward from the analogous peak in Figure 4.9(a). Additionally, the lowest altitudes of Figure 4.9(e) show an increased winter polar warming feature due to the displaced adiabatic heating at these altitudes. Thus it appears that, by minimizing the upward propagating tides from the lower atmosphere, the meridional circulation in the thermosphere does not extend to latitudes north of 70^0 N, except at the lowest altitudes.

Finally, Figures 4.9(c) and (f) depict the thermosphere's simulated response to the global average fixed lower boundary. At this lower boundary, the temperature and geopotential height are specified at the bottom of the model to 150 K and 70 km respectively, while the winds were specified to be zero. Essentially, this represents a "billiard ball" lower atmosphere that remains static throughout the simulation. This figure exhibits significantly weaker meridional winds with maximum velocities of 85 m/s and peak adiabatic heating rates of 400 K/day seen in Figure 4.9(f). Not surprisingly, this weakened circulation does not extend to latitudes poleward of 70^0 N, instead depositing most of its energy between 50^0 N and 70^0 N. This weak circulation results in the temperature structures of Figure 4.9(c), which shows virtually no winter polar warming signatures in the thermosphere.

4.7.3 Brief Summary of the Lower Boundary Comparison

Through a systematic comparison of Figures 4.9(a) – (c) with Figures 4.9(d) – (f), some key results emerge. First, by removing or severely damping out upward propagating tides, as was done in the diurnally averaged and billiard ball cases, the meridional circulation does not extend to latitudes poleward of 70^0 N. This result remains consistent with analogous work by *Wilson* [1997], which finds that upward propagating tides allow lower atmospheric meridional circulation to extend to latitudes poleward of 70^0 , contributing to winter polar warming in the lower

atmosphere. Moreover, this result in the thermosphere appears even more impressive given that, at perihelion ($L_S = 270$), the calculated meridional circulation exhibits a seasonal maximum, meaning that it should have the greatest opportunity of accessing the winter polar latitudes.

Second, by employing the billiard ball lower boundary condition, we eliminate the lower atmosphere's contribution to the circulation that is responsible for the thermosphere's winter polar warming features. The resulting simulations exhibit a weakened meridional circulation, which in turn produces very weak winter polar warming features in the thermosphere. This suggests that the interhemispheric Hadley circulation responsible for strong thermosphere winter polar warming originates in the lower atmosphere and couples with an *in situ* solar EUV driven thermospheric circulation. This combined Hadley circulation results in the adiabatic heating and cooling rates that, in turn, produce the temperature and density structures consistent with winter polar warming in the lower thermosphere. In effect, this last lower boundary simulation reveals the vertical extent of this Hadley circulation and suggests that winter polar warming in the lower thermosphere is a whole atmosphere response, rather than an effect driven by an *in situ* thermospheric circulation only.

4.8 Discussion

4.8.1 Summary of the Three Numerical Investigations

Throughout this work, we delineate the results from three primary numerical experiments: a study of the thermosphere's sensitivity to lower atmospheric dust distributions, a thermospheric interannual study, and finally a lower boundary study. Through these three investigations, we seek to answer key questions about the physics of the thermosphere and about its degree of coupling with the lower atmosphere.

From the first investigation, the dust sensitivity study, we find that the vertical

dust mixing, holding all other variables constant, greatly modifies the simulated winter polar warming features in the MTGCM's thermosphere. As lower atmospheric dust is mixed to higher altitudes, the winter polar warming features become more pronounced, as shown in Table 4.1 and Figures 4.3 and 4.4. From this table and these figures one finds that, for a constant dust opacity of $\tau = 0.3$ and for a constant season of $L_S = 090$, the winter polar warming features systematically increase from a $\Delta T = 20$ K for the lowest dust mixing altitude ($\nu = 0.3$) up to a $\Delta T = 37$ K for the highest dust mixing altitude ($\nu = 0.005$). Also, if the lower atmospheric dust's total opacity is increased, given a constant season and a constant dust mixing height, then the winter polar warming increases. This is illustrated for the case when $L_S = 090$ and $\nu = 0.03$, showing a winter polar warming feature that rises from a $\Delta T = 30$ K for $\tau = 0.3$ up to a $\Delta T = 40$ K for $\tau = 1.0$. Finally, one finds that perihelion possesses a much greater winter polar warming feature ($\Delta T = 73$ K), all things begin equal, than that of aphelion ($\Delta T = 40$ K).

This sensitivity study points out how lower atmospheric dust systematically impacts the temperatures and densities in the upper atmosphere. Furthermore, this sensitivity investigation demonstrates that an interhemispheric summer-to-winter Hadley circulation dominates the thermosphere's dynamics. Additionally, the resulting adiabatic heating and cooling rates, due to the convergence and divergence of meridional and zonal flows, produce the observed winter polar warming features in the thermosphere temperatures shown in Figure 4.3. In summary, this first numerical experiment strongly suggests that interhemispheric dust-driven circulation is the primary determinant for the winter polar thermosphere's densities and temperatures. Further, this circulation is also significantly modified by the lower atmosphere's vertical dust mixing height, the total dust opacity, and the season.

The results from the second major numerical investigation, the interannual study, follow naturally from the results of the sensitivity study. First, as Table 4.2 and Figure 4.1 indicate, the variations in the temperatures at 120 km for the three TES mapping years are directly linked with the lower atmospheric dust variations. Essentially, for each TES mapping year, if the lower atmospheric dust content is enhanced, then the simulated thermosphere winter polar warming is enhanced. Illustrating this point more clearly, by sorting the TES Year aphelion seasons ($L_S = 090$) in order of increasing lower atmospheric dust content, one finds: (1) TES Year 1 with a $\Delta T = 14$ K, (2) TES Year 2 with a $\Delta T = 19$ K, and (3) TES Year 3 with a $\Delta T = 24$ K. Similarly, by sorting the perihelion seasons ($L_S = 270$) for the three TES years in order of increasing lower atmospheric dust content, we find: (1) TES Year 3 has a $\Delta T = 30$ K, (2) TES Year 1 has a $\Delta T = 31$ K, and (3) TES Year 2 has a $\Delta T = 35$ K. This sorting suggests a strong correlation between the lower atmospheric dust levels and the associated winter polar warming signatures.

Second, the perihelion season possesses much greater overall temperature variations, as measured by the winter polar warming, from year to year. At the opposite season of $L_S = 090$, the magnitude of the variations, although still significant, are reduced from year to year in comparison to those of $L_S = 270$. This indicates an interannual variability of the thermosphere's temperatures consistent with the interannual variations found in the lower atmosphere by *Liu et al.* [2003].

Third, the winter polar neutral densities at 120 km in the interannual investigation respond in a manner completely consistent with the sensitivity study's results. As the lower atmospheric dust levels are increased, the winter polar thermosphere neutral densities systematically increase due to an increased heating at lower altitudes, as shown in Figure 4.8 and Table 4.3. Ultimately this interannual study confirms that an

interhemispheric Hadley circulation and its concomitant adiabatic heating/cooling rates, shown in Figure 4.7, to be the primary cause for the variations in the winter polar thermosphere's temperatures and densities.

The third major numerical investigation reveals the vertical extent of this interhemispheric Hadley circulation explored in the earlier two studies. By diurnally averaging the perihelion TES Year 3 lower atmosphere (i.e. turning off the diurnal cycle in the lower atmosphere), we find that the thermosphere's response is greatly modified. The removal of migrating and non-migrating tides reduces the summer-to-winter meridional flow's ability to extend into the thermosphere's winter polar latitudes (poleward of 70^0 N) of Figure 4.9, as was found in the lower atmosphere by *Wilson* [1997]. Furthermore, by removing the lower atmosphere altogether, as was done in the billiard ball case using global average values at the $1.32\text{-}\mu\text{bar}$ pressure level, the strong interhemispheric meridional circulation producing the polar warming weakens and the resulting thermosphere winter polar warming features are greatly reduced. This investigation strongly suggests that upward propagating tides are crucial to producing winter polar warming in the thermosphere, and it indicates that this Hadley circulation extends from the lower atmosphere high into the thermosphere.

4.8.2 Implications of These Results

From all three major numerical studies catalogued in this paper, a clear and simple result emerges. In the Martian atmosphere, there exists a dust driven summer-to-winter interhemispheric Hadley circulation, extending from the lower atmosphere to the thermosphere, that removes energy from the summer hemisphere and deposits that energy in the winter hemisphere. This result has profound implications for the aeronomy of Mars and future aerobraking missions to Mars. First, this paper's

results indicate that the Mars atmosphere is an intimately coupled system, making it necessary to account fully for the lower atmosphere when modeling the structures of the upper atmosphere. Ignoring this coupling results in simulations that lack the dynamical structures observed *in situ*.

In addition to having important implications for Martian upper atmospheric science, the results from this paper also possess significance for future aerobraking missions. As the interannual study reveals, the perihelion season, $L_S = 270$, experiences the greatest temperature and density enhancements at the winter pole. At the opposite season, $L_S = 090$, reduced variations exist, although they remain significant. Hence, if significant variations in the thermosphere's temperatures and densities pose the greatest threat to aerobraking spacecraft, then the aphelion season appears to be most suitable timeframe for aerobraking maneuvers in the lower thermosphere. However, the winter polar thermosphere exhibits significant variability in both densities and temperatures at both solstice seasons for all years simulated. Moreover, these variations relate directly to lower atmospheric dust levels. Thus, aerobraking in the winter polar thermosphere could still expose the spacecraft to significant risks, which remain heavily dependent on the lower atmospheric dust content and distribution.

4.9 Future Work

4.9.1 Suggested Future Studies

The present work and previous studies indicate that the entire Mars atmosphere is an integrated system that is highly coupled dynamically. However, since this work is intended as a baseline theoretical study, we envision several avenues of further research that could directly build upon the results of this investigation.

First, the incorporation of gravity waves into the MGCM-MTGCM is needed to show how these wave features change and modify the inter-hemispheric Hadley cir-

ulation discussed in this work [*Forbes and Hagan, 2000; Forbes et al., 2002; Angelats i Coll et al., 2005*]. The degree to which the dominant interhemispheric circulation is modified by these smaller scale gravity waves has not been documented in the MGCM-MTGCM. Further, such a numerical experiment would better elucidate the details of the energy balances in the upper atmosphere.

Second, a detailed wave analysis investigation, addressing various components of eddy momentum fluxes, would help quantify the impacts of upward propagating waves and tides on the circulation in the thermosphere. This study should examine how planetary waves and tides shift the latitude at which the interhemispheric Hadley circulation deposits energy. Furthermore, this study could better quantify the contribution of migrating tides to the density perturbations at aerobraking altitudes. Moreover, using the interannual results of this work as a starting point, one could explore the existence of a seasonal modulation of the effectiveness of these waves and tides.

Third, a systematic comparison between MGCM-MTGCM outputs and aerobraking datasets would provide a series of constraints against which to test the validity of our simulations. This study could match several possible parameters and compare them with several recent datasets, including the new Mars Reconnaissance Orbiter (MRO) aerobraking and Mars Express (MEX) solar occultation datasets. In such an experiment, more care should be paid to seasonal-specific parameters and solar fluxes in order to reproduce the structures observed.

4.9.2 Further improvements to the Coupled Model

Finally, the development of a self-consistent ground-to-exobase (0-250 km) model for Mars, along the lines of *Angelats i Coll et al. [2005]; González-Galindo et al. [2005, 2006]*, would allow us to further investigate the coupling between the upper

and lower atmospheres. The Global Ionosphere-Thermosphere Model (GITM) of *Ridley et al. [2006]* is presently being used as a suitable modeling framework within which to develop such a self-consistent Mars total atmosphere model.

CHAPTER V

Exploring Titan through T-GITM

Do not keep saying to yourself, if you can possibly avoid it, “But how can it be like that?” because you will get “down the drain,” into a blind alley from which nobody has yet escaped. Nobody knows how it can be like that.

– Richard Feynman

5.1 Introduction

This chapter seeks to establish the Titan Global Ionosphere-Thermosphere Model (T-GITM) as a viable theoretical tool. In order to accomplish this, the following discussion focuses on five segments. First, a brief review of Titan upper atmospheric theoretical work is presented. This establishes the historical scientific context within which T-GITM finds itself. Second, we introduce the major Titan-specific source terms at work in its ionosphere and thermosphere, such as solar EUV/UV heating, HCN rotational cooling, and chemistry. Third, we compare T-GITM simulation results with Cassini Ion-Neutral Mass Spectrometer (INMS) TA flyby datasets in order to benchmark the model and to illustrate how it captures the salient features of Titan’s upper atmosphere. Fourth, the dominant physical drivers responsible for producing these thermospheric structures are explored. Finally, having established the model’s capabilities, the effects of solar cycle, seasonal, and lower boundary

variations on T-GITM fields are quantified. Ultimately, this chapter establishes that the Titan model can reproduce the Cassini INMS *in situ* measurements and can provide valuable insight into the fundamental physical drivers at play in the upper atmosphere.

5.2 Previous Theoretical Work in Titan’s Upper Atmosphere

The present research into Titan’s upper atmosphere builds upon an extensive history of previous theoretical work. Although the T-GITM represents a three-dimensional (3-D) global model, it also incorporates the results of previous one-dimensional (1-D) photochemical, ionospheric, and thermal structure frameworks. Furthermore, this new model builds upon previous 3-D general circulation models of Titan’s upper atmosphere. The following section presents a brief history of Titan theoretical research, selecting those works most influential to T-GITM’s development. While this discussion remains cursory, an excellent review of Titan upper atmospheric theoretical work occurs in *De La Haye* [2005].

5.2.1 Early Chemical and Thermal Structure Modeling: Neutral Atmosphere

Theoretical studies of Titan’s upper atmosphere began with one-dimensional (1-D) models, starting with the pioneering photochemical model of *Strobel* [1974]. Although this work did not include N₂, it did propose the first photochemical scheme for producing ethane, C₂H₂, and acetylene, C₂H₆, from methane. Later, *Allen et al.* [1980] proposed methane-based photochemical processes for producing polyacetylene, C_{2x}H₂, and suggested that this functioned as a likely precursor to Titan’s hazes. After the Voyager 1 encounter with Titan, *Yung et al.* [1984] introduced a new upper atmospheric photochemical model that incorporated components from the earlier works of *Strobel* [1974] and *Allen et al.* [1980]. This newer framework suggested

that chemistry between N_2 and CH_4 produced nitrile compounds, such as HCN , at high altitudes that were subsequently transported to lower altitudes, resulting in the formation of more complex compounds (e.g. HC_3N and C_2N_2). Later, the models of *Toublanc et al.* [1995] and *Lara et al.* [1996] improved upon *Yung et al.* [1984] by introducing improved numerical schemes, photoabsorption cross-sections, and radiative transfer algorithms. Finally, *Lebonnois et al.* [2001] modified the general circulation model of *Hourdin et al.* [1995], producing a two-dimensional (2-D) photochemical framework that characterized the altitude and latitudinal distribution of chemical species in Titan's upper atmosphere.

Friedson and Yung [1984] introduced the first model for the thermal structure of Titan's upper atmosphere, simultaneously solving the coupled equations for energy and hydrostatic balance. They identified CH_4 as a major absorber of Lyman- α radiation and suggested that a mesopause formed due to non-LTE (non-Local Thermodynamic Equilibrium) radiative cooling at 736 km. Later, *Lellouch* [1990] re-examined this earlier model and found numerical errors in its calculation of solar absorption. This correction subsequently required a significant change in the adopted upper atmospheric heating efficiency in order to produce temperatures consistent with Voyager measurements. *Yelle* [1991] later presented a new non-LTE radiative-conduction model for the thermosphere of Titan that included more accurate formulations for radiative heating and cooling terms than previous modeling efforts. This work identified HCN as a major radiative coolant in Titan's upper atmosphere. Furthermore, *Yelle* [1991] indicated that non-LTE radiative transfer of hydrocarbons could also significantly impact this moon's thermal structure at altitudes lower than 800 km.

5.2.2 Early Ionospheric Modeling

Ip [1990] and *Gan et al.* [1992b] produced 1-D photochemical ionospheric models of Titan's upper atmosphere. Among other things, they illustrated that N_2 and CH_4 photoionize to produce: N_2^+ , N^+ , CH_4^+ , CH_3^+ , CH_2^+ , and CH^+ . These models also posited that ion-neutral chemistry quickly converted these ionic species into the major ionic species: HCNH^+ , C_2H_5^+ , CH_5^+ , and HCN^+ . Furthermore, *Gan et al.* [1992b] also found that photoionization represented the dominant ion production mechanism, followed in importance by photoelectron impact and subsequently magnetospheric electron impact. Meanwhile, *Gan et al.* [1992a] introduced one of the first calculations of electron fluxes impacting the upper atmosphere of Titan. This model included both a thermal population calculated by a fluid code and a suprothermal population calculated using a kinetic model.

Later, *Fox and Yelle* [1997] unveiled an ionospheric model that posited C_2H_5^+ as the major ion, in contrast to previous work that showed H_2CN^+ to be the dominant ion. *Keller et al.* [1998] refined the earlier model of *Gan et al.* [1992b], updating kinetic reaction rates and adding more ionic species. This updated model again suggested that H_2CN^+ represented the major ionic constituent. Still later, *Cravens et al.* [2004] improved the earlier ionospheric works of *Gan et al.* [1992a], *Gan et al.* [1992b], and *Keller et al.* [1998] by including higher spectral resolution in the soft X-ray wavelengths and by allowing for photoionization at solar zenith angles beyond the terminator.

5.2.3 Ionosphere-Thermosphere Coupling

Two roughly contemporaneous 1-D models, *Banaszkiewicz et al.* [2000] and *Wilson and Atreya* [2004], emerged that self-consistently coupled the neutral and ion

components of Titan’s upper atmosphere. *Banaszkiewicz et al.* [2000] combined the photochemistry of *Lara et al.* [1996] with the ionosphere of *Gan et al.* [1992b] and updated the reaction rates. They discovered that HCNH^+ represented the major ion at altitudes above 1000 km, while heavy nitrile and hydrocarbon ions dominate at lower altitudes. *Banaszkiewicz et al.* [2000] also illustrated that termolecular reactions became important below 700 km. At the same time, *Wilson and Atreya* [2004] constructed an exhaustive photochemical scheme that including both ions and neutrals, simultaneously solving a coupled continuity-diffusion system of equations. This work suggested that Benzene, C_2H_6 , might play an important role in the formation of Titan hazes.

5.2.4 Previous 3-D Global Circulation Modeling

Rishbeth et al. [2000] first attempted to characterize the 3-D energy inputs and the resulting dynamics in Titan’s upper atmosphere. They estimated thermospheric wind magnitudes through a scale analysis of the momentum equation. From this, *Rishbeth et al.* [2000] proposed that curvature forces and advection of momentum controlled Titan’s thermospheric dynamics. At nearly the same time, the first true 3-D fluid treatment of Titan’s upper atmosphere emerged in the model of *Müller-Wodarg et al.* [2000], which utilized a modified version of the terrestiral Coupled Thermosphere-Ionosphere Model (CTIM) [*Fuller-Rowell and Rees*, 1980b]. This work included solar EUV/UV heating, HCN rotational cooling, and coupling with the lower atmosphere, using both super-rotating and non super-rotating lower boundary conditions. They found that the Titan thermosphere exhibited muted diurnal temperature variations, possessing a maximum day-night asymmetry of approximately 20 K. Later, *Müller-Wodarg et al.* [2003] utilized this same general circulation framework to estimate the effectiveness of global dynamics in redistributing light species, such as CH_4 . However,

neither *Müller-Wodarg et al.* [2000] nor *Müller-Wodarg et al.* [2003] included: (1) self-consistent chemistry calculations, (2) magnetospheric forcing, or (3) true vertical transport. Instead, this 3-D model specified chemistry across the globe and derived vertical winds indirectly by demanding that $\nabla \cdot \mathbf{u} = 0$.

5.2.5 The Coupled Composition-Conduction-Diffusion Model of *De La Haye* [2005]

In 2005, *De La Haye* [2005] unveiled an innovative new 1-D theoretical framework that built upon previous 1-D, 2-D, and 3-D modeling efforts. This new model coupled ion-neutral composition calculations, vertical diffusive transport, thermal calculations, and a full exosphere model above the exobase. It directly accounted for diurnal variations by simulating a rotating 1-D profile. The composition model was composed of 35 neutral species, 47 ionic species, and over 700 chemical reactions. This model utilized diffusive transport only, since it could not directly calculate winds in the thermosphere. Finally, this 1-D framework included thermal conduction, solar EUV/UV heating, and HCN rotational cooling in its calculations of the thermal structure. Key results from this model were: (1) the accurate calculation of heating efficiencies in Titan's upper atmosphere using a two-stream kinetic code coupled with the full chemical, thermal conduction, diffusion code; (2) the identification of a Titan suprothermal corona; and (3) the creation of a theoretical framework within which to analyze the first *in situ* data from the Cassini Ion-Neutral Mass Spectrometer (INMS).

5.2.6 Empirical Upper Atmospheric Research Since Cassini

A great deal of recent research has been devoted to understanding the physics and chemistry of Titan's upper atmosphere, since the arrival of the Cassini-Huygen's mission. The INMS instrument onboard the Cassini spacecraft has provided a wealth of

in-situ data [Waite *et al.*, 2004, 2005]. Yelle *et al.* [2006] employed a one-dimensional (1-D) diffusion model that sought to explain the structure of CH₄ in Titan's upper atmosphere, deriving a range of eddy diffusion coefficients and topside fluxes consistent with measurements. At the same time, Müller-Wodarg *et al.* [2006] developed an empirical model to explain horizontal structures observed by INMS. Although these investigations provided important analyses of observed structures in Titan's thermosphere, neither the 1-D diffusion model nor the empirical model accounted for the feedbacks between the physical mechanisms responsible for the observed structures.

5.2.7 Escape from Titan's upper atmosphere: Hydrodynamic Escape

The work of Yelle *et al.* [2006] and Müller-Wodarg *et al.* [2006] reproduced the vertical profile of CH₄ in Titan's upper atmosphere, utilizing various specifications of the turbulent diffusion coefficient and topside escape fluxes. However, in order to reproduce the *in situ* data from Cassini INMS, both models required topside escape fluxes far in excess of the thermal Jean's escape fluxes. Thus, both Yelle *et al.* [2006] and Müller-Wodarg *et al.* [2006] posited that non-thermal escape processes produced the fluxes necessary to explain density structures measured by the INMS.

However, Strobel [2008] illustrated that hydrodynamic escape alone could account for these fluxes without the need for non-thermal escape processes. Through an energy analysis of Titan's upper atmosphere that included solar EUV/UV heating, HCN cooling, upward pressure gradients, and gravitational potential, this work produced a mass outflow rate of approximately $4 - 6.7 \times 10^{28}$ amu/s. At an altitude of 1500 km above Titan's surface, which possesses a spherical surface area of roughly 3.21×10^{14} m², this translated into an average mass escape flux of $1.91 - 2.39 \times 10^{14}$ amu/m²/s. However, partitioning this mass outflow rate between the major species at the exobase (N₂, CH₄, and H₂) represented an unsolved problem. Only limit-

ing cases were examined, producing estimated escape fluxes of roughly 1.0×10^{13} molecules $\text{CH}_4/\text{m}^2/\text{s}$ and 2.4×10^{13} molecules $\text{H}_2/\text{m}^2/\text{s}$. Ultimately, this paper illustrated that non-thermal escape fluxes or other processes are not necessary to have strong outflows from the topside of Titan’s upper atmosphere.

5.3 The Titan Global Ionosphere-Thermosphere Model

The Titan Global Ionosphere-Thermosphere Model represents a modified version of an extant Earth framework, developed at the University of Michigan and detailed in *Ridley et al.* [2006]. It also owes a great debt to the efforts of *De La Haye* [2005], from which it inherits many of its parametric formulations and its chemical scheme. The Titan-GITM distinguishes itself from other existing general circulation models in many ways. First, the GITM framework solves the Navier-Stokes equations in spherical polar coordinates centered on the planet, utilizing r (height) as the vertical coordinate. Second, this code does not *a priori* enforce hydrostatic equilibrium throughout its domain, instead allowing differences between gravitational and pressure gradient forces to drive dynamics [Deng *et al.*, 2008]. Third, this model explicitly solves the radial momentum equation, providing true vertical transport.

Currently, T-GITM carries 15 neutral species and 5 ionic species, employing a subset of chemical reactions from the detailed 1-D coupled chemical-conduction-diffusion model of *De La Haye et al.* [2007a, b]. This chemical scheme begins with the photodissociation and photoionization of N_2 and CH_4 into: H , H_2 , ${}^3\text{CH}_2$, ${}^1\text{CH}_2$, CH_3 , CH , CH_3^+ , N^+ , $\text{N}({}^4\text{S})$, and N_2^+ . These primary fragments then react to produce a second sequence of constituents: H_2CN , H_2CN^+ , C_2H_4 , C_2H_5^+ , and HCN . Among this last sequence, HCN represents a key thermally active neutral species in Titan’s upper atmosphere, while C_2H_5^+ and H_2CN^+ represent the major ionic constituents.

Additionally, T-GITM carries the chemically inert ^{40}Ar and the isotopes, $^{13}\text{CH}_4$ and ^{15}N - ^{14}N . Finally, the model allows chemistry to sub-cycle, removing the need to assume chemical equilibrium, and provides for multiple chemical time steps within a single dynamical time-step.

The Titan model includes two important radiative sources in the thermosphere. First, N_2 and CH_4 absorb solar EUV/UV radiation in the upper atmosphere, heating it with an efficiency given in *De La Haye* [2005]. Second, HCN rotational cooling helps to balance this solar insolation. Currently, the Titan framework utilizes a full line-by-line treatment of HCN rotational cooling, adapted from the formulations of *Yelle* [1991] and *Müller-Wodarg et al.* [2000], using a spline colocation gaussian quadrature method. Appendix B contains the details of the radiative transfer model employed in T-GITM.

5.4 The Titan-Specific Driving Terms for T-GITM

In this section, we provide the details of the Titan-specific forcing terms included in T-GITM, including: solar EUV Forcing, HCN Radiative cooling, magnetospheric forcing, and finally the chemistry employed for the ionosphere-thermosphere system.

5.4.1 Solar EUV Inputs

Solar insolation represents a primary driver for Titan's ionosphere-thermosphere system. T-GITM includes two models for solar irradiance calculations: (1) the formulation of *Hinteregger et al.* [1981] (SERF1) and (2) the *Tobiska* [1991] update to the *Tobiska and Barth* [1990] (SERF2) model. Both models employ the daily average and the 81-day mean of the $\text{F}_{10.7-cm}$ radio flux. Furthermore, these models are modified to output the solar flux in 55 wavelength bins that are then used in combination with N_2 and CH_4 photoabsorption and photoionization cross sections, which

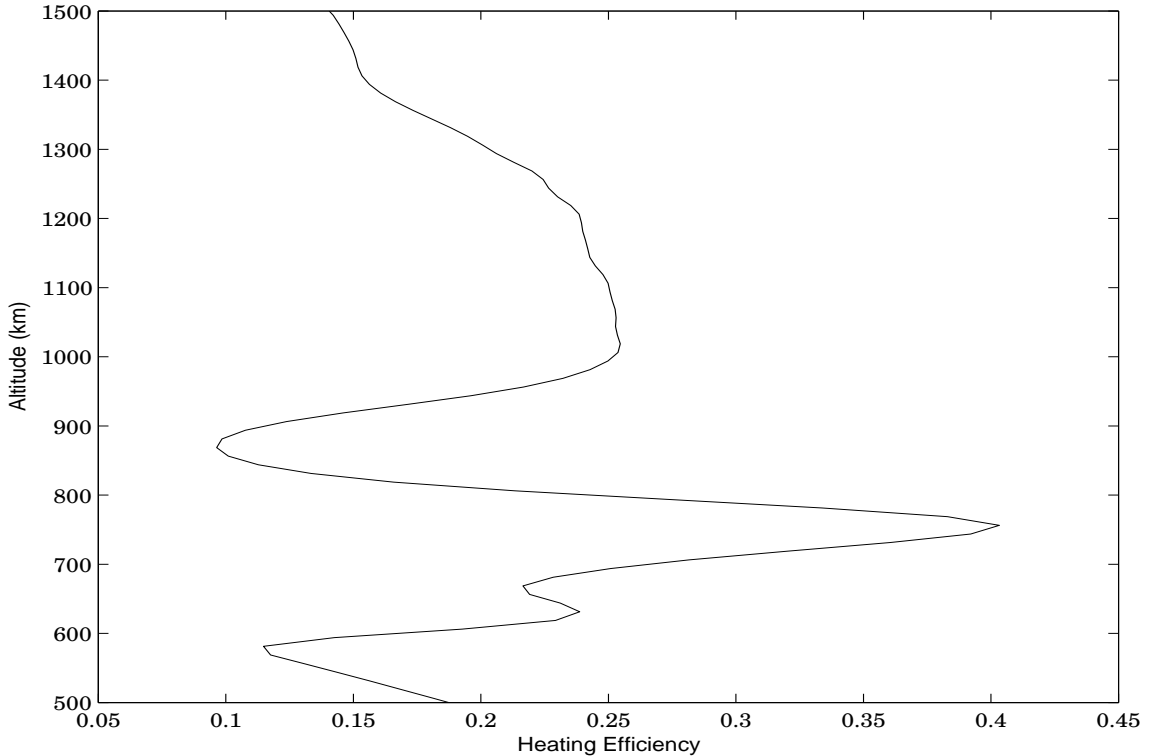


Figure 5.1: Altitude plot of the heating efficiency utilized in Titan GITM. This heating efficiency is assumed to be reasonably valid over the entire Titan globe. Furthermore it takes into consideration both solar and magnetospheric sources and exothermic chemistry. This heating efficiency profile is adapted from *De La Haye* [2005]

are found in Appendix A. Table A.1 contains the N_2 photoabsorption cross-sections and associated quantum yields employed by the Titan GITM, adapted from *Torr et al.* [1979]. Likewise, Table A.2 contains the CH_4 photoabsorption cross sections and quantum yields, which are taken from *Schunk and Nagy* [2000].

The solar fluxes at all wavelengths are taken as Earth values and subsequently scaled for Titan's orbit at roughly 9.5 AU. The model accounts for changes in Titan's orbital position and the associated sub-solar latitude self-consistently over time, allowing for a realistic evolution of solar insulation as the planet orbits the sun. From its calculations of incident fluxes and solar zenith angles, T-GITM then utilizes the method of *Smith and Smith* [1972] to calculate the chapman integrals that determine

the how the intensity attenuates as a function of wavelength and altitude. Furthermore, we employ the heating efficiency of *De La Haye* [2005] as a function of altitude, shown in Figure 5.1, which represents average conditions on Titan. Furthermore, this heating efficiency is derived from the detailed two-stream suprathermal electron code of *De La Haye et al.* [2007a, b] and includes exothermic chemical sources.

5.4.2 HCN Rotational Cooling

Hydrogen Cyanide (HCN) represents the primary radiative coolant in Titan's upper atmosphere that balances solar insolation. HCN possesses a permanent dipole moment, allowing for a substantial rotational spectrum. In particular, the rotational lines between the ground and first excited vibrational states represent a population of molecular lines that remain in approximately local thermodynamic equilibrium (LTE) for the conditions prevailing in Titan's upper atmosphere. T-GITM adopts the formulation for HCN rotational cooling developed in *Yelle* [1991] and utilized by *Müller-Wodarg et al.* [2000], where the radiative cooling rates are given by:

$$h(z) = 2\pi n_{HCN}(z) \sum_{j=1}^{n_{lines}} \left[\int_{\Delta\nu_j} S_{\nu, \nu_j}(z) \phi_{\nu, \nu_j}(z) [C(\tau(z), \nu, \nu_j)] \right] d\nu + 2\pi n_{HCN}(z) \sum_{j=1}^{n_{lines}} \left[\int_{\Delta\nu_j} S_{\nu, \nu_j}(z) \phi_{\nu, \nu_j}(z) [H_1(\tau(z), \nu, \nu_j) + H_2(\tau(z), \nu, \nu_j)] \right] d\nu.$$

In this expression, the three primary radiative transfer terms in the integrand, C , H_1 , and H_2 break down as follows:

1. $C(\tau(z), \nu, \nu_j) = -2B_\nu(\tau(z))$ is the isotropic radiation emitted from an altitude “z” in all directions. This term, because it represents radiation emitted away from a given altitude level, represents a strictly radiative cooling term and would be the only term included in a “cool-to-space” approximation.
2. $H_1(\tau(z), \nu, \nu_j) = B_\nu(0)E_2(\tau_{max} - \tau(z))$ represents the upwelling radiation from

the lower boundary that is absorbed by the atmosphere at an altitude level “z”.

This term thus represents radiative re-absorption of upwelling radiation and so reduces the net cooling rate at the altitude “z”.

3. $H_2(\tau(z), \nu, \nu_j) = \int_{\tau(z)}^{\tau_{max}} B_\nu E_1(\tau(z') - \tau(z)) d\tau' + \int_0^{\tau(z)} B_\nu E_1(\tau(z) - \tau(z')) d\tau'$ represents the radiation incoming to the level “z” from all other altitudes levels in the atmosphere. This term also represents radiative re-absorption of incoming radiation and subsequently reduces the net cooling rate at an altitude “z”.

In this formulation, $\tau(z)$ represents the optical depth of the atmosphere at an altitude level “z,” where τ ranges from 0.0 at the top of the atmosphere and reaches the maximum value, τ_{max} , at the lowest altitude layer in the model [Chandrasekhar, 1960; Goody and Yung, 1989; Houghton, 2002; Mihalas, 1978]. B_ν is the Boltzmann function that represents the radiative source function because the rotational lines of HCN are in LTE. E_2 and E_1 represent the first and second exponential integral functions [Lindfield and Penny, 1999; Press et al., 1992, 1996; Ralston and Rabinowitz, 1978]. $\phi_{\nu, \nu_j}(z)$ represents the line shape, which is taken to be a voigt-broadened line shape [Fels and Schwarzkopf, 1981; Humlícek, 1982; Kuntz, 1997; Lether and Wenston, 1991; Shippony and Read, 1993; Thompson, 1993], and S_{ν, ν_j} represents the rotational line intensity taken from Rothman et al. [2003] and Rothman et al. [1998].

HCN rotational cooling is calculated with a full line-by-line calculation over all 116 ground vibrational state rotational lines [Boughner, 1985; Sparks, 1997]. The HCN rotational cooling is calculated on a plane-parallel grid, which remains inconsistent with both the spherical nature of the real Titan atmosphere and the spherical nature of the T-GITM model. However, due the inherent computational difficulties of true spherical radiative transfer, the plane-parallel approximation was utilized [Martin et al., 1984; Rogers and Martin, 1986, 1984; Peraiah, 2001]. For further details on

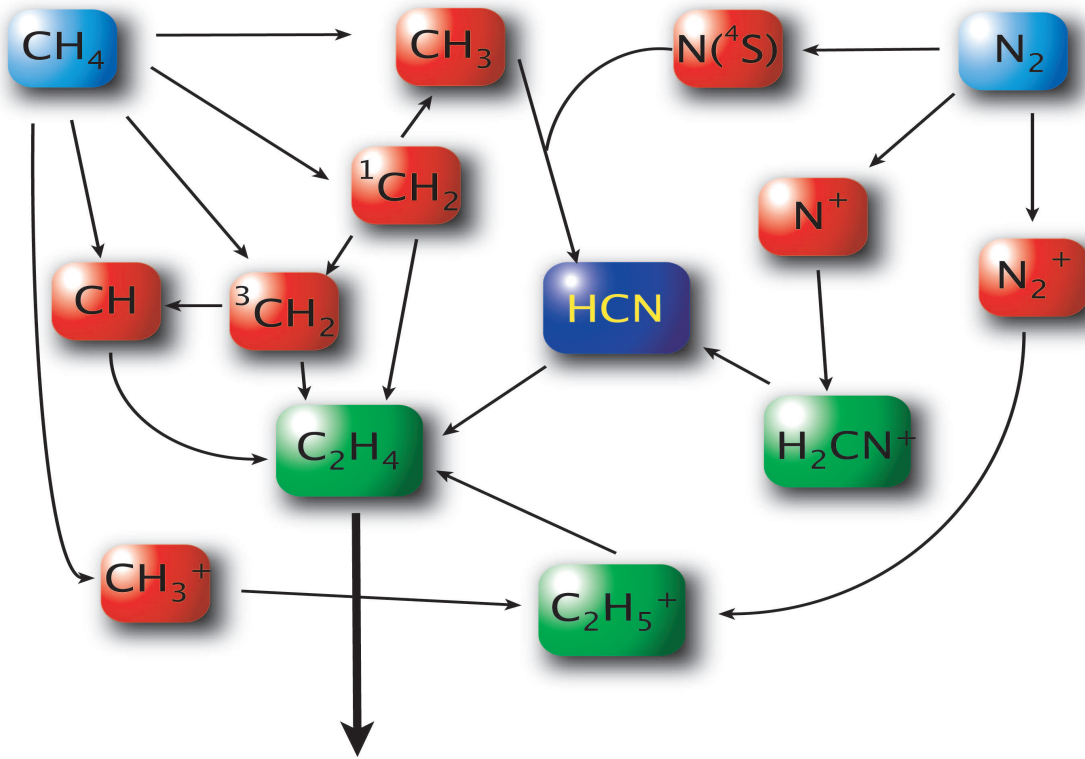


Figure 5.2: Schematic of the Major chemical pathways in T-GITM. This is a subset of chemistry from *De La Haye* [2005]. The light blue species, N_2 and CH_4 , represent photochemical sources for all subsequent chemistry. The red species represent the immediate photochemical products. The green species represent the major products of the subsequent ion-neutral chemistry, C_2H_5^+ , HCNH^+ , and C_2H_4 . Finally the purple species, HCN , is singled out as the primary radiative cooling agent in the upper atmosphere.

the numerical techniques of the HCN rotational cooling utilized in the Titan-GITM, see Appendix B.

5.4.3 Chemistry

T-GITM currently employs a subset of the chemistry found in the detailed 1-D model of *De La Haye* [2005]. This chemical scheme begins with the photodissociation and photoionization (see Table 5.1) of N_2 and CH_4 into: H , H_2 , $^3\text{CH}_2$, $^1\text{CH}_2$, CH_3 , CH , CH_3^+ , N^+ , $\text{N}(^4\text{S})$, and N_2^+ . These primary fragments then react with one another to produce a second sequence of chemical constituents: H_2CN , H_2CN^+ ,

Table 5.1: Photochemical Reactions in T-GITM

Reaction Number	Photochemical & Electron-Impact Reaction
1	$N_2 + h\nu, e^- \rightarrow N(^4S) + N(^2D)$
2	$N_2 + h\nu, e^- \rightarrow N(^4S) + N^+$
3	$N_2 + h\nu, e^- \rightarrow N_2^+$
4	$CH_4 + h\nu, \rightarrow CH + H_2 + H$
5	$CH_4 + h\nu, \rightarrow ^3CH_2 + 2H$
6	$CH_4 + h\nu, \rightarrow ^1CH_2 + H_2$
7	$CH_4 + h\nu, \rightarrow CH_3 + H$
8	$CH_4 + h\nu, e^- \rightarrow CH_3^+ + H$

C_2H_4 , $C_2H_5^+$, and finally HCN . Figure 5.2 illustrates graphically how the various species in T-GITM interact chemically. Furthermore, Table 5.2 contains the various bi-molecular chemical kinetic rates and reactions currently employed in the model. The electron recombination reactions require an electron temperature in order to calculate a proper reaction rate. Since the Titan model does not currently calculate a separate electron temperature, it employs the measured electron temperature from the Cassini Radio and Plasma Wave Science (RPWS) Instrument *Wahlund et al.* [2005], shown in Figure 5.3.

Because T-GITM's chemistry terminates with the formation of C_2H_4 , it employs a set of C_2H_4 loss reactions, detailed in Table 5.2, that are not a part of the core scheme shown in Figure 5.2. This prevents the possibility of C_2H_4 continually growing over the course of model simulations. In these additional loss reactions, the Titan model does not track the ion or neutral products that are not part of its constituent subset. Thus, while this chemistry is not exhaustive, it produces key thermally active species, HCN , and the major ions, $HCNH^+$ and $C_2H_5^+$, in the upper atmosphere.

5.5 Boundary Conditions, Initial Conditions, and Key Parameter Settings

In all theoretical/numerical developments of atmospheres, the region of interest remains spatially and temporally finite. Thus, the imposed boundary conditions

Table 5.2: Intermolecular Chemical Reactions and Associated Rates in T-GITM [De La Haye, 2005; Wilson, 2002a; Wilson and Atreya, 2004].

Reaction Number	Chemical Reaction	Reaction Rate	Units
Neutral Bi-Molecular Chemistry			
1	$^3CH_2 + H \rightarrow H_2 + CH$	$4.70 \times 10^{-16} e^{-370.0/T}$	m^3/s
2	$CH_3 + ^3CH_2 \rightarrow C_2H_4 + H$	7.00×10^{-17}	m^3/s
3	$CH_4 + CH \rightarrow C_2H_4 + H$	$3.96 \times 10^{-14} T^{-1.04} e^{-36.1/T}$	m^3/s
4	$CH_4 + ^1CH_2 \rightarrow CH_3 + CH_3$	6.00×10^{-17}	m^3/s
5	$N(^4S) + CH_3 \rightarrow H_2CN + H$	5.76×10^{-17}	m^3/s
6	$N(^4S) + CH_3 \rightarrow HCN + H_2$	6.00×10^{-18}	m^3/s
7	$N_2 + ^1CH_2 \rightarrow ^3CH_2 + N_2$	$2.36 \times 10^{-20} T$	m^3/s
8	$H_2CN + H \rightarrow HCN + H_2$	7.00×10^{-17}	m^3/s
Ion-Neutral Chemistry			
9	$CH_3^+ + CH_4 \rightarrow C_2H_5^+ + H_2$	$1.10 \times 10^{-15} \pm 20\%$	m^3/s
10	$C_2H_5^+ + HCN \rightarrow H_2CN^+ + C_2H_4$	$2.70 \times 10^{-15} \pm 20\%$	m^3/s
11	$N^+ + CH_4 \rightarrow CH_3^+ + NH$	$5.75 \times 10^{-16} \pm 15\%$	m^3/s
12	$N^+ + CH_4 \rightarrow H_2CN^+ + H_2$	$4.14 \times 10^{-16} \pm 15\%$	m^3/s
13	$N_2^+ + CH_4 \rightarrow CH_3^+ + N_2 + H$	$9.804 \times 10^{-16} \pm 15\%$	m^3/s
Electron Recombination Chemistry			
14	$C_2H_5^+ + e^- \rightarrow C_2H_4 + H$	$7.2 \times 10^{-14} (300.0/T_e)^{0.5}$	m^3/s
15	$H_2CN^+ + e^- \rightarrow HCN + H$	$6.40 \times 10^{-13} (300.0/T_e)^{0.5}$	m^3/s
Special C_2H_4 Losses Section			
16	$C_2H_4 + CH \rightarrow CH_3C_2H + H$	$3.87 \times 10^{-15} T^{-0.546} e^{-26.1/T}$	m^3/s
17	$C_2H_4 + CH \rightarrow CH_2C_2H_2 + H$	$3.87 \times 10^{-15} T^{-0.546} e^{-26.1/T}$	m^3/s
18	$CH_3^+ + C_2H_4 \rightarrow C_3H_5^+ + H_2$	5.406×10^{-16}	m^3/s
19	$CH_3^+ + C_2H_4 \rightarrow C_2H_3^+ + CH_4$	4.876×10^{-16}	m^3/s
20	$C_2H_5^+ + C_2H_4 \rightarrow C_3H_5^+ + CH_4$	3.55×10^{-16}	m^3/s
21	$N^+ + C_2H_4 \rightarrow H_2CN^+ + ^3CH_2$	1.95×10^{-16}	m^3/s
22	$N^+ + C_2H_4 \rightarrow C_2H_4^+ + N(^4S)$	4.55×10^{-16}	m^3/s
23	$N_2^+ + C_2H_4 \rightarrow HCN^+ + HCN + H_2$	1.30×10^{-16}	m^3/s
24	$N_2^+ + C_2H_4 \rightarrow H_2CN^+ + HCN + H$	1.30×10^{-16}	m^3/s

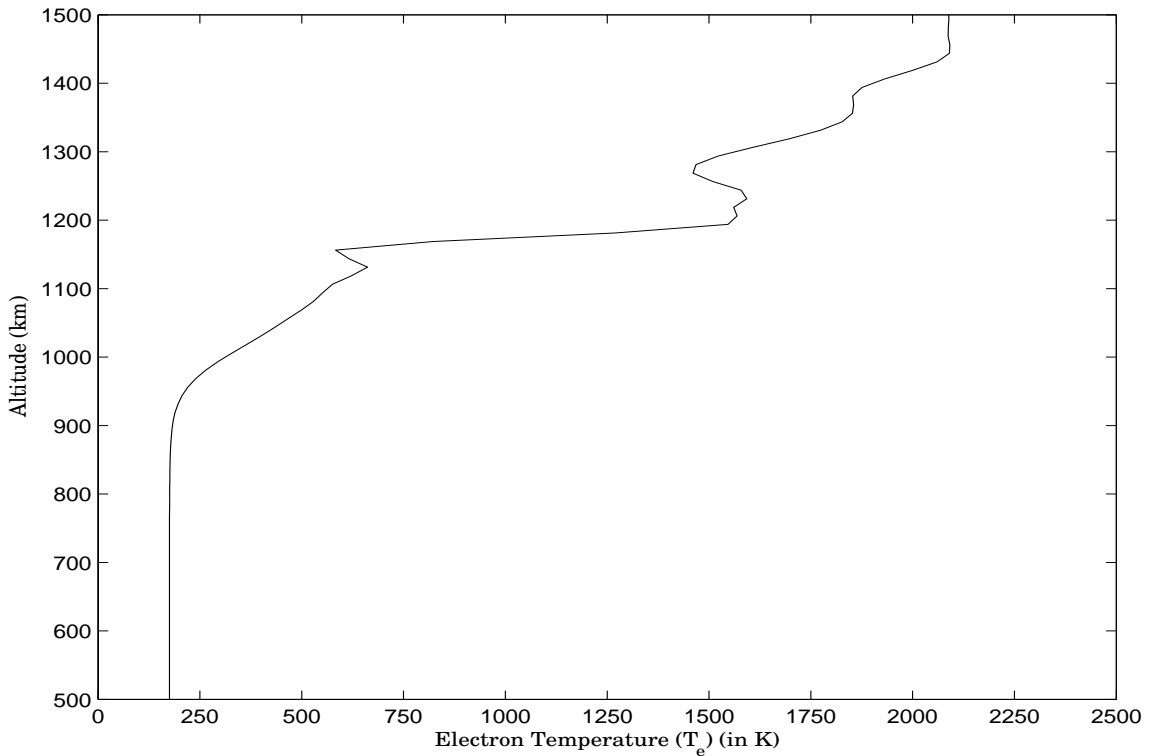


Figure 5.3: Altitude plot of the electron temperature, adopted from *Wahlund et al.* [2005]

must simulate the impacts of the rest of the universe. In the case of theoretical planetary atmospheres, the choices of boundary conditions can drastically impact the end results. Hence, a great deal of effort has been devoted to choosing boundary conditions that best represent inputs from the universe both above and below the modeling domain.

Initial Conditions: Part I

For the TA-flyby simulations, T-GITM is initialized by mapping an average of the ingress and egress Ion-Neutral Mass Spectrometer (INMS) vertical density profiles for N₂, CH₄, and H₂ uniformly across the entire planet [Waite et al., 2005]. Figure 5.4 illustrates the initial vertical density profiles used for N₂ and CH₄. HCN and ⁴⁰Ar adopt volume mixing ratios consistent with key data sets. First, the HCN volume

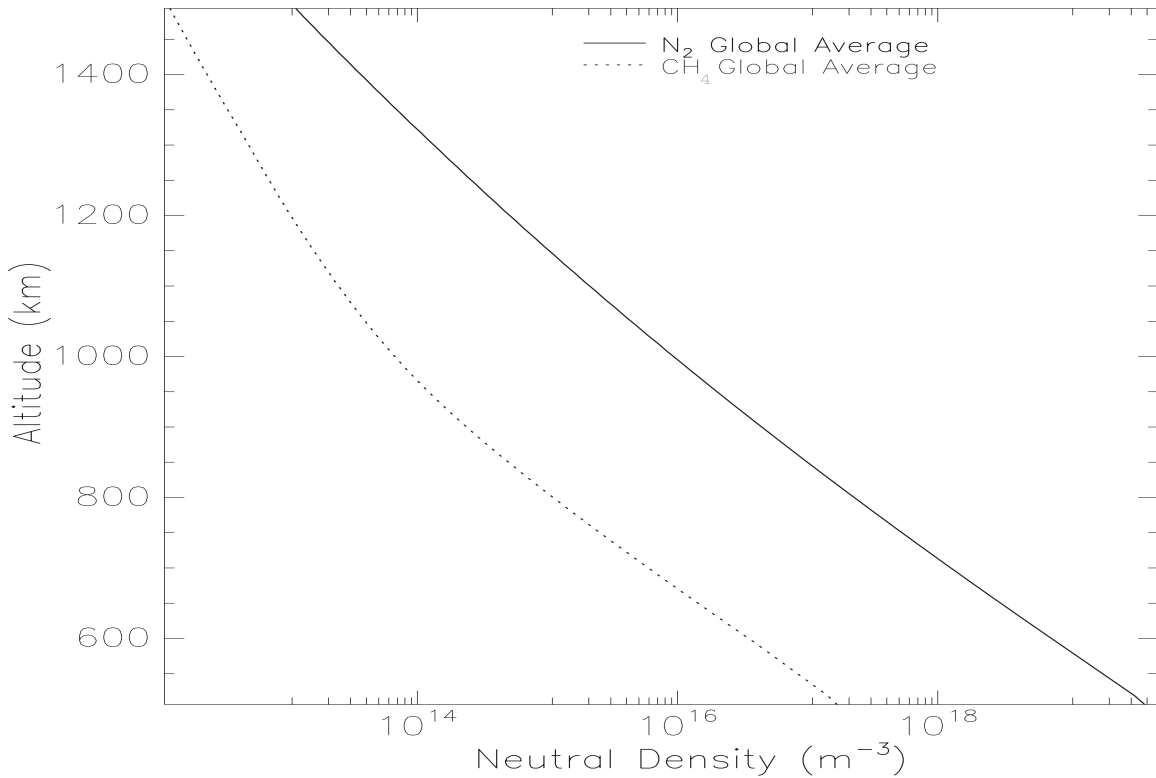


Figure 5.4: Vertical profiles imposed uniformly across the planet to initialize T-GITM. These profiles are taken from an average of ingress and egress measurements of *Waite et al.* [2005]

abundance is set to 1.0×10^{-5} at 500 km, which remains consistent with the errors in measurements by the Cassini Composite InfraRed Spectrometer (CIRS) instrument at this altitude [*Teanby et al.*, 2007]. While this volume mixing ratio represents the highest value obtained in lower atmospheric measurements, we chose to use this mixing ratio in order to limit downward transport of HCN. In the real Titan upper atmosphere, downward transport of HCN would be limited by feedbacks from the lower atmosphere. However, in T-GITM this feedback is unavailable, leading to extremely high downward transport of HCN and subsequently very low volume mixing ratios of HCN at high altitudes. Thus, we approximate this feedback by adopting a volume mixing ratio that sufficiently limits downward transport and allows HCN volume mixing ratios at 1100 km to be consistent with measurements.

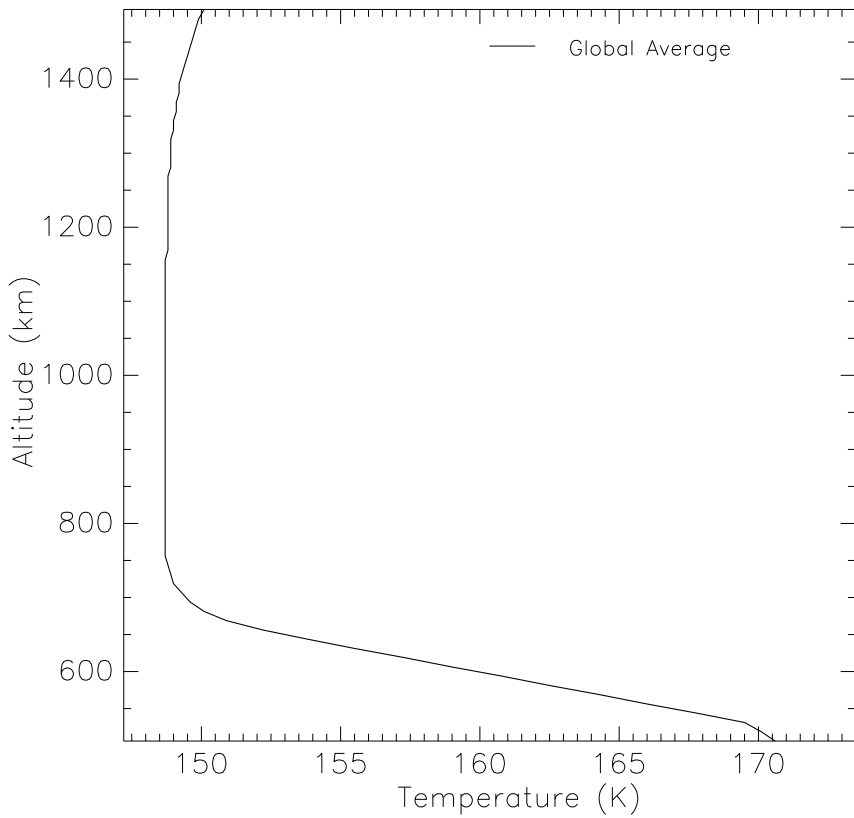


Figure 5.5: Vertical thermal structure imposed uniformly across the planet to initialize T-GITM.

At higher altitudes, the initial mixing ratio of HCN is irrelevant to its temporal evolution, since its eventual profile remains dominated by chemical sources and vertical transport. The noble gas, ^{40}Ar , on the other hand initializes with a volume mixing ratio of 4.32×10^{-5} [Niemann *et al.*, 2005] at the lower boundary and 1.0×10^{-10} at all other altitudes. Thus, diffusive processes from the lower boundary represent the only appreciable sources for this species in T-GITM. All other minor neutral species and ions initially possess constant mixing ratios that function as placeholders, since these species remained relatively insensitive to the initial conditions.

Figure 5.5 contains the initial thermal structure of T-GITM, which is initially

imposed uniformly across the planet. This thermal structure represents the nominal temperature profile adopted by *Waite et al.* [2005]. As found over the course of numerous simulations, T-GITM's thermal evolution depends primarily upon the temperatures adopted at the lower boundary, and remains insensitive to a $\pm 25\%$ change in the initial thermal profile at altitudes above 500 km. However, large changes in the initial thermal structure, such as $\pm 50\%$, significantly alters the model's chemical rates. In addition to these uniform initial conditions in density and temperature, several refinements to the lower boundary's winds, densities, and temperatures are made in order to account for processes at work in Titan's lower atmosphere. The next section provides details of these modifications.

Initial Conditions: Part II – Lower Boundary Temperature, Winds, and Densities

The upper atmosphere of Titan can not exist separately from the influence of the lower atmosphere. In fact, *Bell et al.* [2007] illustrates that planetary atmospheres remain intimately coupled systems, and ignoring this interplay can lead to erroneous results. Thus, several features of Titan's lower atmosphere are adopted at the lower boundary of the Titan-GITM model.

First, the latitude variation in temperature structure derived from the Cassini/CIRS experiment by *Teanby et al.* [2007] and *Flasar et al.* [2005] is incorporated into the lower boundary. A simple plot of how this temperature varies with latitude occurs in Figure 5.6. This thermal structure is mapped uniformly in longitude across the globe at 500 km, resulting in the latitude-longitude variation in temperature shown in Figure 5.7.

At the lower boundary, T-GITM attempts to capture the influence of the lower atmospheric flows measured by *Hubbard et al.* [1993], who detected super-rotating zonal (eastward) winds with two high-latitude zonal peaks at 225 m/s and a mid-

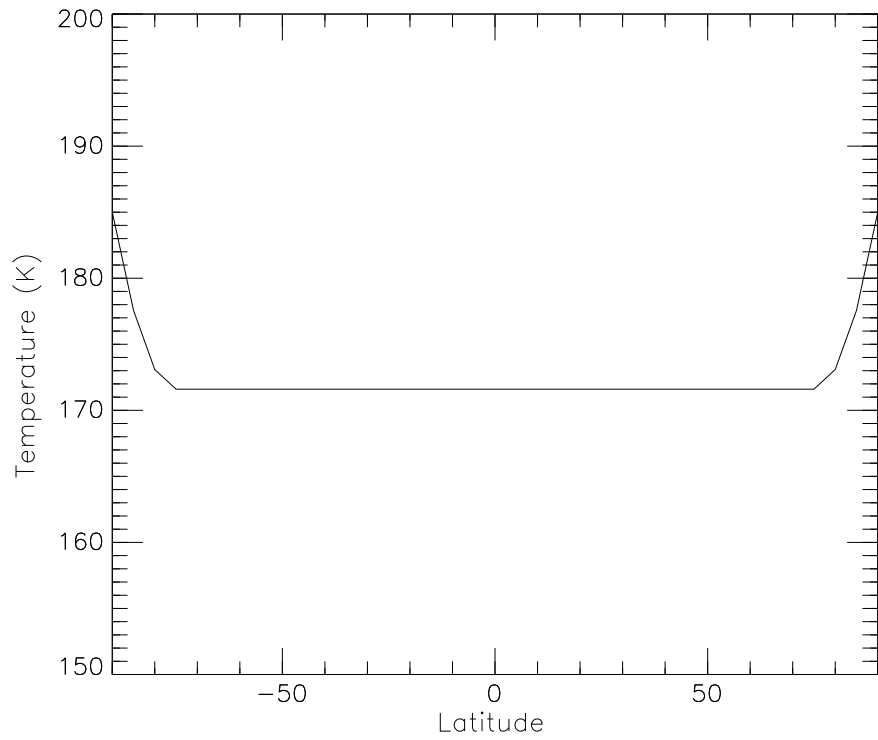


Figure 5.6: A simple line plot of how the lower boundary temperature varies with latitude. This is taken as an approximation of the variations found in *Teanby et al. [2007]*

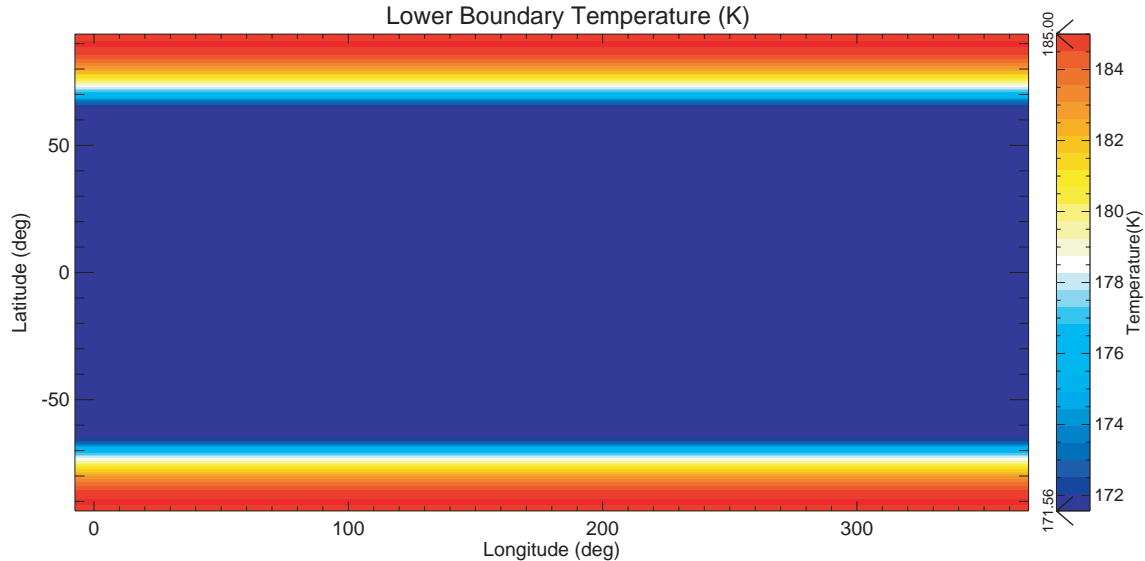


Figure 5.7: A latitude versus longitude plot, demonstrating how the 500 km altitude level maps the temperature of *Teanby et al. [2007]* across the globe.

latitude trough of 175 m/s. Thus, the Titan model's lower boundary is initiated with a zonal wind profile consistent with these measurements. Figure 5.8 depicts a simple line plot showing how the winds vary with latitude in analogy with Figure 5.6. These winds were then mapped uniformly in longitude at 500 km, as shown in Figure 5.9. Finally, because of the imposed winds and temperatures at 500 km, the neutral densities require adjustment in order for the fluid equations to have a physically consistent lower boundary condition. Thus, the meridional (latitude) momentum equation must be solved in order to provide consistent densities as a function of latitude at this altitude. The meridional momentum equation in this case becomes:

$$(5.1) \quad \frac{D_\theta u_\theta}{dt} + \frac{1}{r \rho} \frac{\partial P}{\partial \theta} = \mathcal{F} - \frac{u_\phi^2 \tan \theta}{r} - \frac{u_\theta u_r}{r} - \Omega^2 r \cos \theta \sin \theta - 2\Omega u_\phi \sin \theta.$$

Here, $\frac{D_\theta u_\theta}{dt}$ is the convective or material derivative along the meridional coordinate only, \mathcal{F} is denotes the viscous stress force, Ω is the planetary rotation rate, P is the atmospheric pressure, ρ is the mass density, r is the radial distance to the moon's gravitational center, and finally θ is the latitude.

From this formulation, some additional simplifying assumptions may be employed:

1. Assume a steady state at the bottom, so $\frac{D u_\theta}{dt} = 0$.
2. Set $u_\theta = u_r = 0$ at the bottom boundary.
3. Let $\mathcal{F} = 0$, assuming that it remains a minor correction to the force balance.

After these simplifications, the meridional momentum equation becomes:

$$(5.2) \quad \frac{1}{r \rho} \frac{\partial P}{\partial \theta} = -\frac{u_\phi^2 \tan \theta}{r} - \Omega^2 r \cos \theta \sin \theta - 2\Omega u_\phi \sin \theta.$$

After multiplying both sides by r and after substituting the ideal gas law in for P ($P = nkT$), one obtains:

$$(5.3) \quad \frac{kT}{\rho} \frac{\partial n}{\partial \theta} + \frac{nk}{\rho} \frac{\partial T}{\partial \theta} = -u_\phi^2 \tan \theta - \Omega^2 r^2 \cos \theta \sin \theta - 2r \Omega u_\phi \sin \theta.$$

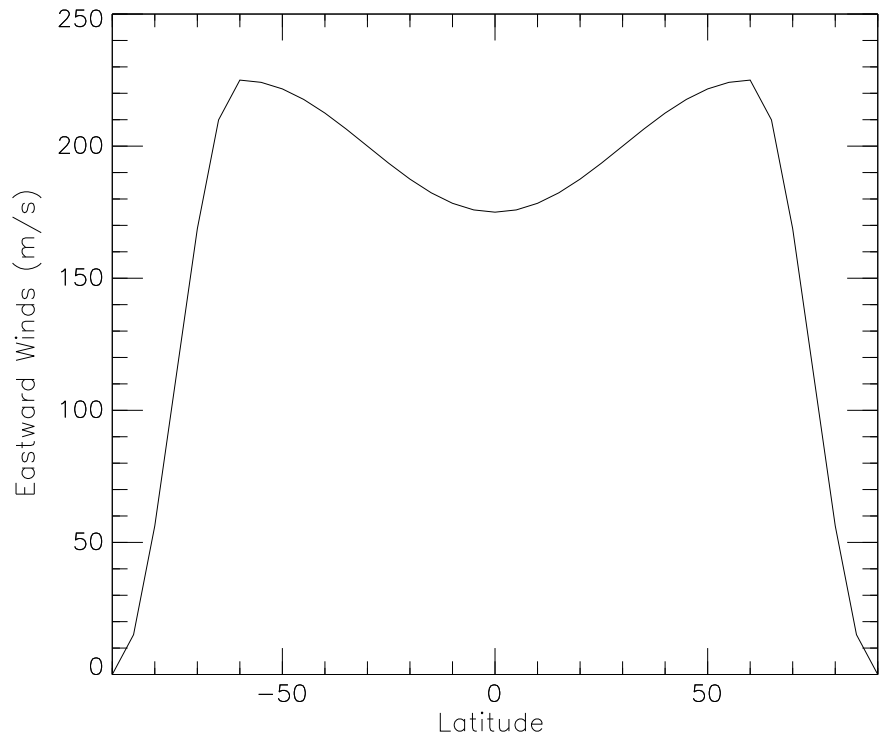


Figure 5.8: A simple line plot of how the lower boundary zonal winds vary with latitude. These are taken as an approximation to those measured by *Hubbard et al.* [1993]

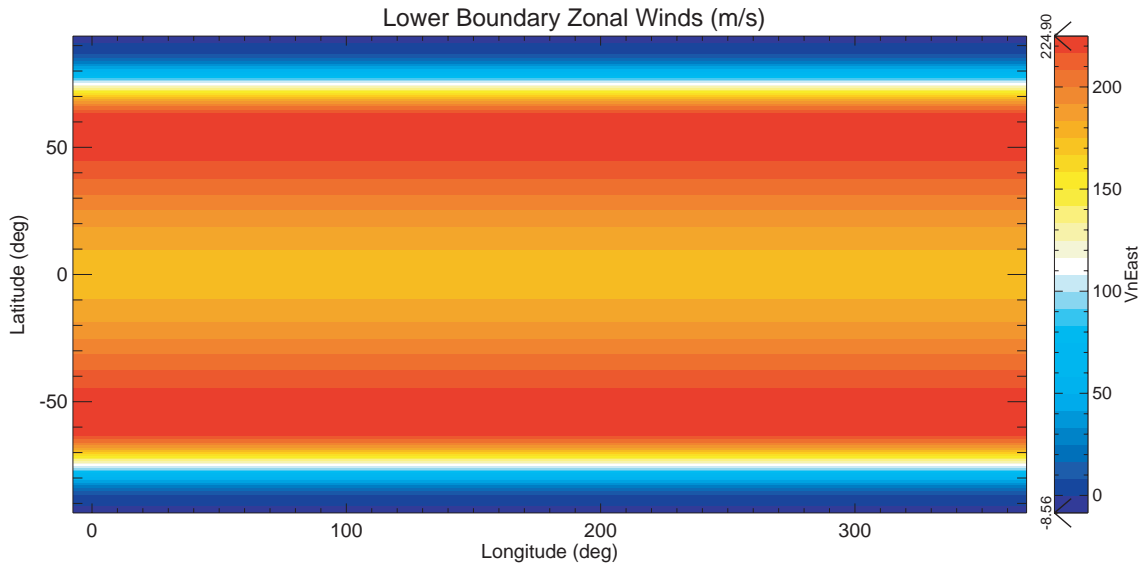


Figure 5.9: A latitude versus longitude plot, demonstrating how the 500 km altitude level maps the winds of *Hubbard et al.* [1993] across the globe.

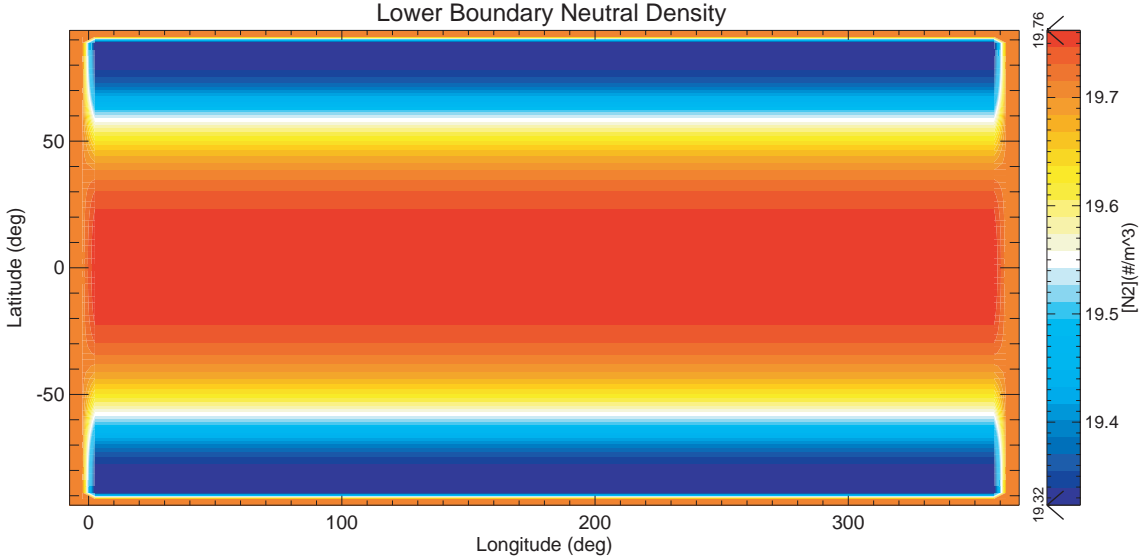


Figure 5.10: A latitude versus longitude plot, demonstrating the behavior of the \log_{10} neutral density ($\log_{10}[\text{m}^{-3}]$) at the 500 km altitude level, taking into account the temperature structure of *Teanby et al.* [2007] and the zonal winds of *Hubbard et al.* [1993] across the globe.

Setting $\rho = \bar{m} n$, a new formula emerges as:

$$(5.4) \quad \frac{kT}{\bar{m} n} \frac{\partial n}{\partial \theta} + \frac{nk}{\bar{m} n} \frac{\partial T}{\partial \theta} = -u_\phi^2 \tan \theta - \Omega^2 r^2 \cos \theta \sin \theta - 2r \Omega u_\phi \sin \theta.$$

Finally, solving for $n(\Theta)$, one obtains:

$$(5.5) \quad \frac{1}{n} \frac{\partial n}{\partial \theta} + \frac{1}{T} \frac{\partial T}{\partial \theta} = - \left(\frac{\bar{m}}{kT} \right) [u_\phi^2 \tan \theta + \Omega^2 r^2 \cos \theta \sin \theta + 2r \Omega u_\phi \sin \theta].$$

Thus, given the functional forms for $T = T(\theta)$ and $u_\phi = u_\phi(\theta)$ depicted in Figures 5.7 and 5.9, one may solve for n as a function of latitude by numerical integration. In order to accomplish this, a reference density, denoted by n_0 , is required and is chosen such that $\nabla (n_0 kT) = -\rho g$. From this n_0 , a straight-forward finite difference method solves for $n(\theta)$ at 500 km. The resulting lower boundary density profile remains oblate, as shown in Figure 5.10. Due to the simplifications used to reduce the meridional pressure balance equation, the derived neutral density structure at 500 km does not provide absolute hydrostatic balance, but it yields very small bulk

vertical velocities (± 0.10 m/s). Ultimately, this set of lower boundary temperatures, winds, and densities represent a best effort to approximate the impact of the lower atmosphere of Titan upon the model domain.

Initial Conditions: Part III – Upper Boundary Conditions

The upper boundary conditions (at 1500 km) on T-GITM's densities, temperatures, and winds remain much less complex than those at 500 km. The model's temperature boundary conditions at 1500 km maintain a constant temperature, meaning the temperature gradient is assumed to be zero. At the upper boundary, each species' neutral density is assumed to decrease with its local scale height, implying the dominance of diffusive separation at 1500 km. Finally, the upper boundary winds simply provide continuity of the model domain without any significant changes.

Initial Conditions: Part IV – Free Parameters

Every theoretical framework possesses components that serve as adjustable parameters. Great care must be exercised when manipulating these parameters in order to maintain a consistent solution without introducing unintended errors, or worse, unintended fixes to unphysical formulations. In T-GITM, two primary free parameters exist: Upper boundary density gradients and the eddy diffusion coefficient.

At the upper boundary, changes in the individual species density gradients impose a radial flux condition (either upward or downward) at the topside boundary. That is, by altering this density gradient, T-GITM self-consistently generates vertical and horizontal velocities consistent with the imposed gradient. This further feeds back into the thermal structure through adiabatic expansion and contraction at the highest altitudes. Currently, escape fluxes are adjusted to match the high altitude T-GITM CH₄ density profile with INMS observations. Finally, the second free pa-

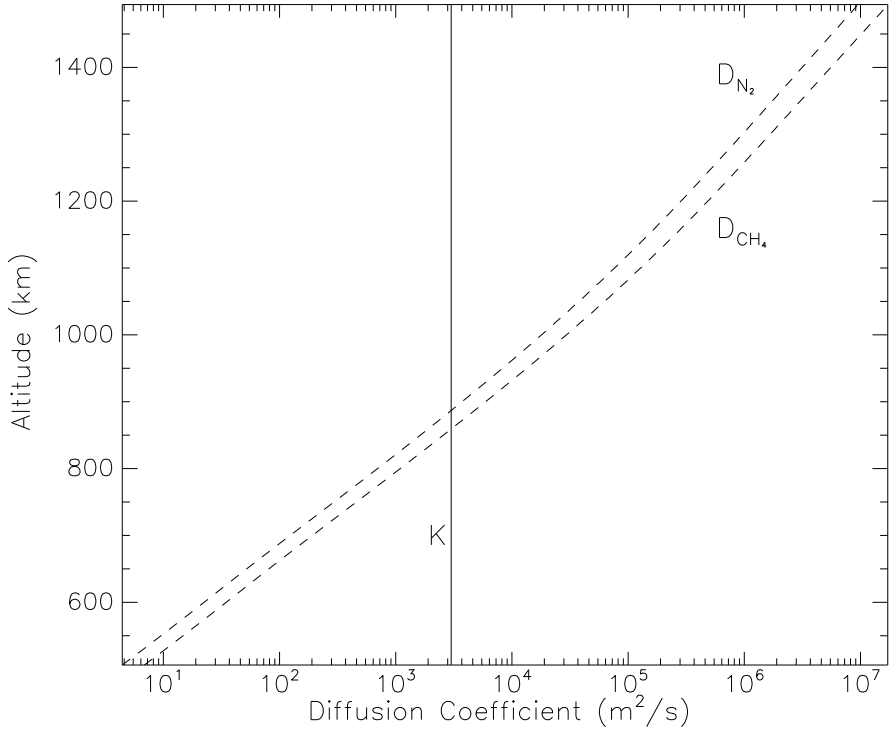


Figure 5.11: Vertical profiles of the eddy diffusion coefficient, K , and the molecular diffusion coefficients for N_2 and CH_4 .

parameter available in T-GITM emerges in the form of the eddy diffusion coefficient. This eddy diffusion coefficient impacts the vertical mixing profiles of minor species. In particular, ^{40}Ar is used to calibrate the choice of eddy profile, because vertical turbulent diffusion and molecular diffusion processes control the vertical distribution of this inert gas in the thermosphere. Thus, this turbulent diffusion is adjusted until reasonable agreement between T-GITM's ^{40}Ar densities and *in situ* measurements is achieved. Currently, the eddy diffusion coefficient is specified as follows [Atreya, 1986]:

$$(5.6) \quad K = K_0 \sqrt{\frac{N_0}{N(r)}}, \quad K \leq K_{max},$$

where $K_0 = K_{max} = 3000 \text{ m}^2/\text{s}$. A depiction of the adopted eddy diffusion profile versus altitude occurs in Figure 5.11. In this figure, the molecular diffusion coeffi-

lients overlie the eddy diffusion, crossing the latter at roughly 850 km.

5.6 Benchmarking T-GITM: A Comparison with Cassini INMS TA Flyby Data

This section compares the T-GITM simulations with *in situ* measurements by the Ion-Neutral Mass Spectrometer (INMS) onboard the Cassini spacecraft [Waite *et al.*, 2004, 2005]. More specifically, we attempt to match the upper atmospheric structures measured during the TA flyby of Titan, which occurred on 26 October 2004. However, as noted in the last section, the adopted boundary conditions remain critical to reproducing the data. Thus, the author remains very much aware of the dangers inherent in “fine-tuning” a theoretical model to match observations. However, with this caveat in mind, the INMS TA flyby data-to-model comparison should still represent an appropriate benchmark case that functions as a “sanity check” on the Titan model’s current physical configuration.

5.6.1 Measuring Error and Consistency

Before discussing how the model compares with *in situ* data, one must adopt a relevant definition of error. For the purposes of this study, the Normalized Root Mean Squared Error (NRMSE) emerges as a suitable candidate. By definition, the NRMSE is given by:

$$(5.7) \quad NRMSE = \frac{\sqrt{\sum_{i=1}^N \frac{(Y_i - X_i)^2}{N}}}{\sqrt{\sum_{i=1}^N \frac{(X_i)^2}{N}}},$$

where X_i represents the INMS data points, N the number of these data points, and Y_i the analogous model results. Although this formulation represents a percentage error (when multiplied by 100.0), it possesses some subtleties that bear mentioning. First, this method weights errors at the lowest altitudes (greatest densities) higher than those at higher altitudes (lower densities). However, because INMS has greater

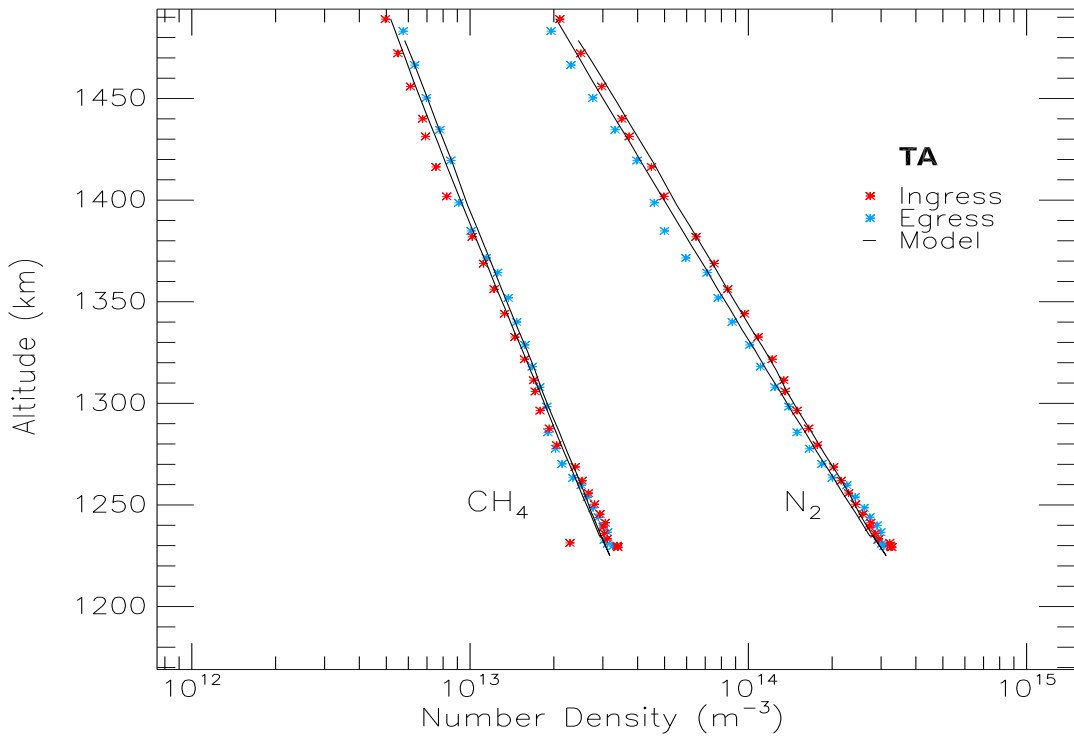


Figure 5.12: N_2 and CH_4 density comparisons between the T-GITM simulation (black lines) and the INMS ingress (red) and egress (blue) datasets. NRMSE deviation of the model simulation from measurements is 0.112 (11.2 %) for N_2 with a correlation coefficient of $r = 0.991$, while the NRSME for CH_4 is 0.113 (11.3 %) with $r = 0.982$.

accuracy at the lowest altitudes, this method ensures that the most accurate data measurements are given the greatest emphasis. Second, this error definition remains less intuitive than a direct percentage error calculation, but one may still define the following general regimes:

1. ($\text{NRMSE} \gg 1.0$): Shows poor overall agreement.
2. ($\text{NRMSE} = 1.0$): illustrates that the average behavior is captured.
3. ($0.5 < \text{NRMSE} < 1.0$): Illustrates good agreement.
4. ($0.0 < \text{NRMSE} \leq 0.5$): Illustrates excellent agreement with data.
5. ($\text{NRMSE} = 0.0$): Perfect agreement with data.

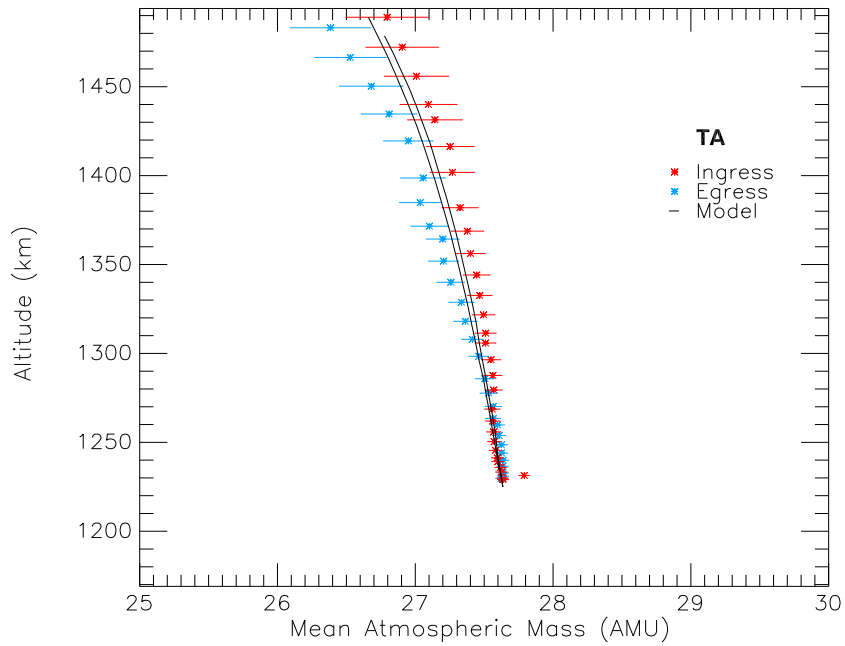
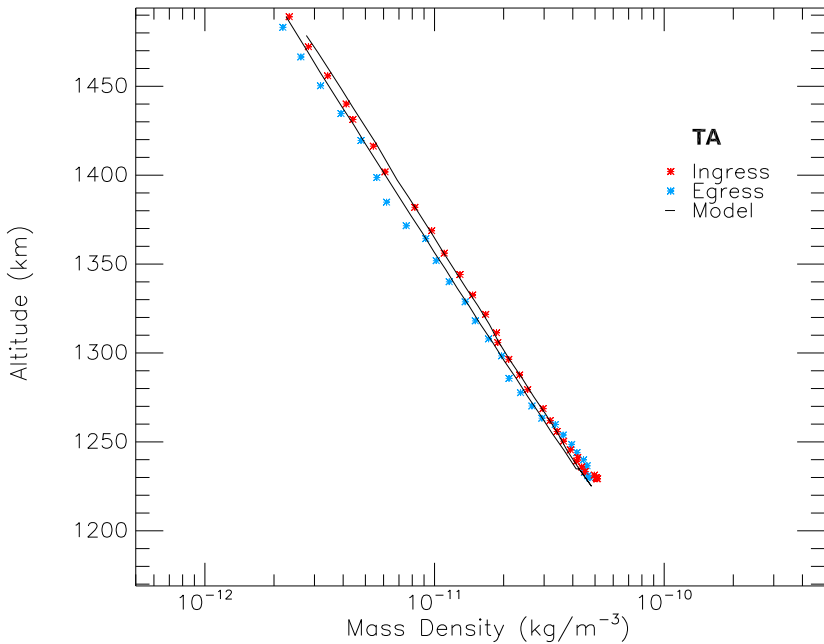
(a) Model to data comparisons of atmospheric \bar{m} (amu) for the TA flyby(b) Model to data comparisons of atmospheric mass density, ρ (kg/m³), for the TA flyby

Figure 5.13: Comparisons between T-GITM fields and associated Cassini INMS ingress (red) and egress (blue) datasets for the TA flyby. The T-GITM mean atmospheric mass, panel (a), possesses NRMSE from INMS measurements of 0.004 and $r = 0.925$. Panel (b), the mass density, possesses a NRMSE from INMS measurements of 0.114 and $r = 0.99$.

Although NRMSE represents an excellent measure of the deviation between the T-GITM and the INMS data, it does not address how well the model reproduces structures in the data. In order to quantify how predictive variations in the T-GITM model are of variations in the actual data, one must introduce the correlation coefficient, r . This coefficient describes how well variations in one dataset predict variations in another dataset. In this case, the correlation coefficient quantifies how well the calculated variations in the model simulations correlate with the structures observed in Titan's upper atmosphere. Furthermore, the square of this coefficient, which statisticians term the coefficient of determination, describes what percentage of the variations in one dataset can be directly linked with the other dataset. In other words, it provides a confidence level for the T-GITM model. For example, if the model-to-data comparison produced a correlation coefficient of 0.60, then the coefficient of determination would then be 0.36. Thus, 36 % of the time, variations in the model are predictive of variations in the real Titan atmosphere.

In the discussion that follows, both the NRMSE and the correlation coefficient, r , emerge as the primary quantifications of the T-GITM's ability to reproduce the *in situ* INMS data.

5.6.2 Direct Comparison Between T-GITM and Cassini INMS

The Cassini flyby trajectory during TA covers both a large vertical and a large horizontal range in Titan's upper atmosphere. Thus, one cannot simply treat the flyby measurements as vertical profiles. Accounting for this fact, a simulated flyby along the TA trajectory is performed through the T-GITM model. Essentially, this method approximates what the Cassini INMS instrument would measure, if it flew through the 3-D model atmosphere along the TA trajectory. The resulting T-GITM fields are plotted against *in-situ* measurements of Titan's upper atmosphere in Fig-

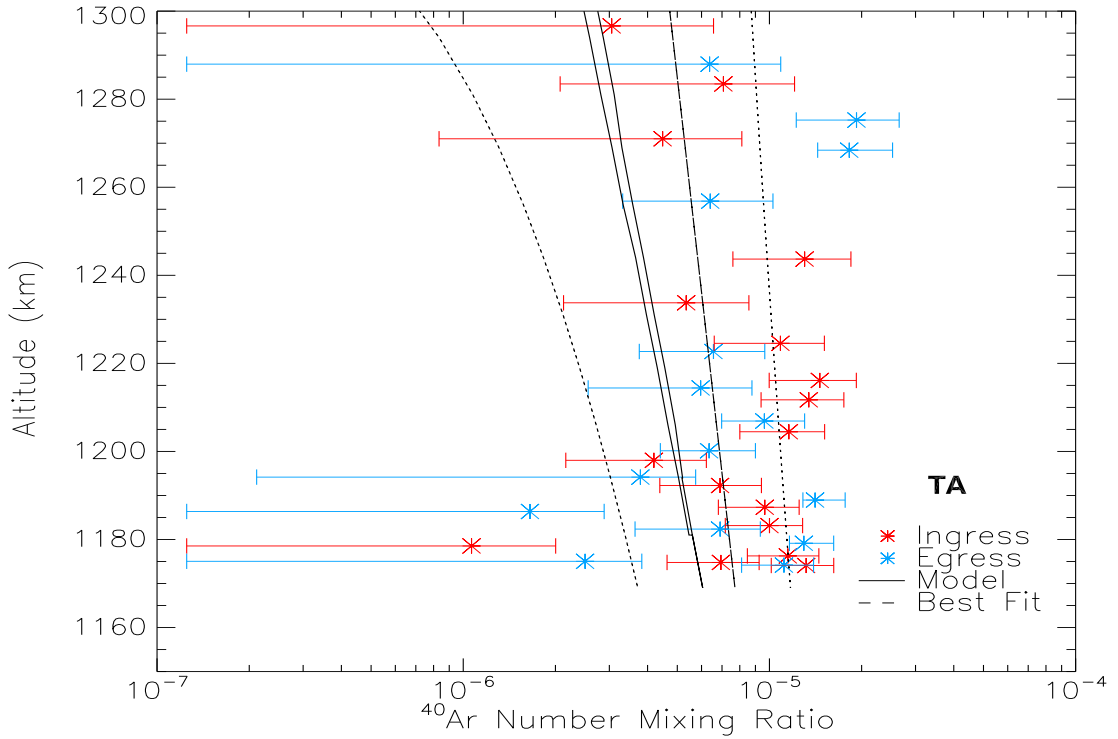


Figure 5.14: Argon mixing ratio comparisons between the T-GITM (solid black line) versus TA flyby ingress (red) and egress (data). Also plotted here is a “best-fit” profile (thick dashed line) with its systematic error envelope (dashed lines). The T-GITM simulation results possess an NRMSE deviation from the best-fit profile of 0.345 (34.5 %), versus the average systematic error of 0.714 (71.4 %). The model also possess a correlation coefficient of $r = 0.994$ with the best-fit profile.

ures 5.12 - 5.16.

Figure 5.12 contains the T-GITM (black line) N_2 and CH_4 densities for the TA flyby and the corresponding INMS *in situ* data, both ingress (red) and egress (blue). The model results show excellent agreement between the model and data. The simulation’s N_2 densities possess an NRMSE of 0.112 (11.2 %) with a correlation coefficient of 0.991. The T-GITM CH_4 densities likewise exhibit NRMSE of 0.113 (11.3 %) and $r = 0.982$. This indicates that, at least for the majors species in the upper atmosphere, the model possesses a predictive r^2 coefficient of roughly 96.4 %.

Over the course of many simulations, the author finds that the vertical profile for

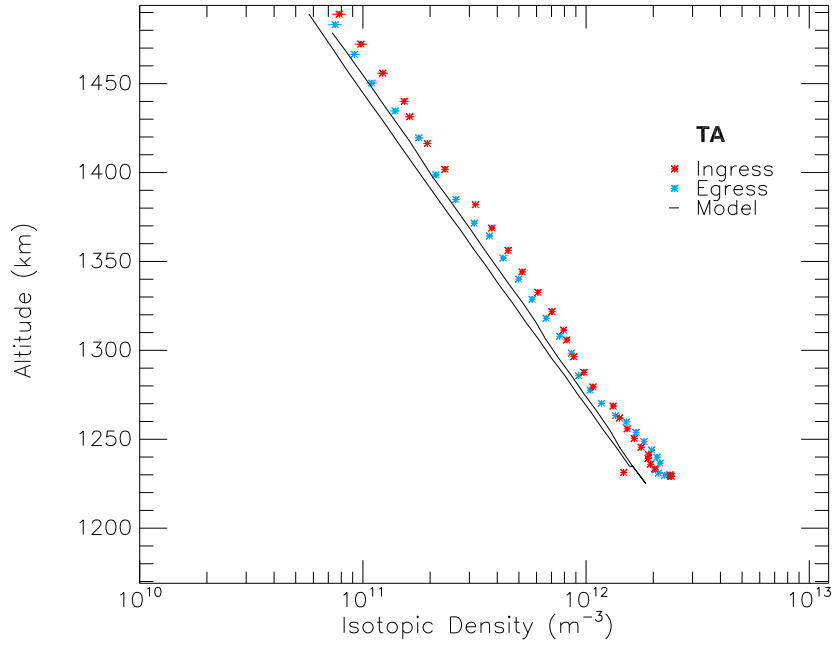
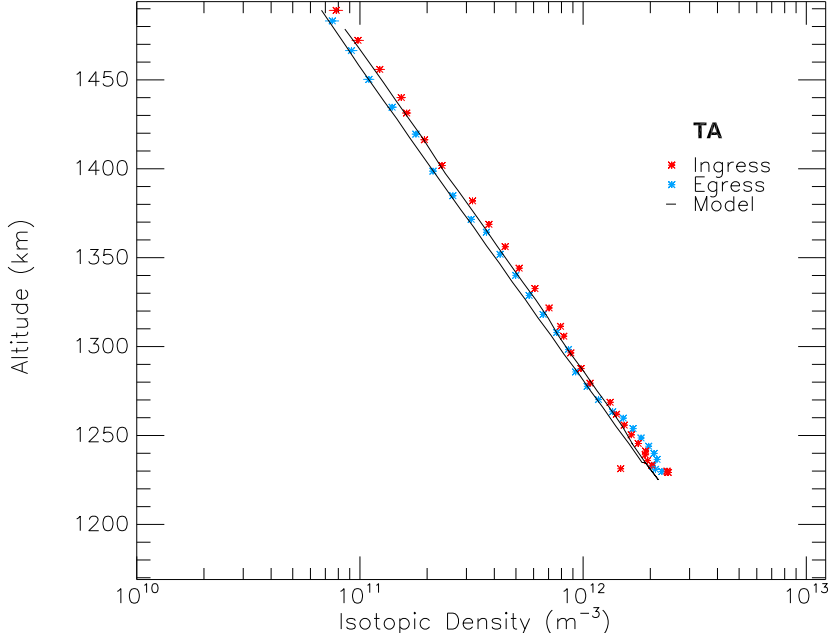
(a) Model to data comparisons of ^{15}N - ^{14}N densities for the TA flyby(b) Model to data comparisons of the Scaled ^{15}N - ^{14}N densities for the TA flyby

Figure 5.15: ^{15}N - ^{14}N neutral density comparisons between the T-GITM (solid black line) versus TA flyby ingress (red) and egress (data). In panel (a), T-GITM employs an $^{14}\text{N}/^{15}\text{N}$ isotopic ratio of 160 at 500 km, resulting in an $\text{NRMSE} = 0.280$ and $r = 0.985$. In panel (b), these results employ an $^{14}\text{N}/^{15}\text{N}$ ratio of 130 at 500 km, resulting in an $\text{NRMSE} = 0.147$ and $r = 0.985$.

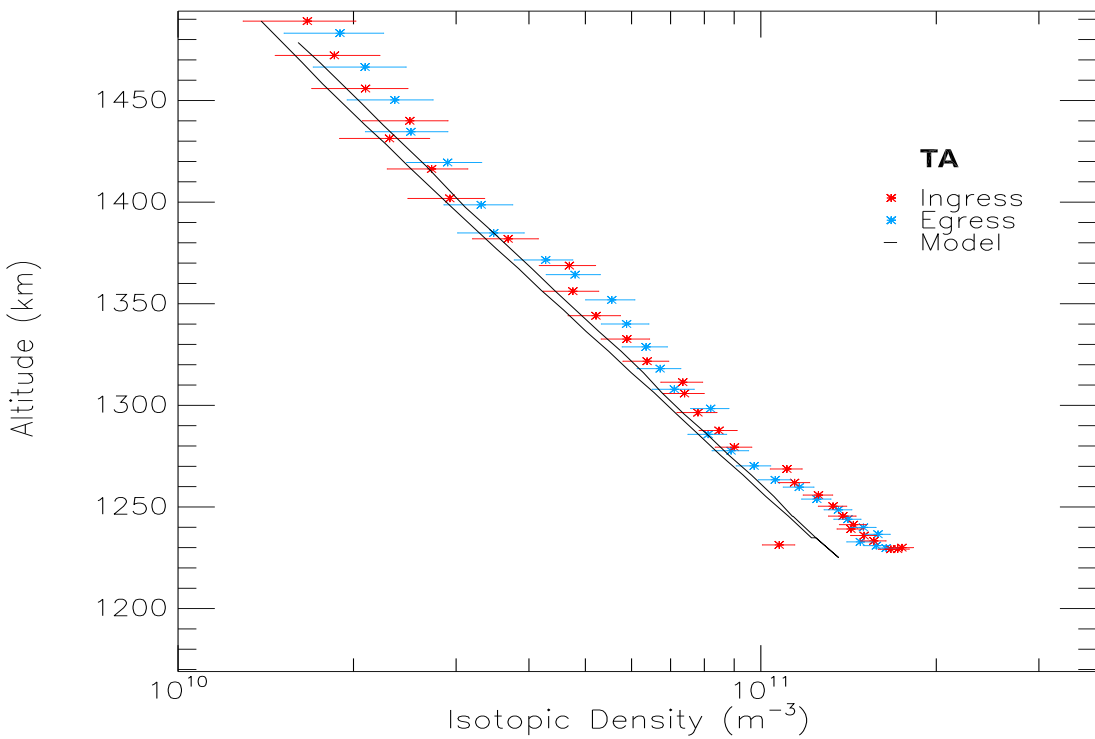


Figure 5.16: $^{13}\text{CH}_4$ neutral density comparisons between the T-GITM (solid black line) versus TA flyby ingress (red) and egress (data). The T-GITM simulation results possess an NRMSE = 0.229 and $r = 0.981$.

CH_4 is primarily governed by two components: (1) the turbulent diffusion coefficient at altitudes between 500 – 1000 km and (2) upward fluxes at altitudes above 1000 km. In the region covered by the INMS comparison plots of Figure 5.12, the topside escape fluxes represent the determining physical process for Methane. In contrast, the vertical density profile for N_2 remains primarily influenced by the local temperature structure and associated scale heights. Thus, deviations in the vertical profile of N_2 most likely indicate deviations in the underlying thermal structure. From the close correlation between the simulated and the measured N_2 densities, one may infer that the T-GITM temperature structure should closely resemble the actual Titan thermal structure.

Figure 5.13(a) compares the Titan-model's atmospheric mean major mass (solid black line) to the TA flyby INMS ingress (red) and egress (blue) *in situ* datasets. The NRMS model deviation from measurements is 0.004 (.4 %) with a correlation coefficient $r = 0.925$, versus a systematic NRMSE of 0.004 in the measurements themselves. The model's mean major mass is derived from contributions of N_2 , CH_4 , and their isotopes. This remains consistent with how this dataset's mean major mass is derived. Figure 5.14 contains the model Argon mixing ratio compared with the INMS-derived values. The model results fall within the systematic error of the data, possessing an NRMSE = 0.345 (34.5 %) and $r = 0.994$, versus the systematic NRMSE of the data itself of 0.714 (71.4 %). Because only diffusive (both turbulent and molecular) and vertical transport processes determine the Argon mixing ratio, this comparison suggests that the T-GITM possesses turbulent and vertical dynamical transport in reasonable agreement with the real Titan upper atmosphere.

Figure 5.15 compares the T-GITM ^{15}N - ^{14}N isotopic density (black line) against the *in situ* INMS ingress (red line) and egress (blue line) data. Clearly, these differ by a significant margin, possessing a NRMSE = 0.280 (28.0 %), which, unlike the Argon error, lies far outside the data's systematic error of (1.1 %). Several possible reasons exist for this. First, the isotopic ratio ($^{14}\text{N}/^{15}\text{N}$) at 500 km is assumed to be near 162 in Figure 5.15(a). However, this value may not represent a realistic isotopic ratio. Instead, a ratio of 130 at 500 km appears to give closer agreement with INMS measurements at TA, as shown in Figure 5.15(b). This scaled version of the ^{15}N - ^{14}N isotope density possesses an NRMSE = 0.147, exhibiting much better agreement with INMS data. Finally, Figure 5.16 contains the $^{13}\text{CH}_4$ isotopic density profiles for the T-GITM (black line), the INMS ingress (red), and the INMS egress (blue) data along the TA flyby trajectory. The Titan model's simulated densities

Table 5.3: T-GITM Comparisons with INMS Data

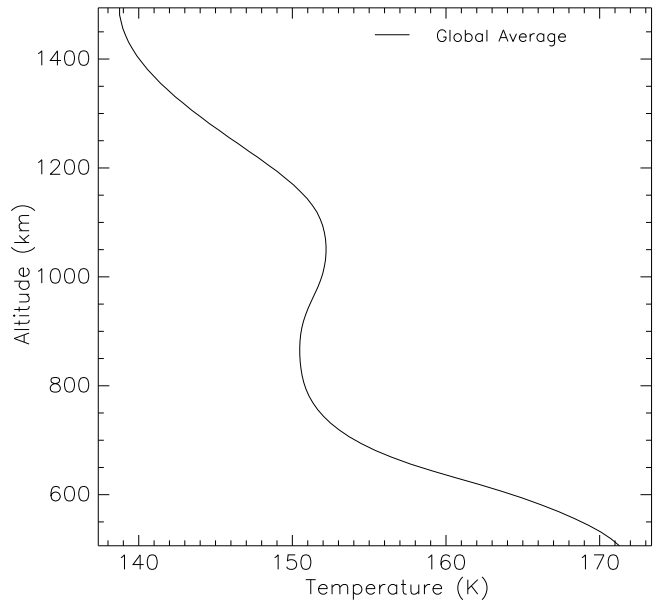
Quantity	Model-to-Data NRMS Error	The Data's Systematic NRMS Error	Correlation Coefficient (r)	Correlation Squared (r^2)
N_2	0.112	0.001	0.991	0.982
CH_4	0.113	0.008	0.982	0.964
ρ	0.114	0.002	0.991	0.982
\overline{m}	0.004	0.004	0.925	0.856
$^{15}N - ^{14}N$	0.28 0	0.011	0.985	0.970
$^{15}N - ^{14}N$ (Scaled)	0.147	0.011	0.985	0.970
$^{13}CH_4$	0.229	0.075	0.981	0.962
Argon	0.345	0.714	0.994	0.970

compare well against the measurements, possessing a NRMSE = 0.229 (22.9 %) and $r = 0.981$.

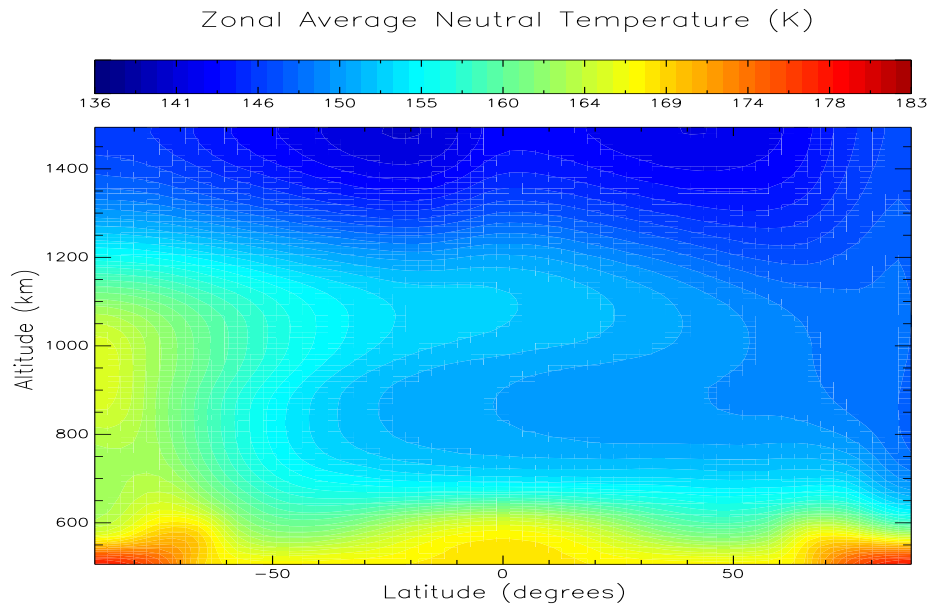
Table 5.3 contains a summary of the T-GITM and INMS TA flyby comparison. Overall, the model possesses excellent agreement with measurements in both an NRMSE sense and in its correlation coefficients over the flyby. This indicates that the model captures the proper trends in key prognostic variables while also producing realistic magnitudes in those same quantities. Thus, as suggested by this analysis, the Titan-GITM represents a viable predictive theoretical tool that can properly characterize the dynamical, compositional, and thermal structures in Titan's upper atmosphere.

5.6.3 T-GITM Structures for TA flyby: Temperatures, Densities, and Dynamics

In this section, the global and zonal averages of key prognostic fields from the Titan model are presented for conditions consistent with the TA flyby comparisons of the previous section. As found in the previous section, the T-GITM possesses a high correlation with the INMS measurements along with a consistently low NRMSE error. Taken together, they imply that the zonal average structures of this section should function as reasonable approximations to those in the real Titan atmosphere.



(a) Global average temperature for TA flyby



(b) Zonal average temperature structure for TA Flyby

Figure 5.17: T-GITM simulated thermal structure consistent with the TA flyby simulations. Panel (a) contains the global average temperature profile, while (b) contains the zonally averaged thermal structure.

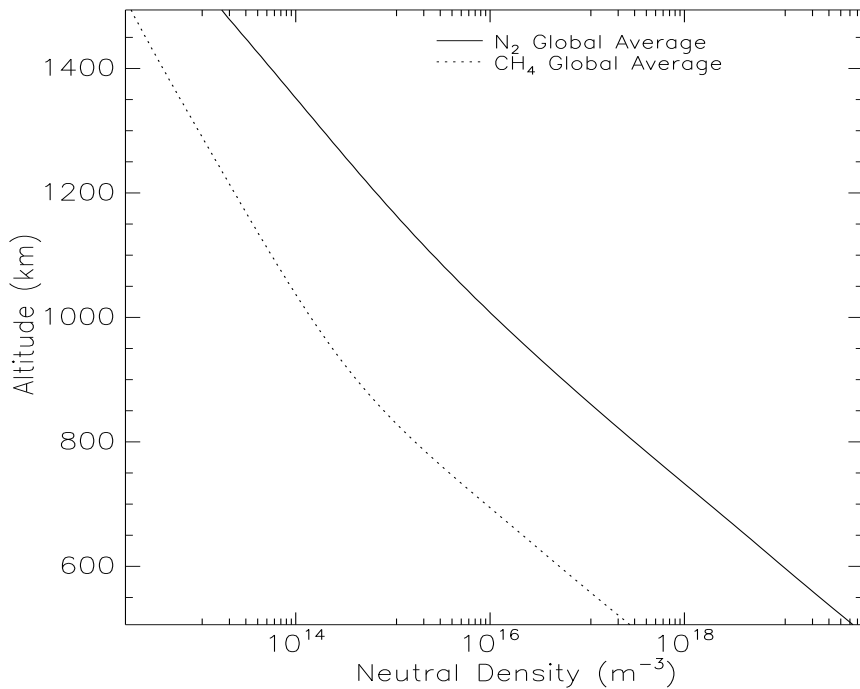


Figure 5.18: T-GITM global average neutral density profiles for both N_2 and CH_4 for the TA flyby Simulation.

Figures 5.17 - 5.23 contain these zonal average structures for the TA conditions.

Figure 5.17(a) contains the T-GITM global average temperature structure for the TA simulation. According to this figure, one may prefer to denote the upper atmosphere of Titan as a “cryosphere” rather than a thermosphere, due to its decrease in temperature with altitude. The thermal structure begins with the warmer 170 K lower boundary at 500 km and steadily decreases until reaching 900 km. At 900 km, the thermal structure exhibits a slow increase from 150 K to 153 K at 1100 km. Then, the temperature resumes its decline, reaching an exobase temperature of roughly 139 K at 1500 km.

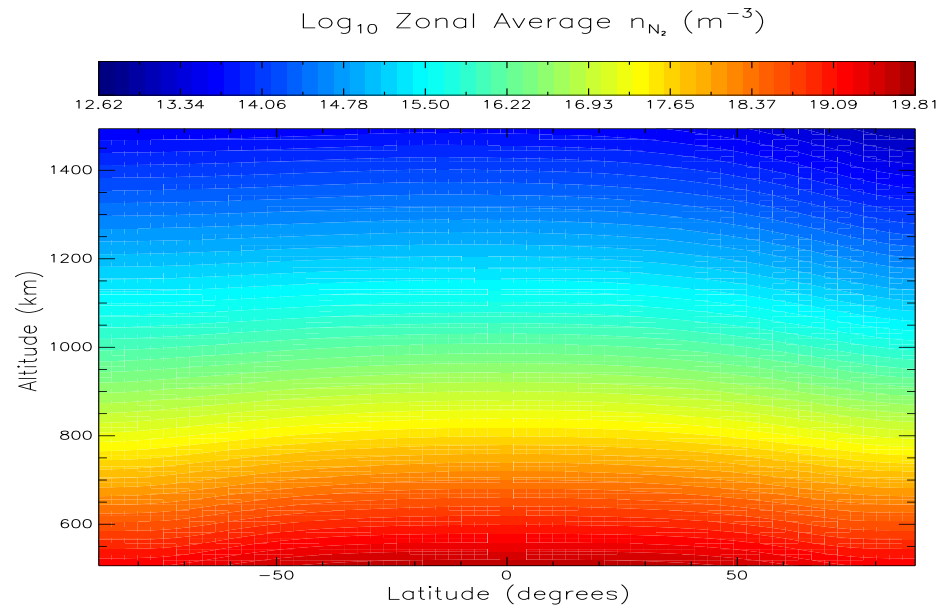
Figure 5.17(b) contains the T-GITM zonally averaged thermal structure for the TA flyby simulation. This figure shows a strong asymmetry between the summer

(southern) and winter (northern) hemispheres at most altitudes. In the south, the thermosphere retains warmer temperatures to higher altitudes. These warmer temperatures between 800 - 1200 km extend to mid and low latitudes in the southern summer hemisphere and extend northward to the low latitude regions of the winter hemisphere. However, at mid to high latitudes in the northern winter hemisphere, colder temperatures dominate. In fact, north of 75° the thermal structure above 700 km remains cold (140 K), isolated, and uniform. Thus, a strong temperature asymmetry exists in the T-GITM simulations for the TA flyby case and the remaining prognostic fields hint at the causes.

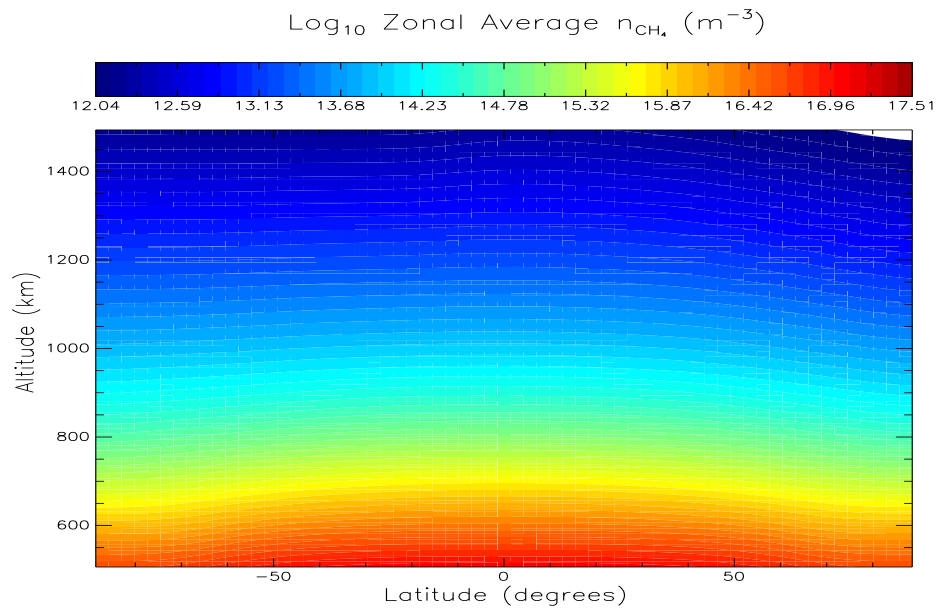
Figure 5.18 contains the Titan model's global average density structure for N_2 and CH_4 consistent with the global temperature structure of Figure 5.17(a). This figure illustrates the average behavior of the two major species as a function of altitude. By inspecting where the gradient of the CH_4 profile changes, one can ascertain the mean homopause altitude in T-GITM. From Figure 5.18, the globally averaged homopause level apparently occurs between 850 - 1000 km, which remains consistent with the approximate homopause level predicted by Figure 5.11.

Figures 5.19(a) and 5.19(b) contain the Titan-GITM's zonal average density structures for N_2 and CH_4 , respectively. These 2-D fields exhibit features similar to those found in Figure 5.17(b). In the southern hemisphere, the neutral densities for both major species remain enhanced, due primarily to atmospheric inflation resulting from the locally warmer thermospheric temperatures. In the northern hemisphere, these neutral densities decrease into the winter pole concomitantly with the decreasing temperatures at high latitudes. Thus, although no new structures emerge from these two plots, they do reinforce the asymmetric structure of Titan's upper atmosphere.

Figures 5.20(a) and 5.20(b) contain the T-GITM globally and zonally averaged

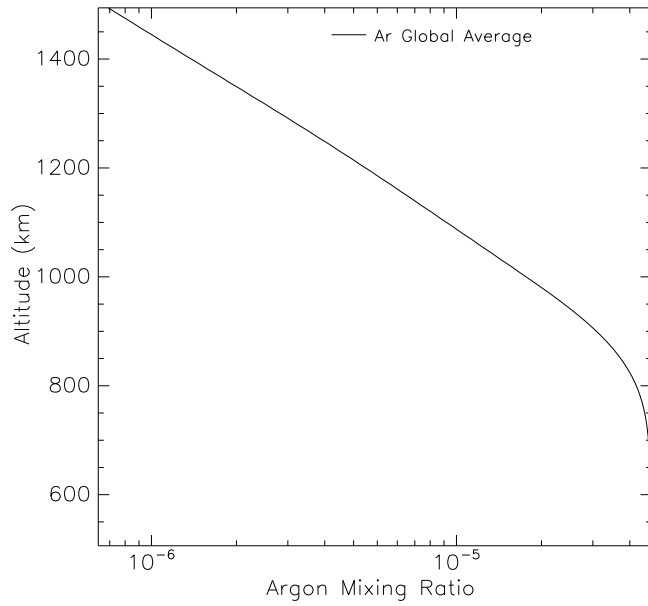


(a) T-GITM zonal average N_2 density structure for the TA flyby simulation.

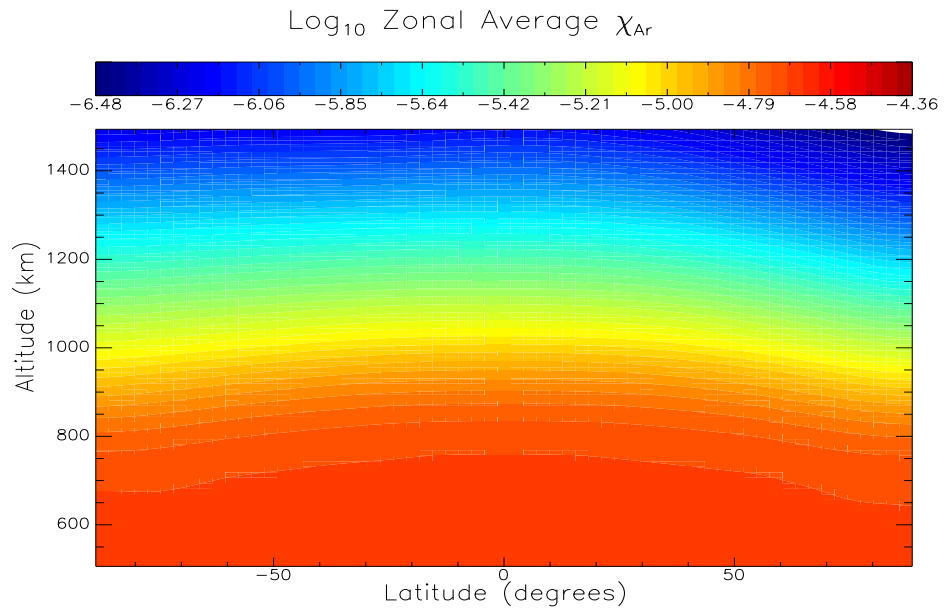


(b) T-GITM zonal average CH_4 density structure for the TA flyby simulation.

Figure 5.19: T-GITM simulated Log_{10} neutral densities.

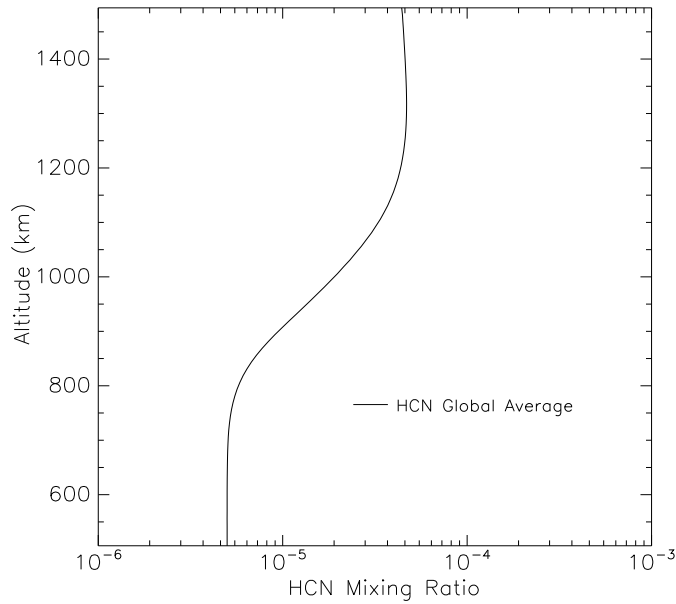


(a) Global average Argon mixing ratio for TA flyby

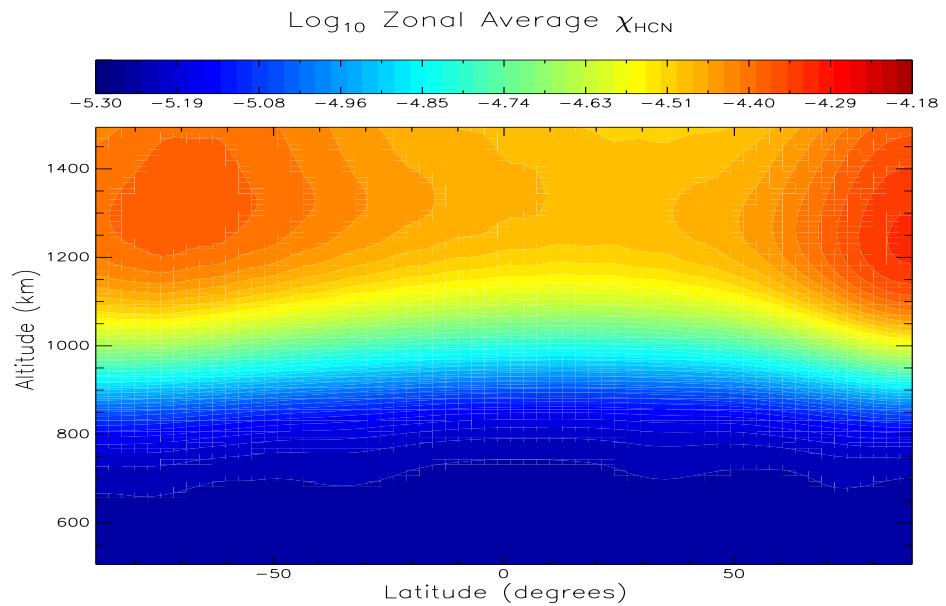


(b) Zonal average Argon mixing ratio for TA Fflyby

Figure 5.20: T-GITM simulated Argon mixing ratios consistent with the TA flyby simulations. Panel (a) contains the global average Ar mixing ratio, while (b) contains the zonally averaged Log_{10} mixing ratio structure.



(a) Global average HCN mixing ratio for TA flyby

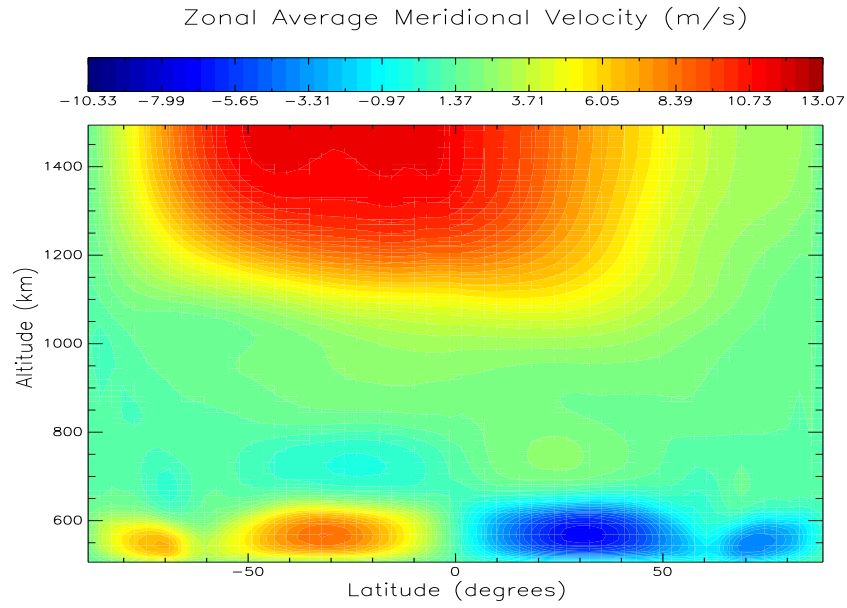


(b) Zonal average HCN mixing ratio for TA Fflyby

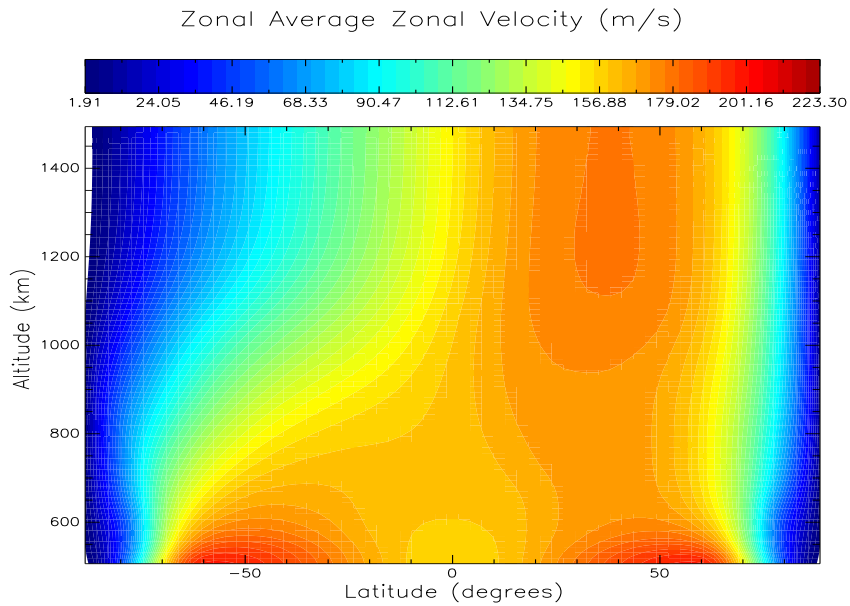
Figure 5.21: T-GITM simulated HCN mixing ratios consistent with the TA flyby simulations. Panel (a) contains the global average HCN mixing ratio, while (b) contains the zonally averaged \log_{10} mixing ratio structure.

^{40}Ar mixing ratio, respectively. In Figure 5.20(a), this species possesses a nearly constant mixing ratio of 4.32×10^{-5} between 500 and 650 km. Above 650 km, the mixing ratio begins to decline systematically to a value of roughly 7.0×10^{-7} at 1500 km. The dominant processes impacting the global structure of Argon are: vertical transport, turbulent diffusion, and molecular diffusive separation. Thus, the global average behavior of Argon represents an ideal constraint to the interplay between eddy diffusion and molecular diffusion in the Titan model. Figure 5.20(b) exhibits the asymmetric behavior found in the previous zonal average fields. This figure shows that, at a given altitude, there is an enhancement of Argon mixing ratios in the southern summer hemisphere with a concomitant reduction in the mixing ratios at high latitudes in the northern winter hemisphere.

Figures 5.21(a) and 5.21(b) contain the Titan model's HCN mixing ratio in analogy with Figures 5.20(a) and 5.20(b) for Argon. As shown in Figure 5.21(a), HCN represents a species dominated by chemical processes, where photochemical production peaks between 1000 - 1300 km. This results in a build up HCN at high altitudes, producing the higher global average mixing ratio in this region. After photochemical production HCN then gets transported downward and eventually through the model's lower boundary at 500 km. The combination of photochemistry and transport results in the mixing ratio structure shown in Figure 5.21(a). In Figure 5.21(b), this species again defies the general trends found before. The HCN mixing ratio peaks at high altitudes in the southern summer hemisphere, due to the enhanced photochemical production in the subsolar latitudes. However, a secondary peak occurs in the winter polar region. Evidently, horizontal winds transport HCN into the northern winter pole, where chemical loss processes are reduced by the lower temperatures and downward transport is similarly inhibited by the vertical temperature structure



(a) T-GITM zonally averaged meridional velocities (positive is northward).



(b) T-GITM zonally averaged zonal velocities (positive is eastward).

Figure 5.22: T-GITM simulated meridional, panel (a), and zonal, panel (b), bulk velocity components in (m/s).

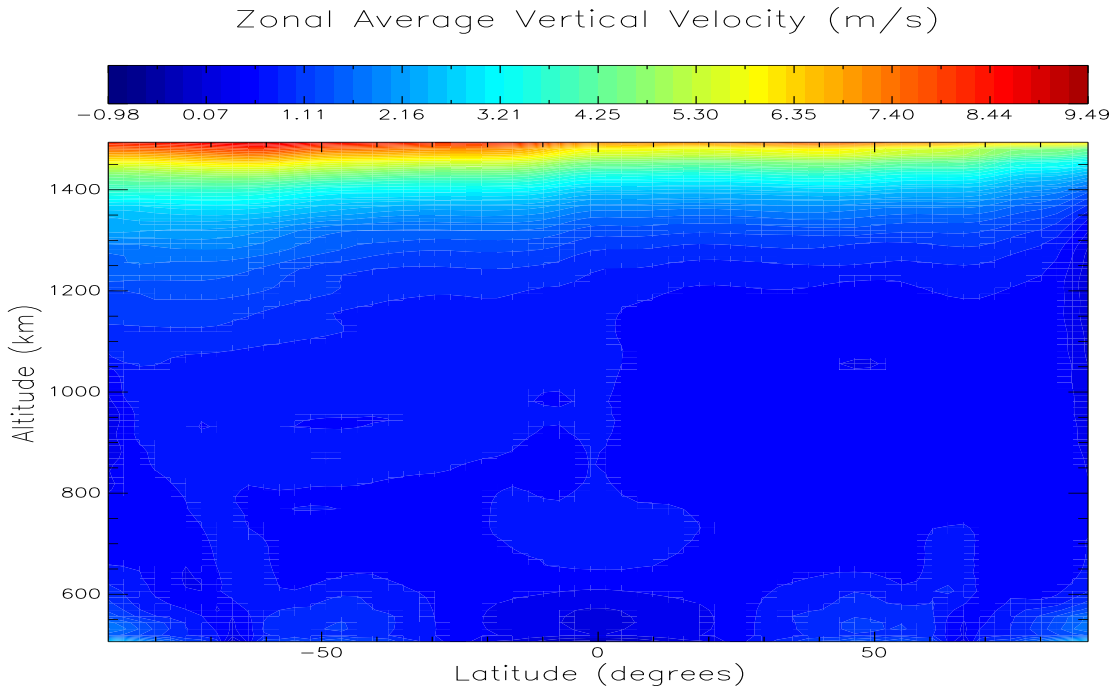


Figure 5.23: T-GITM global average values for u_r , the bulk radial velocity (m/s) for the TA flyby simulation conditions.

at these latitudes. Thus, HCN tends to collect in this winter polar region, most likely contributing to even lower polar temperatures through an enhanced radiative cooling.

Figures 5.22(a), 5.22(b), and 5.23 contain the T-GITM's bulk velocity components consistent with the TA flyby conditions. Figure 5.22(a) seems to suggest that the T-GITM possesses weak overall transport in the north-south direction. However, when applying the zonal average to meridional velocities, typically cells of opposite direction will additively cancel one another out. Thus, this figure represents a potentially muted representation of the meridional circulation. Despite this drawback, organized meridional circulation cells do emerge. At the lower boundary, Hadley circulation cells appear prominently, which most likely result from T-GITM producing

a self-consistent solution to the imposed lower boundary zonal winds at 500 km. A cursory examination of Figure 5.22(b) shows that changes in this Hadley circulation correlate with the peaks of the zonal winds. Near the exobase, a large organized response of the thermosphere transports material from the southern hemisphere to the northern hemisphere, in analogy to similar circulations found in the upper reaches of Mars [Bell *et al.*, 2007]. However, this circulation weakens upon encountering the strong high-latitude zonal jets in the northern hemisphere of Figure 5.22(b).

Figure 5.22(b) contains perhaps one of the most important prognostic fields of T-GITM for this simulation – the zonally average zonal winds. This structure represents a critical factor in determining the simulation’s thermal and dynamical structure. The T-GITM zonal winds develop a pronounced asymmetry at mid-to-high altitudes, possessing a very strong zonal flow in the winter hemisphere with a concomitantly weaker zonal flow in the southern hemisphere. This strong polar jet isolates the northern winter pole, resulting in the very cold, isolated polar temperatures of Figure 5.17(b). This then feeds back into the resulting neutral densities and the overall structure of Titan’s upper atmosphere. Interestingly, this asymmetric zonal wind structure appears consistent with similar findings in the lower atmosphere of Titan, as discussed by Achterberg *et al.* [2008]. Furthermore, the calculated T-GITM zonal wind structure, in combination with the recent findings of Achterberg *et al.* [2008], suggest that the symmetrically imposed zonal winds at the lower boundary of the model may in fact represent an inconsistency with the real Titan atmosphere. This discovery merits further consideration as part of future theoretical research.

However, a conundrum emerges in causal effects: do the zonal winds determine the temperature structure, or does the asymmetric temperature structure determine the zonal winds? A possible explanation emerges when one considers viscosity. Higher

temperatures would result in a higher viscous interaction by raising the dynamic viscosity coefficient (see equations 3.70 and 3.71). This higher viscosity should subsequently result in higher zonal winds, through a higher viscous shear stress that would impart more zonal momentum. However, the opposite trend is found. This implies that the zonal wind structure is not dominated by the simple interplay between temperature and viscosity. This leads one to posit that, instead, the opposite causal relation exists in Titan’s upper atmosphere: the zonal winds instead define the temperature structure and the resulting density structures. Note how the warm southern polar temperatures in Figure 5.17(b) extend northward at altitudes where the zonal jets are simultaneously reduced in the summer hemisphere. This combined with the cold, isolated northern polar temperature structure strongly suggests that the zonal wind structure is dominating the thermal and density structures of Titan’s upper atmosphere.

Finally, Figure 5.23 contains the bulk radial velocity for Titan. As for the meridional velocity, this field possesses muted variations, owing to the process of zonal averaging. However, at 1500 km, the velocities show a definite organized outward flow. This outflow of material from the model’s highest altitude plays a large role in determining the thermal structure at these altitudes. As will be seen in the next section, the vertical transport in Titan’s atmosphere can greatly impact the vertical energy balance in this moon’s upper atmosphere.

5.6.4 Energy Balance Terms for the TA Simulation

The TA flyby density, temperature, and wind structures of the last two sections function to describe the physical state of Titan’s upper atmosphere. In this section, the fundamental energy balance terms are quantified, further illustrating the physical processes dominating this moon’s thermosphere-ionosphere system. Figure 5.24

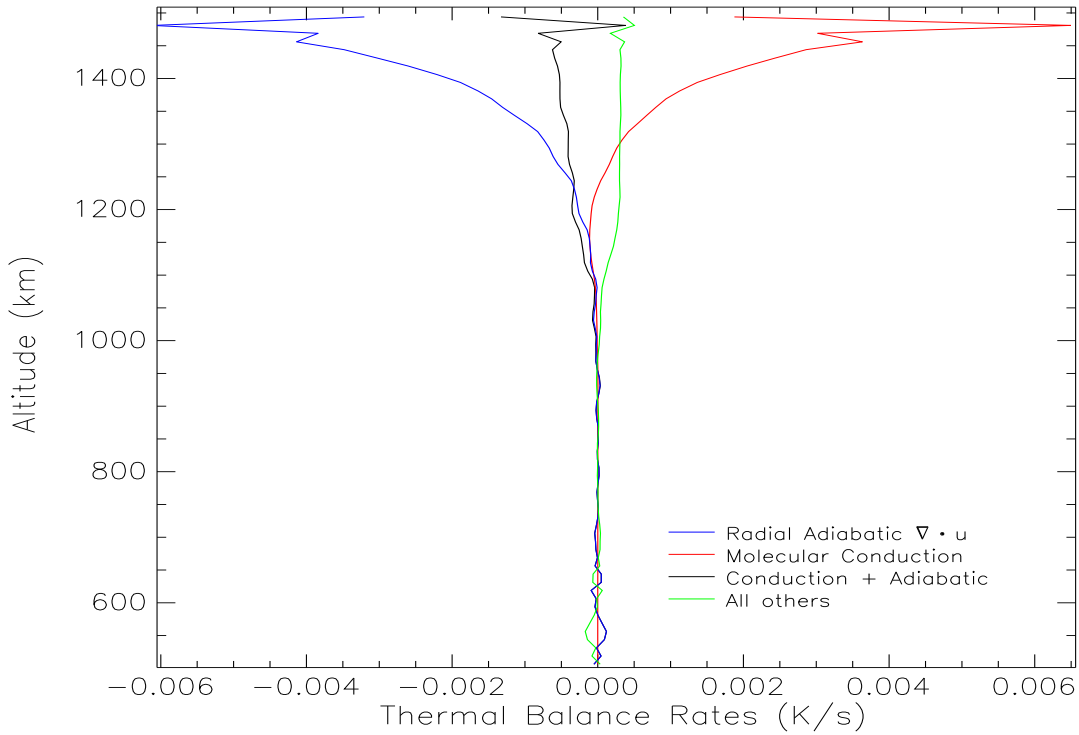
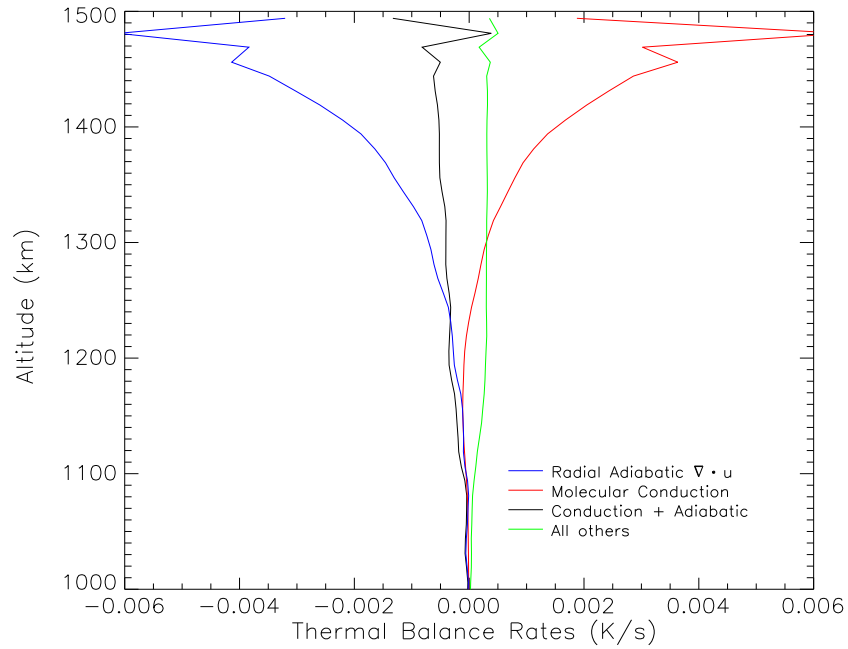


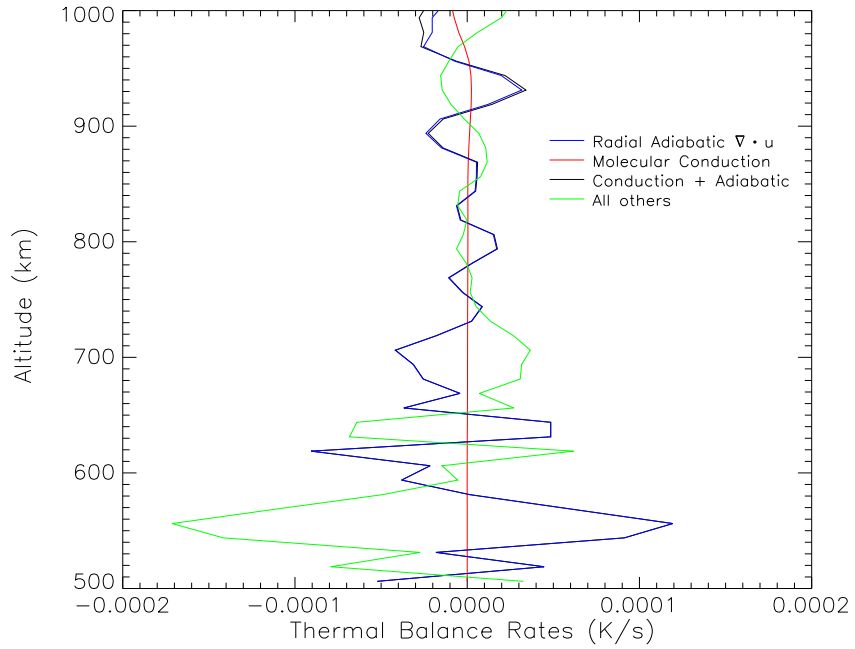
Figure 5.24: T-GITM global average balance terms. Here, the vertical adiabatic term, $\nabla \cdot \mathbf{u}_r$, (blue line) and the molecular conduction term (red line) dominate the overall energy balance in the model. Their sum is shown in black on the same plot. All other contributions have been summed and are shown as the green line.

contains the Titan model's globally averaged energy balance rates (K/s) between 500 and 1500 km. As shown in this figure, three primary source terms dominate the energy balance: (1) vertical adiabatic heating and cooling ($\nabla \cdot \mathbf{u}_r$) shown as the blue line, (2) molecular thermal conduction shown as the red line, and (3) the sum over all other source terms shown as the green line. In particular the vertical adiabatic and molecular conduction energy source terms appear to dominate at altitudes above 1000 km, causing the energy balance between 500 to 1000 km to be “washed out.”

Figure 5.25 breaks down Figure 5.24 into two regimes: altitudes below 1000 km and altitudes above 1000 km. Through these two plots, the energy balances become more easily discerned. Between 500 and 1000 km, molecular conduction (the red



(a) T-GITM global average thermal balance (1000 - 1500 km).



(b) T-GITM global average thermal balance (500 - 1000 km).

Figure 5.25: A split of Figure 5.24 into two subplots with different ranges: (a) the global average energy balance between 1000 - 1500 km and (b) the global average energy balance between 500 - 1000 km. Note how the vertical adiabatic term, $\nabla \cdot \mathbf{u}_r$, balances sources and sinks of energy in the upper and lower regions of T-GITM. This mechanism does not exist in other 3-D modeling frameworks.

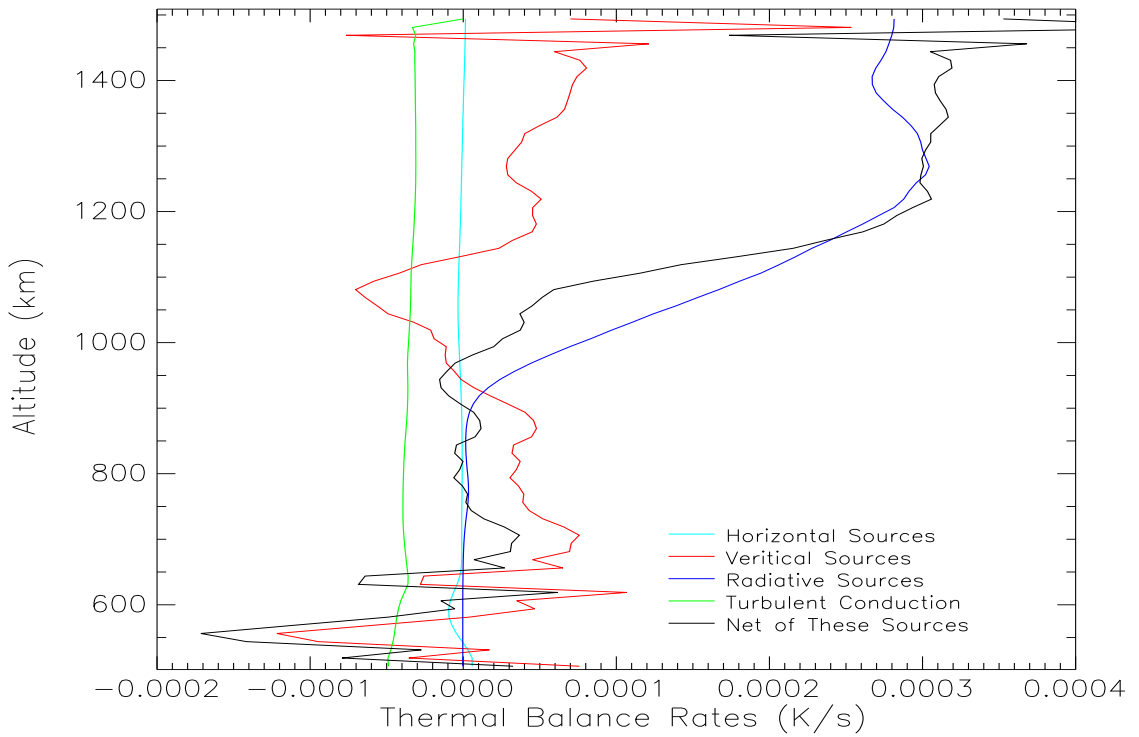
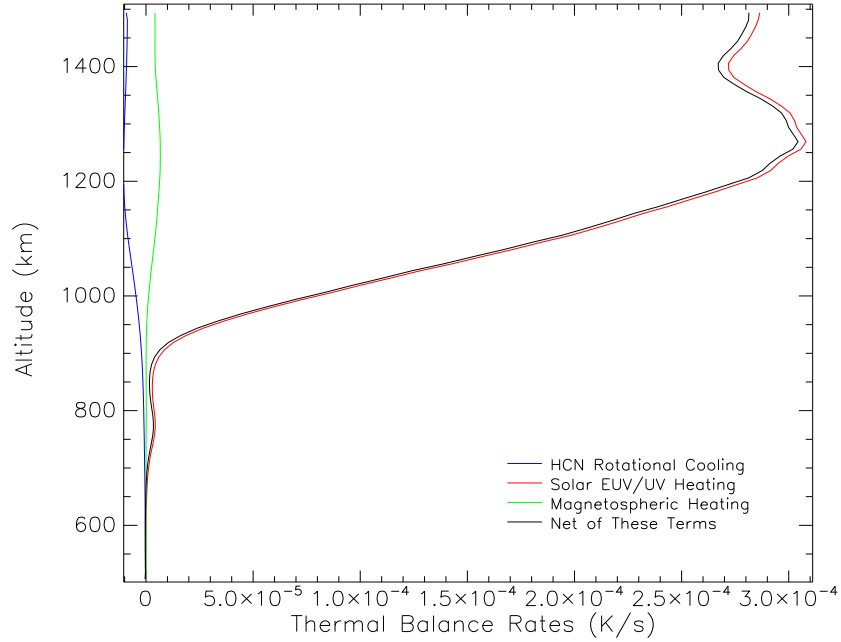


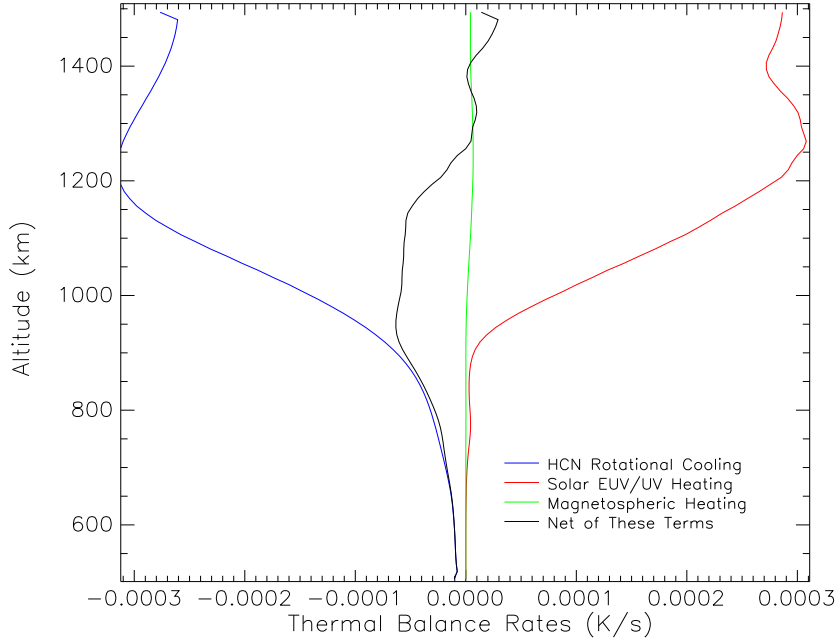
Figure 5.26: T-GITM global average balance terms. Here, the contributions all terms other than that of vertical adiabatic cooling and molecular conduction are shown. This plot effectively illustrates the first order energy balance terms of T-GITM, which are dominated by the radiative balance terms.

line) does not play a major role in the energy balance, except near 1000 km where it begins to cool the atmosphere. Over this altitude range, however, the vertical adiabatic cooling term (blue line) closely balances the sum of all other energy terms (green line). Thus, vertical transport functions to balance all other energy source terms in T-GITM's lowest altitudes. In other modeling frameworks, however, this critical energy balance mechanism does not exist.

At higher altitudes, between 1000 - 1500 km, both vertical adiabatic cooling and molecular conduction heating roughly balance one another. The difference between these two source terms is shown as the black line in the same plot. The sum of all other energy balance terms (green line) also plays an important role at these



(a) Radiative energy balance plot in T-GITM for TA.



(b) Hypothetical radiative energy balance plot, if HCN possessed a higher mixing ratio at 1100km.

Figure 5.27: A breakdown of the major radiative sources for Titan's atmosphere from Figure 5.26. Panel (a) contains the global average energy balance between HCN rotational cooling (blue), Solar EUV/UV heating (red line), and the net heating rate (black line). This is the radiative balance for the TA simulations of this section. Panel (b) illustrates a hypothetical cooling rate, if HCN were to possess a mixing ratio of 10^{-4} at 1100 km. The actual resulting radiative balance could differ from this plot significantly, however, this hypothetical case illustrates the sensitivity of T-GITM to HCN's abundance in the atmosphere.

altitudes. In order to better understand the energetics of Titan’s upper atmosphere, the sum of all other energy contributions should now be separately examined.

Figure 5.26 breaks down the green line in Figure 5.25 into its constituent components. In this Figure, the energy balance is clearly dominated by the radiative forcing terms (blue line), which represents the difference between solar EUV/UV heating and HCN rotational cooling. Horizontal sources (cyan line) do not play a major role in the global average energy balance, but the averaging process itself most likely eliminates local structures that might otherwise exist. The vertical advection sources (red line) also play a large role in the atmospheric energy balance, which do not exist in other modeling frameworks. Finally, the turbulent energy cooling rates (green line) play a significant but secondary role in the atmosphere’s energy balance.

Figure 5.27 breaks down the radiative forcing terms into HCN cooling rates and Solar EUV/UV heating rates. Most importantly on this plot note that the HCN rotational cooling plays an almost negligible role in the overall energy balance in the upper atmosphere in Figure 5.27(a). This most likely indicates that the HCN mixing ratio in the upper atmosphere, shown in Figure 5.21(a), is not correct. This issue is dealt with later in the thesis. However, if one adopts an HCN mixing ratio matching indirect estimates of *Vuitton et al.* [2006], then the energy balance of Figure 5.27(b) occurs. Interestingly enough, the model is still capable of balancing solar inputs through vertical adiabatic cooling without significant radiative cooling.

Ultimately, the most salient point of this section is that vertical transport plays a critical role in the energetics of Titan’s upper atmosphere. Furthermore, this processes is missing from other 3-D modeling frameworks. In later sections, a suggested modification of the HCN mixing ratio is utilized in order to produce an energy balance more akin to that of Figure 5.27(b).

5.7 Solar Cycle Variations and T-GITM

This section discusses how the Titan-GITM responds to changes in the Sun's EUV/UV fluxes over the course of the solar cycle. For the purposes of this study, the orbital position (season) is held constant in order to isolate the impacts of solar cycle impacts. Furthermore, all boundary conditions for this study are held steady. Figures 5.28 - 5.33 contain selected results from this study. Also, an emphasis is placed upon the thermal structure both globally and zonally averaged. The $F_{10.7-cm}$ is used as a proxy for solar flux variations, varying this index from $F_{10.7-cm} = 80$ for solar minimum, 130 for solar moderate, and 200 for solar maximum.

Figure 5.28(a) illustrates how the global average temperatures vary over the solar cycle. As the solar fluxes increase from solar minimum to solar maximum, the exobase temperatures (1500 km) rise from 134 K to 142 K. The global average homopause temperatures (850 km) rise from 140 K to 165 K. Figures 5.28(b) through 5.28(d) illustrate the diurnal variations for each solar cycle case. At solar minimum, the max-to-min variation in the exobase temperatures is 10K. Meanwhile the same metric at solar moderate and solar maximum is 12 K and 19 K, respectively. At the homopause (850 km) the same min-to-max temperature variation is: 12 K at solar minimum, 16 K at solar moderate, and 20 K at solar maximum. Table 5.4 contains a summary of these results, illustrating that both higher altitudes and the lower altitudes of T-GITM exhibit a similar diurnal variation. This differs from the previous 3-D modeling efforts of *Müller-Wodarg et al.* [2000] that showed very muted diurnal variations in the lowest altitudes of 600 - 1000 km.

Figure 5.29 contains Titan model's global averaged profiles for the N_2 and CH_4 neutral density, the Argon mixing ratio, and the HCN mixing ratio responding to the

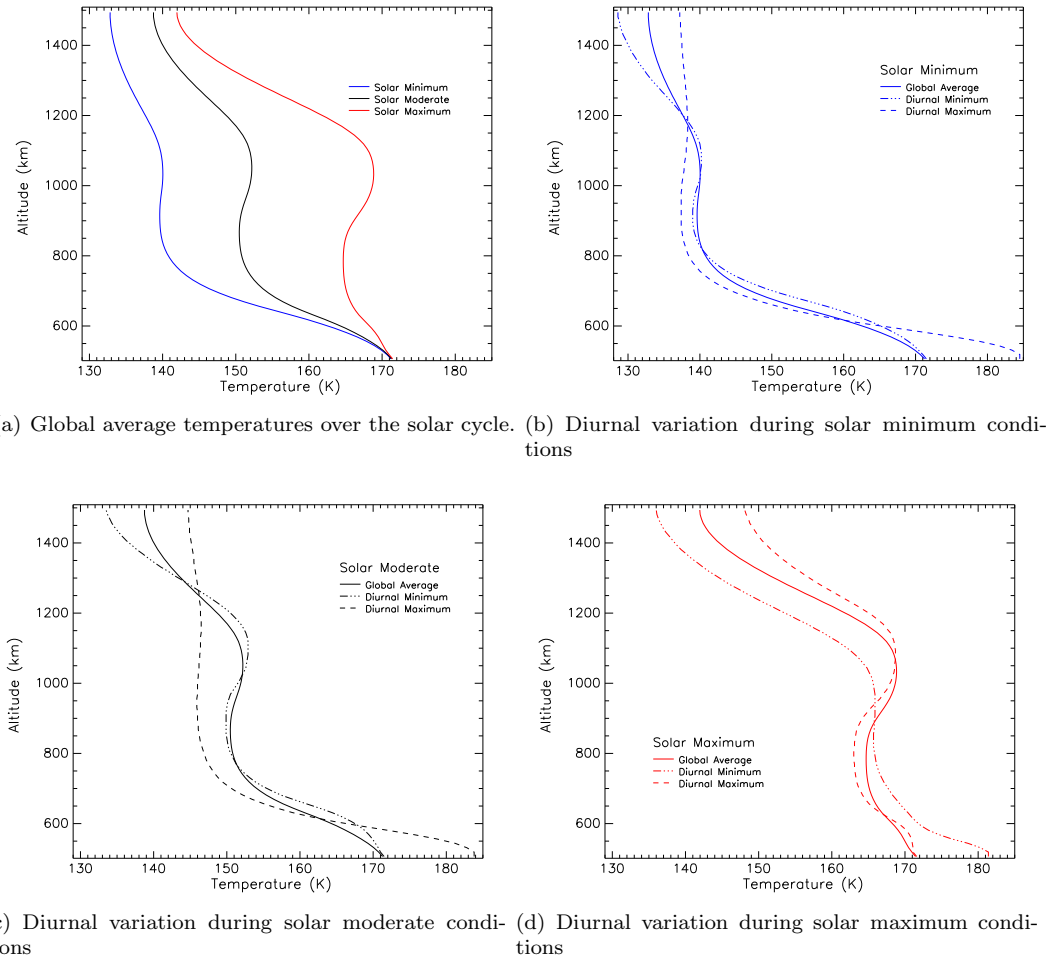


Figure 5.28: Temperatures variations over the Solar Cycle. Global average temperature variations for solar minimum, moderate, and maximum are shown in panel (a). Meanwhile, panels (b) - (d) contain the maximum diurnal variations to be found in the atmosphere at each of these solar conditions.

three solar cycle levels. Figure 5.29(a) shows that the N_2 and CH_4 densities exhibit a variation with solar output commensurate with that of the temperatures. As the temperatures increase in going from solar minimum to solar maximum, the major neutral density profiles inflate due to concomitantly larger scale heights, resulting in larger overall densities at higher solar activity. The Argon mixing ratio, however, does not follow this exact trend, except at the highest altitudes. Instead, Argon remains sensitive to local dynamical and diffusive transport, causing it to depart from the same trend exhibited by the N_2 and CH_4 densities. Likewise, the HCN

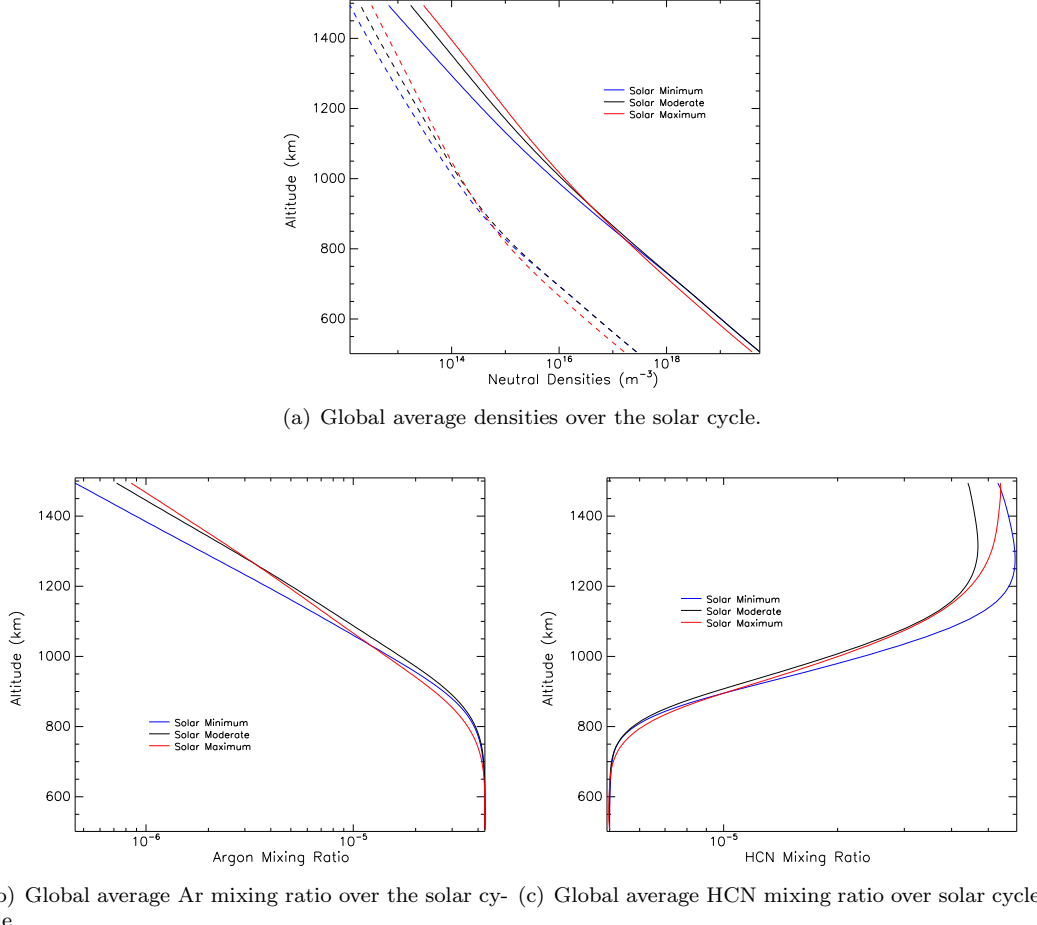
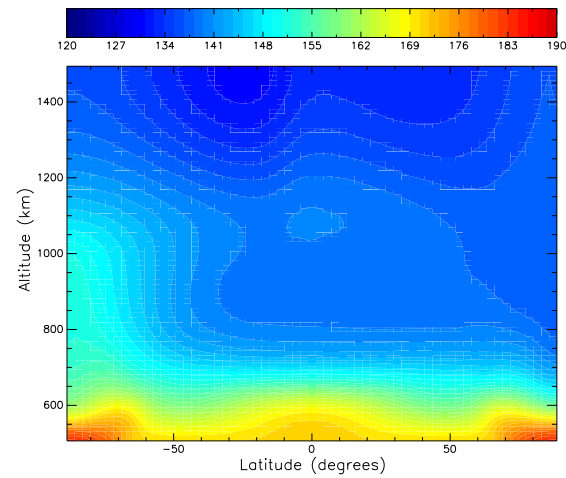


Figure 5.29: The response of T-GITM's key constituents over the solar cycle.

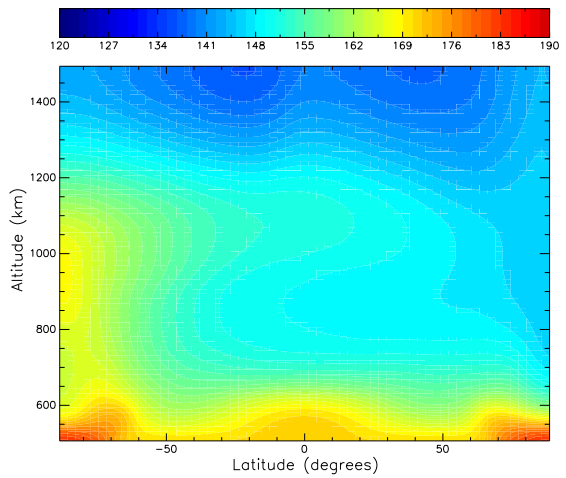
mixing ratio, which represents an interplay between photochemical production at high altitudes and downward transport at the lowest altitudes, also shows a less systematic variation with solar cycle. In fact, the HCN mixing ratios between the three cases exhibit a range-bound peak mixing ratio of $4 - 6 \times 10^{-5}$.

[p]

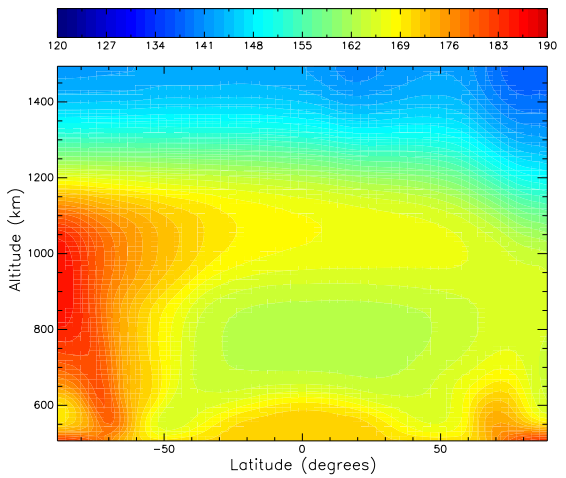
Figures 5.30 - 5.33 contain the Titan model's zonal average response to solar flux variations for key prognostic fields. Figures 5.30(a) - 5.30(c) contain the zonal average temperature structure for solar minimum, moderate, and maximum conditions. The asymmetry structure noted before occurs again here, however, as solar fluxes increase from minimum to maximum, the southern polar temperatures increase sys-



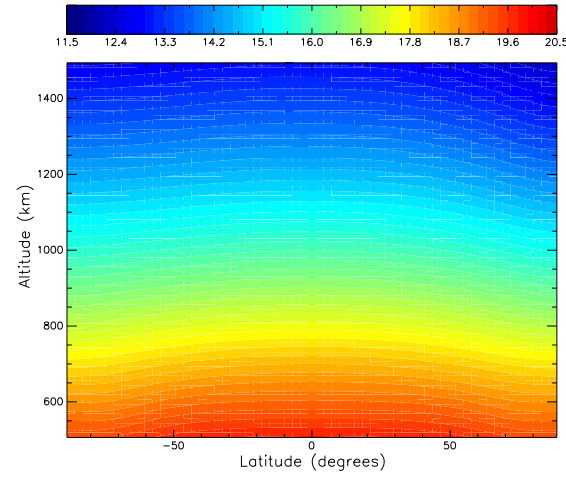
(a) Zonal average temperatures at solar minimum.



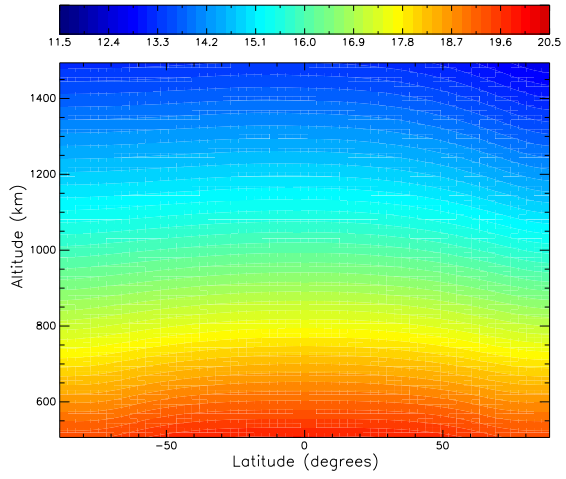
(b) Zonal average temperatures at solar moderate.



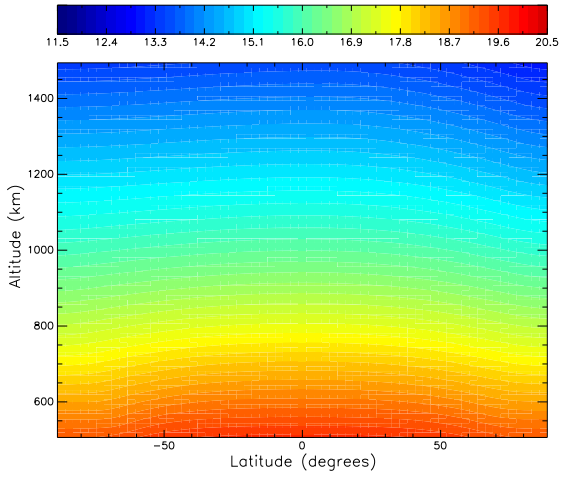
(c) Zonal average temperatures at solar maximum.



(d) Zonal average $\log_{10} N_2$ densities at solar minimum.

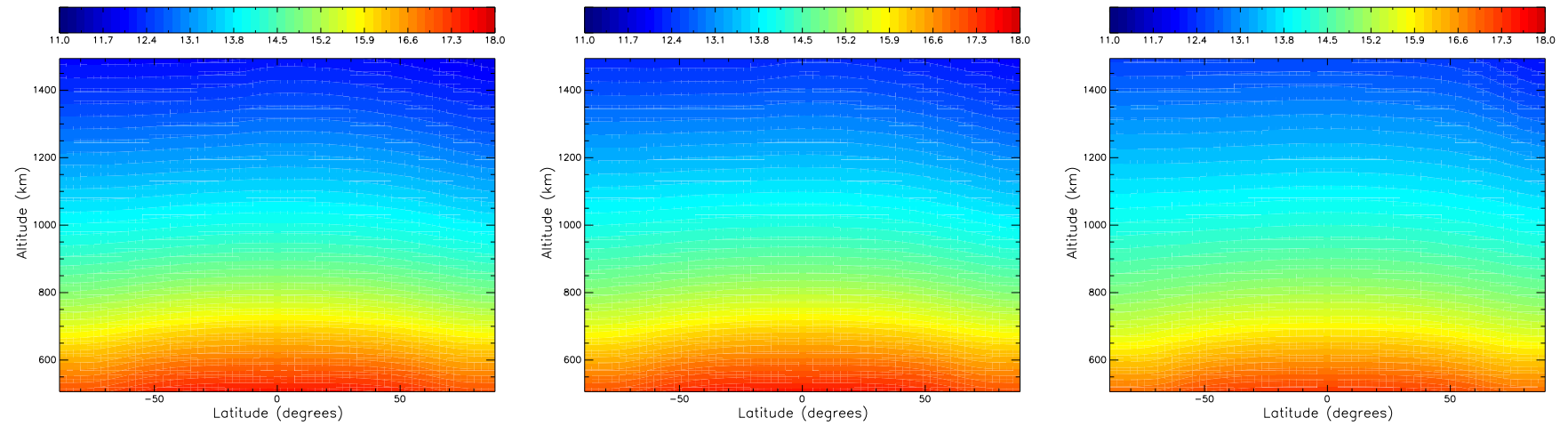


(e) Zonal average $\log_{10} N_2$ densities at solar moderate.



(f) Zonal average $\log_{10} N_2$ densities at solar maximum.

Figure 5.30: Zonal average temperatures, panels (a) - (c), and $\log_{10} N_2$ densities, panels (d) - (f) for solar minimum, moderate, and maximum conditions.



(a) Zonal average \log_{10} CH₄ densities at solar minimum. (b) Zonal average \log_{10} CH₄ densities at solar moderate. (c) Zonal average \log_{10} CH₄ densities at solar maximum.

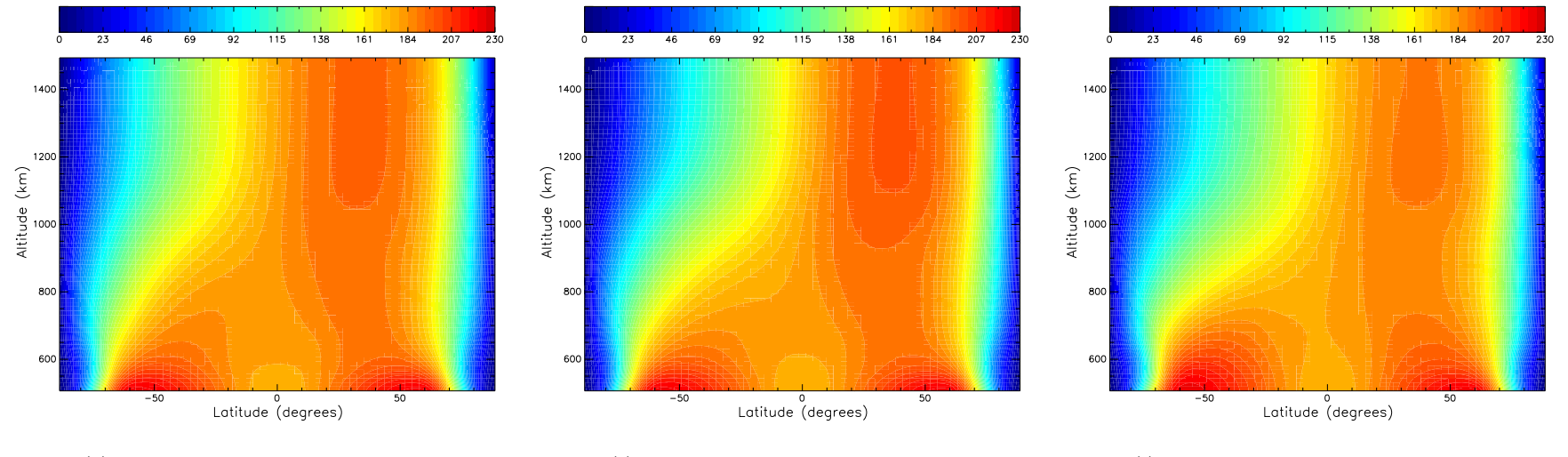


Figure 5.31: Zonal average \log_{10} CH₄ densities, panels (a) - (c), and \mathbf{u}_ϕ , panels (d) - (f), for solar minimum, moderate, and maximum conditions.

Table 5.4: Temperatures at the Exobase (1500 km) over the Solar Cycle

Solar Cycle	T_{MIN} (K)	T_{MAX} (K)	Global Average Temperature (K)	Maximum ΔT
Solar Minimum	128	138	134	10
Solar Moderate	133	145	139	12
Solar Maximum	130	149	142	19

Table 5.5: Temperatures at the Homopause (850 km) over the Solar Cycle

Solar Cycle	T_{MIN} (K)	T_{MAX} (K)	Global Average Temperature (K)	Maximum ΔT
Solar Minimum	136	148	140	12
Solar Moderate	142	168	151	16
Solar Maximum	160	180	165	20

tematically. The northern pole also seems to systematically warm with increasing solar activity. Table 5.6 contains temperature values at 90^0S , 0^0N , and 90^0N over the solar cycle and at three key altitudes: 600 km, 1000 km, and 1400 km. This table shows that, in general, between 600 km and 1000 km, temperatures typically cool from the equator into the norther polar region. At 1000 km, the southern polar region appears much warmer at all solar cycle levels than the equatorial values. However, at 1400 km altitude, the temperature structure is heavily influenced by adiabatic cooling by CH_4 . Thus, these altitudes do not exhibit the zonal structure seen at 600 km or 1000 km.

The T-GITM $\log_{10} N_2$ and CH_4 zonal average neutral densities, found in Figures 5.30(d) through 5.30(f) and Figures 5.31(a) through 5.31(c), parallel the trend found in the zonal average temperatures over the solar cycle. Additionally, Tables 5.7 and 5.8 contain the Titan model's \log_{10} neutral densities for N_2 and CH_4 , respectively, in a manner similar to Table 5.6. First, in general, the neutral densities at a given altitude increase with solar activity, responding to the increasing temperatures and related scale heights. At solar minimum, moderate, and maximum activity levels,

Solar Activity	90°S	0°N	90°N
600 km Altitude			
Minimum	160 (K)	166 (K)	155 (K)
Moderate	165 (K)	167 (K)	157 (K)
Maximum	170 (K)	169 (K)	165 (K)
1000 km Altitude			
Minimum	151 (K)	139 (K)	137 (K)
Moderate	167 (K)	151 (K)	146 (K)
Maximum	185 (K)	167 (K)	163 (K)
1400 km Altitude			
Minimum	137 (K)	134 (K)	137 (K)
Moderate	144 (K)	141 (K)	144 (K)
Maximum	145 (K)	145 (K)	138 (K)

Table 5.6: Zonal average variations in T-GITM temperatures for solar minimum, solar moderate, and solar maximum conditions at three key altitudes and three key latitudes.

the densities show a sharp decrease with latitude, moving from low and mid-latitudes into the northern winter pole. Concomitantly, these neutral densities possess a much shallower drop into the southern polar region. At solar maximum, this trend is repeated, but with shallower gradients into the northern winter pole. This trend in the densities parallels that in the thermal structures. Ultimately, the neutral densities over the solar cycle increase with solar activity, however the overall structure of the atmosphere does not significantly change.

The Titan model's zonally averaged bulk winds occur in Figures 5.31(d) through 5.32(f). The zonal averaged eastward winds, shown in Figures 5.31(d) through 5.31(f) again show a strongly asymmetric structure and function to isolate the northern winter polar hemisphere. However, with increasing solar activity, this mechanism apparently becomes less and less effective, as evinced by the increasingly shallower temperature gradients from low latitudes into the winter pole during solar maximum conditions.

T-GITM's zonal averaged meridional flows in Figures 5.32(a) - 5.35(c) also show solar cycle variability. However, the variations in this quantity are most likely artifi-

Solar Activity	90°S	0°N	90°N
600 km Altitude ($\times 10^{18} \text{ m}^{-3}$)			
Minimum	4.35	10.99	4.429
Moderate	4.28	10.96	4.395
Maximum	4.06	10.99	4.168
1000 km Altitude ($\times 10^{15} \text{ m}^{-3}$)			
Minimum	4.43	8.88	2.49
Moderate	7.00	12.33	3.41
Maximum	7.77	13.72	4.90
1400 km Altitude ($\times 10^{13} \text{ m}^{-3}$)			
Minimum	1.67	2.60	0.60
Moderate	4.90	5.96	1.26
Maximum	7.36	10.24	3.09

Table 5.7: Zonal average variations in T-GITM N₂ densities for solar minimum, solar moderate, and solar maximum conditions at three key altitudes and three key latitudes.

Solar Activity	90°S	0°N	90°N
600 km Altitude ($\times 10^{16} \text{ m}^{-3}$)			
Minimum	2.23	5.51	2.27
Moderate	2.19	5.50	2.25
Maximum	2.09	5.51	2.24
1000 km Altitude ($\times 10^{13} \text{ m}^{-3}$)			
Minimum	8.53	12.00	6.09
Moderate	11.24	14.93	7.35
Maximum	12.14	15.78	8.88
1400 km Altitude ($\times 10^{12} \text{ m}^{-3}$)			
Minimum	2.33	3.06	1.53
Moderate	4.00	4.96	2.13
Maximum	6.23	6.96	2.73

Table 5.8: Zonal average variations in T-GITM CH₄ densities for solar minimum, solar moderate, and solar maximum conditions at three key altitudes and three key latitudes.

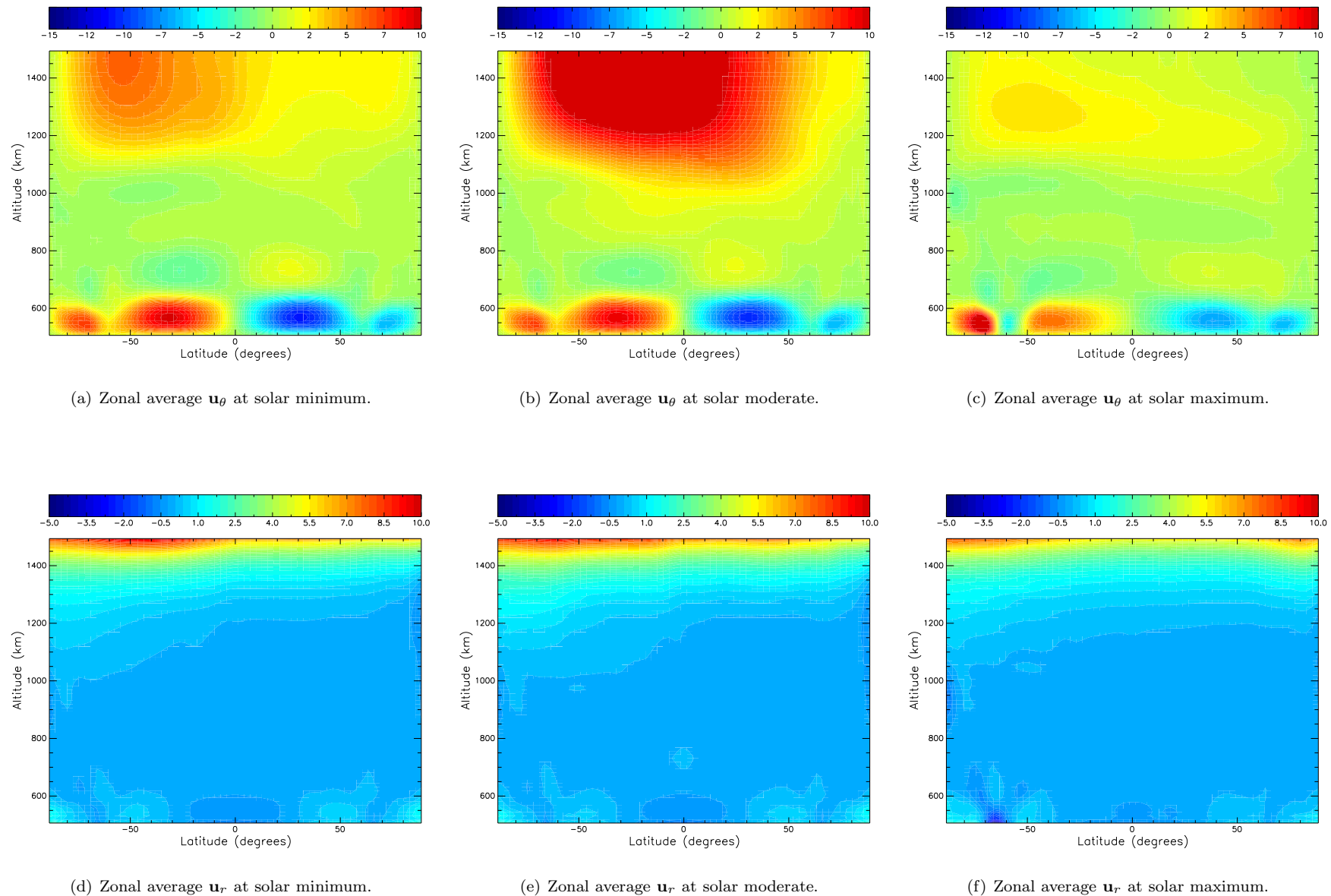
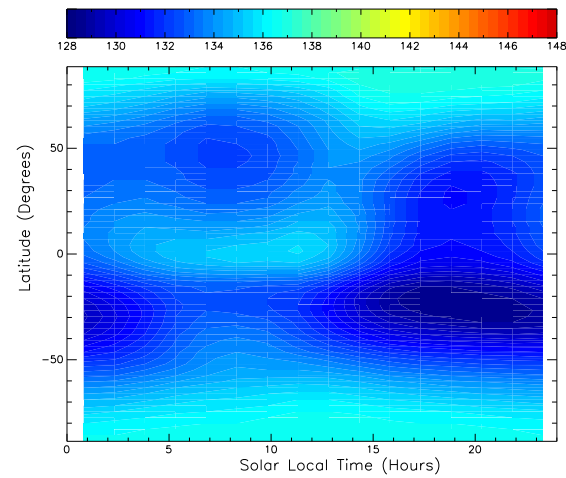
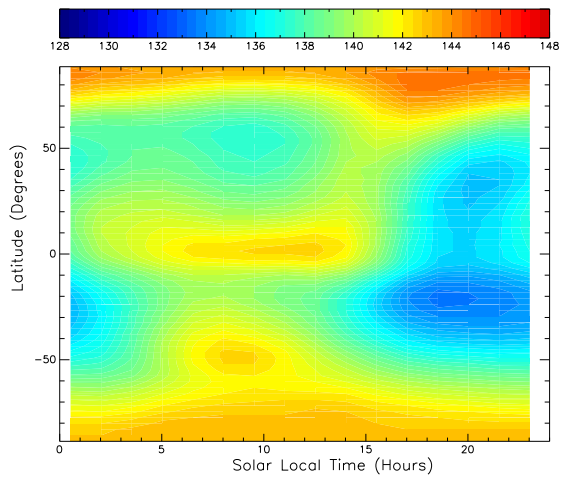


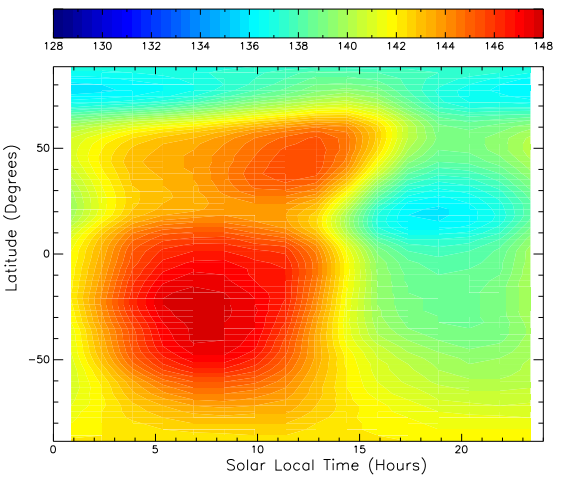
Figure 5.32: Zonal average u_θ velocities, panels (a) - (c), and u_r , panels (d) - (f), for solar minimum, moderate, and maximum conditions.



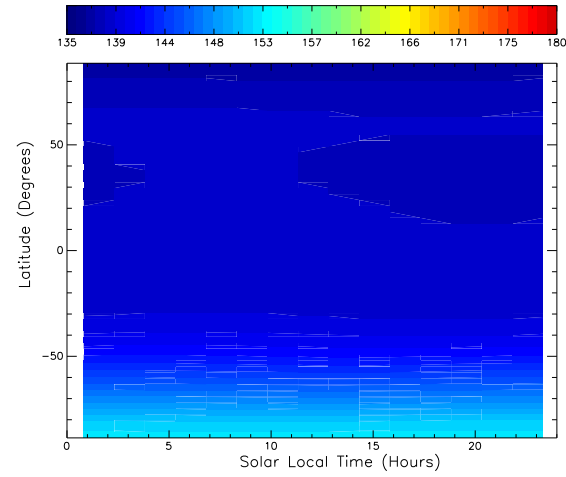
(a) Solar Minimum Exobase Temperatures.



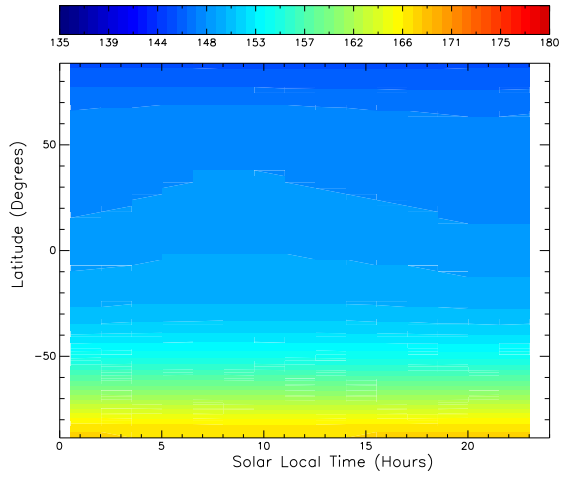
(b) Solar Moderate Exobase Temperatures.



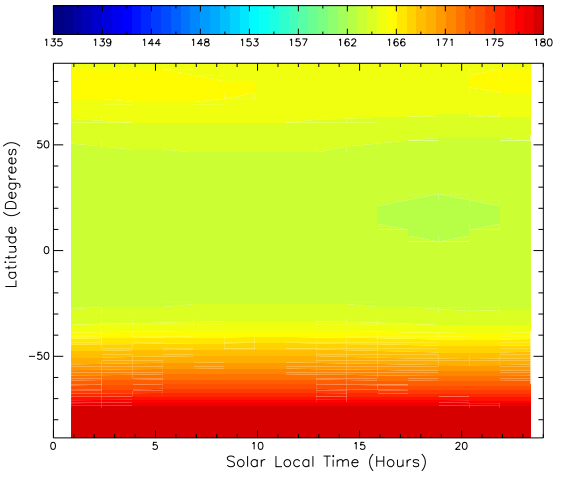
(c) Solar Maximum Exobase Temperatures.



(d) Solar Minimum Homopause Temperatures.



(e) Solar Moderate Homopause Temperatures.



(f) Solar Maximum Homopause Temperatures.

Figure 5.33: Constant altitude plots of temperatures at the exobase, panels (a) - (c), and the homopause, panels (d) - (f), for solar minimum, moderate, and maximum conditions.

cially depressed due to the averaging process and so result in the relatively shallow variations depicted in these figures. Despite this, organized cells do occur, especially in the lower altitudes where the Hadley circulation cells form in response to the strong zonal flows at the lower boundary. In the upper altitudes, some variation with solar activity does occur. However, solar moderate possesses the strongest summer -to-winter meridional circulation of 10 m/s, while the circulation at solar minimum and maximum are relegated to flows at 5 m/s and 2 m/s. This apparent trend could be the result of the decreasing summer-to-winter meridional temperature gradient with solar activity. However, ultimately, these values should be treated skeptically, as the zonal averaging process certainly integrates out a significant amount of structure.

Finally, Figures 5.32(d) - 5.32(f) contain the T-GITM zonally average bulk vertical winds. Much like the Meridional winds, this field shows muted variations over much of the domain, except at the highest altitudes, where escaping CH₄ imparts a great deal of upward drag to the atmosphere. These plots suffer from the same integration effect that the meridional winds experience, erasing much of the overall structure through the zonal averaging. However, these plots do show a systematically higher escape rate with solar activity at 1500 km.

Constant altitude plots of T-GITM temperatures at the exobase and homopause occur in Figures 5.33(a) through 5.33(f). These plots provide examples of how the Titan model structures vary in longitude and latitude at two key altitude levels. These plots, in concert with the zonal average plots should provide another perspective on the variability of Titan's upper atmosphere over a solar cycle. Figures 5.33(a) - 5.33(c) contain the temperatures at the exobase of Titan over the solar cycle. All three plots possess the same temperature scale for immediate comparison. As can be seen the temperatures systematically increase with solar activity level. However,

in all three plots, a very warm southern polar thermosphere emerges.

Figures 5.33(d) - 5.33(f) show a similar trend with solar cycle, where the overall temperatures rise with solar activity level. However, whereas the exobase temperatures exhibited a diurnal variation, temperatures at the homopause appear to be organized primarily by latitude with little local time variation. This can be attributed to the strong zonal super-rotation at these altitudes, which serves to smooth out longitude variations.

5.8 Seasonal Variations and T-GITM

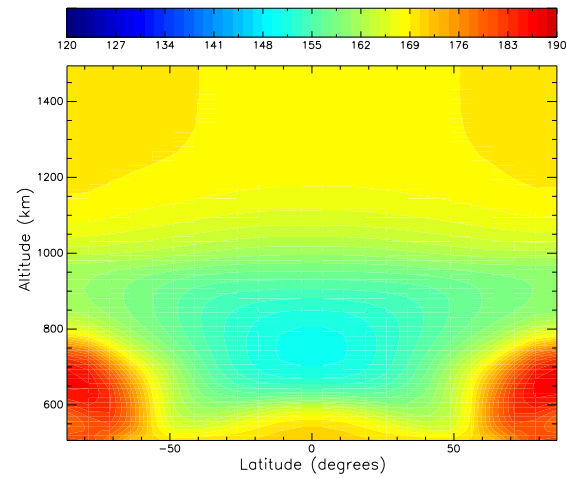
In this section, a numerical study of TItan's season is presented. For this theoretical experiment, all of the boundary conditions are held constant (both top and bottom), the symmetric zonal wind profiles of *Hubbard et al.* [1993] are imposed, and the solar flux is held constant at $F_{10.7-cm} = 80$ for solar minimum conditions. Keeping the solar flux constant represents an artificial imposition, since Titan's year lasts 29.5 Earth years. Thus, the solar activity output would transition between maximum activity level back to minimum activity level at least 4 times during a full Titan year. Also, there is evidence that Titan's lower atmospheric winds also possess a strong seasonal modulation, which would have a pronounced impact on the T-GITM lower boundary [Achterberg *et al.*, 2008]. Furthermore, the upper boundary condition for all of these simulations do not include any hydrodynamic escape, instead only molecular diffusive fall-off is allowed. This stipulation could also materially impact the results. Finally, the resolution, due to computational resource and time constraints, was reduced to 6^0 latitude and 10^0 longitude resolution, a significant decrease from the other simulations presented here. Currently, the impacts of this coarser resolution are not fully known, but should be dealt with in future

research. However, for the purposes of this theoretical study, all parameters are held constant except the orbital position of Titan and the simultaneous change in the subsolar latitude.

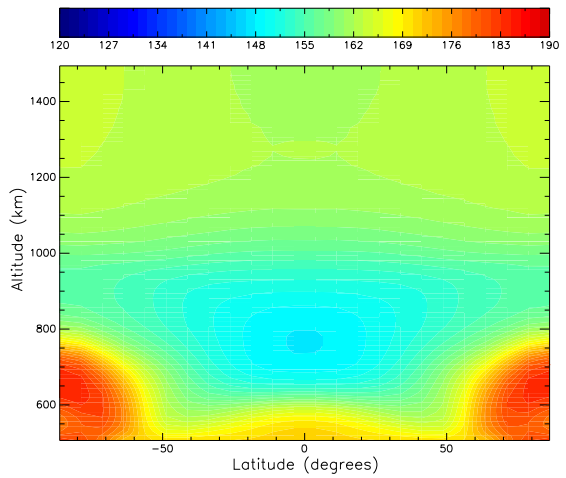
As shown in Figures 5.35(a) - 5.36(f), the overall seasonal variations at Titan, keeping all other factors constant, remain muted compared with the solar cycle variations of the last chapter. The zonally averaged exobase temperatures in Figures 5.35(a) - 5.34(c) vary between 162 - 168 K. This represents a very small shift in exobase temperature compared with the solar cycle variations. Furthermore, the zonally averaged zonal circulation, shown in Figures 5.34(d) - ?? show similarly muted variations overall. However, note that at high altitudes, the super-rotating jet does travel to the winter hemisphere at both solstice periods, while remaining over the equator during equinox. However, this peak only shifts by roughly 10-15° at either solstice. This muted variation is most likely due to the symmetry lower boundary conditions, which pre-condition the T-GITM simulation to maintain a symmetric zonal circulation.

The zonally averaged meridional circulation in Figures 5.32(a) - 5.35(c) also show very small seasonal modulations. At all three seasons, a very similar Hadley circulation pattern forms in the lower atmosphere, consistent with the very repeatable zonal winds occurring at these altitudes. However, at the highest altitudes, seasonal differences do emerge, with northern winter solstice, Figure 5.32(a), having a higher northward meridional velocity in the southern hemisphere. Similarly, the conjugate season in Figure 5.35(c) exhibits stronger meridional flow southward in the northern hemisphere. Finally, equinox shows a very symmetric circulation pattern at all altitudes.

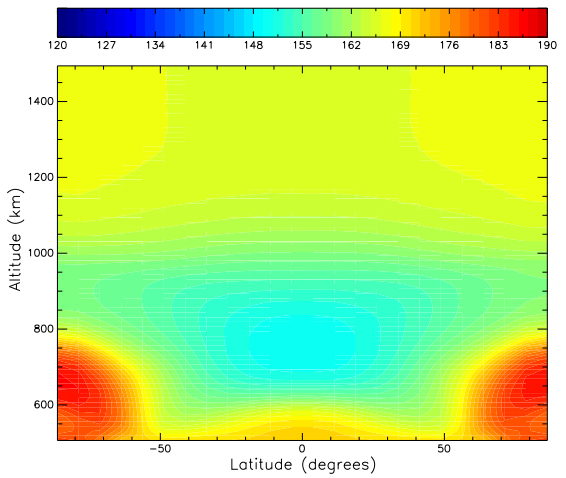
Finally Figure 5.36 contains constant altitude plots of temperatures at the exobase,



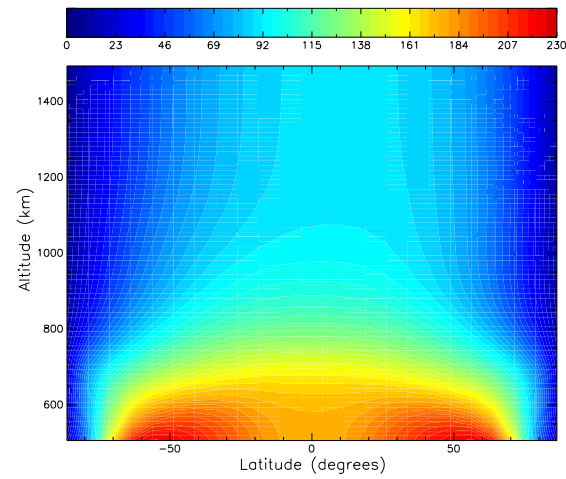
(a) Zonal average Temperatures during northern winter solstice.



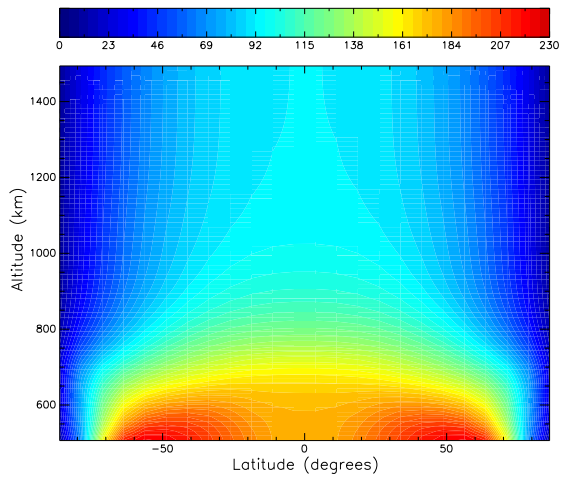
(b) Zonal average Temperatures during equinox.



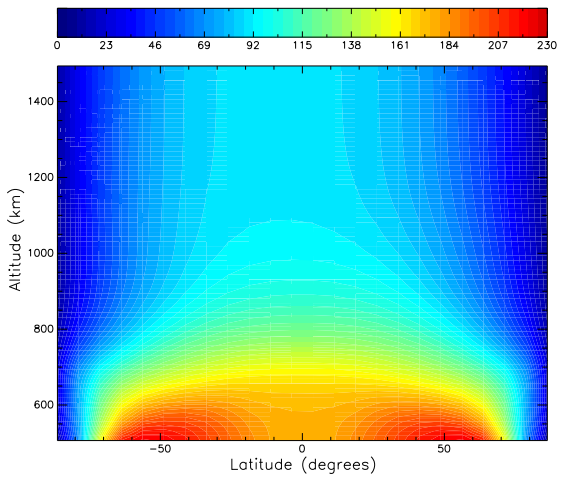
(c) Zonal average Temperatures during northern summer solstice.



(d) Zonal average \mathbf{u}_ϕ during northern winter solstice.



(e) Zonal average \mathbf{u}_ϕ during equinox.



(f) Zonal average \mathbf{u}_ϕ during northern summer solstice.

Figure 5.34: Zonal average temperature, panels (a) - (c), and \mathbf{u}_ϕ , panels (d) - (f), for all the seasons.

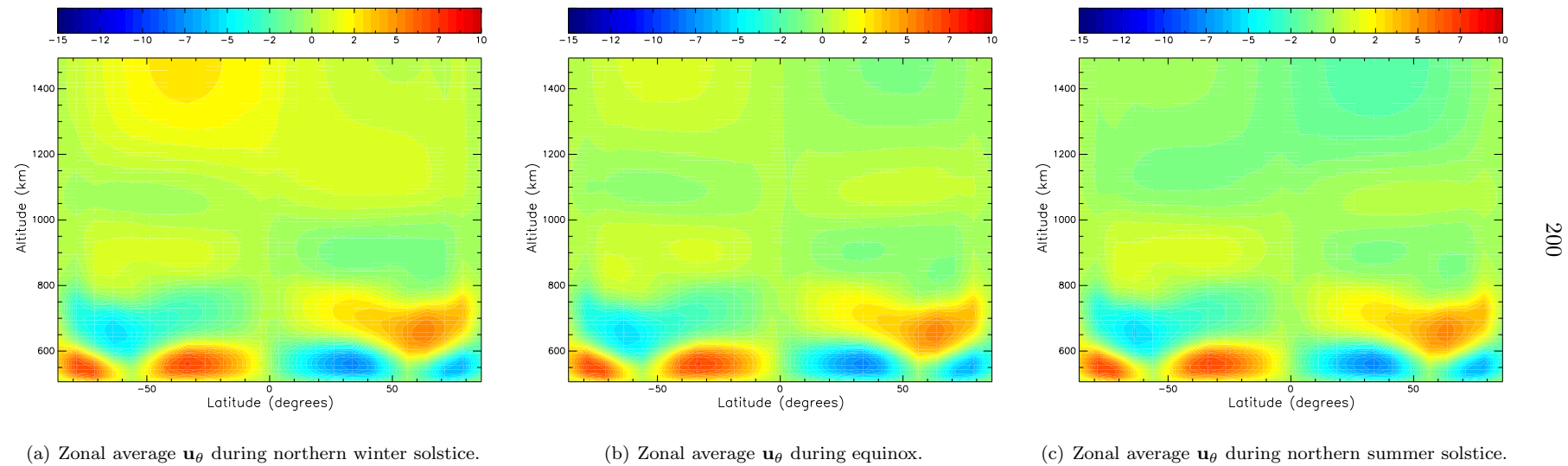


Figure 5.35: Zonal average u_θ velocities, panels (a) - (c) for all the seasons

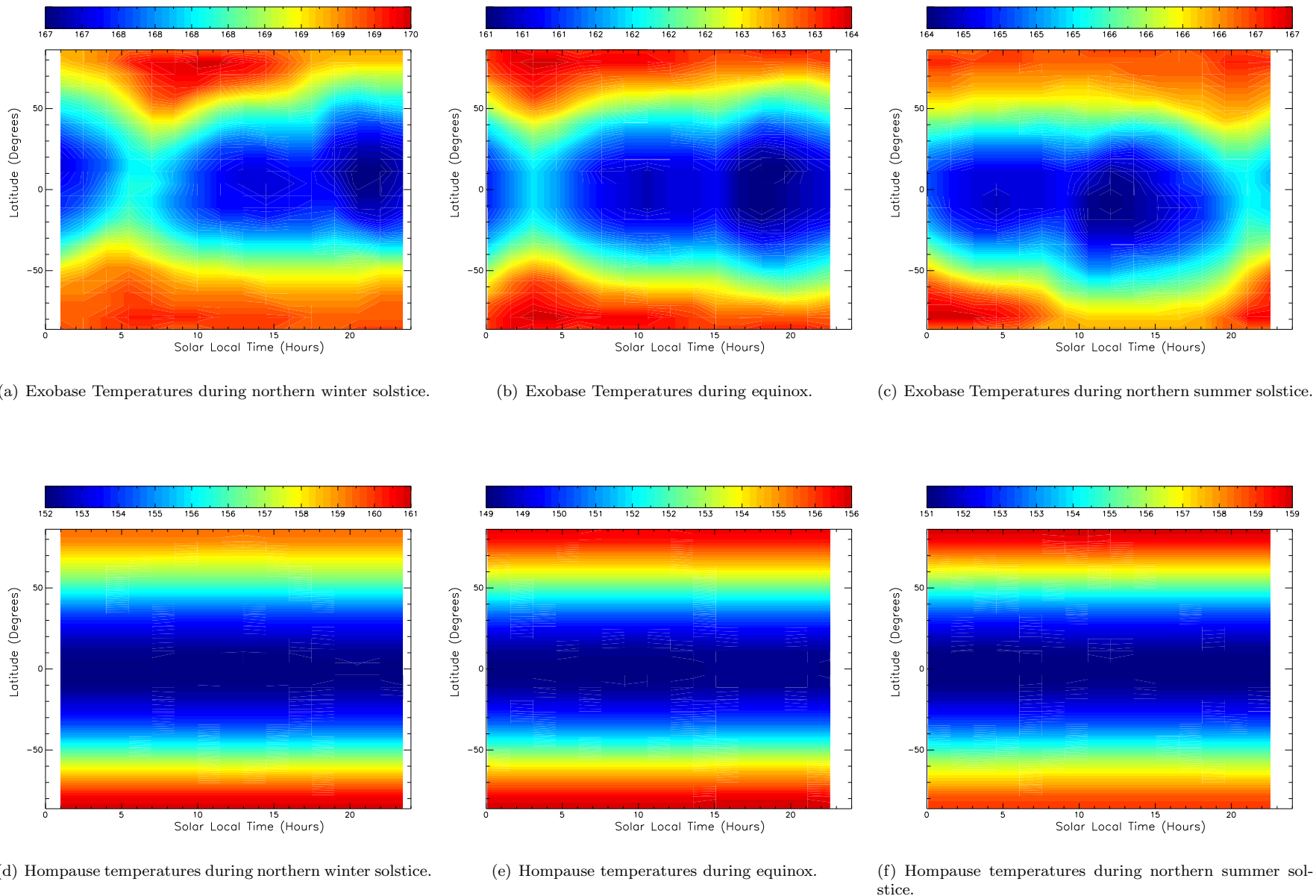


Figure 5.36: Exobase temperature, panels (a) - (c), and homopause temperatures, panels (d) - (f), for all the seasons.

Figures 5.36(a) - 5.36(c), and the homopause, Figures 5.36(d) - 5.36(f). As with the zonally averaged fields, these constant altitude plots reinforce the constancy of T-GITM over seasonal variations alone. The exobase temperatures possess a striking similarity in structure, possessing the highest temperatures at high latitudes, while the temperature minimum occurs at mid-latitudes. Also, the range of temperatures at the exobase remains very repeatable throughout the seasonal cycle, ranging between 164 - 170 K over the entire suite of seasonal runs. Similarly, at the homopause, the temperatures exhibit a very repeatable thermal structure, owing to the strong super-rotation at these altitudes. Much like the exobase temperatures, the maximum temperatures remain confined to high latitudes, while the minimum temperatures occur at mid and low latitudes. The temperatures at this altitude also remain very much range-bound between 152-161 K. Thus, at the exobase and the homopause, the T-GITM for the conditions presented, shows very little variation with seasons while all other parameters are held constant.

5.9 Key Takeaways and Final Thoughts

Through the three major studies of this chapter, several key takeaways emerge. First, through the comparison with the TA flyby as a benchmark evaluation, the T-GITM apparently re-produces the structures in Titan's upper atmosphere with excellent accuracy given the consistently low overall NRMSE values. Furthermore, the correlation coefficients indicate that the Titan model also reproduces the data's overall behavior with altitude to an excellent degree. These two metrics suggest that this new modeling framework represents a viable and useful theoretical tool to use as a proxy for the conditions in the upper atmosphere of Titan.

Using this validated theoretical tool, one may explore the impact of solar activ-

ity upon Titan's upper atmosphere. The numerical solar cycle experiment of this section sought to quantify the impact of representative solar flux variations on the thermosphere of Titan, while keeping all other parameters constant. From this study, the upper atmosphere of Titan, throughout most of its altitudes, exhibit discernable and significant variations with solar activity, as shown . The global average thermal structure at the exobase increases from a temperature of 134 K to 142 K. Concomitantly, the diurnal variation at this altitude increases from 10 K at solar minimum to 19 K a solar maximum fluxes. Likewise, at the homopause, the global average temperatures rise from 140 K at the lowest solar activity to 165 K at the highest solar activity. At this same altitude, the diurnal variations also systematically rise from 12 K to 20 K. Thus, the middle altitudes of the Titan thermosphere apparently respond more than the upper altitudes to solar activity, which differs from previous work by *Müller-Wodarg et al.* [2000].

The final numerical study of this chapter focuses on the impact of orbital position (or seasons) on the Titan-GITM. This study reveals that the thermosphere of Titan exhibits very muted variations with seasons, while keeping all other variables, such as solar fluxes, constant. This, of course, represents a completely artificial constraint, since Titan's year remains much longer than the typical solar cycle variation timescale. However, this numerical experiment seeks to quantify the impacts of orbital angle alone. The results indicate that, on both a global average and zonal average scale, no significant variability occurs. Of course, migration of the sub-solar latitude results in shifts in the strongest meridional and zonal circulation, but these remain apparently minor changes. Additionally, another potential pitfall of this study remains the coarser resolution, 6^0 latitude by 10^0 longitude, than that of the previous two studies: 2.5^0 latitude by 10^0 longitude.

Ultimately, these studies illustrate the promise of the T-GITM and point to future theoretical studies and improvements in the framework.

CHAPTER VI

Comparing T-GITM to Cassini Data

It doesn't matter how beautiful your theory is, it doesn't matter how smart you are.

If it doesn't agree with experiment, it's wrong.

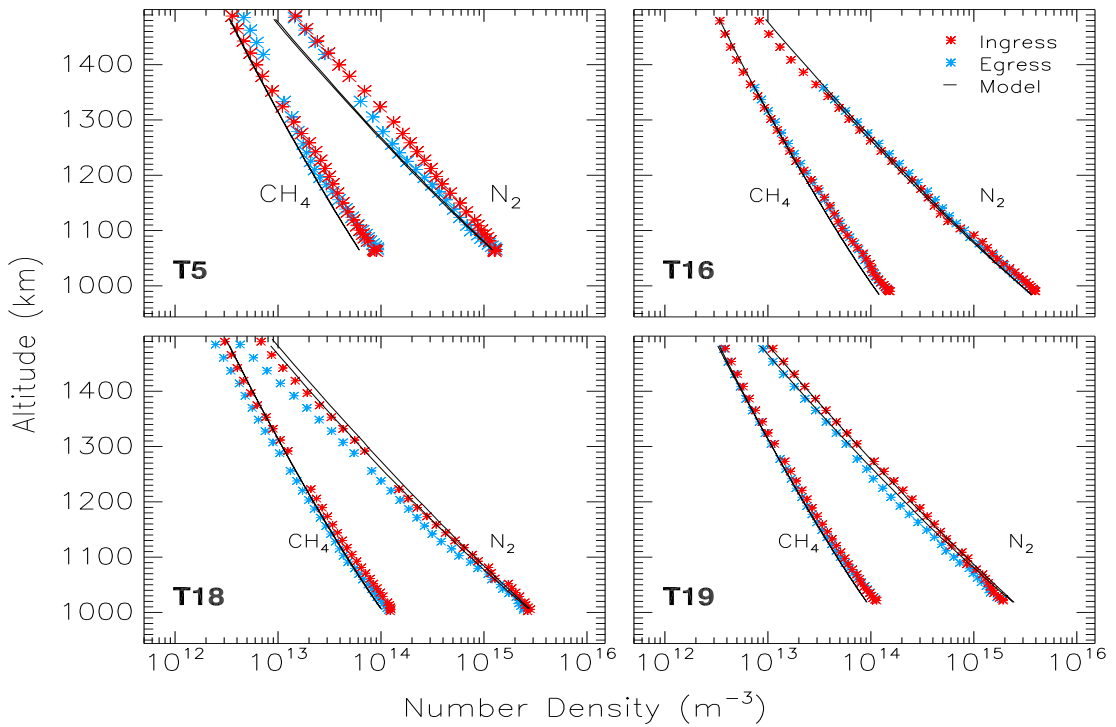
—Richard Feynman

6.1 Flyby Comparisons

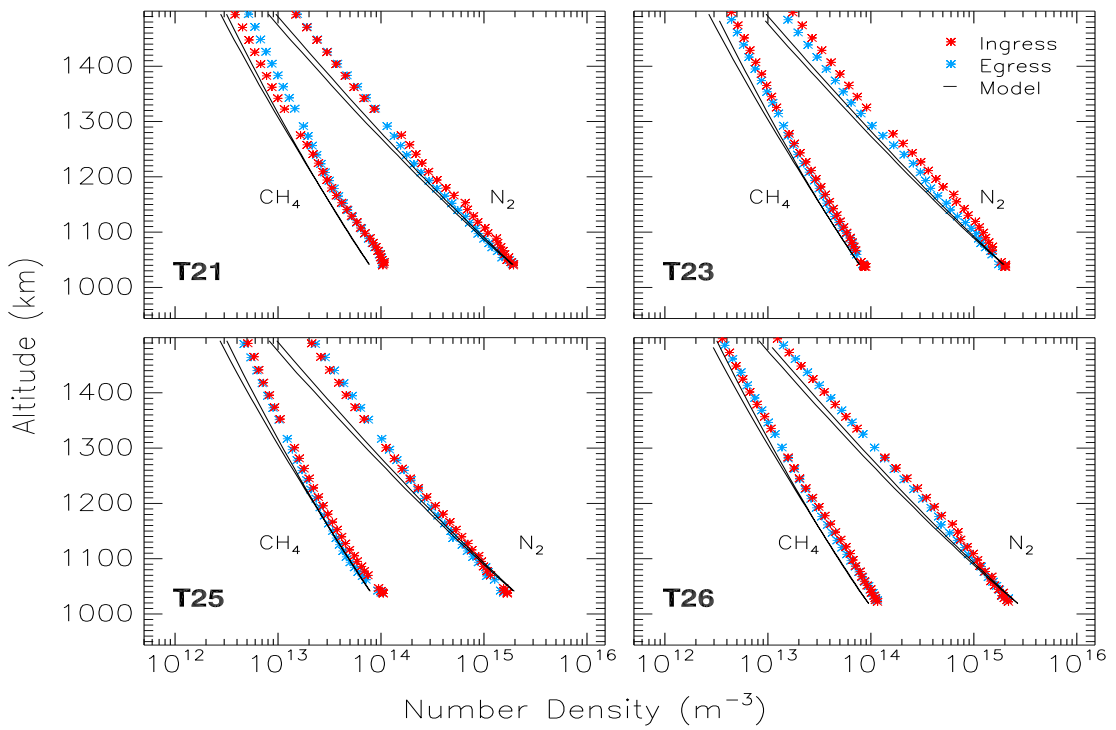
In this section, a systematic comparison between the T-GITM and the flybys following T5 is performed. This provides a further validation of the model in several respects: (1) it functions as a statistical calibration for the model, (2) it illustrates what parameters and fields the model can best reproduce, and (3) it shows what aspects in the modeling framework require the most improvement. In this section, the normalized root mean square error (NRMSE) again emerges as the best candidate for error, while the correlation coefficient again quantifies of how well the Titan model captures the *in situ* structures. Lastly, at the end of this chapter, a brief exploration of the impacts of super-rotation on the results is performed.

6.2 Comparing the T-GITM against 15 flybys: T5 - T40

In this section, a systematic comparison between the Titan Global Ionosphere-Thermosphere Model and Cassini INMS measurements is presented. Only one simu-

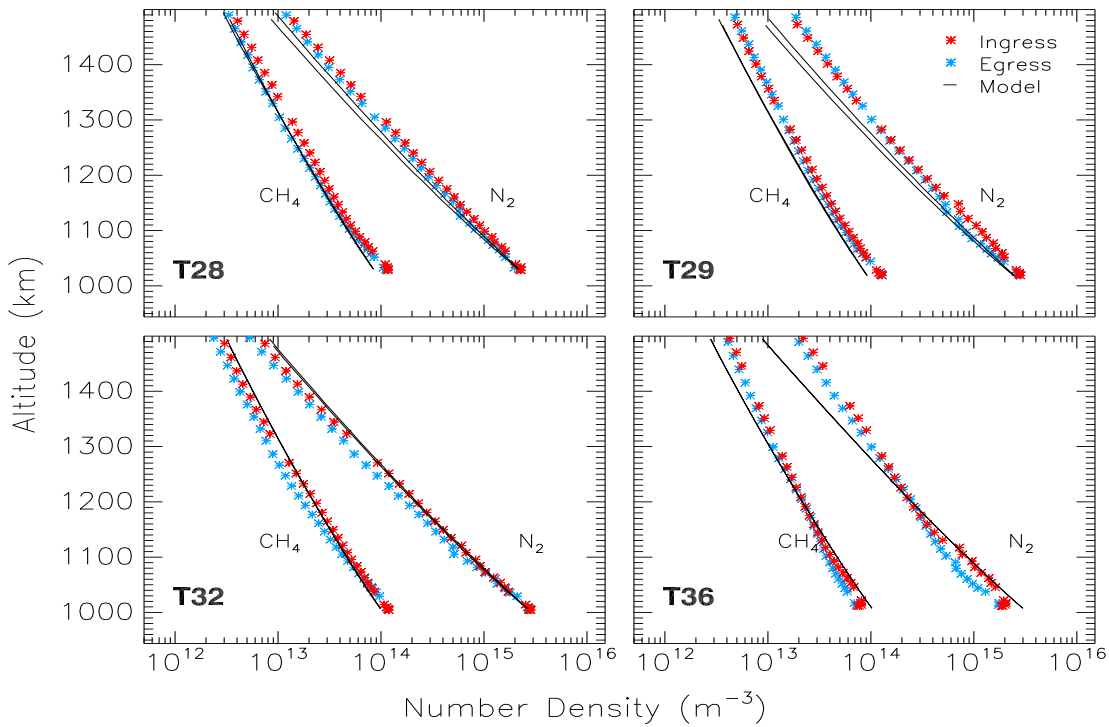


(a) T-GITM and INMS flyby comparison for T5 - T19

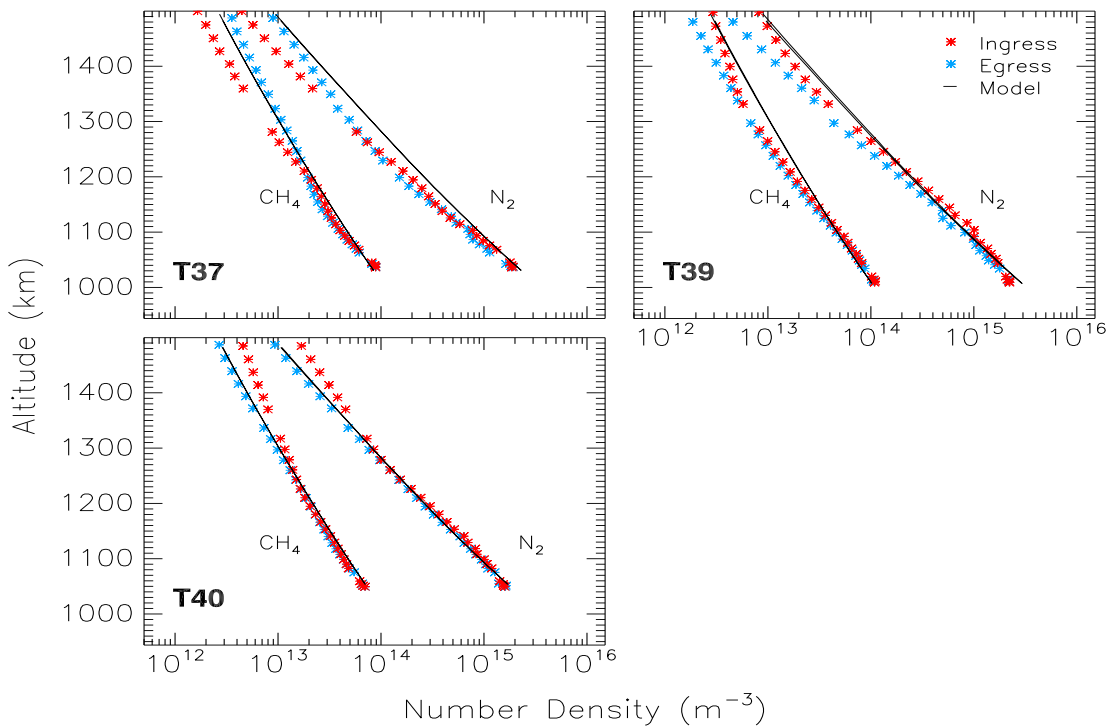


(b) T-GITM and INMS flyby comparison for T21 - T26

Figure 6.1: T-GITM and INMS N₂ and CH₄ density comparisons for the T5 through the T26 flybys.

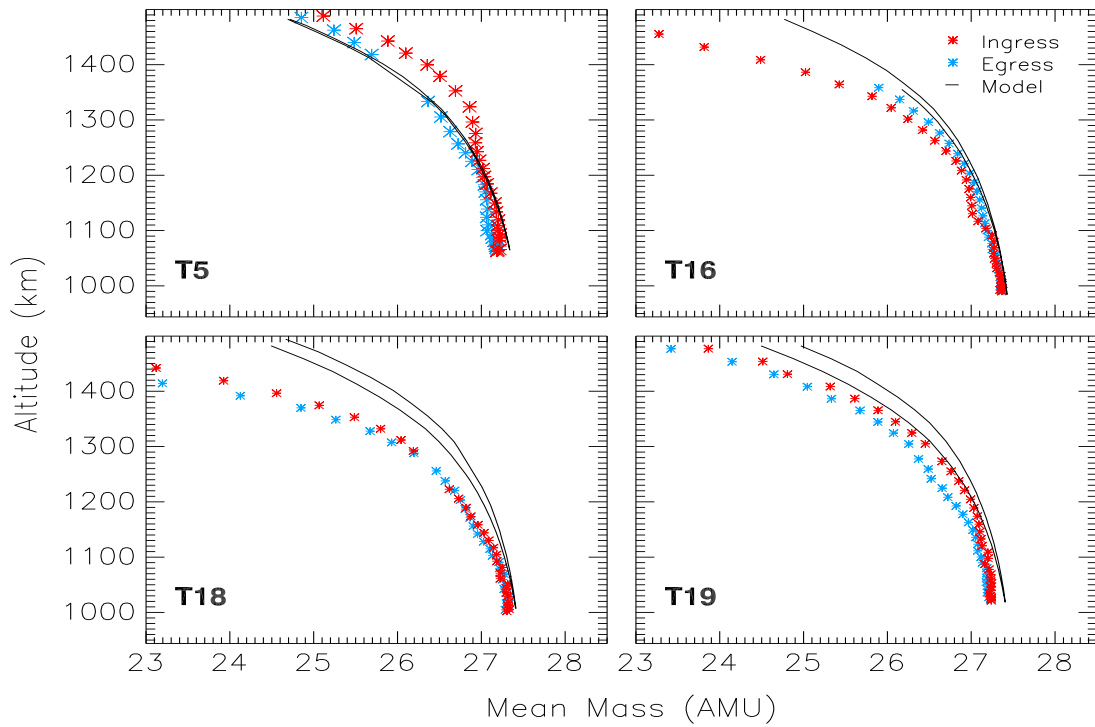


(a) T-GITM and INMS flyby comparison for T28 - T36

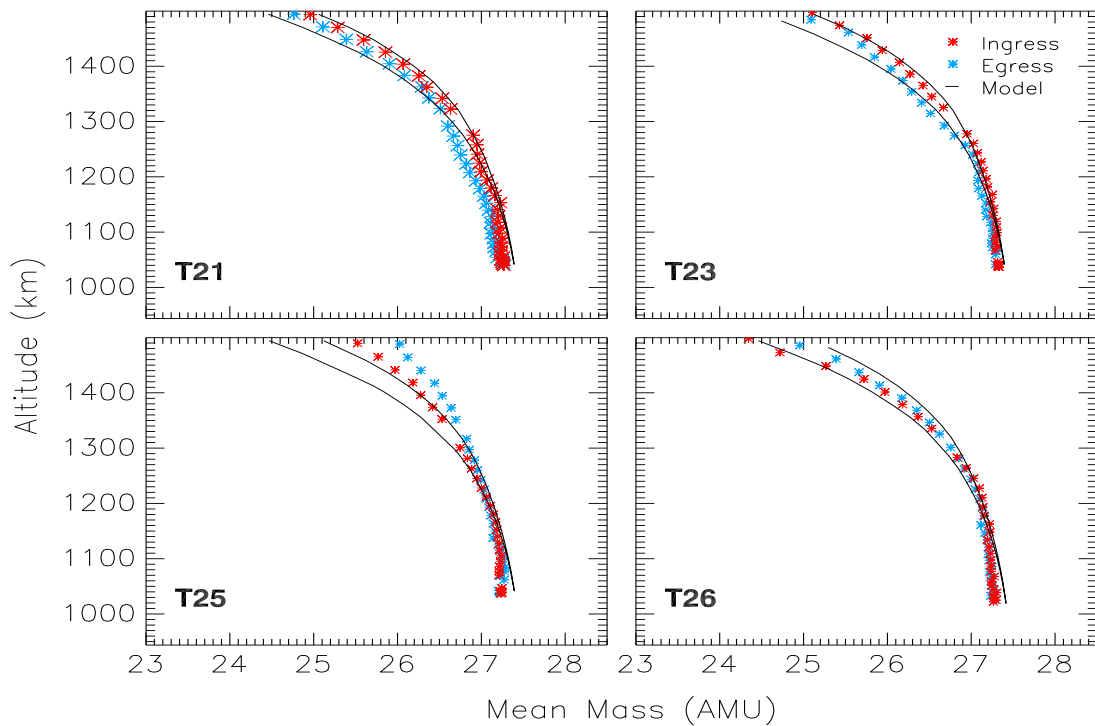


(b) T-GITM and INMS flyby comparison for T37 - T40

Figure 6.2: T-GITM and INMS N_2 and CH_4 density comparisons for the T28 through the T40 flybys.

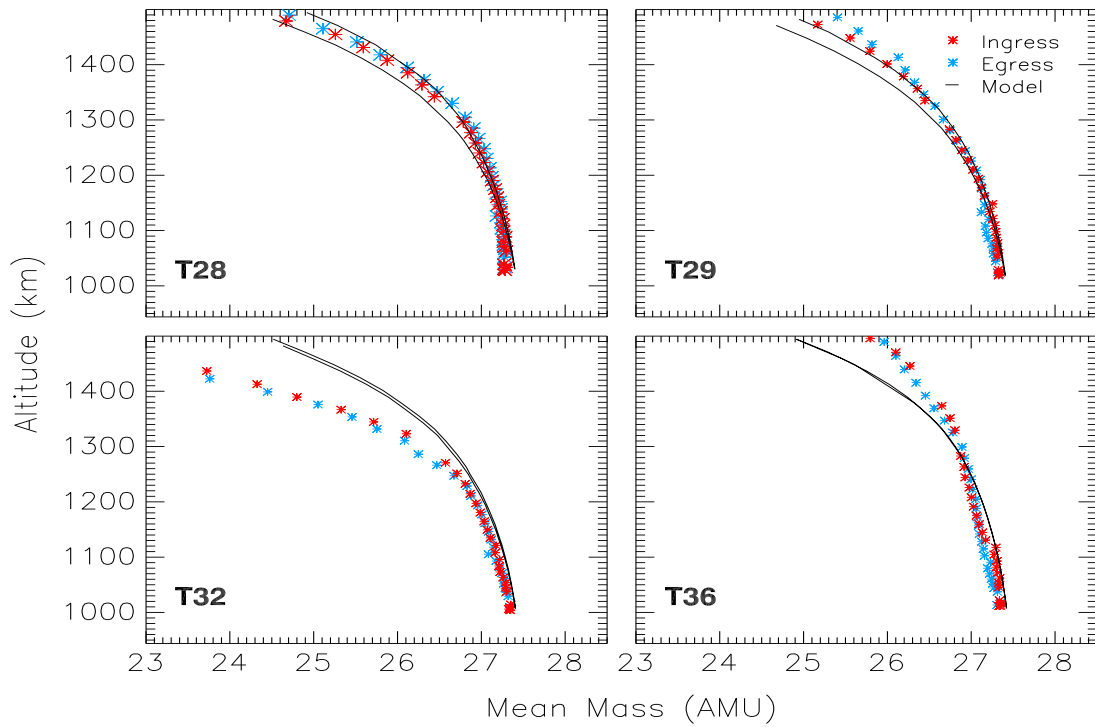


(a) T-GITM and INMS flyby comparison for T5 - T19

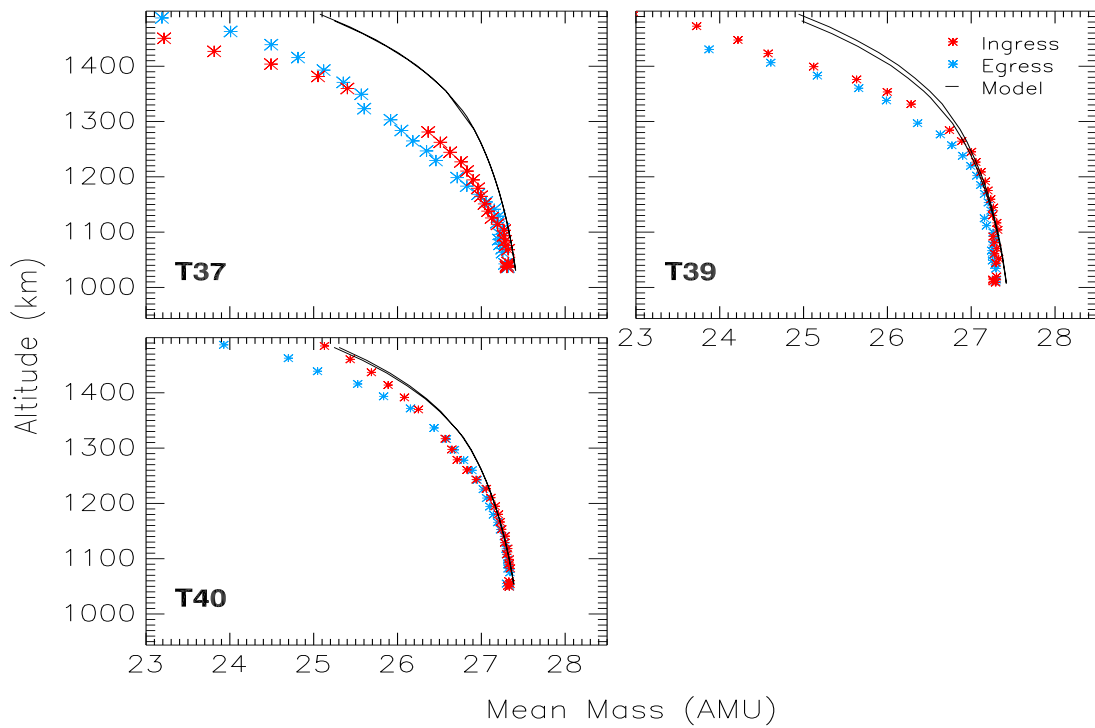


(b) T-GITM and INMS flyby comparison for T21 - T26

Figure 6.3: T-GITM and INMS \bar{m} comparisons for the T5 through the T26 flybys.



(a) T-GITM and INMS flyby comparison for T28 - T36



(b) T-GITM and INMS flyby comparison for T37 - T40

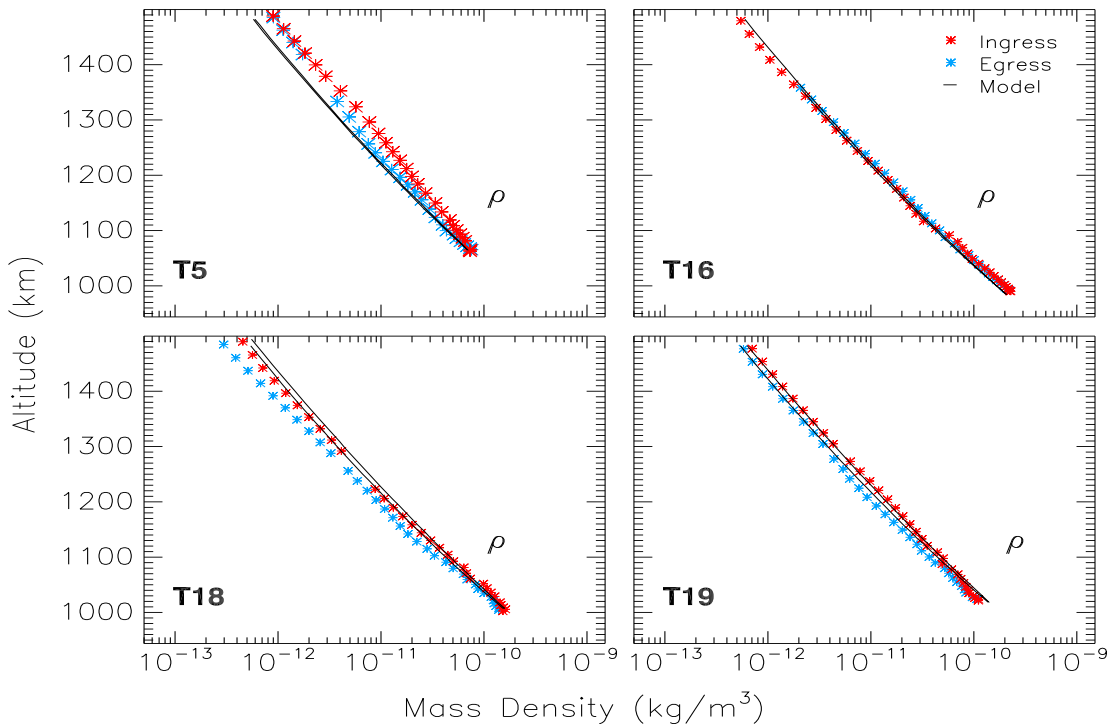
Figure 6.4: T-GITM and INMS \bar{m} comparisons for the T28 through the T40 flybys.

lation at solar minimum is utilized in this study with $F_{10.7-cm} = 80$. Thus, the model simulation cannot capture temporal changes that potentially occur over in the flyby datasets, which are spaced out over several years. Additionally, a new super-rotating lower boundary condition is specified for these simulations. This new lower boundary differs from the profile in Chapter 5 only in magnitude, with the zonal jets at high latitude possessing a maximum super-rotating zonal velocity of 135 m/s and a mid-latitude minimum speed of 75 m/s (see Figure 5.8 for the profile shape).

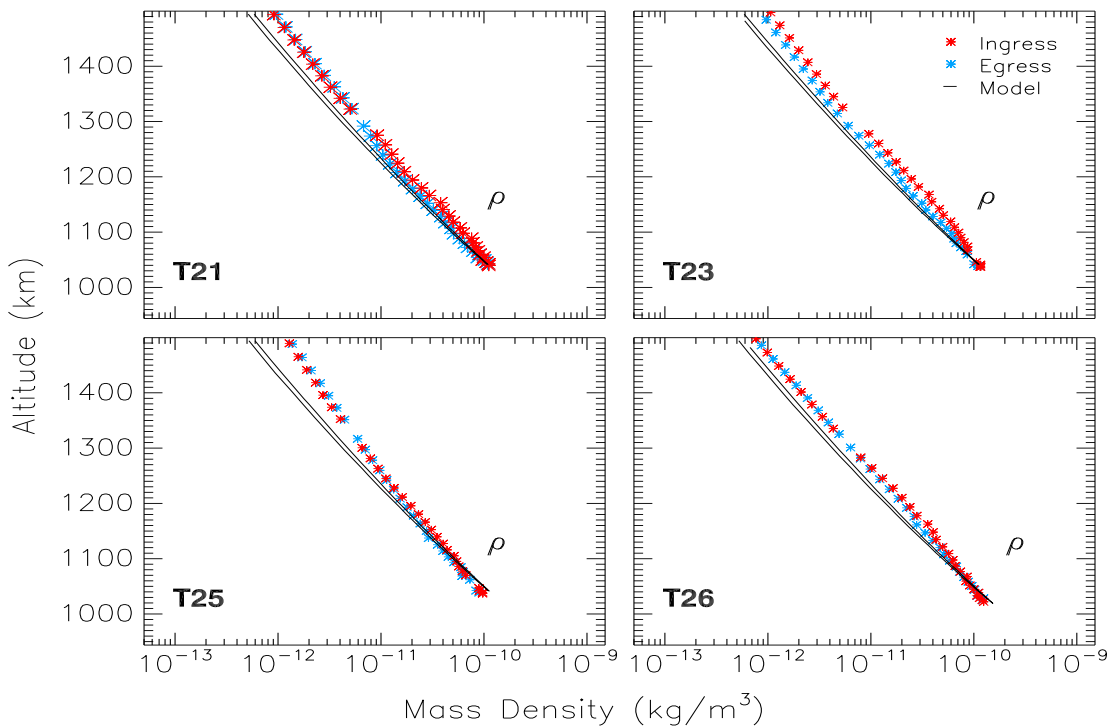
The simulation comparisons are structured as in chapter 5, where the Cassini INMS trajectories for every flyby are extracted from the model. This process simulates what the instrument would measure, if it were to fly through the model atmosphere. In order to accomplish this, the latitude, altitude, and local solar time corresponding to each *in situ* data point is extracted from the model simulations. However, due to its finite resolution, these data points may co-exist in a single cell, introducing a smoothing effect to the model's results when compared with the data. Ultimately, through this comparison over many datasets, the capabilities of T-GITM and its short comings should emerge more clearly than they did with just the single TA flyby benchmark run in the last chapter.

The comparison between T-GITM N_2 and CH_4 densities (m^{-3}) and Cassini INMS measurements, both ingress (red) and egress (blue), occur in Figures 6.1(a) - 6.2(b). As can be seen from these figures, the model does well overall in capturing the density values for both N_2 and CH_4 , while also possessing a reasonably good approximation to their variations with altitude. Flybys T36 – T40 possess variations that are not captured well by the model, implying that perhaps temporal evolution and/or local variations in the regions sampled are not captured by the simulation. Also, T-GITM could also be missing key physics at work in the regions sampled here. However, as

shown in Table 6.1 and Table 6.2, this single simulation possesses excellent overall agreement with measurements for the flybys. Also, by combining all the data into a single flyby data set, a total NRSRM error of .228 (22.8 %) for N_2 and correlation coefficient for N_2 of 0.96 result, indicating excellent overall agreement between the model and the measurements. Likewise, T-GITM's CH_4 density profiles possess an overall NRMSE = 0.273 (27.3 %) with a correlation coefficient, $r = 0.968$. Thus, the Titan model seems to capture the behavior of the major species very well.

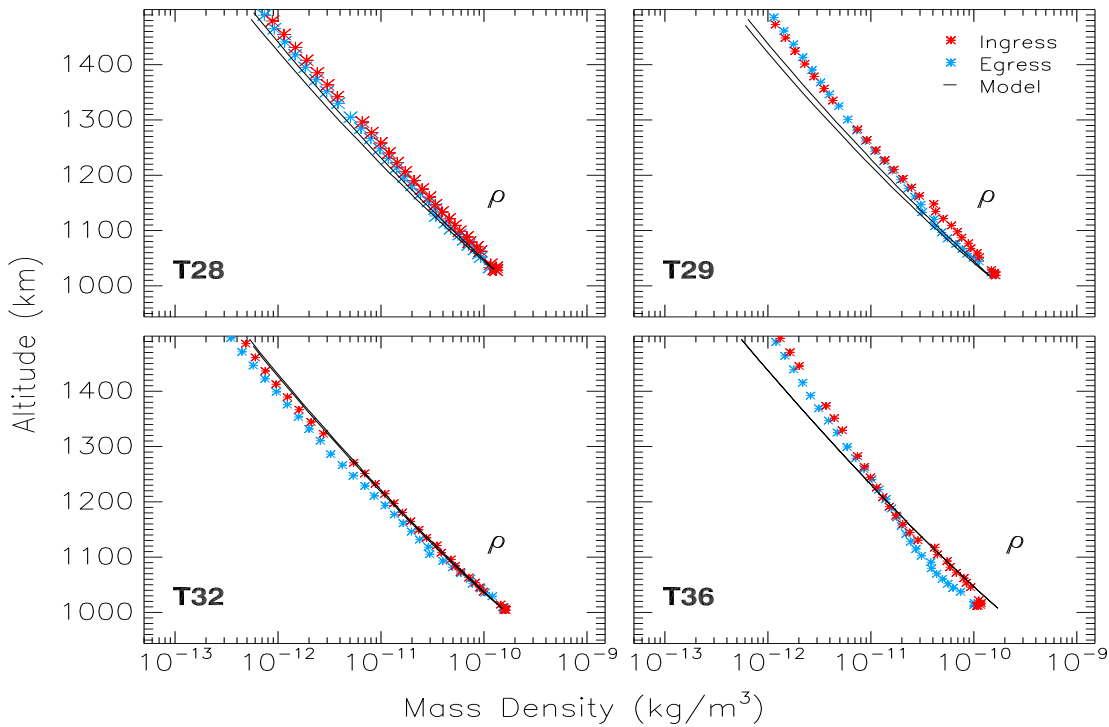


(a) T-GITM and INMS flyby comparison for T5 - T19

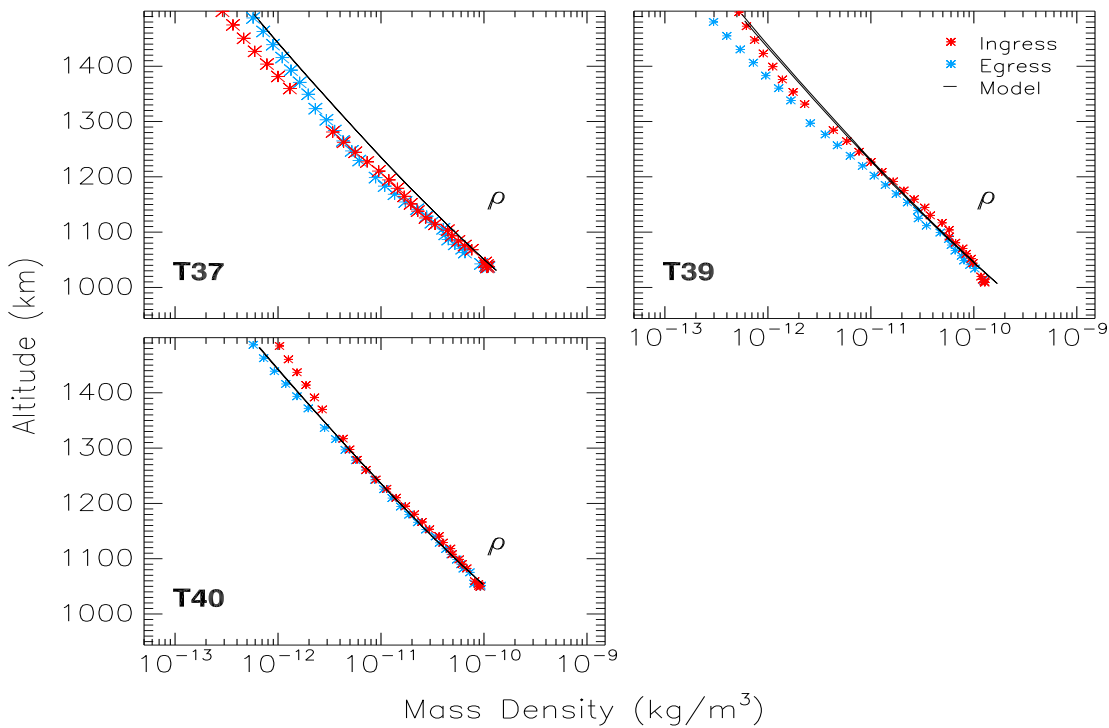


(b) T-GITM and INMS flyby comparison for T21 - T26

Figure 6.5: T-GITM and INMS ρ comparisons for the T5 through the T26 flybys.

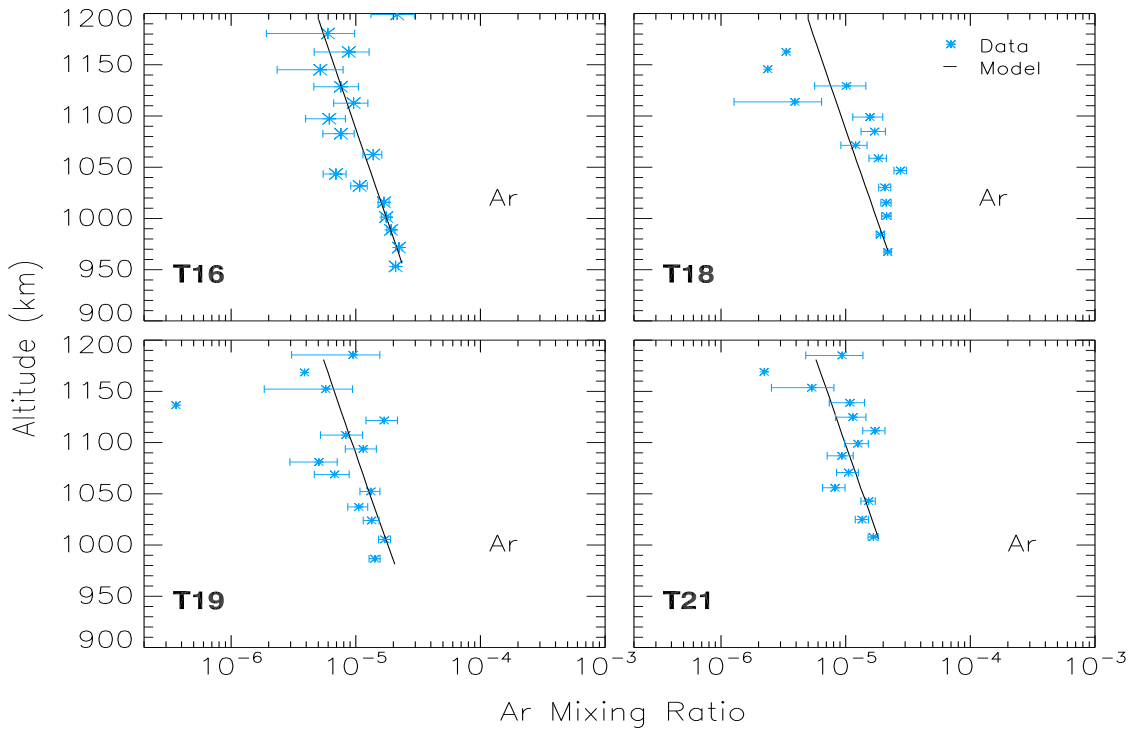


(a) T-GITM and INMS flyby comparison for T28 - T36

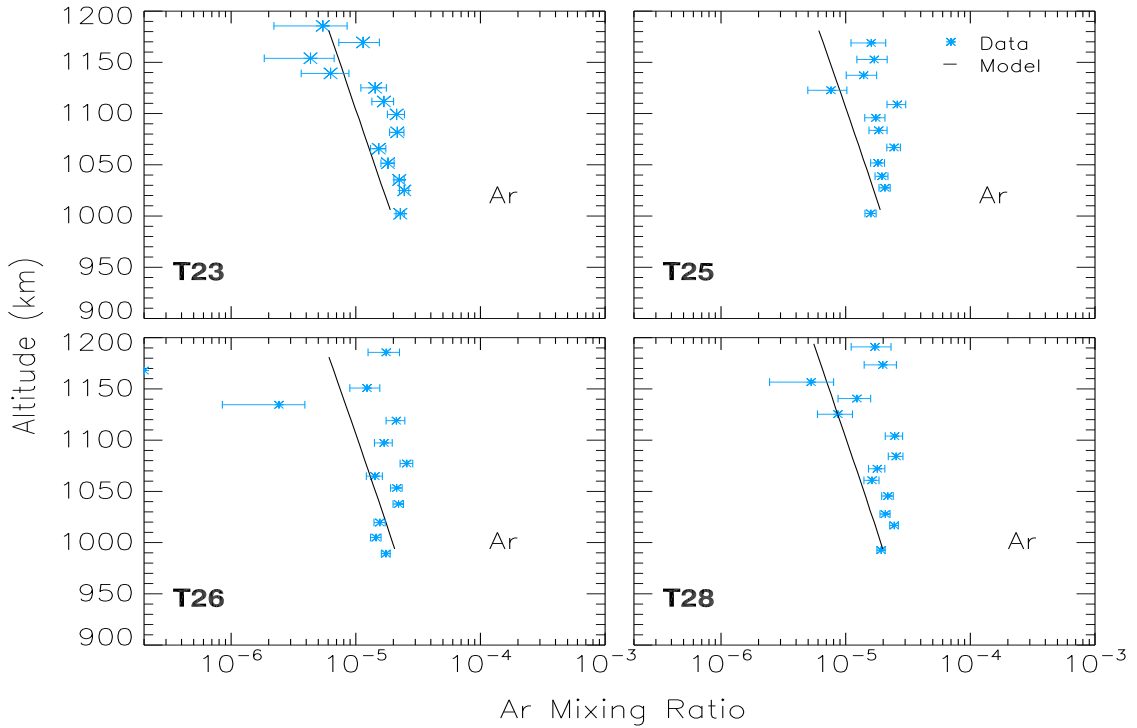


(b) T-GITM and INMS flyby comparison for T37 - T40

Figure 6.6: T-GITM and INMS ρ comparisons for the T28 through the T40 flybys.

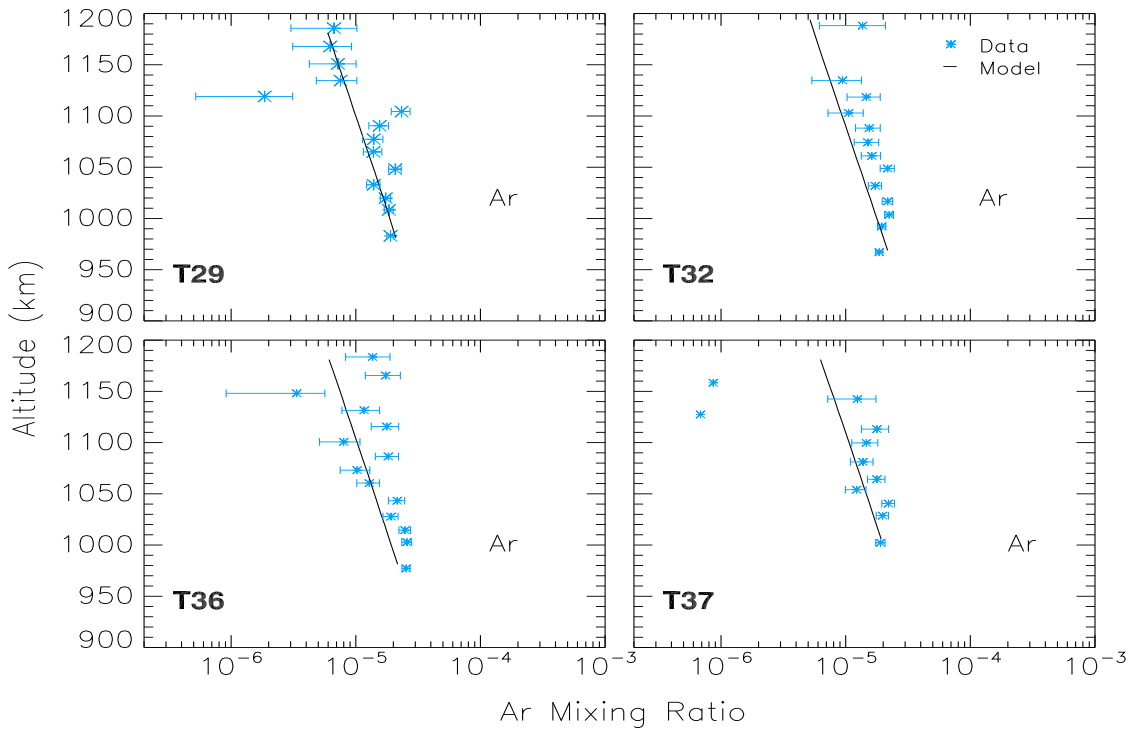


(a) T-GITM and INMS flyby comparison for T16 - T21

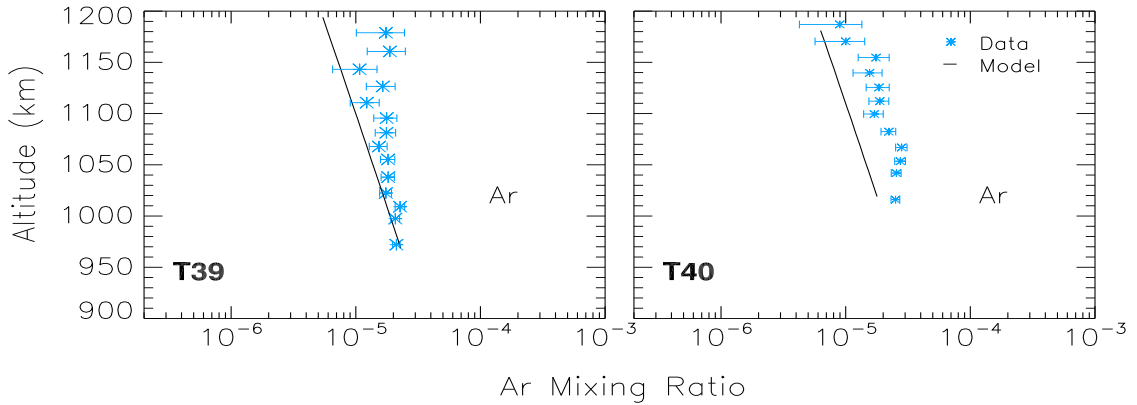


(b) T-GITM and INMS flyby comparison for T23 - T28

Figure 6.7: T-GITM and INMS Argon mixing ratio comparisons for the T16 through the T28 flybys.



(a) T-GITM and INMS flyby comparison for T29 - T37



(b) T-GITM and INMS flyby comparison for T39 - T40

Figure 6.8: T-GITM and INMS Argon mixing ratio comparisons for the T28 through the T40 flybys.

Figures 6.3(a) - 6.4(b) compare the T-GITM mean major masses (AMU) with the mean mass derived from INMS measurements. Deviations in mean majors mass essentially indicate that the model's relative abundance of N₂ and CH₄ contains errors, because this field remains dominated by these two constituents. Thus, discrepancies in the mean major mass serve as a proxy for the CH₄ mixing ratio at the highest altitudes. For the most part, the T-GITM reproduces the mean major mass very well, with NRMS errors ranging between 0.9 % and 4.8 %. The total NRMSE, as shown in Table 6.1, is 2.3 % along with a total correlation coefficient of 0.960. Visually, the differences between the Titan model and the data appear much larger, but the scale of the plot indicates that even 5 % differences will appear prominently.

Figures 6.5(a) - 6.6(b) overlay the T-GITM mass densities (kg/m³) with the measurements, both ingress (red) and egress (blue). Given the close correlation between the model and INMS N₂ and CH₄ densities and the mean major mass, the mass density comparisons also show excellent agreement between model and data. The flybys that exhibit larger differences also possess large deviations in both the neutral densities and the mean mass. As shown in Tables 6.1 and 6.2, the mass density NRMS error ranges from 10.2 % to 57.1 %, possessing a correlation coefficient ranging between 0.983 - 0.995. Summing over the flybys the T-GITM mass density possesses a total NRMSE of 22.7 % and a correlation coefficient of 0.960.

Figures 6.7(a) - 6.8(b) possess the T-GITM Argon mixing ratios compared against the Cassini INMS-derived mixing ratios (blue), along with the data's systematic error bars. This particular field exhibits the largest deviation between the model and measurements, possessing an NRMSE = 0.405 and an $r = 0.610$. Clearly, the model does not reproduce these derived Argon mixing ratios as well as the major species. However, as can be seen in these figures, the model does relatively good

Table 6.1: Normalized Root Mean Squared Error (NRMSE) between T-GITM and Cassini INMS data for T5 - T40 flybys

Flyby	N ₂	CH ₄	\overline{m}	ρ	Ar Mixing	¹⁴ N/ ¹⁵ N	¹² C/ ¹³ C
T5	0.155	0.375	0.009	0.156	—	0.137	0.112
T16	0.224	0.294	0.019	0.222	0.362	0.189	0.106
T18	0.107	0.211	0.048	0.107	0.372	0.192	0.064
T19	0.317	0.223	0.015	0.312	0.421	0.164	0.078
T21	0.127	0.383	0.005	0.128	0.319	0.141	0.083
T23	0.166	0.176	0.004	0.165	0.369	0.121	0.088
T25	0.269	0.254	0.011	0.265	0.467	0.116	0.086
T26	0.202	0.288	0.005	0.201	0.469	0.136	0.073
T28	0.125	0.301	0.005	0.125	0.470	0.131	0.108
T29	0.213	0.317	0.007	0.212	0.347	0.138	0.129
T32	0.103	0.187	0.039	0.102	0.334	0.164	0.058
T36	0.571	0.329	0.011	0.571	0.361	0.123	0.061
T37	0.246	0.137	0.042	0.250	0.366	0.160	0.083
T39	0.317	0.114	0.032	0.315	0.371	0.118	0.118
T40	0.141	0.124	0.011	0.140	0.483	0.109	0.103
Total	0.228	0.273	0.023	0.227	0.405	0.147	0.100

job lying reproducing the data's values and overall trend. Again, the later flybys, T36-T40, pose the largest problem for the model. And, Argon in general, represents the model's worst comparison with data values.

6.3 The State of Titan's Thermosphere During T5 - T40

6.4 Changing the Super-Rotation Speed at 500 km

6.4.1 Two Sample Changes: No Super-Rotation and Strong Super-Rotation

Non Super-Rotating

Strong Super-Rotating

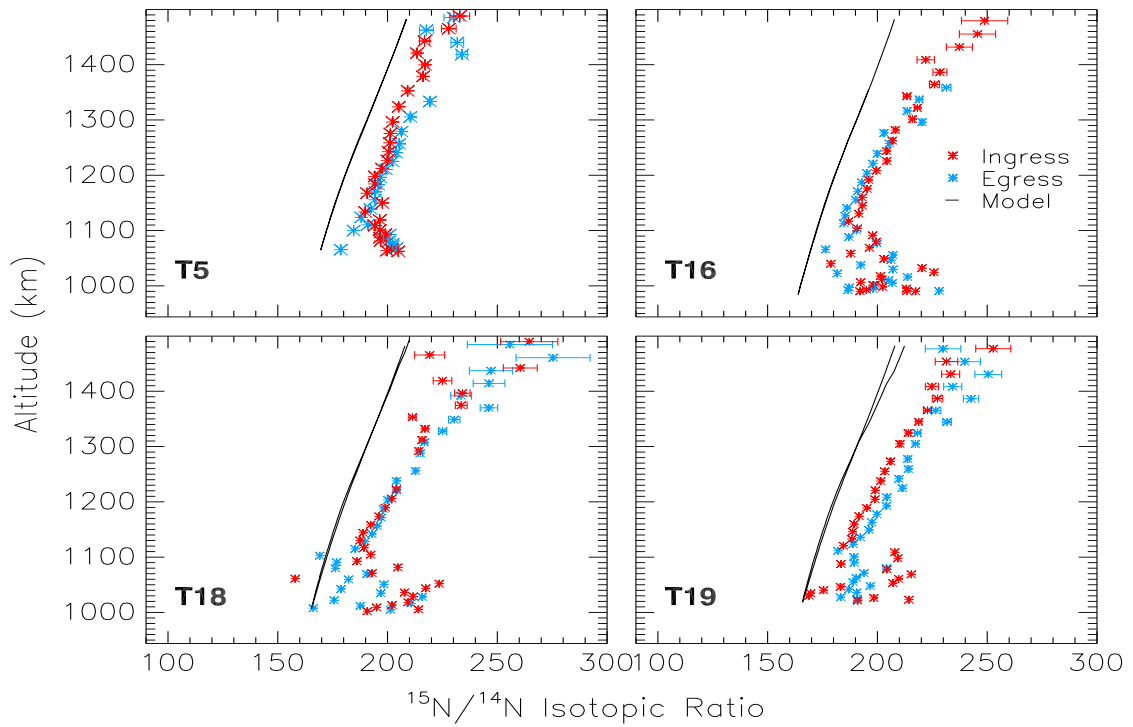
6.4.2 Direct Comparison Between the Super-Rotating Lower Boundaries

Table 6.2: Correlation Coefficient (r) between T-GITM and Cassini INMS data for T5 - T40 flybys

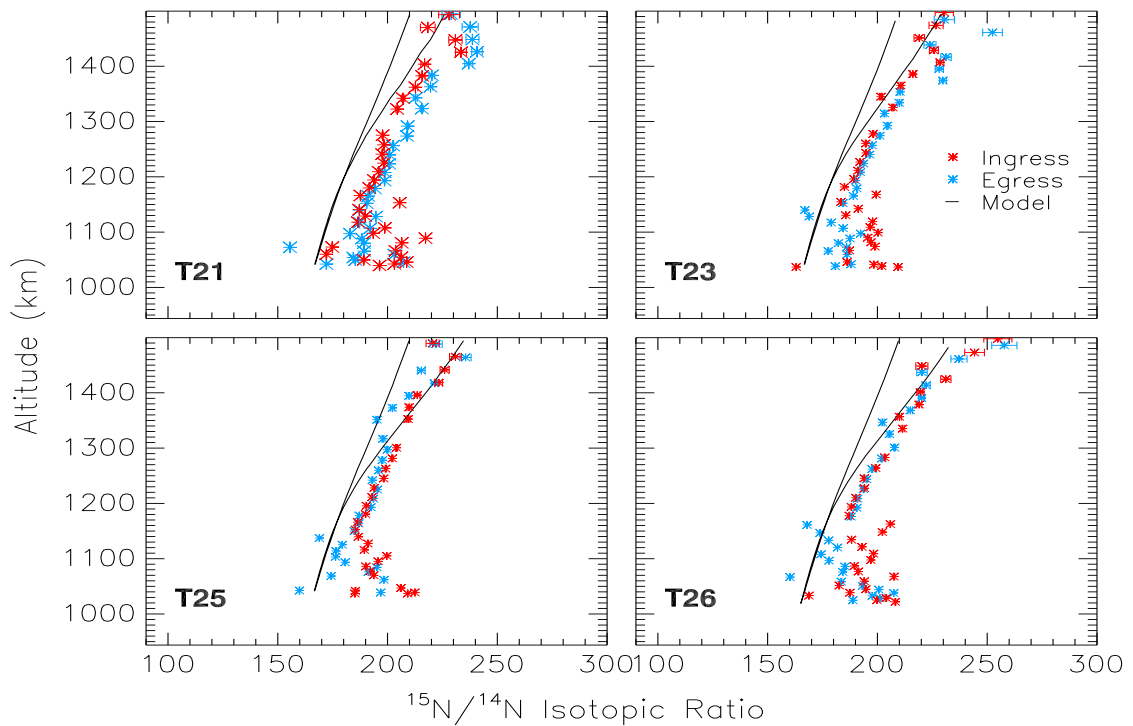
Flyby	N ₂	CH ₄	\bar{m}	ρ	Ar Mixing	¹⁴ N/ ¹⁵ N	¹² C/ ¹³ C
T5	0.991	0.994	0.975	0.991	—	0.840	0.766
T16	0.995	0.995	0.982	0.995	0.668	0.600	0.003
T18	0.992	0.993	0.989	0.992	0.817	0.784	0.694
T19	0.993	0.997	0.997	0.993	0.600	0.856	0.712
T21	0.991	0.996	0.994	0.991	0.612	0.765	0.809
T23	0.983	0.996	0.992	0.984	0.842	0.798	0.695
T25	0.990	0.981	0.995	0.990	0.438	0.730	0.721
T26	0.982	0.998	0.989	0.983	0.347	0.763	0.776
T28	0.991	0.987	0.985	0.992	0.475	0.754	0.551
T29	0.988	0.995	0.995	0.988	0.667	0.740	0.136
T32	0.995	0.994	0.985	0.995	0.748	0.891	0.742
T36	0.969	0.986	0.983	0.969	0.732	0.753	0.768
T37	0.991	0.985	0.985	0.991	0.765	0.792	0.733
T39	0.984	0.997	0.983	0.985	0.641	0.852	0.386
T40	0.990	0.995	0.982	0.990	0.861	0.837	0.795
Total	0.960	0.968	0.960	0.960	0.610	0.741	0.55

Table 6.3: Total NRMSE and Correlation Coefficient for the Non Super-Rotating and Strongly Super-Rotating Lower Boundaries for the T5 - T40 flybys

Non Super-Rotating		
	N ₂	CH ₄
Total NRMSE	0.204	0.243
Total r	0.972	0.973
Strongly Super-Rotating		
	N ₂	CH ₄
Total NRMSE	0.410	0.321
Total r	0.860	0.930

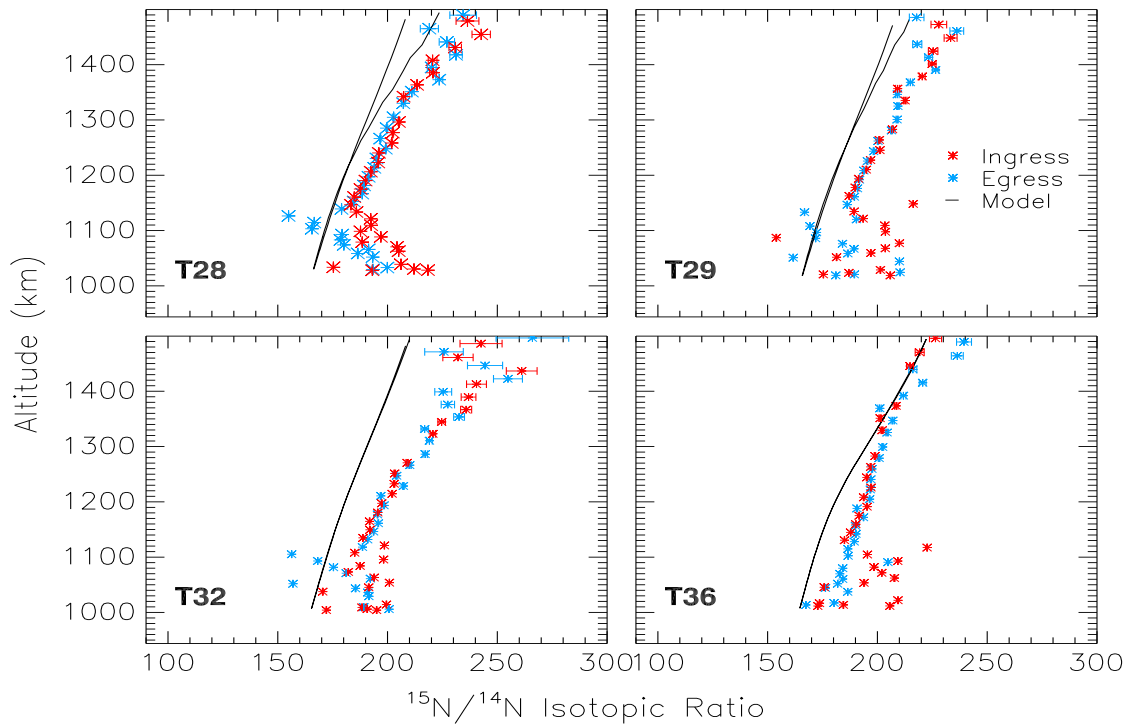


(a) T-GITM and INMS flyby comparison for T5 - T19

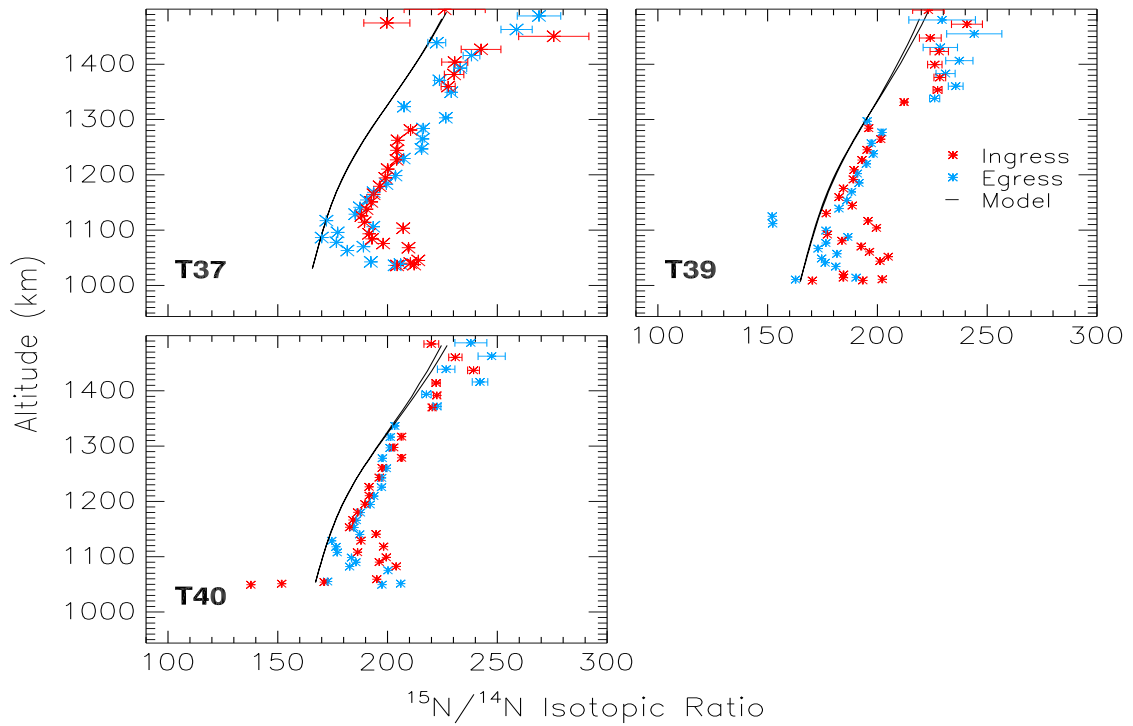


(b) T-GITM and INMS flyby comparison for T21 - T26

Figure 6.9: T-GITM and INMS $^{14}\text{N}/^{15}\text{N}$ comparisons for the T5 through the T26 flybys.

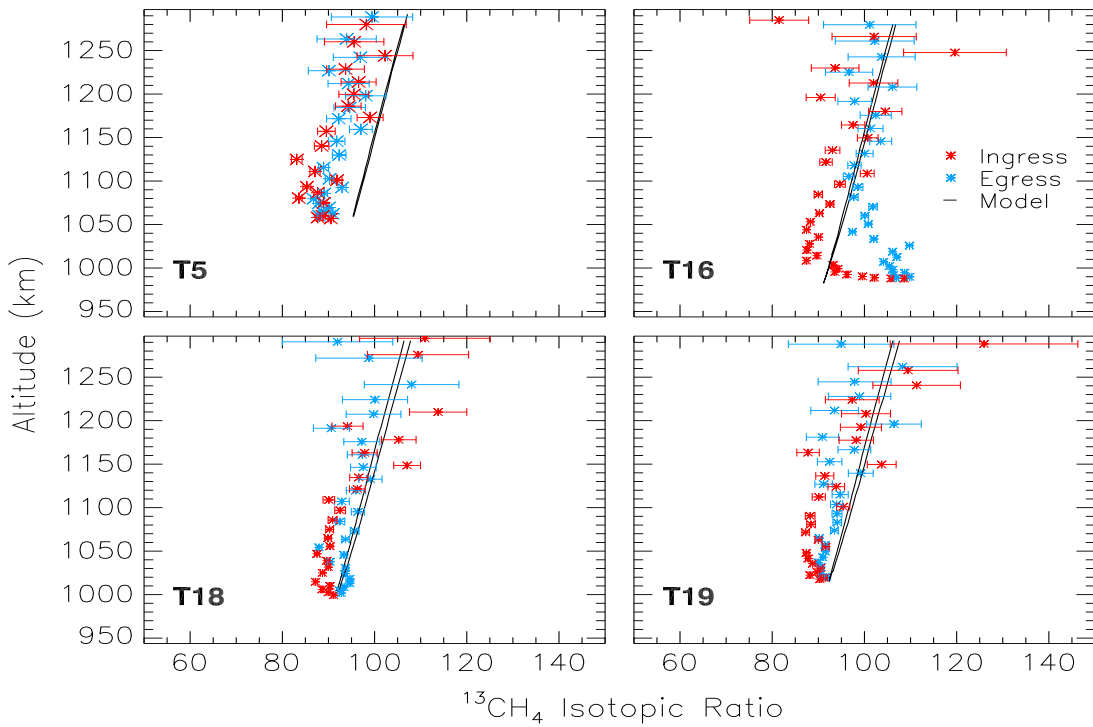


(a) T-GITM and INMS flyby comparison for T28 - T36

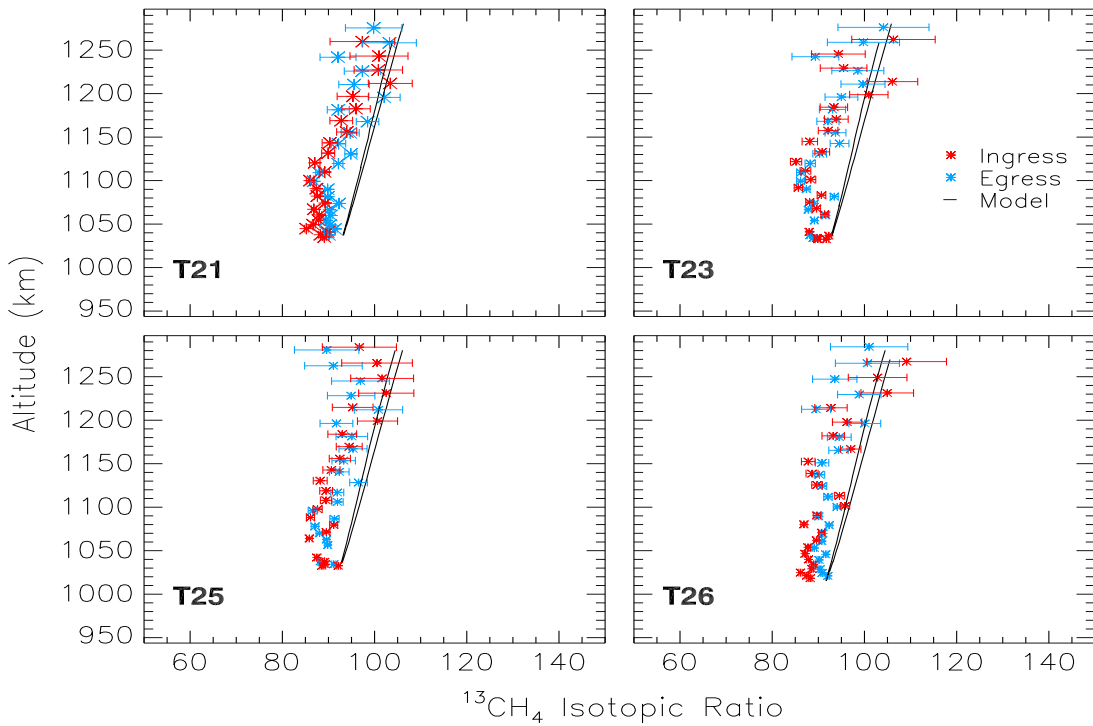


(b) T-GITM and INMS flyby comparison for T37 - T40

Figure 6.10: T-GITM and INMS $^{14}\text{N}/^{15}\text{N}$ comparisons for the T28 through the T40 flybys.

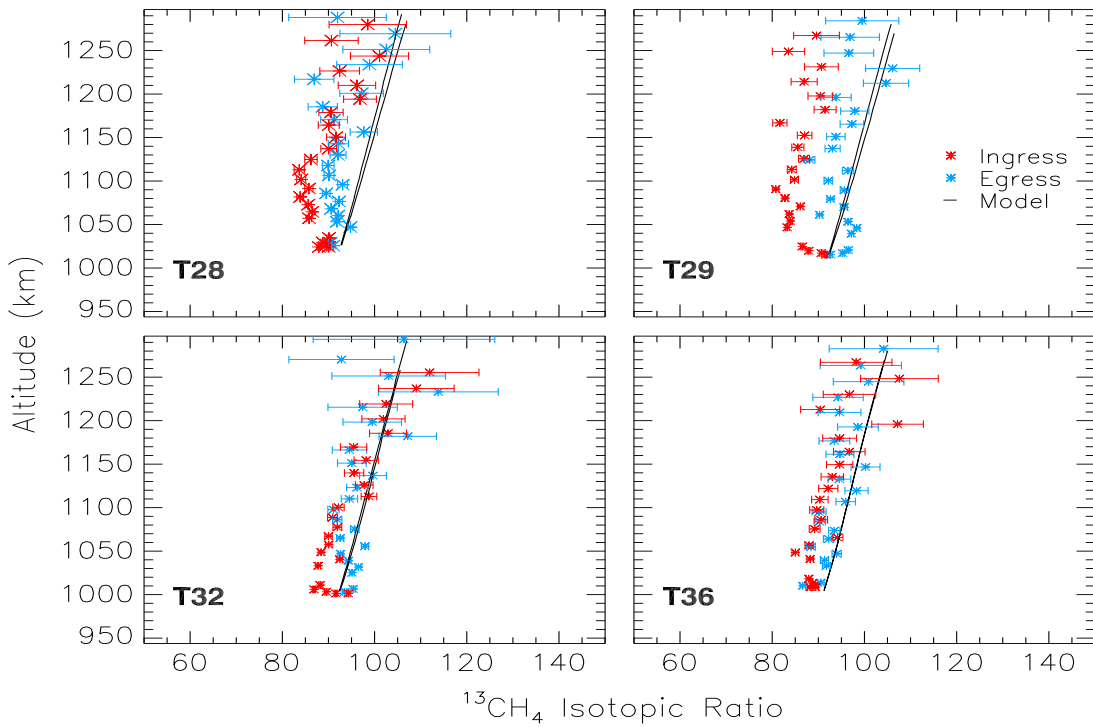


(a) T-GITM and INMS flyby comparison for T5 - T19

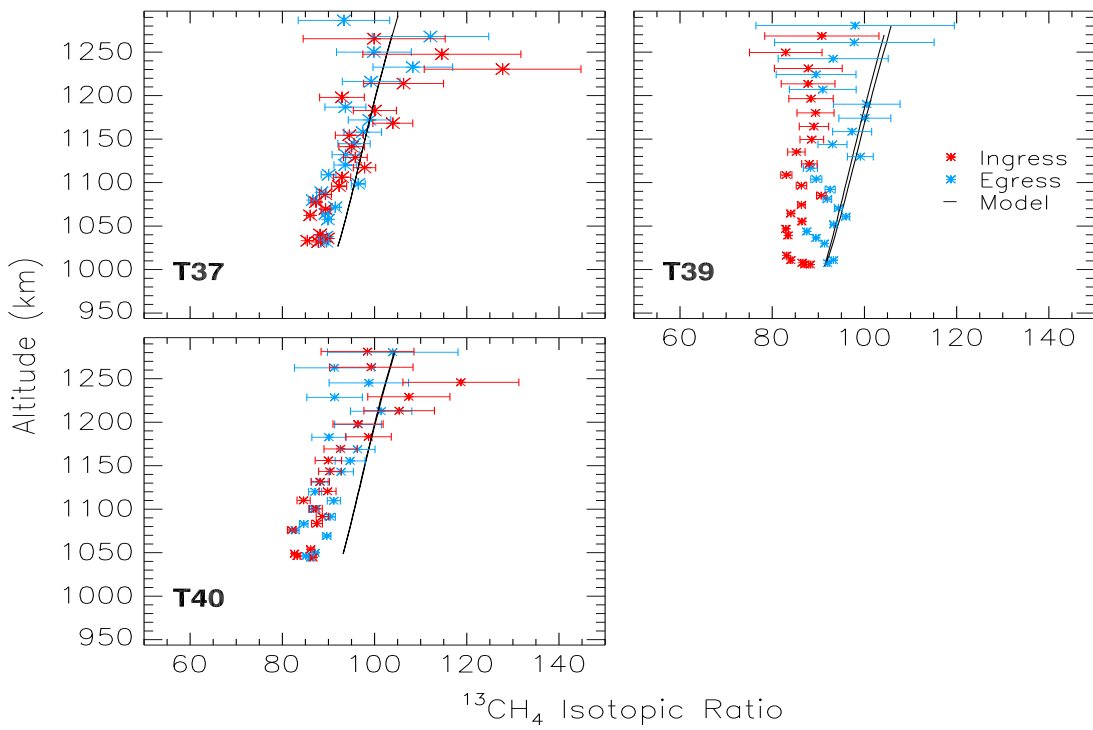


(b) T-GITM and INMS flyby comparison for T21 - T26

Figure 6.11: T-GITM and INMS $^{12}\text{C}/^{13}\text{C}$ comparisons for the T5 through the T26 flybys.



(a) T-GITM and INMS flyby comparison for T28 - T36



(b) T-GITM and INMS flyby comparison for T37 - T40

Figure 6.12: T-GITM and INMS $^{12}\text{C}/^{13}\text{C}$ comparisons for the T28 through the T40 flybys.

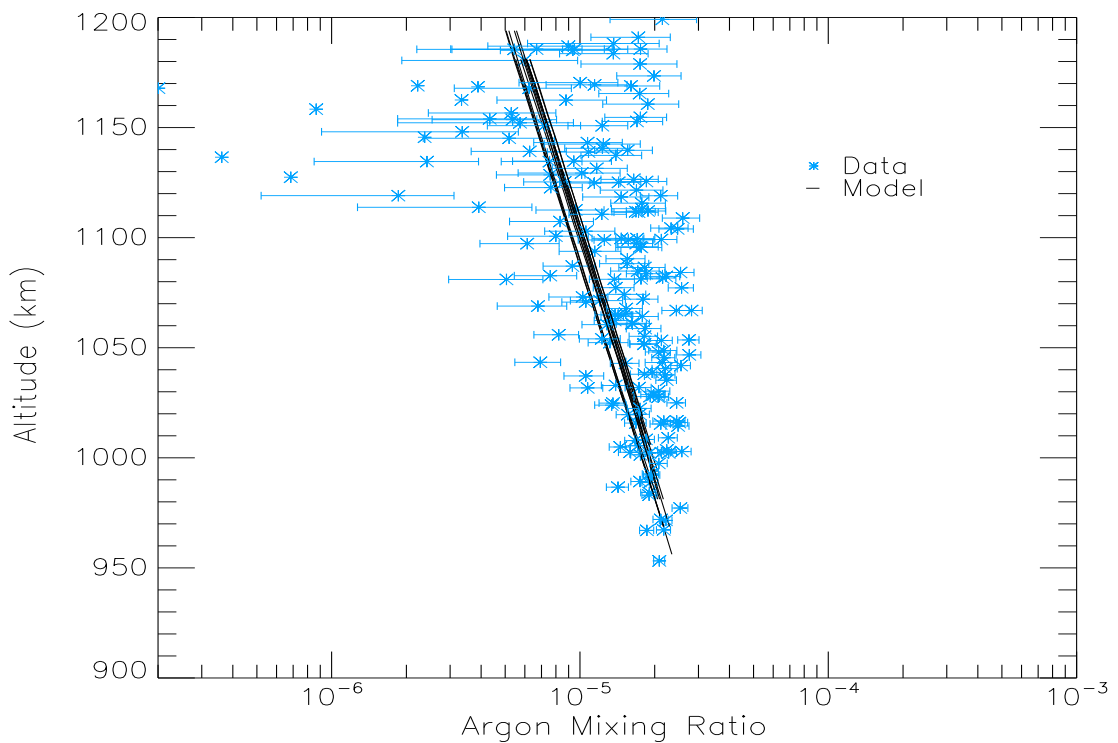


Figure 6.13: T-GITM and INMS Ar mixing ratio scatter plot over all available flybys.

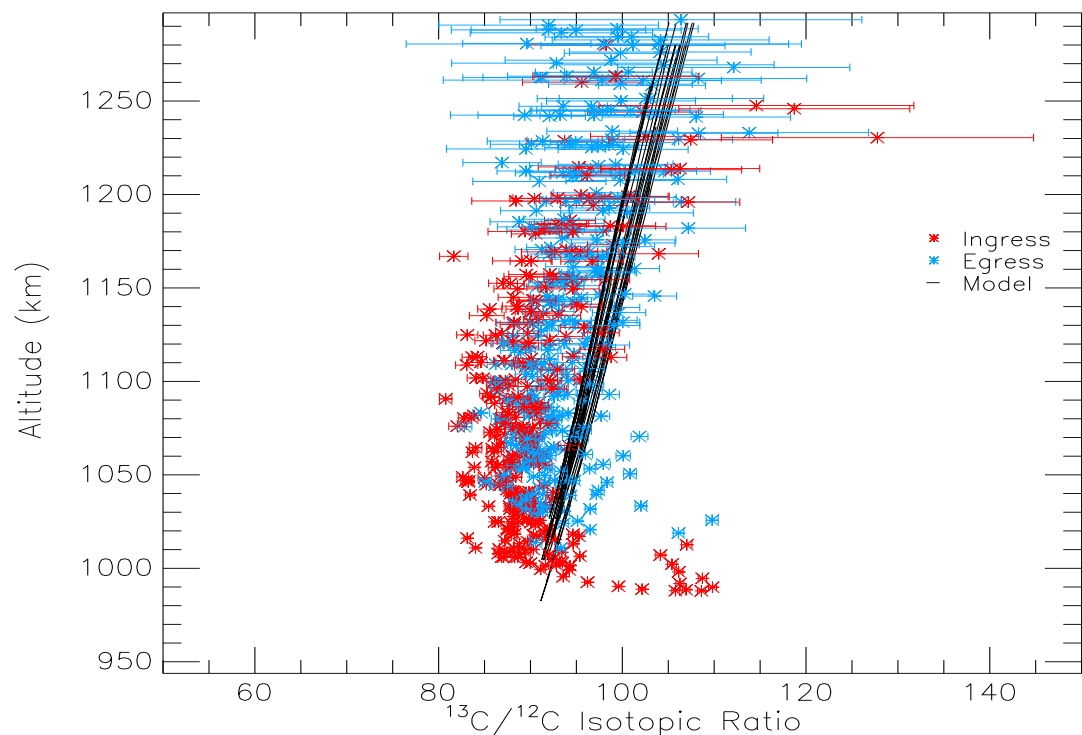


Figure 6.14: T-GITM and INMS $^{12}\text{C}/^{13}\text{C}$ scatter plot over all available flybys.

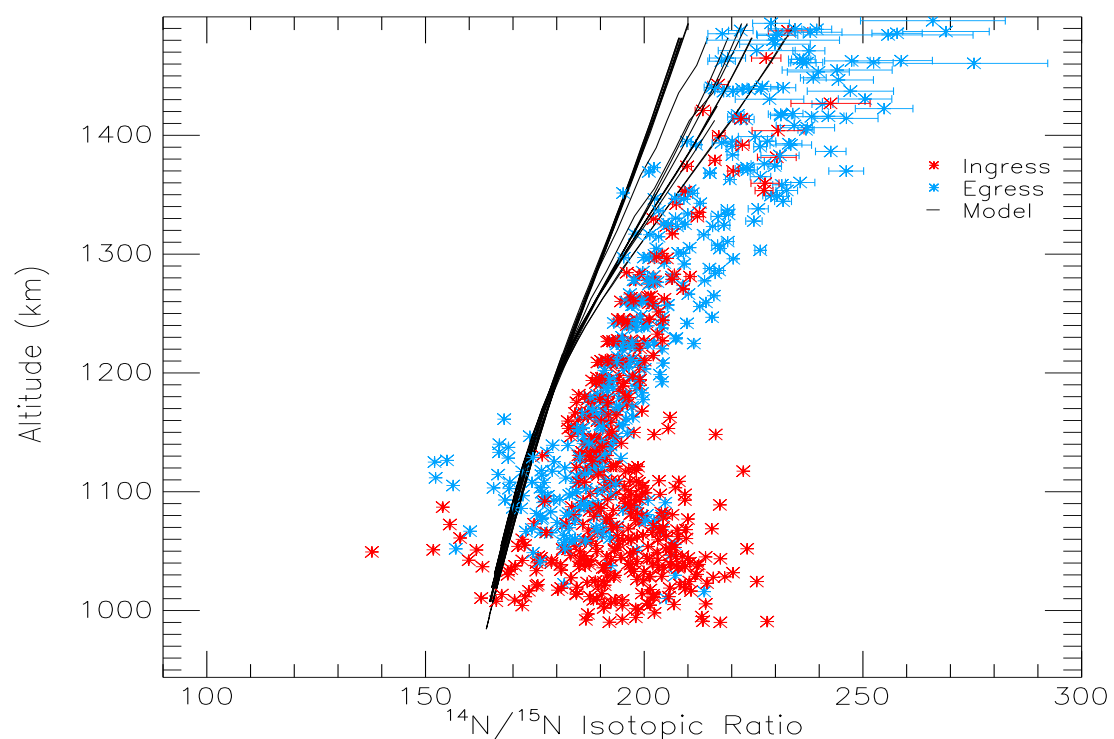


Figure 6.15: T-GITM and INMS $^{14}\text{N}/^{15}\text{N}$ scatter plot comparisons.

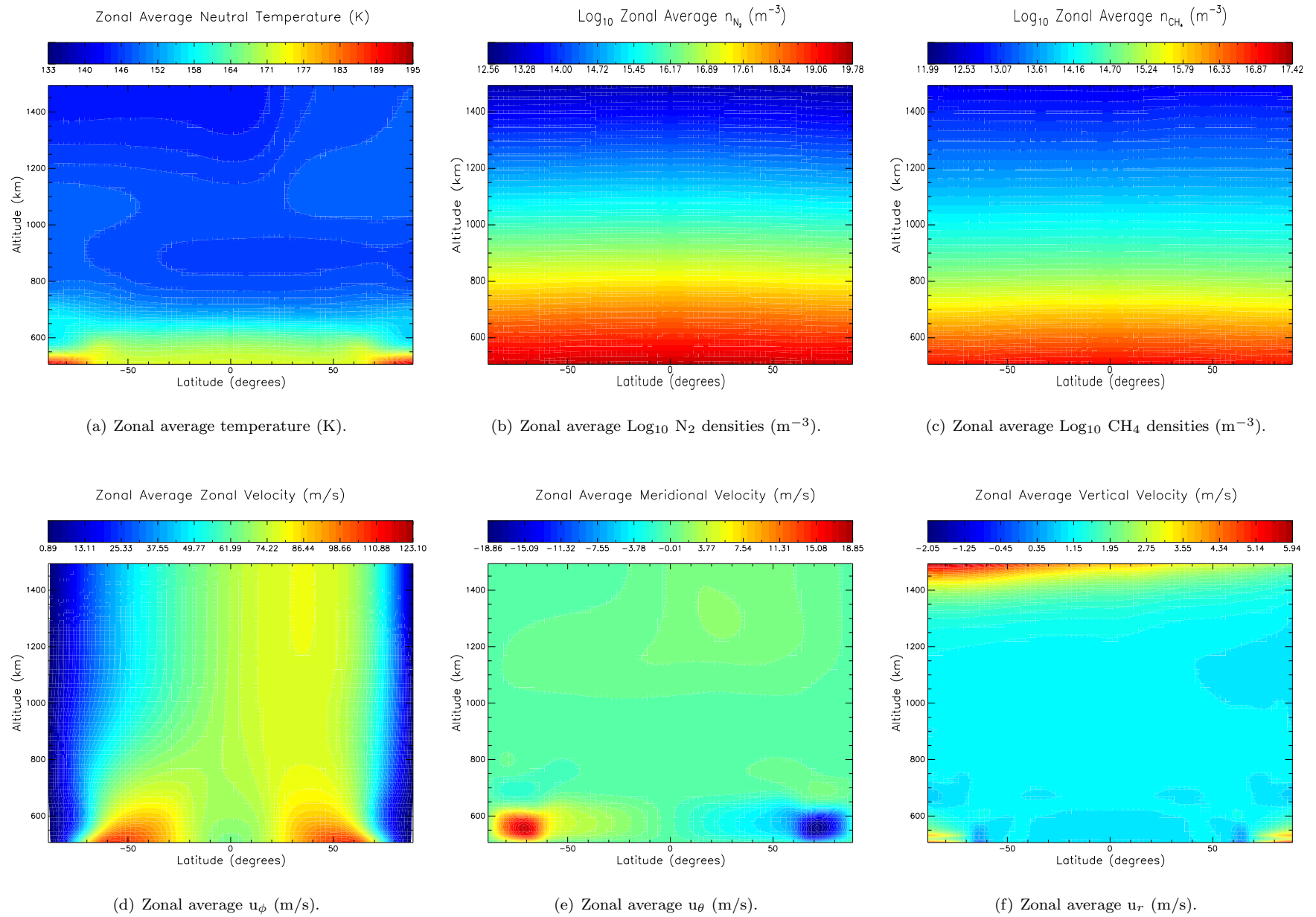


Figure 6.16: Key zonal average prognostic fields for the T5-T40 flyby simulation.

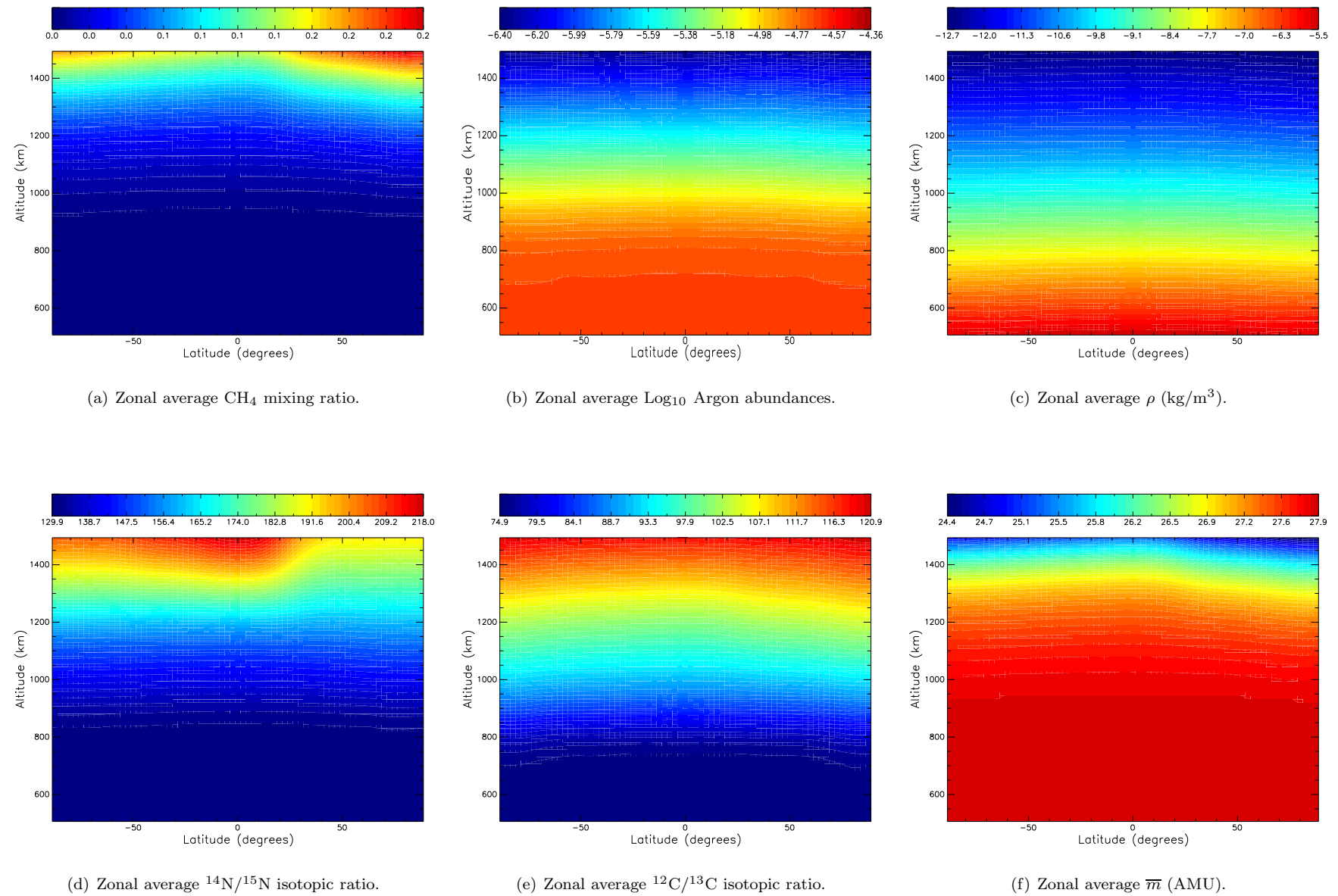


Figure 6.17: Additional key zonal average prognostic fields for the T5-T40 flyby simulation.

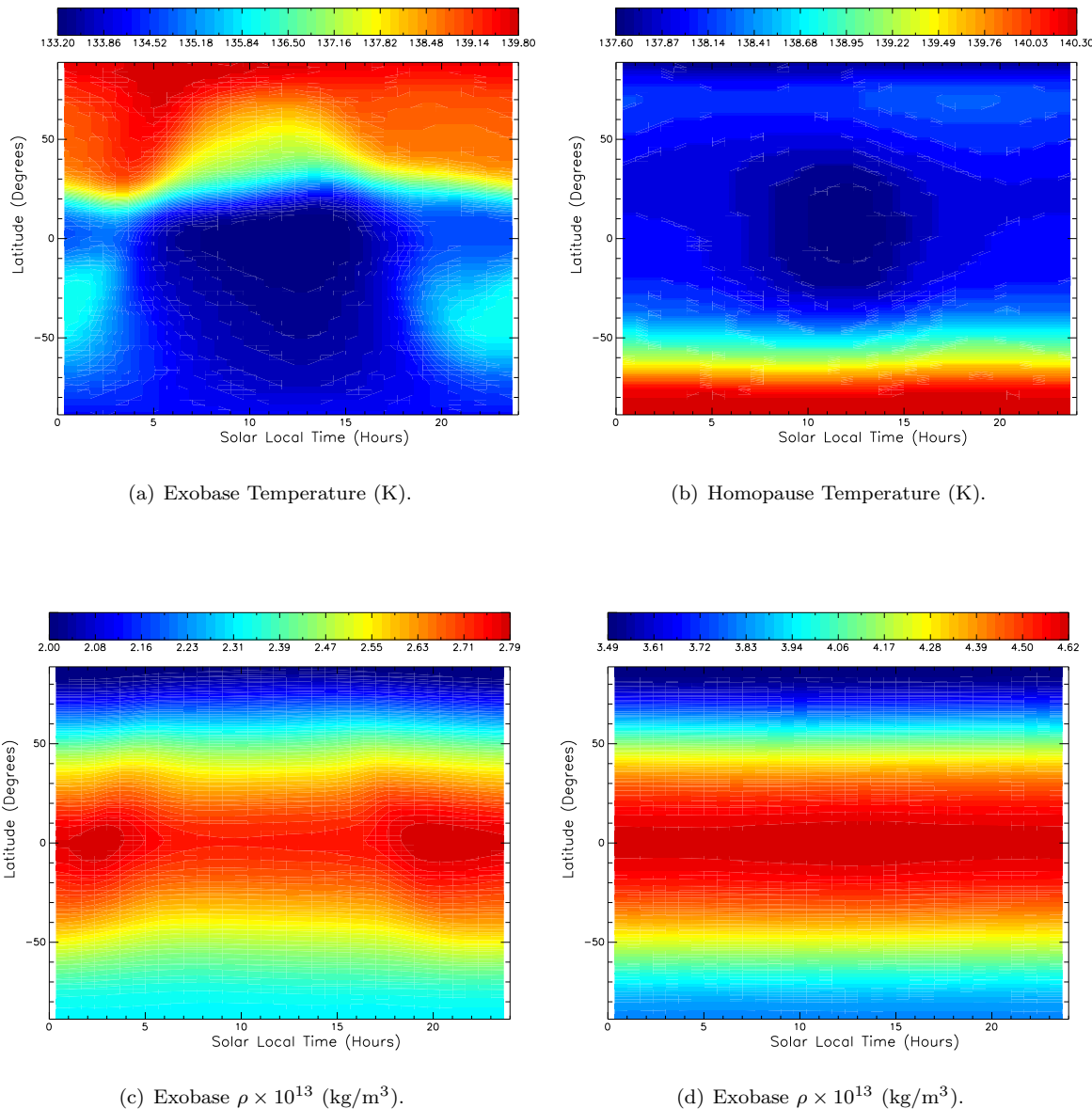
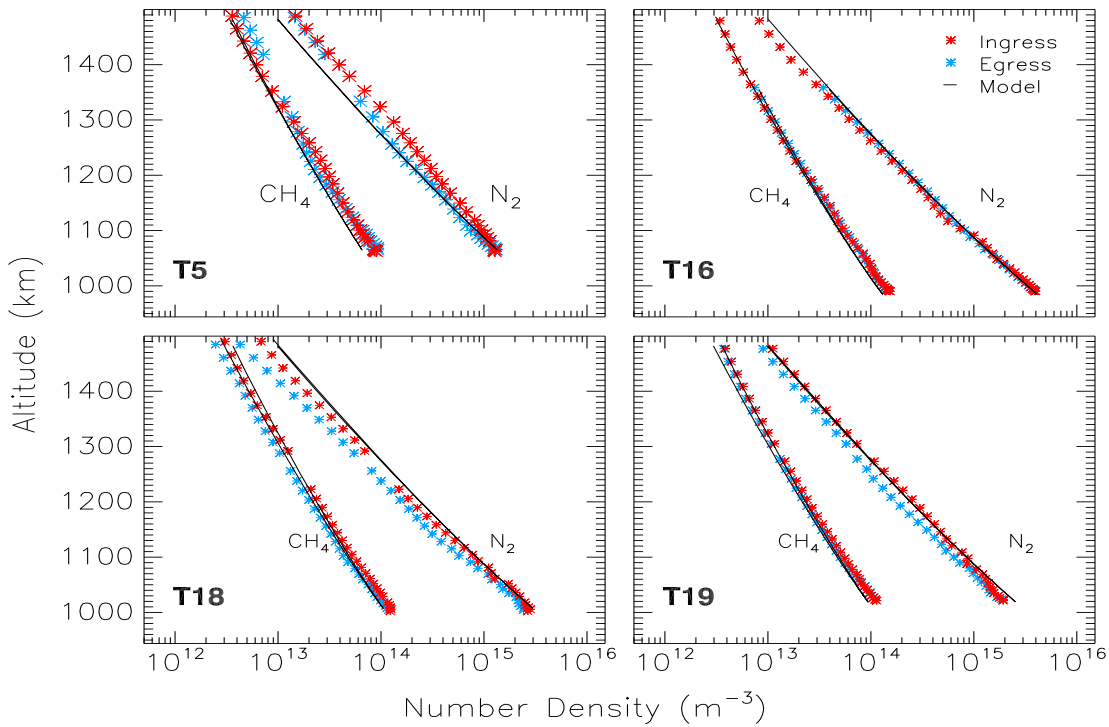
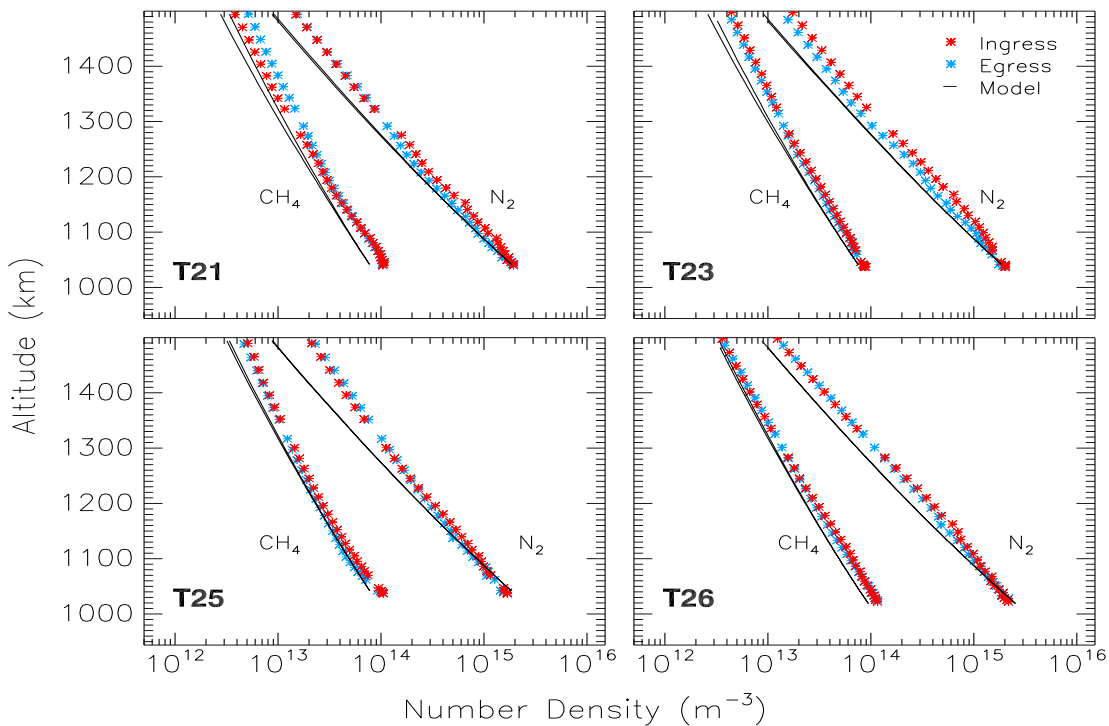


Figure 6.18: Altitude slices of temperature and mass density, ρ at the exobase and homopause for the T5-T40 flyby simulation. Note that ρ is scaled by 10^{13} in panel (c) and by 10^9 in panel (d) for ease of plotting.

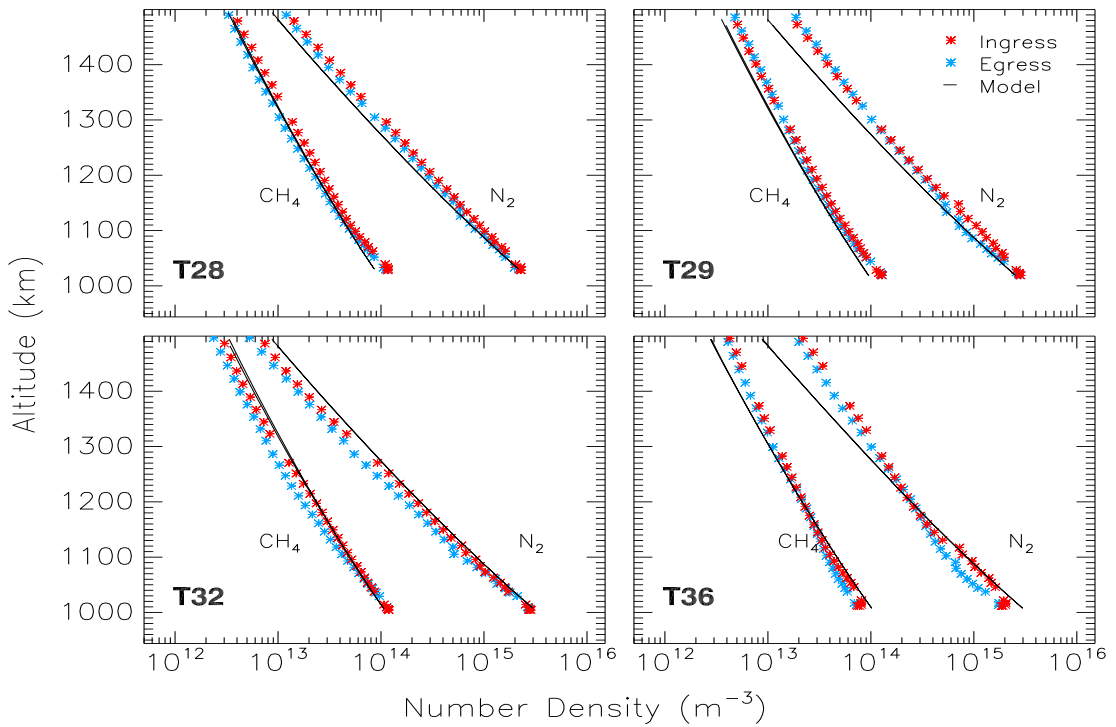


(a) T-GITM and INMS flyby comparison for T5 - T19 (Non Super-Rotating).

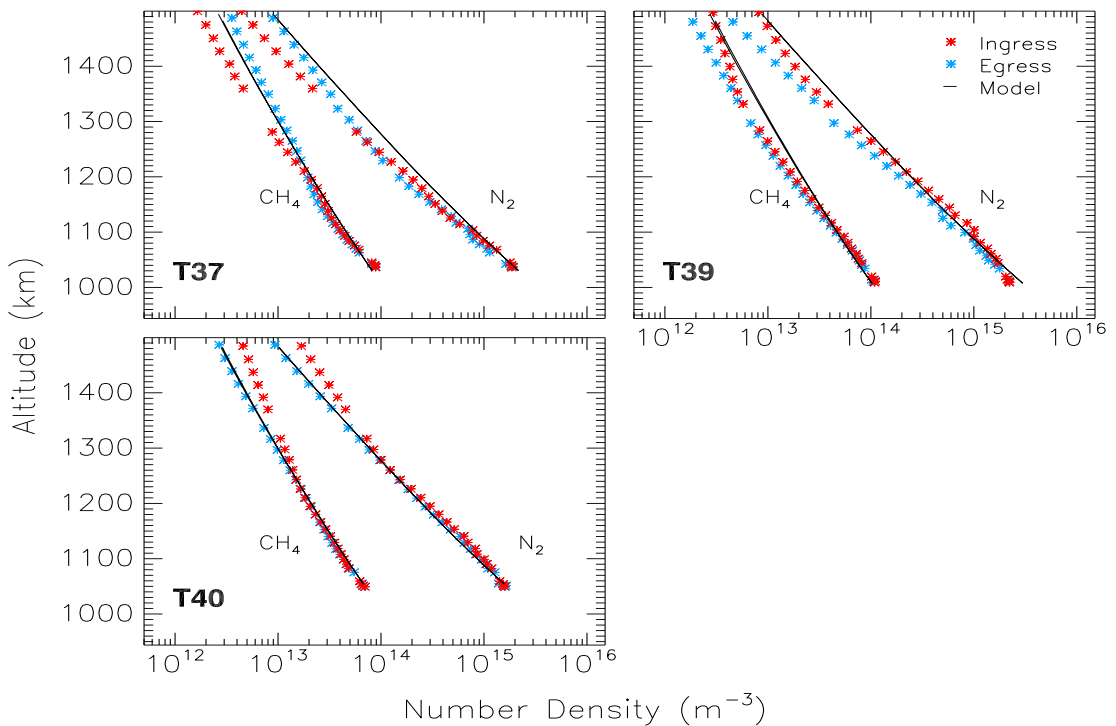


(b) T-GITM and INMS flyby comparison for T21 - T26 (Non Super-Rotating).

Figure 6.19: T-GITM and INMS N_2 and CH_4 density comparisons for the T5 through the T26 flybys (Non Super-Rotating).

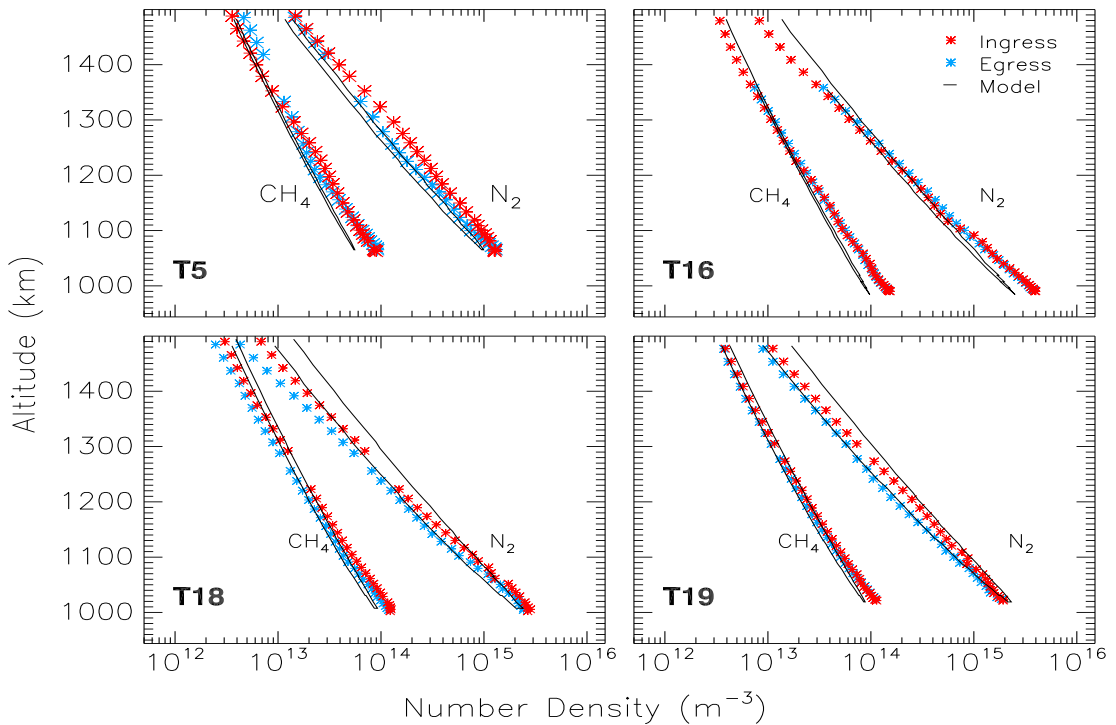


(a) T-GITM and INMS flyby comparison for T28 - T36 (Non Super-Rotating)

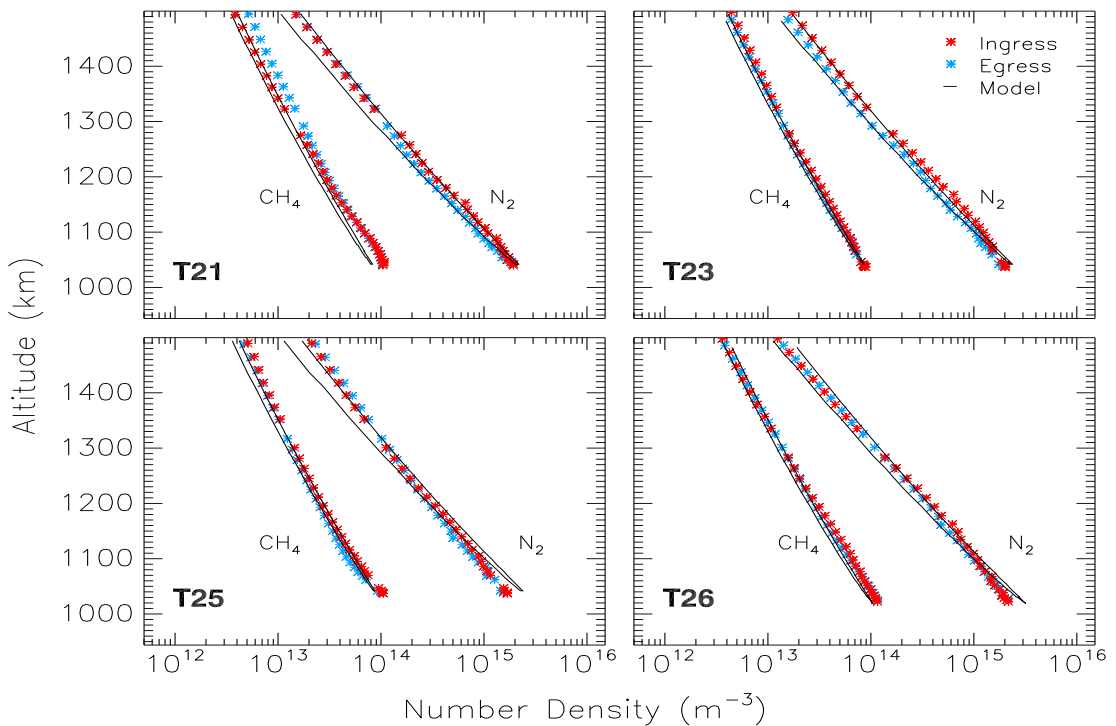


(b) T-GITM and INMS flyby comparison for T37 - T40 (Non Super-Rotating)

Figure 6.20: T-GITM and INMS N₂ and CH₄ density comparisons for the T28 through the T40 flybys (Non Super-Rotating).

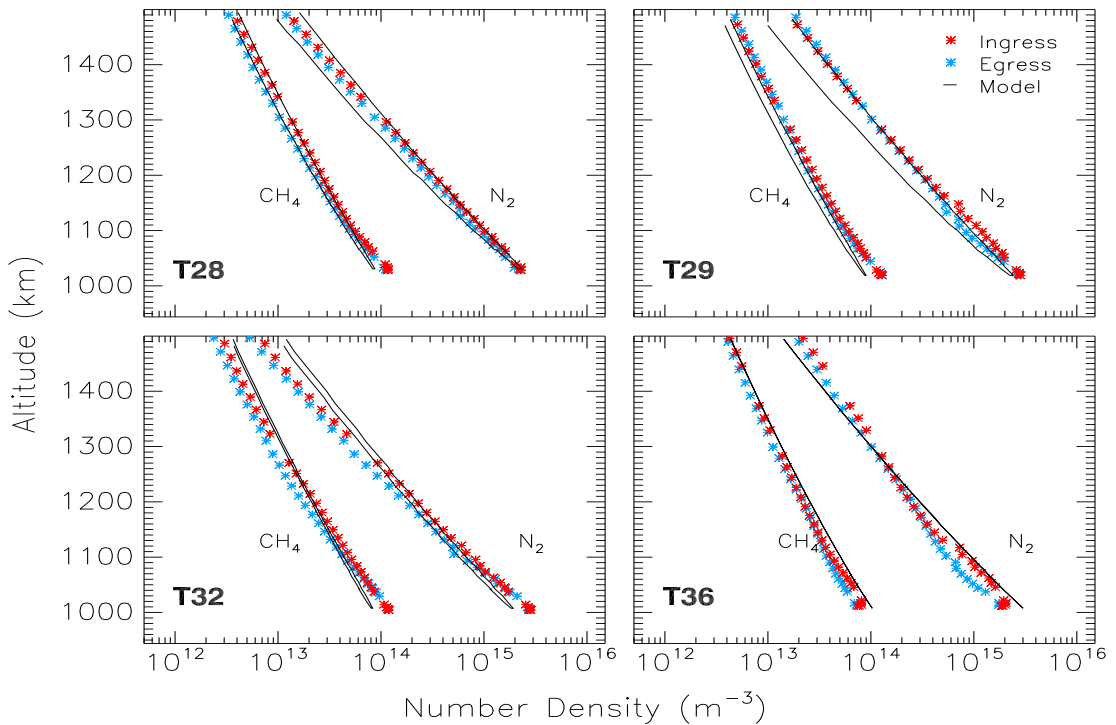


(a) T-GITM and INMS flyby comparison for T5 - T19 (Strongly Super-Rotating).

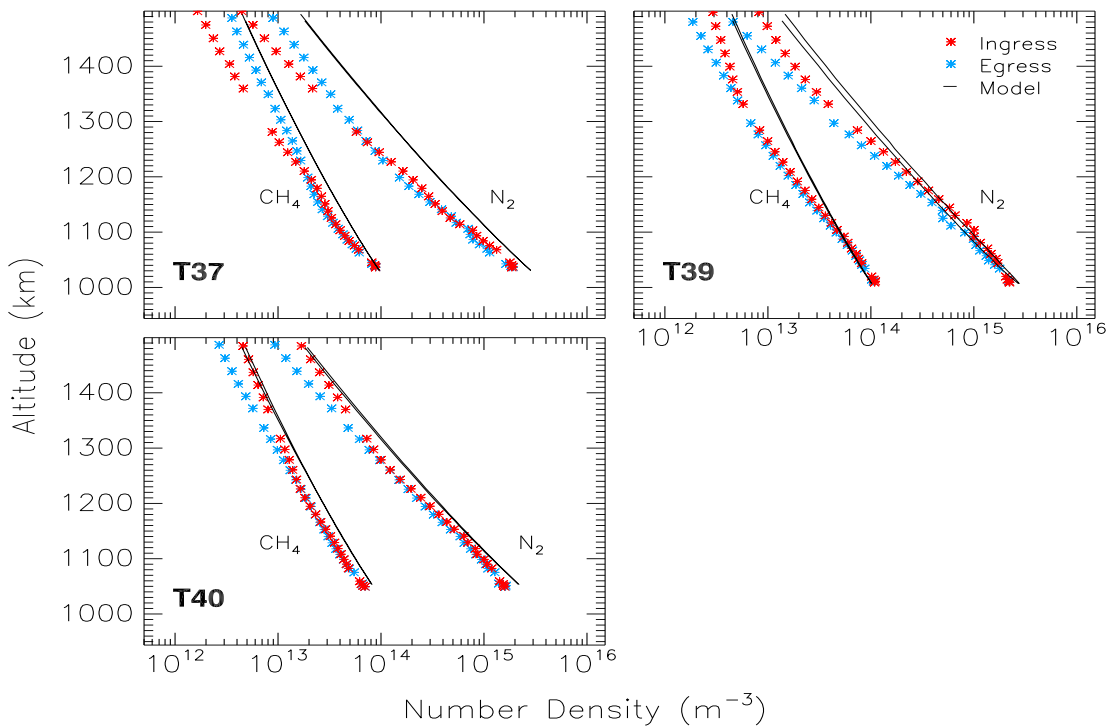


(b) T-GITM and INMS flyby comparison for T21 - T26 (Strongly Super-Rotating).

Figure 6.21: T-GITM and INMS N_2 and CH_4 density comparisons for the T5 through the T26 flybys (Strongly Super-Rotating).

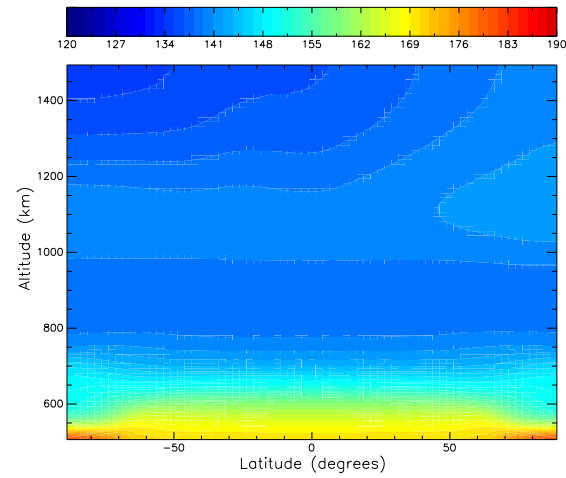


(a) T-GITM and INMS flyby comparison for T28 - T36 (Strongly Super-Rotating)

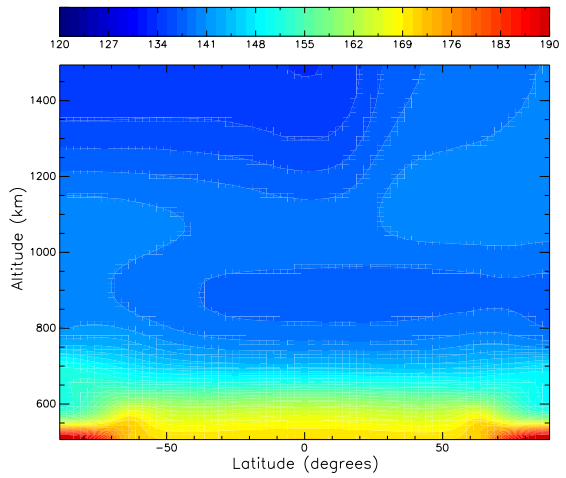


(b) T-GITM and INMS flyby comparison for T37 - T40 (Strongly Super-Rotating)

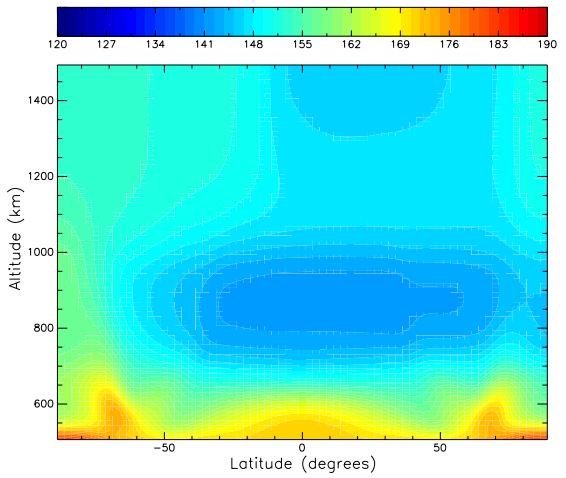
Figure 6.22: T-GITM and INMS N_2 and CH_4 density comparisons for the T28 through the T40 flybys (Strongly Super-Rotating).



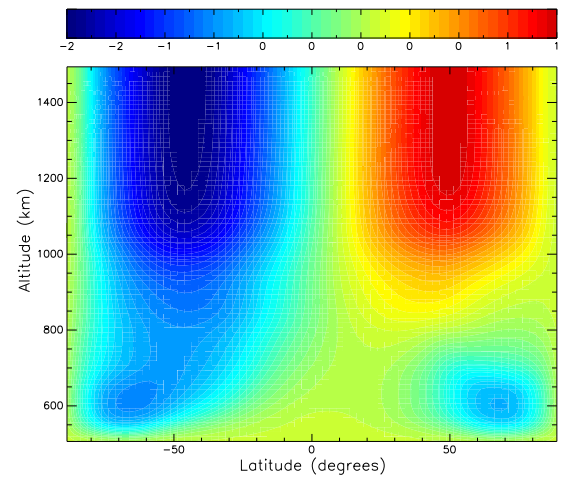
(a) Non super-rotating zonal average temperature (K).



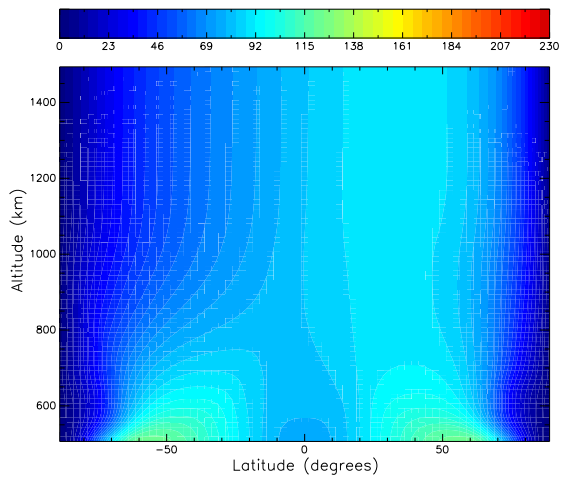
(b) Moderately super-rotating zonal average temperature (K).



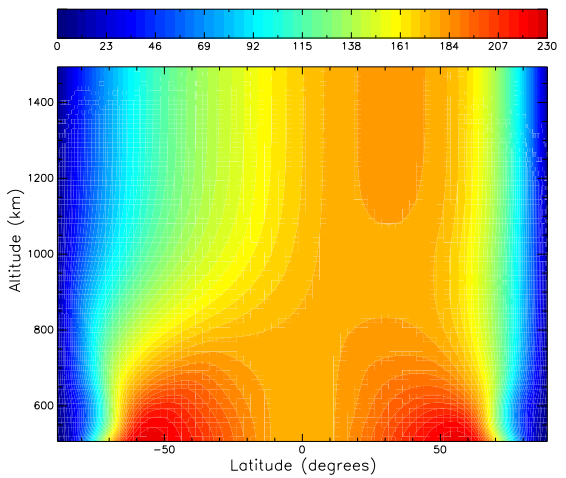
(c) Strongly super-rotating zonal average temperature (K).



(d) Non super-rotating zonal average u_ϕ (m/s).



(e) Moderately super-rotating zonal average u_ϕ (m/s).



(f) Strongly super-rotating zonal average u_ϕ (m/s).

Figure 6.23: Zonal average temperatures and u_ϕ for the three lower boundary cases.

CHAPTER VII

Conclusions and Discussion

APPENDICES

APPENDIX A**Photoabsorption Cross-Sections**

Table A.1: N_2 Photoabsorption Cross-Sections and Quantum Yields

Wavelength Bins (Å)	N ₂ Photoabsorption Cross-Section (10^{-18} cm^2)	Quantum Yield		
		N(⁴ S) + N(² D)	N ₂ ⁺	N ⁺ + N(⁴ S)
1700 – 1750	0.0	0	0	0
1650 – 1700	0.0	0	0	0
1600 – 1650	0.0	0	0	0
1550 – 1600	0.0	0	0	0
1500 – 1550	0.0	0	0	0
1450 – 1500	0.0	0	0	0
1400 – 1450	0.0	0	0	0
1350 – 1400	0.0	0	0	0
1300 – 1350	0.0	0	0	0
1250 – 1300	0.0	0	0	0
1200 – 1250	0.0	0	0	0
1215.67	0.0	0	0	0
1150 – 1200	0.0	0	0	0
1100 – 1150	0.0	0	0	0
1050 – 1100	0.0	0	0	0
1000 – 1050	0.0	0	0	0
1031.91	0.0	0	0	0
1025.72	0.0	0	0	0
950 – 1000	50.980	1.0	0	0
977.02	2.240	1.0	0	0
900 – 950	9.680	1.0	0	0
850 – 900	20.249	1.0	0	0
800 – 850	16.992	1.0	0	0
750 – 800	33.579	0.5749	0.4251	0
789.36	16.487	0.4626	0.5374	0
770.41	14.180	0.4006	0.5994	0
765.15	120.490	0.4539	0.5461	0
700 – 750	24.662	0.3893	0.6107	0
703.36	26.540	0.0399	0.9601	0
650 – 700	31.755	0.0794	0.9206	0
600 – 650	23.339	0	1.0	0
629.73	23.370	0	1.0	0
609.76	22.790	0	1.0	0
550 – 600	22.787	0	1.0	0
584.33	22.400	0	1.0	0
554.37	24.130	0	1.0	0
500 – 550	24.501	0	0.9987	0.0013
450 – 500	23.471	0	0.9702	0.0298
465.22	23.160	0	0.9542	0.0458
400 – 450	21.675	0	0.9546	0.0453
350 – 400	16.395	0	0.8947	0.1053
368.07	16.910	0	0.9077	0.0923
300 – 350	13.857	0	0.8371	0.1629
303.78	11.700	0	0.7872	0.2128
303.31	11.670	0	0.7866	0.2134
250 – 300	10.493	0	0.7002	0.2997
284.78	10.900	0	0.7431	0.2569
256.30	10.210	0	0.6642	0.3350
200 – 250	8.392	0	0.6227	0.3773
150 – 200	4.958	0	0.6359	0.3641
100 – 150	2.261	0	0.6541	0.3459
50 – 100	0.720	0	0.6153	0.3847
32 – 50	0.152	0	0.4350	0.5360
23 – 32	1.190	0	0.0151	0.8150
16 – 23	0.504	0	0.0151	0.7320

Table A.2: CH_4 Photoabsorption Cross-Sections and Quantum Yields

Wavelength Bins (\AA)	CH ₄ Photoabsorption Cross-Section (10^{-18} cm^2)	Quantum Yield				
		CH ₃	³ CH ₂	¹ CH ₂	CH	CH ₃ ⁺
1700 – 1750	0.0	1	0	0	0	0
1650 – 1700	0.0	1	0	0	0	0
1600 – 1650	0.0	1	0	0	0	0
1550 – 1600	7.0×10^{-6}	1	0	0	0	0
1500 – 1550	1.4×10^{-5}	1	0	0	0	0
1450 – 1500	7.99×10^{-4}	1	0	0	0	0
1400 – 1450	0.126	1	0	0	0	0
1350 – 1400	3.2898	1	0	0	0	0
1300 – 1350	12.826	1	0	0	0	0
1250 – 1300	19.068	1	0	0	0	0
1200 – 1250	18.318	1	0	0	0	0
1215.67	17.86	0.41	0.21	0.28	0.10	0
1150 – 1200	19.2	1	0	0	0	0
1100 – 1150	18.0	1	0	0	0	0
1050 – 1100	28.4	1	0	0	0	0
1000 – 1050	29.108	1	0	0	0	0
1031.91	30.121	1	0	0	0	0
1025.72	32.7	1	0	0	0	0
950 – 1000	38.192	0.9876	0	0	0	0
977.02	41.154	0.9967	0	0	0	0
900 – 950	48.001	0.7112	0	0	0	0
850 – 900	48.968	0.4787	0	0	0	0.264
800 – 850	48.327	0.1664	0	0	0	0.3032
750 – 800	45.921	0.0267	0	0	0	0.4605
789.36	46.472	0.0401	0	0	0	0.4497
770.41	45.716	0.0201	0	0	0	0.4663
765.15	45.458	0.0145	0	0	0	0.4716
700 – 750	42.927	0	0	0	0	0.4857
703.36	41.069	0	0	0	0	0.4892
650 – 700	39.280	0	0	0	0	0.4905
600 – 650	34.990	0	0	0	0	0.4979
629.73	35.276	0	0	0	0	0.4959
609.76	33.178	0	0	0	0	0.5039
550 – 600	30.697	0	0	0	0	0.5008
584.33	31.052	0	0	0	0	0.4992
554.37	27.924	0	0	0	0	0.4961
500 – 550	24.644	0	0	0	0	0.4859
450 – 500	21.449	0	0	0	0	0.4761
465.22	18.770	0	0	0	0	0.4676
400 – 450	14.701	0	0	0	0	0.4471
350 – 400	9.776	0	0	0	0	0.4195
368.07	10.165	0	0	0	0	0.4235
300 – 350	7.829	0	0	0	0	0.3970
303.78	6.059	0	0	0	0	0.3799
303.31	6.033	0	0	0	0	0.3791
250 – 300	4.36	0	0	0	0	0.3472
284.78	5.053	0	0	0	0	0.3610
256.30	3.857	0	0	0	0	0.3345
200 – 250	2.794	0	0	0	0	0.3164
150 – 200	1.496	0	0	0	0	0.2734
100 – 150	0.593	0	0	0	0	0.2563
50 – 100	0.204	0	0	0	0	0.2549
32 – 50	0.4535	0	0	0	0	0.5835
23 – 32	0.421	0	0	0	0	0.6684
16 – 23	0.1643	0	0	0	0	0.6875

APPENDIX B

Hydrogen Cyanide (HCN) Radiative Transfer Model

B.1 HCN Rotational Cooling: Formalism

This appendix covers the details of the University of Michigan Titan Global Thermosphere-Ionosphere Model (T-GITM's) Hydrogen Cyanide (HCN) Rotational Cooling Routine. This program represents a line-by-line radiative transfer calculation routine, dealing with the rotational levels in the ground vibrational state. Furthermore, the HCN molecule's rotational levels are assumed to be in Local Thermodynamic Equilibrium (LTE). LTE allows us to use Planck's function as the source function, which depends only on the local temperatures and densities. Thus, no redistribution functions are needed in order to solve a non-local scattering process.

The proper empirical parameters were gathered and used to numerically calculate the solution to the radiative transfer equation:

$$(B.1) \quad \frac{\partial I_\nu(p, \theta, \phi)}{\partial \tau} = I_\nu(p, \theta, \phi) - S_\nu(p, \theta, \phi)$$

B.2 HCN's Rotational Lines

As stated in the introduction, HCN's ground vibrational state has 116 spectroscopically distinct rotational lines. These lines are assumed to be in LTE, which

ensures that their populations remain governed by the easily calculated Planck Function. Furthermore, we may ignore such processes as scattering which are non-local in character.

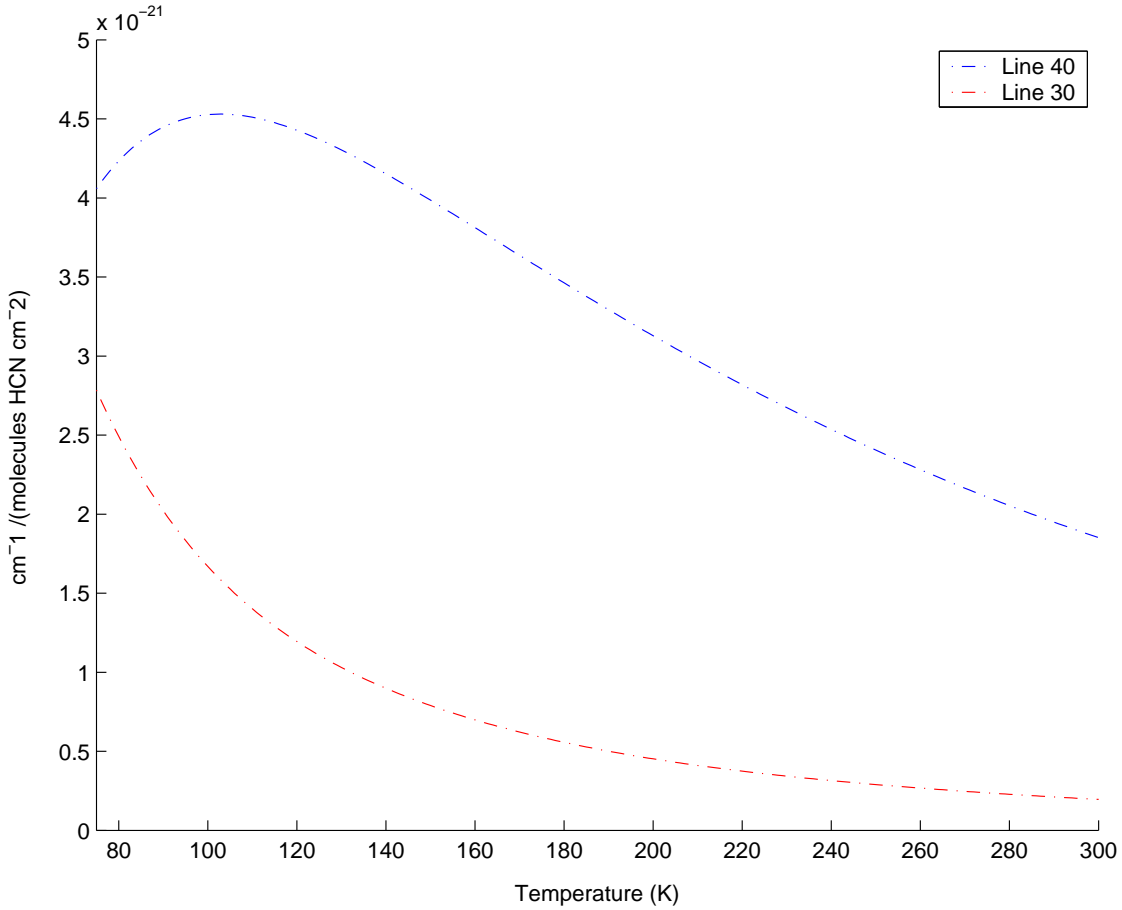
The 116 lines were obtained from the 2001 edition of the HITRAN database (L Rothmann et al 2003). From this database, all necessary line parameters were extracted:

1. Line strength
2. Pressure Broadening coefficient (Lorentz halfwidth)
3. The line position in wavenumbers, cm^{-1}

Furthermore, each line parameter could be varied as a function of temperature. Extensive testing was performed on this database to produce a set of data that spanned temperature ranges from 75K to 300K. With this database compiled, the resulting line strengths were interpolated with an 8-degree polynomial that was then incorporated into the 1-D and 3-D HCN cooling routines. MATLAB was used to generate the 8-th order polynomial for this purpose. For a single rotational line, one can easily plot the line intensity as a function of Temperature from 75 K to 300 K, as shown in Figure B.2.

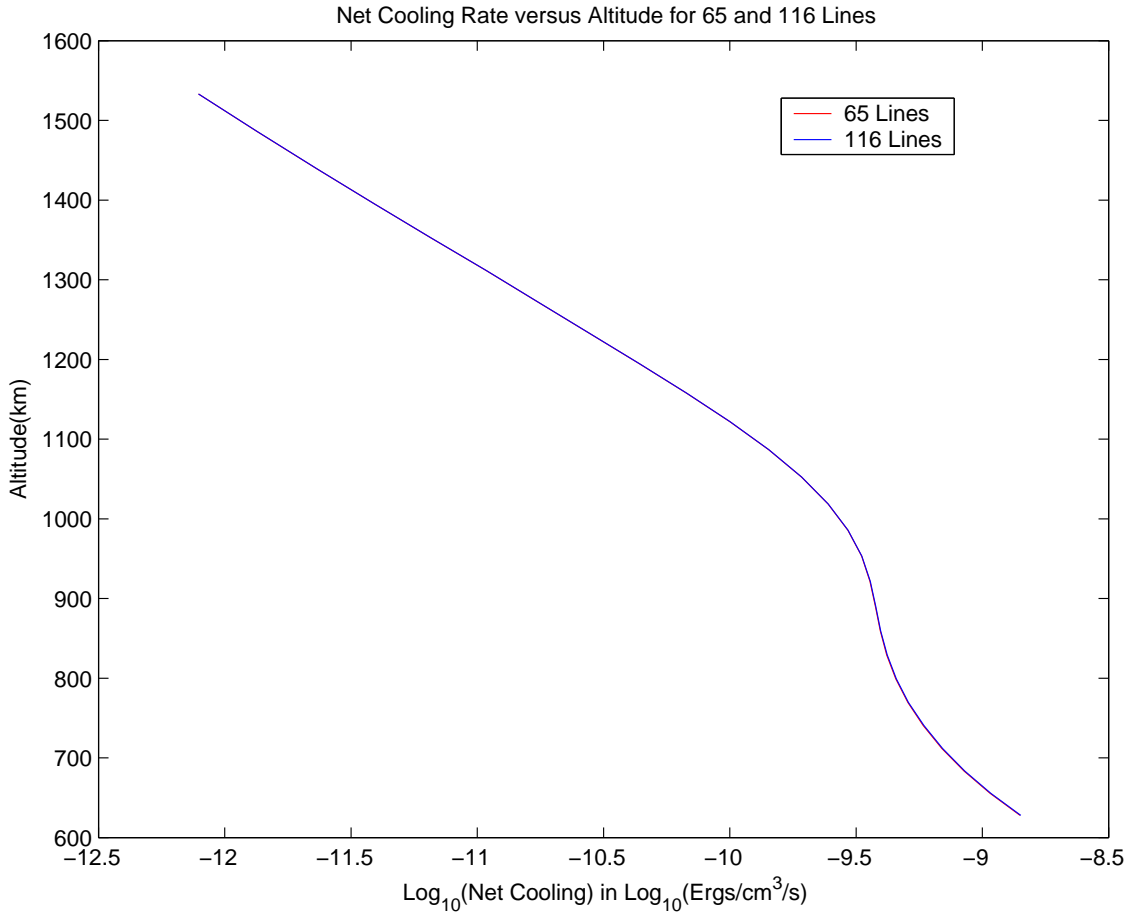
This figure illustrates how the HCN Cooling Routines calculate intensity as a function of temperature and individual line number. Thus, there are necessarily 116 8-degree polynomials to describe the intensity of the rotational lines given atmospheric conditions.

However, we next evaluated how many of these rotational lines significantly contributed to the overall cooling between the temperatures of 75K to 300K. We found that a significant number of the original 116 distinct rotational lines of HCN could be



eliminated from the cooling calculations without affecting the results. We did this by defining a mean intensity at a given temperature and eliminated all lines that were a factor of 10^{-3} of that mean given the expected thermal range in Titan's upper atmosphere (75K to 300K). Clearly, for $T < 75\text{K}$ and $T > 300\text{ K}$, our approximations will break down and we will necessarily need to include all 116 original rotational lines.

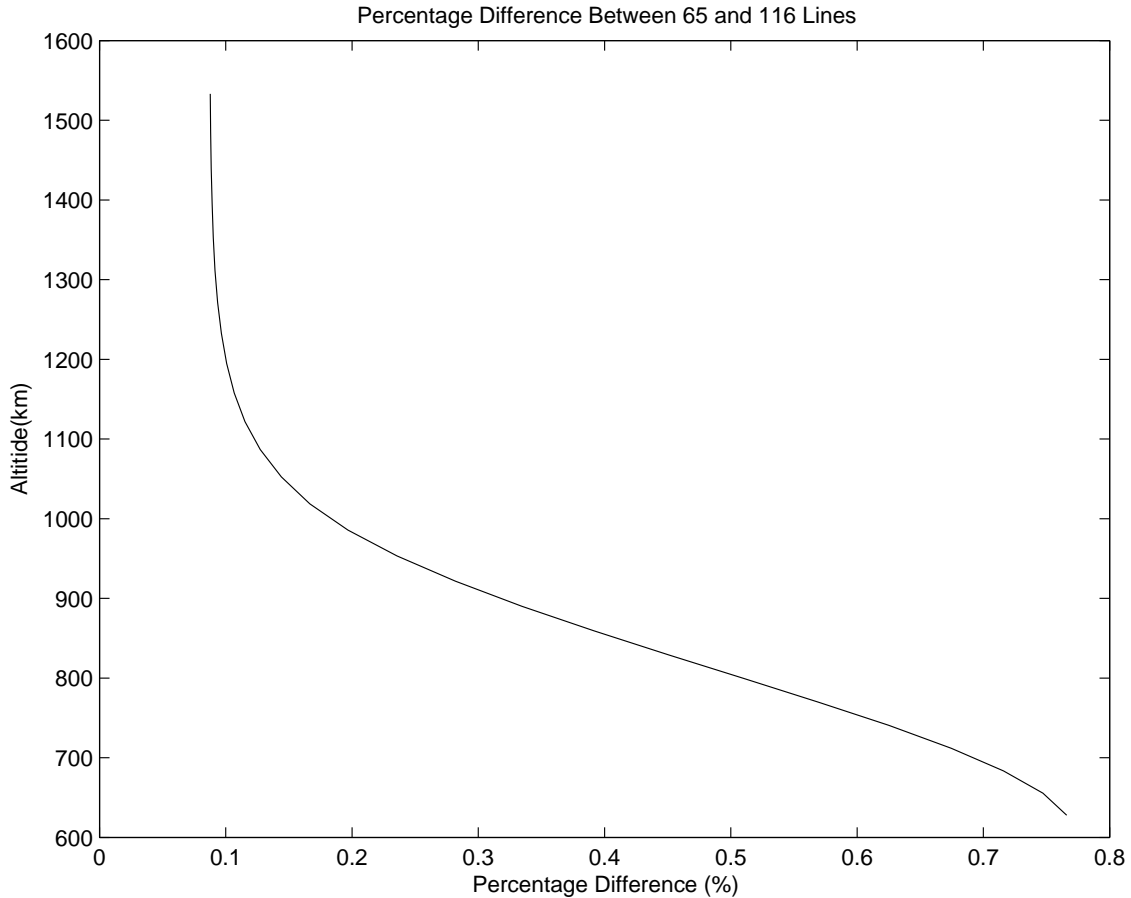
The results of our approximations are illustrated in figures 2 and 3 below. Figure B.2 shows the full line-by-line code's results using the same density input profiles (Lebonnois 2001) with 116 lines and 65 lines alternatively. Clearly the differences are hardly discernable. This fact is made concrete in Figure B.2. Figure B.2 illustrates the percentage difference between the two methods. Again, we see that the



percentage difference remains quite small. When comparing this small systematic error in the number of lines with the nearly 50 % error in the number density of HCN in Titan's upper atmosphere one can truly see how this remains essentially in the noise. Also, the computational time costs significantly decrease by reducing the number of rotational lines from 116 to 65.

B.3 Line Profiles

In the previous chapter, we looked into reducing the overall number of lines from 116 to 65, thereby greatly increasing overall numerical efficiency and introducing a negligible amount of error. Next, given these well-separated 65 individual rotational lines, how do we go about describing their interactions with radiation? The lineshape

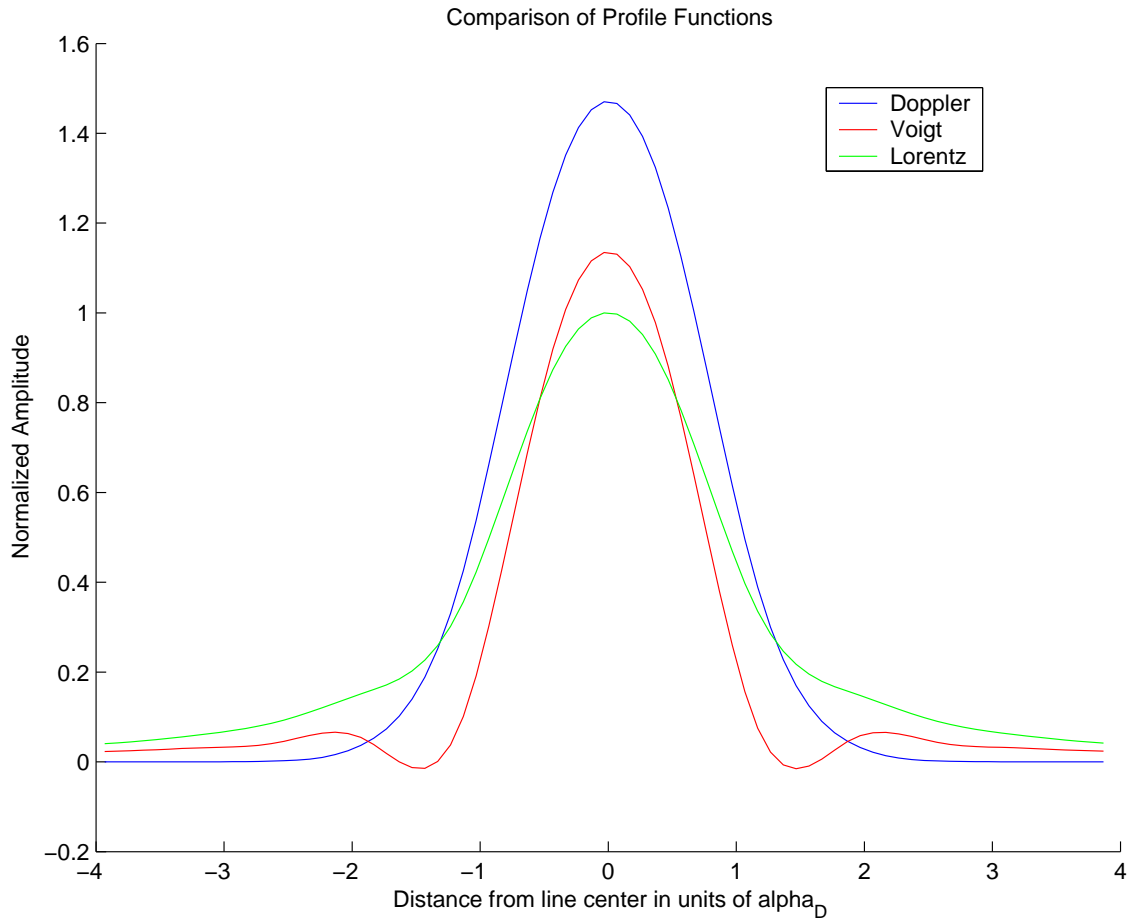


or line profile is effectively a response function for each rotational line to incident radiation. These line shapes vary in flavor according to which processes dominate the species under consideration. In what follows, we'll explore the impacts of choosing the various line shapes and the results from the radiative transfer model will be illustrated.

B.3.1 Lorentz Profiles

The Lorentz Profile represents the shape of a spectral line when collisions dominate the particle's motion. The mathematical description of the Lorentz Profile is as follows:

$$(B.2) \quad \phi_L(\nu) = \left(\frac{\alpha_L}{\pi}\right) \frac{1}{\alpha_L^2 + (\nu - \nu_j)^2}$$



where

1. ν is the frequency of interest.
2. ν_j is the line center corresponding to a specific rotational transition.
3. α_L is the pressure broadening halfwidth empirically acquired from HITRAN.

The Lorentz profile, like all line profiles, effectively describe how a given line will respond to incident radiation as a function of frequency. Thus, the profile looks like the famous Lorentz function, instead of an idealized dirac-delta function at the line center. Hence, the line is "smeared out" in appearance, as shown in Figure B.3.1.

B.3.2 Doppler Profile

The Doppler profile emerges as the dominant spectral line shape when collisions no longer dominate a particle's dynamics (i.e. at higher altitudes in the atmosphere). The Doppler profile is mathematically simply a gaussian centered on the spectral line frequency. However, the doppler profile depends upon the speed at which the particles are moving, hence the "Doppler" portion in the name. Mathematically, the doppler profile is as follows:

$$(B.3) \quad \phi_D(\nu) = \left(\frac{1}{\alpha_D \sqrt{\pi}} \right) \exp - \left(\frac{(\nu - \nu_j)^2}{\alpha_D^2} \right)$$

In this equation the terms are as follows:

1. ν is the frequency of interest.
2. ν_j is the line center corresponding to a specific rotational transition.
3. α_D doppler halfwidth given by:
4. Where $\alpha_D = \frac{\nu_j}{c} v_{th} = \frac{\nu_j}{c} \left(\sqrt{\frac{2kT}{m}} \right)$
5. k is boltzmann's constant, T is the local temperature, m is the species' mass
6. c is the speed of light.
7. v_{th} is the species' thermal velocity.

The Doppler profile for a species is illustrated on Figure B.3.1.

B.3.3 The Voigt Profile

When both pressure broadening and doppler broadening matter, then we must introduce a convolution of both processes known as the Voigt Profile. This profile, because it must include both the Lorentz effects and Doppler effects emerges as mathematically and numerically more complicated tool than either of the two previous

profiles. This profile remains the most relevant to the present study of HCN cooling in Titan's atmosphere because near 600 km the neutral densities reach a point where pressure broadening must be considered. However, at the upper boundary of the model, at 1500 km, only Doppler broadening mechanisms matter to any degree. Thus, we must employ the Voigt Profile in order to properly account for line shape at all points in the Titan atmosphere.

The Voigt profile emerges as follows:

$$(B.4) \quad \phi_V(\nu) = \int_{-\infty}^{\infty} \phi_D(\nu') \phi_L(\nu - \nu') d\nu'$$

Which becomes upon substitution of the two profiles from before:

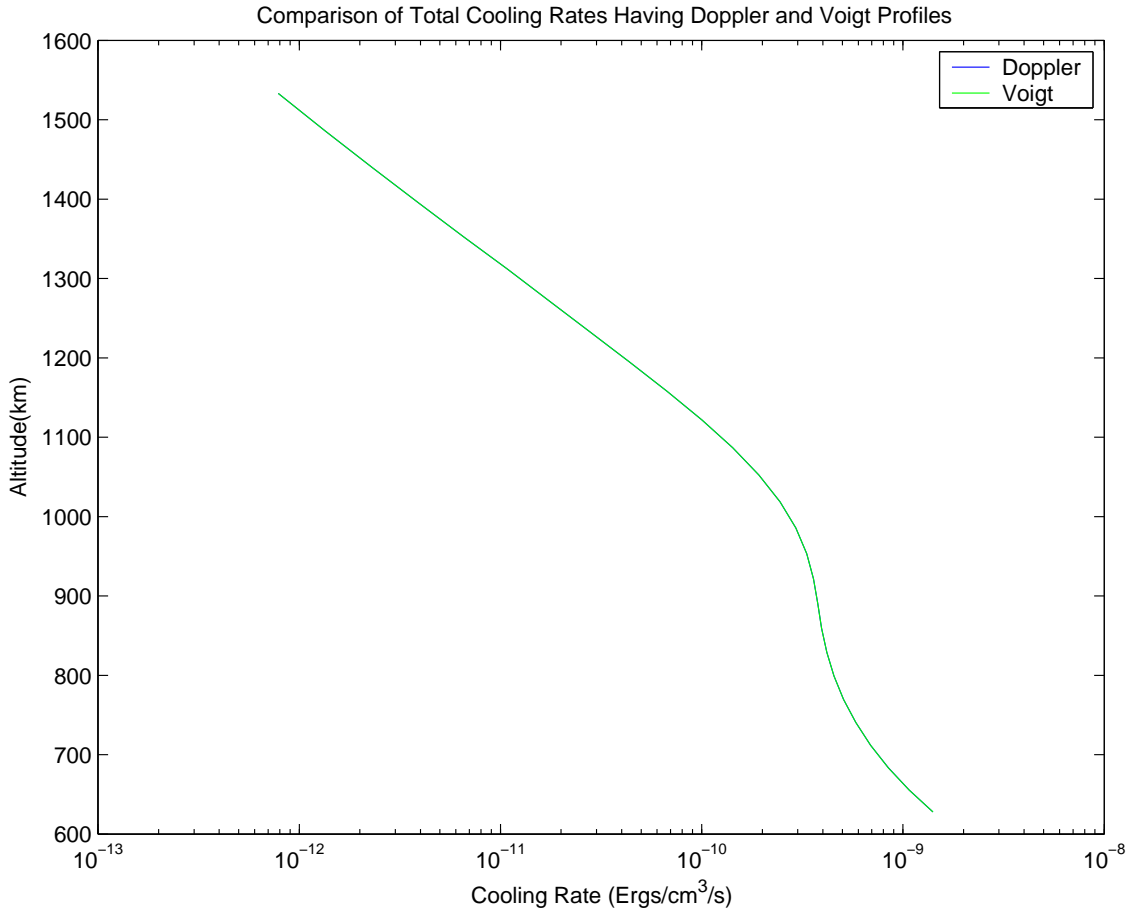
$$(B.5) \quad \phi_V(\nu) = \frac{\alpha_L}{\alpha_D \pi^{3/2}} \int_{-\infty}^{\infty} \frac{\exp -\left(\frac{(\nu' - \nu_j)^2}{\alpha_D^2}\right)}{\alpha_L^2 + ((\nu - \nu') - \nu_j)^2} d\nu'$$

Next, authors choose among a plethora of simplifications of this formula. We apply the transformation suggested by Shippoly and Read (2001) in order to make numerical computation much easier. The shape of the voigt profile is also shown in Figure B.3.1.

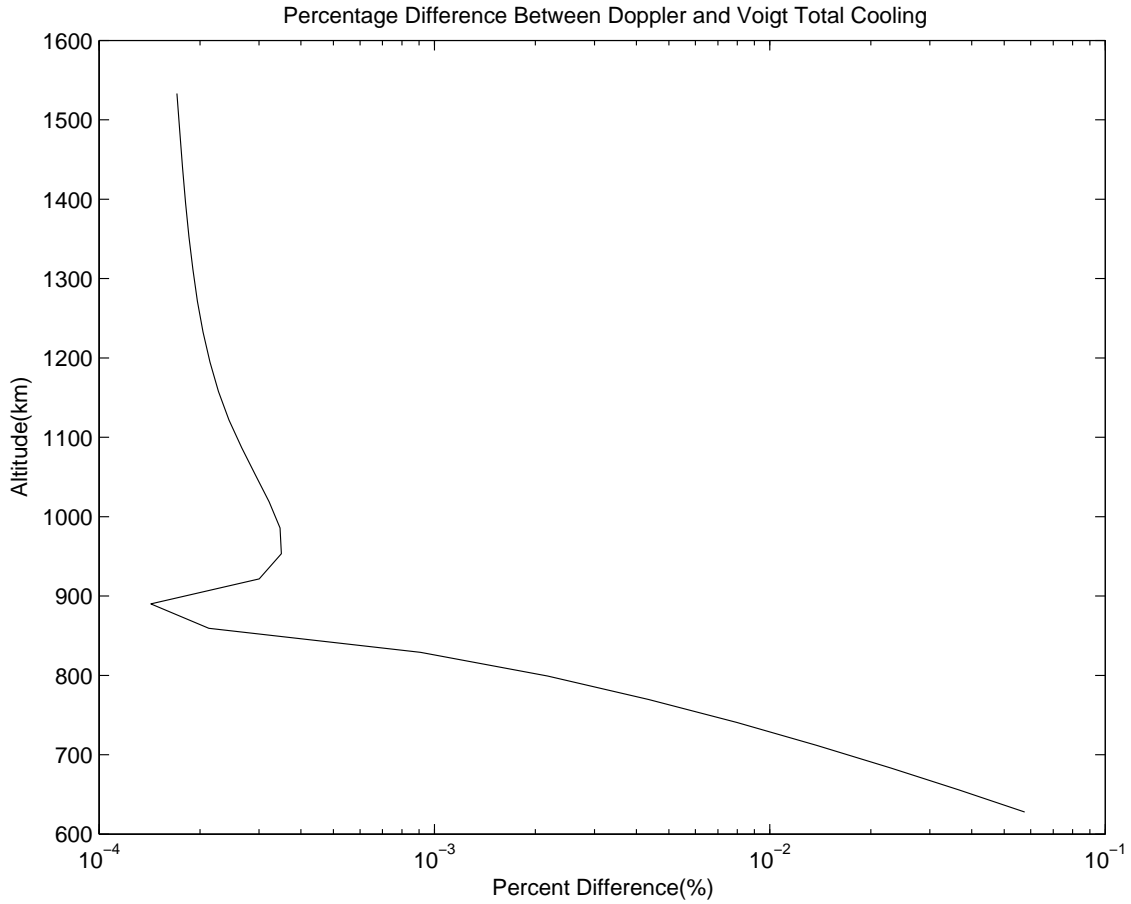
B.3.4 Cooling Rates as a function of Line Profile

Having discussed the facets of the three major spectral line profiles, we must next turn to the benefits and detriments of employing any of the three afore-mentioned line profiles. First, the Lorentz profile remains mostly inapplicable in the regions of interest to us at Titan ($> 300\text{km}$). Thus, we need only consider the Doppler and Voigt profiles in what follows. A comparison between the total cooling function using the voigt profile and using the doppler profile is shown in Figures B.3.4 and B.3.4 below:

From Figures B.3.4 and B.3.4 , there is little numerical difference at these altitudes between the Voigt or Doppler Profile. However, a caveat exists. If we extend



our model down to pressures even two orders of magnitude greater than our lower boundary pressure at 600 km, then we must consider the use of the Voigt profile alone, as illustrated by Figure B.3.4. Figure B.3.4 represents the differences between the Total cooling of a Voigt profile versus a Doppler profile when all densities are scaled by a common factor of 100. Clearly, at the bottom of this scaled plot, the error begins to reach several % points. Hence, at greater pressures than those at 600 km, we must indeed rely on the Voigt profile alone. However, the voigt profile comes with a significant computational cost that is alleviated in our current altitude regime by utilizing the much more efficient doppler profile at the moment.



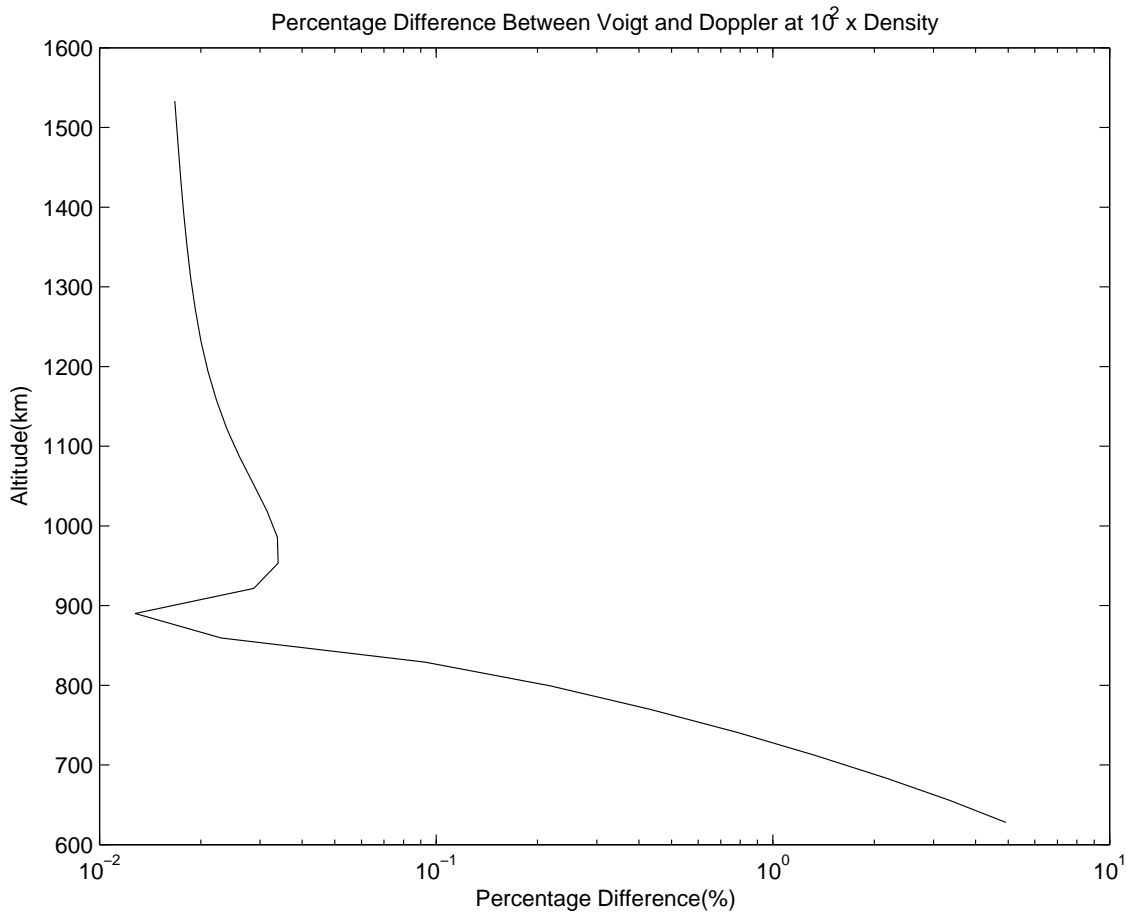
B.4 Radiative Transfer and HCN Cooling

Having discussed the approximations and validations for selecting 65 of the distinct 116 rotational lines of HCN and the validations for assuming simple doppler profiles throughout our region of concern, we next turn to delineating the heart of the radiative transfer code. At the heart of any radiative transfer code, regardless of implementation schemes or numerical approximations, rely on the fundamental radiative transfer equation (Goody, Chandrasekhar):

$$(B.6) \quad \mu \frac{\partial I_\nu(p, \theta, \phi)}{\partial \tau} = I_\nu(p, \theta, \phi) - S_\nu(p, \theta, \phi)$$

Where we have now:

1. μ is $\cos(\theta)$. θ being the angle w/respect to the vertical of the radiation.



2. I_ν is the intensity (W/m^2) at a specific frequency, ν .
3. τ is the optical depth, measured vertically downward from the "top" of the atmosphere.
4. S_{nu} is the Source Function for the radiation at a given frequency.

B.4.1 Simplifications in Titan's Atmosphere

In Titan's upper atmosphere, we can assume several simplifying aspects about the nature of the radiative transfer among the rotational levels of HCN:

1. The rotational lines are in LTE (Local Thermodynamic Equilibrium). Thus,

$S_\nu \Rightarrow B_\nu$, which is the Planck Blackbody function given by

$$B_\nu = \frac{2h\nu^3}{c} \frac{1}{e^{\frac{h\nu}{kT}}}$$

Thus we have now that:

$$\mu \frac{\partial I_\nu(p, \theta, \phi)}{\partial \tau} = I_\nu(p, \theta, \phi) - B_\nu(p, \theta, \phi)$$

2. Next, each rotational line is distinct, so that we may write down a simplified form for the optical depth, τ , without any need for complex accounting for line overlapping as:

$$\tau = \int_{z_0}^{z_{top}} k_{\nu, \nu_j}(z) N_{HCN}(z) dz$$

where

$$k_{\nu, \nu_j}(z) = \phi_{\nu, \nu_j} B_\nu$$

3. Also, we may simplify the following discussion by applying a plane-parallel formulation, along the lines of (Goody) in order to describe the radiative transfer. Although in the upper regions of Titan's atmosphere, we must be careful of curvature terms, we may effectively neglect this (Yelle 1991).

B.4.2 Solving the Transfer Equation

Now that we have simplified matters in Titan's atmosphere, we next turn to finding a formal solution to the transfer equation, along the lines of (Goody, Chanrasekhar). In plane parallel geometry, the optical path length is given by $ds = dz/\mu$. For an excellent diagram of this, see (Gombosi 1998, Goody 1985). Hence the appearance of the μ terms in all of the previous and following formulations of the radiative transfer equation.

Next, along the lines of (Goody) we now define a relative optical depth variable, $\tau' = \tau(z) - \tau(z')$ This variable describes directly the change in optical depth along a vertical path in the atmosphere from z to z' . In what follows, we will use this τ' to describe the radiative transfer of HCN rotational cooling. Also, for brevity, we will also drop the explicit dependences of the terms on the state variables of p, T, z, \dots etc.

One begins by employing a "well chosen" integrating factor and multiplying by this chosen factor of $e^{-\frac{\tau'}{\mu}}$, which gives us now:

$$\mu \frac{\partial I_\nu}{\partial \tau'} e^{-\frac{\tau'}{\mu}} = I_\nu e^{-\frac{\tau'}{\mu}} - B_\nu e^{-\frac{\tau'}{\mu}}$$

The two I_ν terms represent now the expansion of a product rule of differentiation and can be combined to produce:

$$\frac{\partial (I_\nu e^{-\frac{\tau'}{\mu}})}{\partial \tau'} = -B_\nu \frac{e^{-\frac{\tau'}{\mu}}}{\mu}$$

The next step is simply to integrate along the variable τ' from the limits of $\tau' = 0$, to $\tau' = \tau_{max}$. What these limits correspond to is explained in what follows:

1. $\tau' = 0 \Rightarrow \tau(z) = \tau(z')$, which means both z and z' are collocated (i.e. there is no atmosphere between them).
2. $\tau' = \tau_{max} \Rightarrow \tau(z)$ and $\tau(z')$ are separated by the distance of the entire atmospheric region under consideration. Think of $\tau' = \tau_{max}$ as saying that z and z' are at the top and bottom boundaries of our atmospheric model.

After Integrating the newly formed Radiative Transfer Equation, we arrive at two possible solutions

1. When $0 < \mu \leq 1$ (Upward Propogating Radiation) we get

$$I_\nu = \left(I_\nu e^{-\frac{\tau'}{\mu}} \right)_{z=0, \tau=\tau_{max}} - \int_0^{\tau_{max}} B_\nu \frac{e^{-\frac{\tau'}{\mu}}}{\mu} d\tau'$$

2. When $0 > \mu \geq -1$ (Downward Propogating Radiation) we get

$$I_\nu = \left(I_\nu e^{-\frac{\tau'}{\mu}} \right)_{z=z_{top}, \tau=0} - \int_0^{\tau_{max}} B_\nu \frac{e^{-\frac{\tau'}{\mu}}}{\mu} d\tau'$$

Next, we must now carefully consider the appropriate boundary conditions for our problem. For the upward propogating radiation, the lower boundary of the model can be thought of as a blackbody radiating at its given temperature. Similarly, for downward propogating radiation, we can assume that no HCN is re-radiating downward from the exobase and so we can regard the intensity from the "upper boundary" to be zero.

Thus, we have the following simplifications:

1.

$$\left(I_\nu e^{-\frac{\tau'}{\mu}} \right)_{z=0, \tau=\tau_{max}} \Rightarrow B_\nu(0) e^{-\frac{\tau_{max}-\tau(z')}{\mu}}$$

2.

$$\left(I_\nu e^{-\frac{\tau'}{\mu}} \right)_{z=z_{top}, \tau=0} \Rightarrow 0.0$$

Thus we finally arrive at the following final expressions for the intensities for upward and downward propogation:

$$\text{For } (0 < \mu \leq 1): I_\nu^+ = B_\nu(0) e^{-\frac{\tau_{max}-\tau(z')}{\mu}} - \int_{tau(z')}^{\tau_{max}} B_\nu \frac{e^{-\frac{\tau'}{\mu}}}{\mu} d\tau'$$

$$\text{For } (0 > \mu \geq -1): I_\nu^- = - \int_0^{\tau_{z'}} B_\nu e^{-\frac{\tau'}{\mu}} d\tau'$$

B.4.3 Flux and Heating Functions

Now that we've solved for the specific intensities throughout Titan's atmosphere, we must next consider the Fluxes associated with these intensities, because fluxes lead directly to energy production and losses in the atmosphere.

Flux is defined mathematically as follows:

$$F_\nu = \int_\Omega I_\nu d\Omega = 2\pi \int_{-\pi/2}^{\pi/2} I_\nu \sin \theta d\theta = 2\pi \int_{-1}^1 I_\nu \mu d\mu = 2\pi \left(\int_0^1 I_\nu^+ \mu d\mu + \int_{-1}^0 I_\nu^- \mu d\mu \right)$$

Now, we may substitute the above expressions in for I_ν^+ and I_ν^- to arrive at the following definition of F_ν :

$$F_\nu = 2\pi \left[B_\nu(0) \int_0^1 e^{-\frac{\tau_{max} - \tau(z')}{\mu}} d\mu - \int_{\tau(z')}^{\tau_{max}} B_\nu \left(\int_0^1 \frac{e^{-\frac{\tau'}{\mu}}}{\mu} d\mu \right) d\tau' \right] \\ - 2\pi \left[\int_0^{\tau(z')} B_\nu \left(\int_{-1}^0 \frac{e^{-\frac{\tau'}{\mu}}}{\mu} d\mu \right) d\tau' \right]$$

Exponential Integrals

A Useful subclass of functions exist called the Exponential Integrals and are defined as follows:

$$E_n(x) = \int_1^\infty \frac{e^{-xw}}{w^n} dw$$

This can be transformed with a substitution of

$$\alpha = \frac{1}{w} \quad d\alpha = -\frac{dw}{w^2}$$

into the following:

$$E_n(x) = - \int_1^0 \frac{e^{\frac{-x}{\alpha}}}{w^n} w^2 d\alpha = \int_0^1 e^{\frac{-x}{\alpha}} \alpha^{n-2} d\alpha$$

Some useful properties of the Exponential Function are as follows:

$$1. \frac{dE_n(x)}{dx} = -E_{n-1}(x)$$

$$2. nE_{n+1}(x) = e^{-x} - xE_n(x)$$

$$3. E_n(0) = \frac{1}{n-1}$$

$$4. E_1(0) = \infty$$

The actual evaluation of the exponential requires numerical approximations given in (refs) and will not be discussed further in this paper.

Rewriting the Flux Functions

Thus, with the numerical tools given to us by the exponential functions, we may re-write our earlier flux functions as:

$$F_\nu = 2\pi B_\nu(0)E_2(\tau_{max} - \tau(z')) - 2\pi \int_{\tau(z')}^{\tau_{max}} B_\nu E_3(\tau') d\tau' - 2\pi \int_0^{\tau(z')} B_\nu E_3(\tau') d\tau'$$

Whereupon, rewriting τ' as it's earlier form: $\tau' = \tau(z) - \tau(z')$ and where we note that now $d\tau' = d\tau(z')$ and use the shorthand $d\tau'$ for $d\tau'(z')$.

Thus, we arrive a new formula for the total radiation flux at a given altitude, z , as:

$$\begin{aligned} F_\nu(z) = & 2\pi B_\nu(0)E_2(\tau_{max} - \tau(z)) - 2\pi \int_{\tau(z)}^{\tau_{max}} B_\nu E_3(\tau(z') - \tau(z)) d\tau' \\ & - 2\pi \int_0^{\tau(z)} B_\nu E_3(\tau(z) - \tau(z')) d\tau' \end{aligned}$$

Heating Rates

Now, having found a succinct form for the total flux at a given frequency, we now turn to calculating the heating rate at a given frequency. The heating rate, h_ν , at a given frequency is given by:

$$h_\nu = \frac{dF_\nu}{dz} = \frac{dF_\nu}{d\tau} \frac{d\tau}{dz}$$

Next we may consider the terms comprising the whole of $\frac{dF_\nu}{dz}$:

1.

$$\frac{d}{d\tau} [2\pi B_\nu(0)E_2(\tau_{max} - \tau(z))] = 2\pi B_\nu(0) \frac{d}{d\tau} [E_2(\tau_{max} - \tau(z))] = 2\pi B_\nu(0)E_1(\tau_{max} - \tau(z))$$

2.

$$\frac{d}{d\tau} \left(2\pi \int_{\tau(z)}^{\tau_{max}} B_\nu E_3(\tau(z') - \tau(z)) d\tau' \right) = 2\pi \frac{d}{d\tau} \left(\int_{\tau(z)}^{\tau_{max}} B_\nu E_3(\tau(z') - \tau(z)) d\tau' \right)$$

3.

$$\frac{d}{d\tau} \left(2\pi \int_0^{\tau(z)} B_\nu E_3 (\tau(z) - \tau(z')) d\tau' \right) = 2\pi \frac{d}{d\tau} \left(\int_0^{\tau(z)} B_\nu E_3 (\tau(z) - \tau(z')) d\tau' \right)$$

For parts (2) and (3) above pose a problem because of the limits of integration being a function as well. Thus, a simpler example should elucidate how to treat such mathematical constructs.

In general, people apply the following useful property of integrals and derivatives:

$$\frac{d}{dx} \int f(x) dx = \int \frac{\partial f(x)}{\partial x} dx$$

Now, an extended version of this emerges from the Second Fundamental Theorem of Calculus as:

$$\frac{d}{dx} \int_{a(x)}^{b(x)} f(x) dx = \int_{a(x)}^{b(x)} \frac{\partial f(x)}{\partial x} dx + b'(x)f(b(x)) - a'(x)f(x)$$

The Net result of these tranformations is that the flux derivative becomes

$$\begin{aligned} \frac{dF_\nu}{d\tau} = & -4\pi (B_\nu(\tau(z))) + 2\pi B_\nu(0)E_2 (\tau_{max} - \tau(z)) + 2\pi \int_{\tau(z)}^{\tau_{max}} B_\nu E_1 (\tau(z') - \tau(z)) d\tau' \\ & + 2\pi \int_0^{\tau(z)} B_\nu E_1 (\tau(z) - \tau(z')) d\tau' \end{aligned}$$

Now, we may finally write a closed form for the heating rates in terms of quantities that are either known or can be immediately derived from known quantities (taken after Muller-Wodarg (2000)):

$$\begin{aligned} h_\nu = & (S_\nu \phi_\nu N_{HCN}) \left[-4\pi (B_\nu(\tau(z))) + 2\pi B_\nu(0)E_2 (\tau_{max} - \tau(z)) + 2\pi \int_{\tau(z)}^{\tau_{max}} B_\nu E_1 (\tau(z') - \tau(z)) d\tau' \right] \\ & + (S_\nu \phi_\nu N_{HCN}) \left[2\pi \int_0^{\tau(z)} B_\nu E_1 (\tau(z) - \tau(z')) d\tau' \right] \end{aligned}$$

Next, we must now integrate over a sizeable range of frequencies such that we cover the shape function, ϕ_ν . Also, we must not forget that these functions all possess an intrinsic dependence on the line number, ν_j embedded in the function of τ and ϕ . Thus, we must also sum over the line numbers.

In finality, what you get is the following:

$$h(z) = 2\pi N_{HCN}(z) \sum_{j=1}^{N=65} \left[\int_{\Delta\nu_j} S_{\nu, \nu_j}(z) \phi_{\nu, \nu_j}(z) [C(\tau(z), \nu, \nu_j) + H_1(\tau(z), \nu, \nu_j) + H_2(\tau(z), \nu, \nu_j)] \right] d\nu$$

Where

1.

$$C(\tau(z), \nu, \nu_j) = -2B_\nu(\tau(z))$$

This the radiation emitted from a level z in all directions (hence the factor of 4π) in the above equation. This would be the only cooling term in the cool-to-space approximation.

2.

$$H_1(\tau(z), \nu, \nu_j) = B_\nu(0)E_2(\tau_{max} - \tau(z))$$

This is the incoming radiation from the lower boundary.

3.

$$H_2(\tau(z), \nu, \nu_j) = \int_{\tau(z)}^{\tau_{max}} B_\nu E_1(\tau(z') - \tau(z)) d\tau' + \int_0^{\tau(z)} B_\nu E_1(\tau(z) - \tau(z')) d\tau'$$

This is the radiation incoming to the level (z) from all other altitudes in the atmosphere under consideration.

The above form of the heating rates was used to calculate the total heating/cooling from HCN rotational lines at every altitude level (pressure level) in the cooling routines. In what follows, we shall take a tour of the numerical techniques and processes by which the HCN code performs the cooling calculations.

B.5 Numerical Methods for the HCN Cooling Routine

The heating rate equation presented at the end of the last chapter consists of a series of nested integrals over frequency, tau, and a summation over the rotational lines. In what follows, we will divulge exactly how the various terms in the heating function were evaluated.

B.5.1 Optical Depth

The first function to be evaluated in the HCN radiative transfer routine is the optical depth, τ , which was defined previously as:

$$\tau = \int_{z_0}^{z_{top}} k_{\nu, \nu_j}(z) N_{HCN}(z) dz = \int_{z_0}^{z_{top}} \phi_{\nu, \nu_j}(z) S_{\nu, \nu_j} N_{HCN}(z) dz$$

In order to evaluate this integral the following steps were taken:

1. $\phi_{\nu, \nu_j}(z)$ was calculated from the Doppler Profile at every altitude point in chapter 3.
2. S_{ν, ν_j} was calculated at every altitude point from the interpolation scheme in chapter 2.
3. N_{HCN} was input at every altitude point.
4. Multiplying (1) - (3) above gave us the integrand at every altitude point in the atmosphere.

Next, 16-point Gauss-Legendre Quadrature was employed, using the integrand obtained in step(4) above, in order to evaluate the integrand above. The details of this method are explored in several good references (Press et al, Lindfield and Perry), but we shall discuss some aspects of the more general method below.

Gauss-Legendre Quadrature

The basic premise of an n-point Guassian Quadrature in general and an n-point Gauss-Legendre Quadrature in particular is based on the following paradigm:

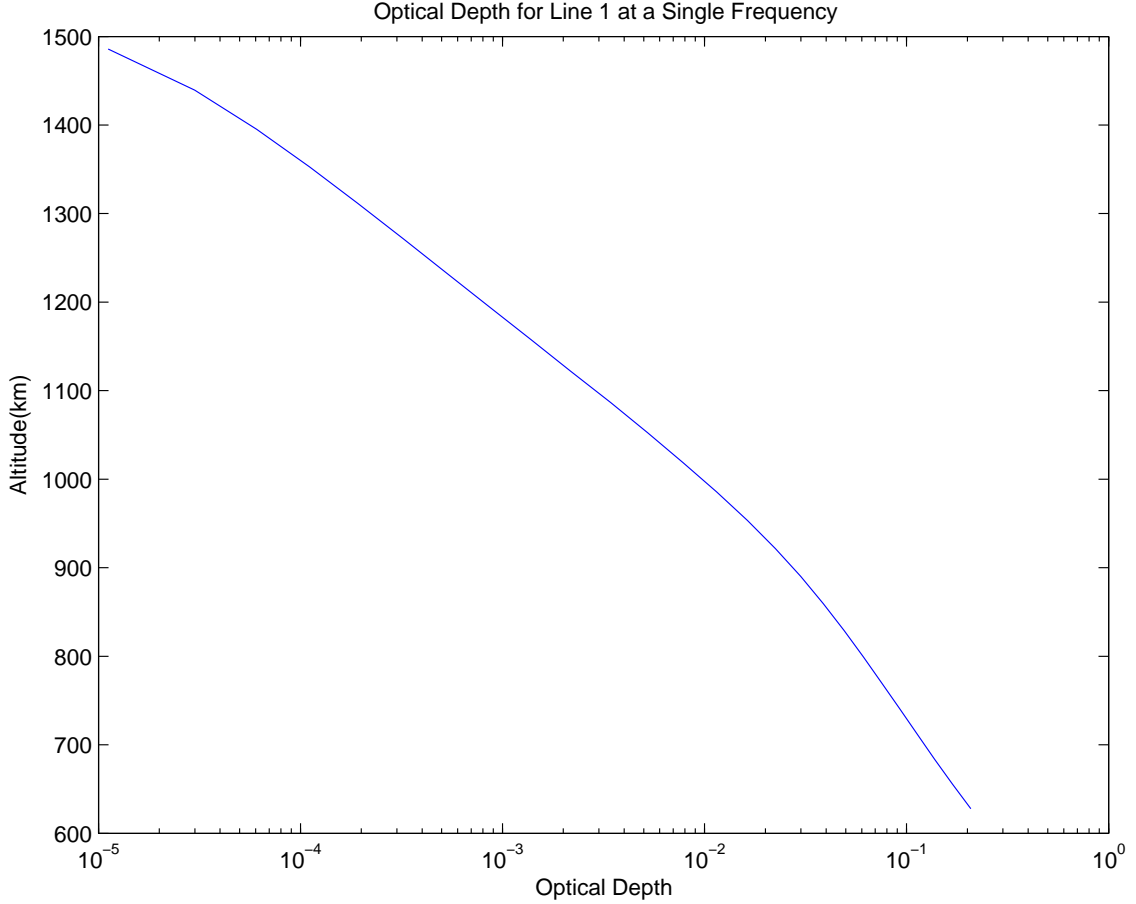
$$\int_a^b f(x) dx \approx \sum_1^n w_i f(x_i) \Delta x_i$$

Where the w_i are denoted as the "weights" that correspond to the Gaussian points, x_i . Determining the weights and associated gaussian points would take us too far beyond the scope of the current discussion, but several good references on the subject can be found (Press et al, Lindsfield and Perry, Abramowitz and Stegun). These weights and points are simply tabulated within the HCN code; however, the problem arises that these gaussian points do not usually correspond exactly with the altitudes that the model has information. Thus, interpolation must be utilized to approximate the value of the integrand at each of the 16 Gaussian Points. It was found that both linear interpolation and cubic spline interpolation produced the same results to within 1 % maximum error. Hence, since cubic spline interpolation cost almost 10 times as much computational time, linear interpolation was employed everywhere within the code.

B.5.2 Calculating τ

From the methods discussed above, the optical depth profiles for each line and at each frequency were calcuated for all altitudes in the atmosphere, producing profiles such as the one shown below in Figure B.5.2:

From this figure, one finds that τ is a monotonic function of z so that, instead of treating key variables in the HCN cooling routine as functions of altitude, we may instead think of them as functions of optical depth, τ . Hence, now that we have



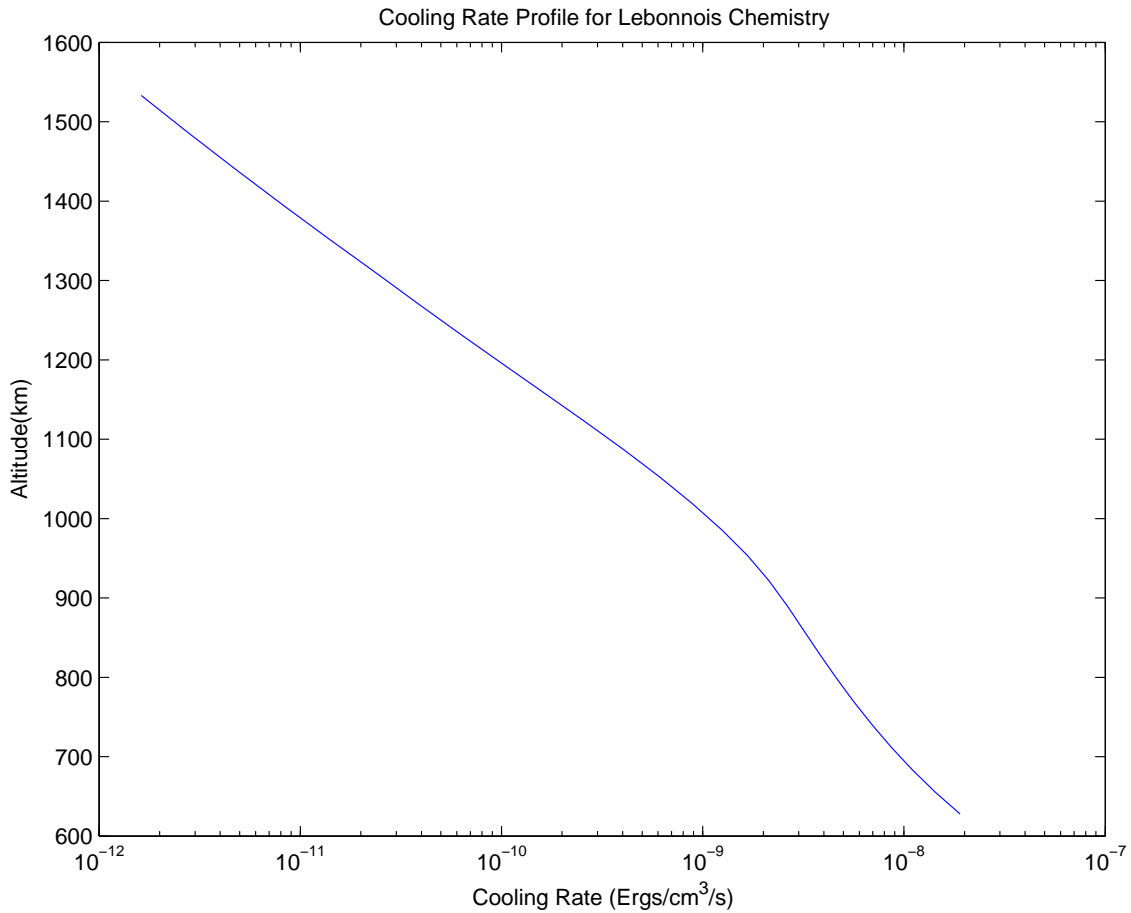
calculated τ as a function of (ν, ν_j, z) we may now simply employ the formulation of the heating function $h_\nu(\tau)$ given above in chapter 3, as will be done in the following discussions.

B.6 Cooling to Space

The next function that the HCN cooling routine evaluates is the strictly cooling function from section 4.3.3 above, $C(\nu, \nu_j, \tau)$. Thus, the code must evaluate the term:

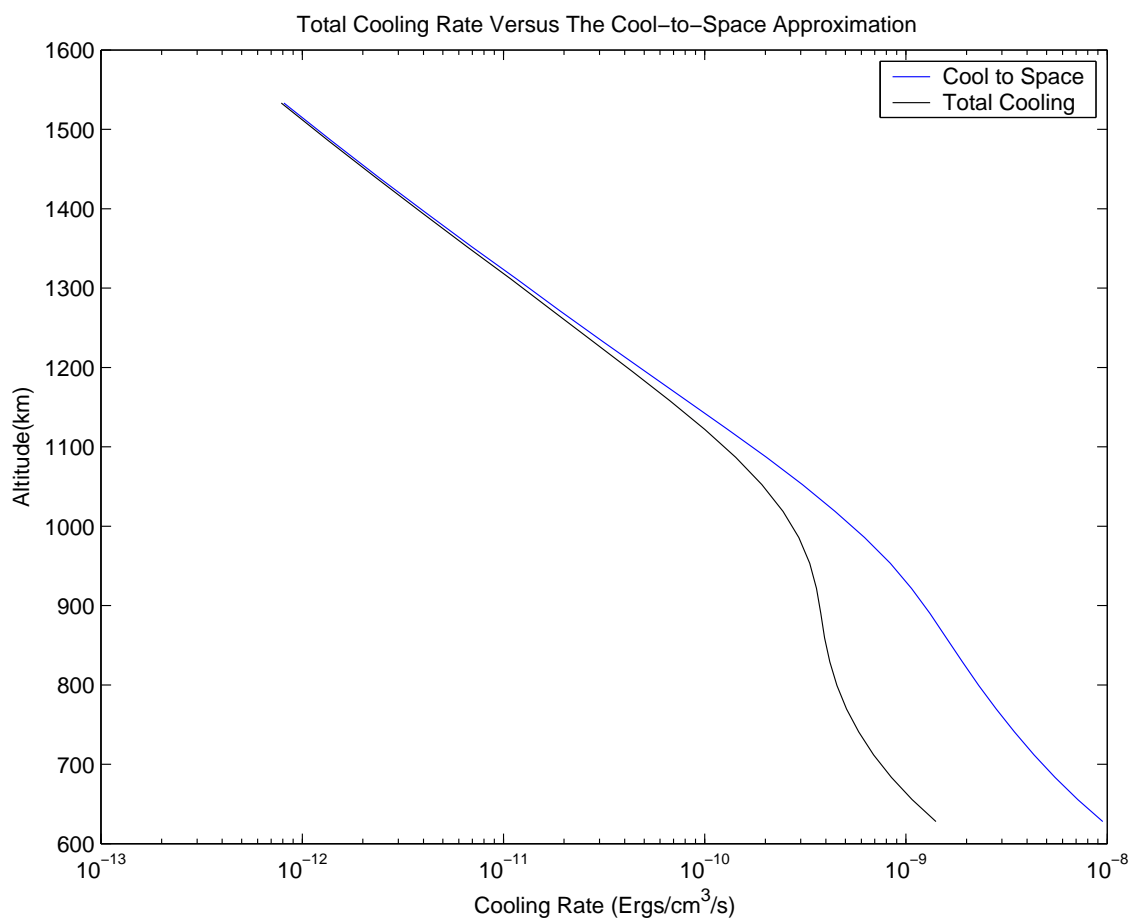
$$2\pi N_{HCN}(z) \sum_{j=1}^{N=65} \left[\int_{\Delta\nu_j} S_{\nu, \nu_j}(\tau) \phi_{\nu, \nu_j}(\tau) (-2B_\nu(\tau(z))) d\nu \right]$$

The outer integral over frequency was performed using Gaussian Quadrature over the integrand of $S_{\nu, \nu_j}(\tau) \phi_{\nu, \nu_j}(\tau) (-2B_\nu(\tau(z)))$, which was easily tabulated at each



altitude/ τ point in the atmosphere, using the interpolated intensities, the doppler profile, and the formulation for the Planck Blackbody function. Calculation of this cooling function represents the easiest and quickest term to evaluate in the radiative transfer formulation. The cooling rate as a function of altitude for the Lebonnois density profile is shown below in Figure B.6:

It should be noted that by dividing this cooling function by a factor of 2.0 results in the well known "cool-to-space" approximation that accounts only for radiation emitted upward from any given level and assumes that the radiation escapes to space. In the upper reaches of Titan's atmosphere (above 1200 km) this approximation does apply (Yelle 1991) as is shown below in Figure B.6



Bibliography

- Achterberg, R. K., B. J. Conrath, P. J. Gierasch, F. M. Flasar, and C. A. Nixon, Titan's middle-atmospheric temperatures and dynamics observed by the Cassini Composite Infrared Spectrometer, *Icarus*, 194, 263–277, doi: 10.1016/j.icarus.2007.09.029, 2008.
- Allen, M., Y. L. Yung, and J. P. Pinto, Titan - Aerosol photochemistry and variations related to the sunspot cycle, *Astrophysical Journal*, 242, L125–L128, doi: 10.1086/183416, 1980.
- Anderson, D. N., A theoretical study of the ionospheric F region equatorial anomaly-II. results in the American and Asian sectors., *Planetary and Space Sciences*, 21, 421–441, 1973.
- Anderson, D. N., Modeling the ambient, low latitude F-region ionosphere - a review., *Journal of Atmospheric and Terrestrial Physics*, 43, 753–762, 1981.
- Angelats i Coll, M., F. Forget, M. A. López-Valverde, P. L. Read, and S. R. Lewis, Upper atmosphere of Mars up to 120 km: Mars Global Surveyor accelerometer data analysis with the LMD general circulation model, *Journal of Geophysical Research (Planets)*, 109, 1011–+, doi:10.1029/2003JE002163, 2004.
- Angelats i Coll, M., F. Forget, M. A. López-Valverde, and F. González-Galindo, The first Mars thermospheric general circulation model: The Martian atmosphere from the ground to 240 km, *Geophysical Research Letters*, 32, 4201–+, doi:10.1029/2004GL021368, 2005.
- Atreya, S. K., Atmospheres and ionospheres of the outer planets and their satellites, *Springer Verlag Springer Series on Physics Chemistry Space*, 15, 1986.
- Banaszkiewicz, M., L. M. Lara, R. Rodrigo, J. J. López-Moreno, and G. J. Molina-Cuberos, A Coupled Model of Titan's Atmosphere and Ionosphere, *Icarus*, 147, 386–404, doi:10.1006/icar.2000.6448, 2000.
- Banks, P. M., and G. Kockarts, *Aeronomy*, third ed., Academic Press, 1973.
- Bell, J. M., S. W. Bougher, and J. R. Murphy, Vertical dust mixing and the interannual variations in the Mars thermosphere, *Journal of Geophysical Research (Planets)*, 112, 12,002–+, doi:10.1029/2006JE002856, 2007.
- Boqueho, V., and P.-L. Blelly, Contributions of a multimoment multispecies approach in modeling planetary atmospheres: Example of Mars, *Journal of Geophysical Research (Space Physics)*, 110, 1313–+, doi:10.1029/2004JA010414, 2005.
- Bougher, S., G. Keating, R. Zurek, J. Murphy, R. Haberle, J. Hollingsworth, and R. T. Clancy, Mars global surveyor aerobraking : atmospheric trends and model interpretation, *Advances in Space Research*, 23, 1887–1897, 1999a.
- Bougher, S. W., and R. E. Dickinson, Mars mesosphere and thermosphere. I - Global mean heat budget and thermal structure, *Journal of Geophysical Research*, 93, 7325–7337, 1988.

- Bougher, S. W., R. E. Dickinson, R. G. Roble, and E. C. Ridley, Mars thermospheric general circulation model - Calculations for the arrival of PHOBOS at Mars, *Geophysical Research Letters*, 15, 1511–514, 1988a.
- Bougher, S. W., R. G. E. Roble, R. E. Dickinson, and E. C. Ridley, Venus mesosphere and thermosphere. III - Three-dimensional general circulation with coupled dynamics and composition, *Icarus*, 73, 545–573, doi:10.1016/0019-1035(88)90064-4, 1988b.
- Bougher, S. W., R. G. Roble, E. C. Ridley, and R. E. Dickinson, The Mars thermosphere. II - General circulation with coupled dynamics and composition, *Journal of Geophysical Research*, 95, 14,811–14,827, 1990.
- Bougher, S. W., S. Engel, R. G. Roble, and B. Foster, Comparative terrestrial planet thermospheres 2. Solar cycle variation of global structure and winds at equinox, *Journal of Geophysical Research*, 104, 16,591–16,611, doi:10.1029/1998JE001019, 1999b.
- Bougher, S. W., S. Engel, R. G. Roble, and B. Foster, Comparative terrestrial planet thermospheres 3. Solar cycle variation of global structure and winds at solstices, *Journal of Geophysical Research (Planets)*, 105, 17,669–17,692, doi:10.1029/1999JE001232, 2000.
- Bougher, S. W., S. Engel, D. P. Hinson, and J. R. Murphy, MGS Radio Science electron density profiles: Interannual variability and implications for the Martian neutral atmosphere, *Journal of Geophysical Research (Planets)*, 109, 3010–+, doi:10.1029/2003JE002154, 2004.
- Bougher, S. W., J. M. Bell, J. R. Murphy, M. A. Lopez-Valverde, and P. G. Withers, Polar warming in the Mars thermosphere: Seasonal variations owing to changing insolation and dust distributions, *GRL*, 33, 2203–+, doi:10.1029/2005GL024059, 2006.
- Boughner, R. E., Comparison of band model calculations of upper atmospheric cooling rates for the 15-micrometer carbon dioxide band, *Journal of Geophysical Research*, 90, 8011–8018, 1985.
- Broadfoot, A. L., et al., Extreme ultraviolet observations from Voyager 1 encounter with Saturn, *Science*, 212, 206–211, 1981.
- Carr, M. H., *The Surface of Mars*, The Surface of Mars, by Michael H. Carr. ISBN-10 0-521-87201-4; ISBN-13 978-0-521-87201-0. Published by Cambridge University Press, Cambridge, UK, 2006., 2006.
- Carr, M. H., and J. W. Head, Basal melting of snow on early Mars: A possible origin of some valley networks, *Geophysical Research Letters*, 30, 3–1, 2003.
- Chamberlain, J. W., and D. M. Hunten, Theory of planetary atmospheres: an introduction to their physics and chemistry /2nd revised and enlarged edition/, *Orlando FL Academic Press Inc International Geophysics Series*, 36, 1987.
- Chandrasekhar, S., *Radiative transfer*, New York: Dover, 1960, 1960.
- Chassefière, E., F. Leblanc, and B. Langlais, The combined effects of escape and magnetic field histories at Mars, *Planetary and Space Science*, 55, 343–357, doi:10.1016/j.pss.2006.02.003, 2007.
- Chaufray, J. Y., R. Modolo, F. Leblanc, G. Chanteur, R. E. Johnson, and J. G. Luhmann, Mars solar wind interaction: Formation of the Martian corona and atmospheric loss to space, *Journal of Geophysical Research (Planets)*, 112, 9009–+, doi:10.1029/2007JE002915, 2007.

- Christensen, P. R., et al., Mars Global Surveyor Thermal Emission Spectrometer experiment: Investigation description and surface science results, *Journal of Geophysical Research*, 106, 23,823–23,872, doi:10.1029/2000JE001370, 2001.
- Clancy, R. T., B. J. Sandor, M. J. Wolff, P. R. Christensen, M. D. Smith, J. C. Pearl, B. J. Conrath, and R. J. Wilson, An intercomparison of ground-based millimeter, MGS TES, and Viking atmospheric temperature measurements: Seasonal and interannual variability of temperatures and dust loading in the global Mars atmosphere, *Journal of Geophysical Research*, 105, 9553–9572, doi:10.1029/1999JE001089, 2000.
- Clarke, D. W., and J. P. Ferris, Chemical Evolution on Titan: Comparisons to the Prebiotic Earth, *Origins of Life and Evolution of the Biosphere*, 27, 225–248, 1997.
- Colegrove, F. D., F. S. Johnson, and W. B. Hanson, Atmospheric Composition in the Lower Thermosphere, *JGR*, 71, 2227–+, 1966.
- Conrath, B. J., Thermal structure of the Martian atmosphere during the dissipation of the dust storm of 1971, *Icarus*, 24, 36–46, 1975.
- Crane, Flow of fluids through valves, fittings, and pipes, *Technical Paper 410*, 1988.
- Cravens, T. E., J. Vann, J. Clark, J. Yu, C. N. Keller, and C. Brull, The ionosphere of Titan: an updated theoretical model, *Advances in Space Research*, 33, 212–215, doi:10.1016/j.asr.2003.02.012, 2004.
- Danielson, R. E., J. J. Caldwell, and D. R. Larach, An Inversion in the Atmosphere of Titan, *Icarus*, 20, 437–+, 1973.
- De La Haye, V., Coronal Formation and Heating Efficiencies in Titan's Upper Atmosphere: Construction of a Coupled Ion, Neutral and Thermal Structure Model to Interpret the First INMS Cassini Data, Ph.D. thesis, AA(THE UNIVERSITY OF MICHIGAN.), 2005.
- De La Haye, V., J. H. Waite, T. E. Cravens, A. F. Nagy, R. E. Johnson, S. Lebonnois, and I. P. Robertson, Titan's corona: The contribution of exothermic chemistry, *Icarus*, 191, 236–250, doi:10.1016/j.icarus.2007.04.031, 2007a.
- De La Haye, V., et al., Cassini Ion and Neutral Mass Spectrometer data in Titan's upper atmosphere and exosphere: Observation of a suprathermal corona, *Journal of Geophysical Research (Space Physics)*, 112, 7309–+, doi:10.1029/2006JA012222, 2007b.
- De Pater, I., and J. J. Lissauer, *Planetary Science*, Cambridge University Press, 2001., 2001.
- Deming, D., M. J. Mumma, F. Espenak, T. Kostiuk, and D. Zipoy, Polar warming in the middle atmosphere of Mars, *Icarus*, 66, 366–379, doi:10.1016/0019-1035(86)90165-X, 1986.
- Deng, Y., A. D. Richmond, A. J. Ridley, and H.-L. Liu, Assessment of the non-hydrostatic effect on the upper atmosphere using a general circulation model (GCM), *Geophysical Research Letters*, 35, 1104–+, doi:10.1029/2007GL032182, 2008.
- Dickinson, R. E., E. C. Ridley, and R. G. Roble, Meridional circulation in the thermosphere. I - Equinox conditions, *Journal of Atmospheric Sciences*, 32, 1737–1754, 1975.
- Dickinson, R. E., E. C. Ridley, and R. G. Roble, Meridional Circulation in the Thermosphere. II. Solstice Conditions., *Journal of Atmospheric Sciences*, 34, 178–192, 1977.

- Dickinson, R. E., E. C. Ridley, and R. G. Roble, A three-dimensional general circulation model of the thermosphere, *Journal of Geophysical Research*, **86**, 1499–1512, 1981.
- Dickinson, R. E., E. C. Ridley, and R. G. Roble, Thermospheric general circulation with coupled dynamics and composition., *Journal of Atmospheric Sciences*, **41**, 205–219, 1984.
- Fedder, J. A., and P. M. Banks, Convection Electric Fields and Polar Thermospheric Winds, *Journal of Geophysical Research (Planets)*, **13**, 2328–2340, doi: 10.1029/2002JE001921, 1972.
- Fels, S. B., and M. D. Schwarzkopf, An efficient, accurate algorithm for calculating CO₂ 15 μ m band cooling rates., *Journal of Geophysical Research*, **86**, 1205–1232, 1981.
- Fesen, C. G., R. G. Roble, and R. E. Dickinson, Simulation of the thermospheric tides at equinox with the National Center for Atmospheric Research thermospheric general circulation model, *Journal of Geophysical Research*, **91**, 4471–4489, 1986.
- Flasar, F. M., et al., Titan's Atmospheric Temperatures, Winds, and Composition, *Science*, **308**, 975–978, doi:10.1126/science.1111150, 2005.
- Forbes, J. M., and M. E. Hagan, Diurnal Kelvin wave in the atmosphere of Mars: Towards an understanding of 'stationary' density structures observed by the MGS accelerometer, *Geophysical Research Letters*, **27**, 3563–3566, doi: 10.1029/2000GL011850, 2000.
- Forbes, J. M., A. F. C. Bridger, S. W. Bougher, M. E. Hagan, J. L. Hollingsworth, G. M. Keating, and J. Murphy, Nonmigrating tides in the thermosphere of Mars, *Journal of Geophysical Research (Planets)*, **107**, 5113–+, doi: 10.1029/2001JE001582, 2002.
- Forget, F., F. Hourdin, and O. Talagrand, Simulation of the martian atmospheric polar warming with the LMD general circulation model, *Annales Geophysicae*, **14**, 797–+, 1996.
- Forget, F., F. Hourdin, R. Fournier, C. Hourdin, O. Talagrand, M. Collins, S. R. Lewis, P. L. Read, and J.-P. Huot, Improved general circulation models of the Martian atmosphere from the surface to above 80 km, *Journal of Geophysical Research*, **104**, 24,155–24,176, doi:10.1029/1999JE001025, 1999.
- Fox, J. L., and R. V. Yelle, Hydrocarbon ions in the ionosphere of Titan, *Geophysical Research Letters*, **24**, 2179–+, 1997.
- Friedson, A. J., and Y. L. Yung, The thermosphere of Titan, *JGR*, **89**, 85–90, 1984.
- Fuller-Rowell, T. J., and D. Rees, A three-dimensional time-dependent global model of the thermosphere., *Journal of Atmospheric Sciences*, **37**, 2545–2567, 1980a.
- Fuller-Rowell, T. J., and D. Rees, A three-dimensional time-dependent global model of the thermosphere., *Journal of Atmospheric Sciences*, **37**, 2545–2567, 1980b.
- Fuller-Rowell, T. J., and D. Rees, Derivation of a conservation equation for mean molecular weight for a two-constituent gas within a three-dimensional, time-dependent model of the thermosphere, *PSS*, **31**, 1209–1222, doi:10.1016/0032-0633(83)90112-5, 1983.
- Fuller-Rowell, T. J., D. Rees, S. Quegan, R. J. Moffett, and G. J. Bailey, Interactions between neutral thermospheric composition and the polar ionosphere using a coupled ionosphere-thermosphere model, *Journal of Geophysical Research*, **92**, 7744–7748, 1987.

- Gan, L., C. N. Keller, and T. E. Cravens, Electrons in the ionosphere of Titan, *Journal of Geophysical Research*, 97, 12,137–+, 1992a.
- Gan, L., C. N. Keller, and T. E. Cravens, Electrons in the ionosphere of Titan, *JGR*, 97, 12,137–+, 1992b.
- Gangale, T., and M. Dudley-Rowley, Issues and options for a Martian calendar, *Planetary and Space Science*, 53, 1483–1495, doi:10.1016/j.pss.2005.07.012, 2005.
- Geisler, J. E., A numerical study of the wind system in the middle thermosphere, *Journal of Atmos. Terr. Phys.*, 29, 1469–1482, 1967.
- Gillett, F. C., Further observations of the 8-13 micron spectrum of Titan, *APJ*, 201, L41–L43, 1975.
- Gillett, F. C., W. J. Forrest, and K. M. Merrill, 8-13 Micron Observations of Titan, *APJ*, 184, L93+, 1973.
- Gombosi, T. I., *Physics of the Space Environment*, Physics of the Space Environment, ISBN 052159264X, Cambridge University Press, 1999., 1999.
- González-Galindo, F., M. A. López-Valverde, M. Angelats i Coll, and F. Forget, Extension of a Martian general circulation model to thermospheric altitudes: UV heating and photochemical models, *Journal of Geophysical Research (Planets)*, 110, 9008–+, doi:10.1029/2004JE002312, 2005.
- González-Galindo, F., S. Bouger, M. A. López-Valverde, F. Forget, and J. Bell, Thermal structure of the martian thermosphere: LMD-IAA GCM and MTGCM intercomparisons, in *Mars Atmosphere Modelling and Observations*, edited by F. Forget, M. A. Lopez-Valverde, M. C. Desjean, J. P. Huot, F. Lefevre, S. Lebonnois, S. R. Lewis, E. Millour, P. L. Read, and R. J. Wilson, pp. 625–+, 2006.
- Goody, R. M., and Y. L. Yung, *Atmospheric radiation : theoretical basis*, Atmospheric radiation : theoretical basis, 2nd ed., by Richard M. Goody and Y.L. Yung. New York, NY: Oxford University Press, 1989, 1989.
- Haberle, R. M., et al., General circulation model simulations of the Mars Pathfinder atmospheric structure investigation/meteorology data, *Journal of Geophysical Research*, 104, 8957–8974, doi:10.1029/1998JE900040, 1999.
- Harris, I., and W. Priester, Time-Dependent Structure of the Upper Atmosphere., *Journal of Atmospheric Sciences*, 19, 286–301, 1962.
- Harris, I., and W. Priester, Of the Diurnal Variation of the Upper Atmosphere., *Journal of Atmospheric Sciences*, 22, 3–10, 1965.
- Harris, M. J., N. F. Arnold, and A. D. Aylward, A study into the effect of the diurnal tide on the structure of the background mesosphere and thermosphere using the new coupled middle atmosphere and thermosphere (CMAT) general circulation model, *Annales Geophysicae*, 20, 225–235, 2002.
- Hedin, A. E., A revised thermospheric model based on mass spectrometer and incoherent scatter data - MSIS-83, *Journal of Geophysical Research*, 88, 10,170–10,188, 1983.
- Hedin, A. E., MSIS-86 thermospheric model, *Journal of Geophysical Research*, 92, 4649–4662, 1987.
- Hedin, A. E., Extension of the MSIS thermosphere model into the middle and lower atmosphere, *Journal of Geophysical Research*, 96, 1159–1172, 1991.
- Hinteregger, H. E., K. Fukui, and B. R. Gilson, Observational, reference and model data on solar EUV, from measurements on AE-E, *GRL*, 8, 1147–1150, 1981.

- Houghton, J. T., *The physics of atmospheres*, The physics of atmospheres, 3rd ed. by John Houghton. Cambridge, UK: Cambridge University Press, 2002 xv, 320 p. ISBN #0521011221, 2002.
- Hourdin, F., O. Talagrand, R. Sadourny, R. Courtin, D. Gautier, and C. P. McKay, Numerical simulation of the general circulation of the atmosphere of Titan., *Icarus*, 117, 358–374, doi:10.1006/icar.1995.1162, 1995.
- Hubbard, W. B., et al., The occultation of 28 SGR by Saturn - Saturn pole position and astrometry, *Icarus*, 103, 215–234, doi:10.1006/icar.1993.1067, 1993.
- Humlícek, J., Optimized computation of the Voigt and complex probability functions., *Journal of Quantitative Spectroscopy and Radiative Transfer*, 27, 437–444, 1982.
- Hunten, D. M., Energetics of Thermospheric Eddy Transport., *JGR*, 79, 2533–2534, 1974.
- Hunten, D. M., A Titan atmosphere with a surface temperature of 200K, in *The Saturn System*, edited by D. M. Hunten and D. Morrison, pp. 127–140, 1978.
- Hunten, D. M., M. G. Tomasko, F. M. Flasar, R. E. Samuelson, D. F. Strobel, and D. J. Stevenson, *Titan*, pp. 671–759, Saturn, 1984.
- Ip, W.-H., Titan's upper ionosphere, *Astrophysical Journal*, 362, 354–363, doi: 10.1086/169271, 1990.
- Jaffe, W., J. Caldwell, and T. Owen, Radius and brightness temperature observations of Titan at centimeter wavelengths by the Very Large Array, *APJj*, 242, 806–811, doi:10.1086/158515, 1980.
- Jakosky, B. M., A. P. Zent, and R. W. Zurek, The Mars Water Cycle: Determining the Role of Exchange with the Regolith, *Icarus*, 130, 87–95, doi: 10.1006/icar.1997.5799, 1997.
- Jakosky, B. M., M. T. Mellon, E. S. Varnes, W. C. Feldman, W. V. Boynton, and R. M. Haberle, Mars low-latitude neutron distribution: Possible remnant near-surface water ice and a mechanism for its recent emplacement, *Icarus*, 175, 58–67, doi:10.1016/j.icarus.2004.11.014, 2005.
- Kasting, J. F., Runaway and moist greenhouse atmospheres and the evolution of earth and Venus, *Icarus*, 74, 472–494, doi:10.1016/0019-1035(88)90116-9, 1988.
- Keating, G., R. Tolson, M. Theriot, S. Bouger, and F. Forget, Detection of north polar winter warming from the Mars Odyssey 2001 accelerometer experiment, in *34th COSPAR Scientific Assembly, COSPAR, Plenary Meeting*, vol. 34, 2002.
- Keating, G. M., M. Theriot, Jr., R. Tolson, S. Bouger, F. Forget, and J. Forbes, Global Measurements of the Mars Upper Atmosphere: In Situ Accelerometer Measurements from Mars Odyssey 2001 and Mars Global Surveyor, in *Lunar and Planetary Institute Conference Abstracts, Lunar and Planetary Institute Conference Abstracts*, vol. 34, edited by S. Mackwell and E. Stansbery, pp. 1142–+, 2003.
- Keating, G. M., et al., The Structure of the Upper Atmosphere of Mars: In Situ Accelerometer Measurements from Mars Global Surveyor, *Science*, 279, 1672–+, 1998.
- Keller, C. N., V. G. Anicich, and T. E. Cravens, Model of Titans ionosphere with detailed hydrocarbon ion chemistry, *Planetary and Space Science*, 46, 1157–1174, 1998.

- Killeen, T. L., and R. G. Roble, An analysis of the high-latitude thermospheric wind pattern calculated by a thermospheric general circulation model. I - Momentum forcing, *Journal of Geophysical Research*, **89**, 7509–7522, 1984.
- Killeen, T. L., R. G. Roble, and N. W. Spencer, A computer model of global thermospheric winds and temperatures, *Advances in Space Research*, **7**, 207–215, doi: 10.1016/0273-1177(87)90314-0, 1987.
- Knudsen, W. C., Magnetospheric convection and the high-latitude F_2 ionosphere., *Journal of Geophysical Research*, **79**, 1046–1055, 1974.
- Knudsen, W. C., P. M. Banks, J. D. Winningham, and D. M. Klumpar, Numerical model of the convecting F_2 ionosphere at high latitudes, *Journal of Geophysical Research*, **82**, 4784–4792, 1977.
- Kohl, H., and J. W. King, Atmospheric winds between 100 and 700 km and their effects on the ionosphere, *Journal of Atmos. Terr. Phys.*, **29**, 1045–1062, 1967.
- Kuiper, G. P., Titan: a Satellite with an Atmosphere., *APJ*, **100**, 378–+, 1944.
- Kundu, P. K., and I. M. Cohen, *Fluid Mechanics*, third ed., Elsevier Academic Press, 2004.
- Kuntz, M., A new implementation of the Humlicek algorithm for the calculation of the Voigt profile function., *Journal of Quantitative Spectroscopy and Radiative Transfer*, **57**, 819–824, 1997.
- Lara, L. M., E. Lellouch, J. J. López-Moreno, and R. Rodrigo, Vertical distribution of Titan's atmospheric neutral constituents, *JGR*, **101**, 23,261–23,283, doi: 10.1029/96JE02036, 1996.
- Leblanc, F., and R. E. Johnson, Role of molecular species in pickup ion sputtering of the Martian atmosphere, *Journal of Geophysical Research (Planets)*, **107**, 5010–+, doi:10.1029/2000JE001473, 2002.
- Lebonnois, S., D. Toublanc, F. Hourdin, and P. Rannou, Seasonal Variations of Titan's Atmospheric Composition, *Icarus*, **152**, 384–406, doi:10.1006/icar.2001.6632, 2001.
- Lellouch, E., Atmospheric models of Titan and Triton, *Annales Geophysicae*, **8**, 653–660, 1990.
- Lether, F. G., and P. R. Wenston, The numerical computation of the Voigt function by a correlated midpoint quadrature rule for $(-\infty, \infty)$, *Journal of Computational and Applied Mathematics*, **34**, 75–92, 1991.
- Lindfield, G. R., and J. Penny, *Numerical Methods Using Matlab*, Prentice-Hall, —c1999, 2nd ed., 1999.
- Liu, J., M. I. Richardson, and R. J. Wilson, An assessment of the global, seasonal, and interannual spacecraft record of Martian climate in the thermal infrared, *Journal of Geophysical Research (Planets)*, **108**, 5089–+, doi:10.1029/2002JE001921, 2003.
- López-Valverde, M. A., D. P. Edwards, M. López-Puertas, and C. Roldán, Non-local thermodynamic equilibrium in general circulation models of the Martian atmosphere 1. Effects of the local thermodynamic equilibrium approximation on thermal cooling and solar heating, *Journal of Geophysical Research*, **103**, 16,799–16,812, doi:10.1029/98JE01601, 1998.
- Malin, M. C., K. S. Edgett, L. V. Posiolova, S. M. McColley, and E. Z. Noe Dobrea, Present-Day Impact Cratering Rate and Contemporary Gully Activity on Mars , *Science*, **314**, 1573, doi:10.1126/science.1135156, 2006.

- Martin, P. G., C. Rogers, and G. B. Rybicki, Half-range moment methods for radiative transfer in spherical geometry. II - Implementation of the method, *Astrophysical Journal*, 284, 317–326, doi:10.1086/162410, 1984.
- Mason, E. A., and T. R. Marrero, The diffusion of atoms and molecules, *Advances in Atomic and Molecular Physics*, 6, 155–232, 1970.
- Mason, E. A., and S. C. Saxena, Approximate Formula for the Thermal Conductivity of Gas Mixtures, *Physics of Fluids*, 1, 361–369, 1958.
- Massman, W. J., A Review of the molecular diffusivities of H_2O , CO_2 , CH_4 , CO , O_3 , SO_2 , NH_3 , N_2O , NO , and NO_2 near STP, *Atmospheric Environment*, 32, 1111–1127, 1998.
- McCormac, F. G., T. L. Killeen, A. G. Burns, J. W. Meriwether, Jr., R. G. Roble, L. E. Wharton, and N. W. Spencer, Polar cap diurnal temperature variations - Observations and modeling, *Journal of Geophysical Research*, 93, 7466–7477, 1988.
- Mihalas, D., *Stellar atmospheres /2nd edition/*, San Francisco, W. H. Freeman and Co., 1978. 650 p., 1978.
- Mikkelsen, I. S., and M. F. Larsen, An analytic solution for the response of the neutral atmosphere to the high-latitude convection pattern, *Journal of Geophysical Research*, 88, 8073–8080, 1983.
- Mikkelsen, I. S., T. S. Jorgensen, M. C. Kelley, M. F. Larsen, and E. Pereira, Neutral winds and electric fields in the dust auroral oval. II - Theory and model, *Journal of Geophysical Research*, 86, 1525–1536, 1981.
- Müller-Wodarg, I. C. F., and R. V. Yelle, The effect of dynamics on the composition of Titan's upper atmosphere, *GRL*, 29, 54–1, 2002.
- Müller-Wodarg, I. C. F., R. V. Yelle, M. Mendillo, L. A. Young, and A. D. Aylward, The thermosphere of Titan simulated by a global three-dimensional time-dependent model, *JGR*, 105, 20,833–20,856, doi:10.1029/2000JA000053, 2000.
- Müller-Wodarg, I. C. F., R. V. Yelle, M. J. Mendillo, and A. D. Aylward, On the global distribution of neutral gases in Titan's upper atmosphere and its effect on the thermal structure, *Journal of Geophysical Research (Space Physics)*, 108, 1453–+, doi:10.1029/2003JA010054, 2003.
- Müller-Wodarg, I. C. F., R. V. Yelle, N. Borggren, and J. H. Waite, Waves and horizontal structures in Titan's thermosphere, *Journal of Geophysical Research (Space Physics)*, 111, 12,315–+, doi:10.1029/2006JA011961, 2006.
- Murphy, J. R., C. B. Leovy, and J. E. Tillman, Observations of Martian surface winds at the Viking Lander 1 site, *Journal of Geophysical Research*, 95, 14,555–14,576, 1990.
- Murphy, J. R., R. M. Haberle, O. B. Toon, and J. B. Pollack, Martian global dust storms - Zonally symmetric numerical simulations including size-dependent particle transport, *Journal of Geophysical Research*, 98, 3197–3220, 1993.
- Niemann, H. B., et al., The abundances of constituents of Titan's atmosphere from the GCMS instrument on the Huygens probe, *Nature*, 438, 779–784, doi:10.1038/nature04122, 2005.
- Oehmke, R., High performance dynamic array structures, Ph.D. thesis, AA(THE UNIVERSITY OF MICHIGAN.), 2004.

- Oehmke, R., and Q. Stout, Parallel adaptive blocks on the sphere. In: Proceedings of the 11th SIAM Conference on Parallel Processing for Scientific Computing, *PSS*, 2001.
- Paxton, L. J., and D. E. Anderson, Far ultraviolet remote sensing of Venus and Mars, *Washington DC American Geophysical Union Geophysical Monograph Series*, 66, 113–189, 1992.
- Peraiah, A., *An Introduction to Radiative Transfer*, An Introduction to Radiative Transfer, by Annamaneni Peraiah, pp. 492. ISBN 0521770017. Cambridge, UK: Cambridge University Press, December 2001., 2001.
- Pollack, J. B., R. M. Haberle, J. Schaeffer, and H. Lee, Simulations of the general circulation of the Martian atmosphere. I - Polar processes, *Journal of Geophysical Research*, 95, 1447–1473, 1990.
- Press, W. H., S. A. Teukolsky, W. T. Vetterling, and B. P. Flannery, *Numerical recipes in FORTRAN. The art of scientific computing*, Cambridge: University Press, —c1992, 2nd ed., 1992.
- Press, W. H., S. A. Teukolsky, W. T. Vetterling, and B. P. Flannery, *Numerical recipes in FORTRAN 90. The art of parallel computing*, Cambridge: University Press, —c1996, 2nd ed., 1996.
- Quegan, S., G. J. Bailey, R. J. Moffett, R. A. Heelis, T. J. Fuller-Rowell, D. Rees, and R. W. Spiro, A theoretical study of the distribution of ionization in the high-latitude ionosphere and the plasmasphere: first results on the mid-latitude trough and the light-ion trough., *Journal of Atmospheric and Terrestrial Physics*, 44, 619–640, 1982.
- Ralston, A., and P. Rabinowitz, *A First Course in Numerical Analysis*, Dover Publications, —c1978, 2nd ed., 1978.
- Reid, R. C., J. M. Prausnitz, and B. E. Poling, *Properties of Gases and Liquids*, third ed., McGraw-Hill, 1987.
- Richmond, A. D., Large-amplitude gravity wave energy production and dissipation in the thermosphere, *Journal of Geophysical Research*, 84, 1880–1890, 1979.
- Richmond, A. D., Thermospheric Dynamics and Electrodynamics, in *SOLAR-TERRESTRIAL PHYSICS: BOSTON COLLEGE: 82AUG P.523*, 1983, edited by R. L. Carovillano and J. M. Forbes, pp. 523–+, 1983.
- Richmond, A. D., and S. Matsushita, Thermospheric response to a magnetic sub-storm, *Journal of Geophysical Research*, 80, 2839–2850, 1975.
- Richmond, A. D., E. C. Ridley, and R. G. Roble, A thermosphere/ionosphere general circulation model with coupled electrodynamics, *Geophysical Research Letters*, 19, 601–604, 1992.
- Ridley, A. J., Y. Deng, and G. Tóth, The global ionosphere thermosphere model, *Journal of Atmospheric and Terrestrial Physics*, 68, 839–864, doi: 10.1016/j.jastp.2006.01.008, 2006.
- Rishbeth, H., R. V. Yelle, and M. Mendillo, Dynamics of Titan's Thermosphere, *Planetary and Space Science*, 48, 51–58, 2000.
- Roble, R. G., and E. C. Ridley, An auroral model for the NCAR thermospheric general circulation model (TGCM), *Annales Geophysicae*, 5, 369–382, 1987.
- Roble, R. G., and E. C. Ridley, A thermosphere-ionosphere-mesosphere-electrodynamics general circulation model (time-GCM): Equinox solar cycle minimum simulations (30-500 km), *GRL*, 21, 417–420, 1994.

- Roble, R. G., R. E. Dickinson, and E. C. Ridley, Seasonal and solar cycle variations of the zonal mean circulation in the thermosphere, *Journal of Geophysical Research*, **82**, 5493–5504, 1977.
- Roble, R. G., E. C. Ridley, and R. E. Dickinson, On the global mean structure of the thermosphere, *Journal of Geophysical Research*, **92**, 8745–8758, 1987.
- Roble, R. G., E. C. Ridley, A. D. Richmond, and R. E. Dickinson, A coupled thermosphere/ionosphere general circulation model, *GRL*, **15**, 1325–1328, 1988.
- Rogers, C., and P. G. Martin, Half-range moment methods for radiative transfer in spherical geometry. III - Numerical solution and applications, *Astrophysical Journal*, **284**, 327–336, doi:10.1086/162411, 1984.
- Rogers, C., and P. G. Martin, Half-range moment methods for radiative transfer in spherical geometry. IV - Multifrequency problems with radiative equilibrium, *Astrophysical Journal*, **311**, 800–804, doi:10.1086/164818, 1986.
- Rothman, L. S., et al., The HITRAN Molecular Spectroscopic Database and HAWKS (HITRAN Atmospheric Workstation): 1996 Edition, *Journal of Quantitative Spectroscopy and Radiative Transfer*, **60**, 665–710, 1998.
- Rothman, L. S., et al., The HITRAN Molecular Spectroscopic Database: Edition of 2000 including updates through 2001, *Journal of Quantitative Spectroscopy and Radiative Transfer*, **82**, 5–44, 2003.
- Sagan, C., and W. R. Thompson, Production and condensation of organic gases in the atmosphere of Titan, *Icarus*, **59**, 133–161, doi:10.1016/0019-1035(84)90018-6, 1984.
- Samuelson, R. E., R. A. Hanel, V. G. Kunde, and W. C. Maguire, Mean molecular weight and hydrogen abundance of Titan's atmosphere, *Nature*, **292**, 688–693, 1981.
- Santee, M., and D. Crisp, Thermal structure and dust loading of the Martian atmosphere during late southern summer - Mariner 9 revisited, *Journal of Geophysical Research*, **98**, 3261–3279, 1993.
- Schunk, R., and A. F. Nagy, *Ionospheres*, Cambridge University Press, 2000., 2000.
- Schunk, R. W., A mathematical model of the middle and high latitude ionosphere, *Pure and Applied Geophysics*, **127**, 255–303, doi:10.1007/BF00879813, 1988.
- Schunk, R. W., and J. C. G. Walker, Theoretical ion densities in the lower ionosphere, *Planetary and Space Sciences*, **21**, 1875–1896, doi:10.1016/0032-0633(73)90118-9, 1973.
- Schunk, R. W., J. J. Sojka, and M. D. Bowline, Theoretical study of the electron temperature in the high-latitude ionosphere for solar maximum and winter conditions, *Journal of Geophysical Research*, **91**, 12,041–12,054, 1986.
- Schunk, R. W. e. a., Global assimilation of ionospheric measurements (GAIM), *Radio Science*, **39**, doi:10.1029/2002RS002, 2004.
- Serway, R. A., *Physics for Scientists and Engineers*, Saunders College Publishing, 1996., 1996.
- Shippony, Z., and W. G. Read, A highly accurate Voigt function algorithm., *Journal of Quantitative Spectroscopy and Radiative Transfer*, **50**, 635–646, 1993.
- Smith, F. I., and C. Smith, Numerical evaluation of Chapman's grazing incidence integral $\text{ch}(x, \chi)$, *JGR*, **77**, 3592, 1972.

- Smith, G. R., D. F. Strobel, A. L. Broadfoot, B. R. Sandel, D. E. Shemansky, and J. B. Holberg, Titan's upper atmosphere - Composition and temperature from the EUV solar occultation results, *JGR*, 87, 1351–1359, 1982.
- Smith, M. D., Interannual variability in TES atmospheric observations of Mars during 1999–2003, *Icarus*, 167, 148–165, doi:10.1016/S0019-1035(03)00287-2, 2004.
- Smith, M. D., TES atmospheric temperature, aerosol optical depth, and water vapor observations 1999–2004, in *Mars Atmosphere Modelling and Observations*, edited by F. Forget, M. A. Lopez-Valverde, M. C. Desjean, J. P. Huot, F. Lefevre, S. Lebonnois, S. R. Lewis, E. Millour, P. L. Read, and R. J. Wilson, pp. 211–+, 2006.
- Sojka, J. J., and R. W. Schunk, A theoretical study of the global F region for June solstice, solar maximum, and low magnetic activity, *Journal of Geophysical Research*, 90, 5285–5298, 1985.
- Sojka, J. J., W. J. Raitt, and R. W. Schunk, A theoretical study of the high-latitude winter F region at solar minimum for low magnetic activity, *Journal of Geophysical Research*, 86, 609–621, 1981.
- Sparks, L., Efficient line-by-line calculation of absorption coefficients to high numerical accuracy., *Journal of Quantitative Spectroscopy and Radiative Transfer*, 57, 631–650, 1997.
- Strobel, D. F., The Photochemistry of Hydrocarbons in the Atmosphere of Titan, *Icarus*, 21, 466–+, 1974.
- Strobel, D. F., Aeronomic Systems on Planets, Moons, and Comets, in *Atmospheres in the Solar System: Comparative Aeronomy*, edited by M. Mendillo, A. Nagy, and J. H. Waite, p. 7–23, AGU, Washington, D.C., 2002.
- Strobel, D. F., Titan's hydrodynamically escaping atmosphere, *Icarus*, 193, 588–594, doi:10.1016/j.icarus.2007.08.014, 2008.
- Stubbe, P., Simultaneous solution of the time dependent coupled continuity equations, heat conduction equations, and equations of motion for a system consisting of a neutral gas, an electron gas, and a four component ion gas., *Journal of Atmospheric and Terrestrial Physics*, 32, 865–903, 1970.
- Teanby, N. A., et al., Vertical profiles of HCN, HC₃N, and C₂H₂ in Titan's atmosphere derived from Cassini/CIRS data, *Icarus*, 186, 364–384, doi:10.1016/j.icarus.2006.09.024, 2007.
- Theodore, B., E. Lellouch, E. Chassefiere, and A. Hauchecorne, Solstitial temperature inversions in the Martian middle atmosphere - Observational clues and 2-D modeling, *Icarus*, 105, 512–+, doi:10.1006/icar.1993.1145, 1993.
- Thomas, G. E., Dissipation of temperature perturbations in the middle atmosphere, *Advances in Space Research*, 1, 127–130, doi:10.1016/0273-1177(81)90426-9, 1981.
- Thompson, W. J., Numerous Neat Algorithms for the Voigt Profile Function, *Computers in Physics*, 7, 627–631, 1993.
- Tobiska, W. K., Revised solar extreme ultraviolet flux model, *Journal of Atmospheric and Terrestrial Physics*, 53, 1005–1018, 1991.
- Tobiska, W. K., and C. A. Barth, A solar EUV flux model, *JGR*, 95, 8243–8251, 1990.
- Torr, D. G., et al., An experimental and theoretical study of the mean diurnal variation of O^{+/}, NO^{+/}, O₂^{+/}, and N₂^{+/} ions in the mid-latitude F1 layer of the ionosphere, *JGR*, 84, 3360–3372, 1979.

- Tóth, G., et al., Space Weather Modeling Framework: A new tool for the space science community, *Journal of Geophysical Research (Space Physics)*, 110, 12,226–+, doi:10.1029/2005JA011126, 2005.
- Toublanc, D., J. P. Parisot, J. Brillet, D. Gautier, F. Raulin, and C. P. McKay, Photochemical modeling of Titan's atmosphere, *Icarus*, 113, 2–26, doi: 10.1006/icar.1995.1002, 1995.
- Šuráň, J., A calendar for Mars, *Planetary and Space Science*, 45, 705–708, 1997.
- van Leer, B., Towards the ultimate conservative difference scheme. V - A second-order sequel to Godunov's method, *Journal of Computational Physics*, 32, 101–136, 1979.
- Vervack, R. J., B. R. Sandel, and D. F. Strobel, New perspectives on Titan's upper atmosphere from a reanalysis of the Voyager 1 UVS solar occultations, *Icarus*, 170, 91–112, doi:10.1016/j.icarus.2004.03.005, 2004.
- Vuitton, V., R. V. Yelle, and V. G. Anicich (Retired), The Nitrogen Chemistry of Titan's Upper Atmosphere Revealed, *Astrophysical Journal*, 647, L175–L178, doi:10.1086/507467, 2006.
- Wahlund, J.-E., et al., Cassini Measurements of Cold Plasma in the Ionosphere of Titan, *Science*, 308, 986–989, doi:10.1126/science.1109807, 2005.
- Waite, J. H., et al., The Cassini Ion and Neutral Mass Spectrometer (INMS) Investigation, *Space Science Reviews*, 114, 113–231, doi:10.1007/s11214-004-1408-2, 2004.
- Waite, J. H., et al., Ion Neutral Mass Spectrometer Results from the First Flyby of Titan, *Science*, 308, 982–986, doi:10.1126/science.1110652, 2005.
- Wang, W., A thermosphere-ionosphere nested grid (TING) model, Ph.D. thesis, UNIVERSITY OF MICHIGAN, 1998.
- Wang, W., T. L. Killeen, A. G. Burns, and R. G. Roble, A high-resolution, three-dimensional, time dependent, nested grid model of the coupled thermosphere - ionosphere., *Journal of Atmospheric and Terrestrial Physics*, 61, 385–397, 1999.
- Weast, R. C., *CRC Handbook of Chemistry and Physics*, CRC, 1984.
- Wilson, E. H., Investigations into the photochemistry of the current and primordial atmosphere of Titan, Ph.D. thesis, AA(UNIVERSITY OF MICHIGAN), 2002a.
- Wilson, E. H., and S. K. Atreya, Current state of modeling the photochemistry of Titan's mutually dependent atmosphere and ionosphere, *Journal of Geophysical Research (Planets)*, 109, 6002–+, doi:10.1029/2003JE002181, 2004.
- Wilson, R. J., A general circulation model simulation of the Martian polar warming, *Geophysical Research Letters*, 24, 123–126, doi:10.1029/96GL03814, 1997.
- Wilson, R. J., Evidence for nonmigrating thermal tides in the Mars upper atmosphere from the Mars Global Surveyor Accelerometer Experiment, *Geophysical Research Letters*, 29, 24–1, 2002b.
- Withers, P., Mars Global Surveyor and Mars Odyssey Accelerometer observations of the Martian upper atmosphere during aerobraking, *Geophysical Research Letters*, 33, 2201–+, doi:10.1029/2005GL024447, 2006.
- Withers, P., S. W. Bouger, and G. M. Keating, The effects of topographically-controlled thermal tides in the martian upper atmosphere as seen by the MGS accelerometer, *Icarus*, 164, 14–32, doi:10.1016/S0019-1035(03)00135-0, 2003.

- Yaws, C. L., *Handbook of Transport Property Data, Viscosity, Thermal Conductivity, and Diffusion Coefficients of Liquids and Gases*, Butterworth-Heinemann, 1995.
- Yaws, C. L., *Handbook of Thermal Conductivity, Vol. 4, Inorganic Compounds and Elements*, Gulf Professional Publishing, 1997.
- Yelle, R. V., Non-LTE models of Titan's upper atmosphere, *APJ*, 383, 380–400, doi:10.1086/170796, 1991.
- Yelle, R. V., D. F. Strobell, E. Lellouch, and D. Gautier, The Yelle Titan Atmosphere Engineering Models, in *ESA Special Publication*, *ESA Special Publication*, vol. 1177, edited by A. Wilson, pp. 243–+, 1997.
- Yelle, R. V., N. Borggren, V. de La Haye, W. T. Kasprzak, H. B. Niemann, I. Müller-Wodarg, and J. H. Waite, The vertical structure of Titan's upper atmosphere from Cassini Ion Neutral Mass Spectrometer measurements, *Icarus*, 182, 567–576, doi: 10.1016/j.icarus.2005.10.029, 2006.
- Yung, Y. L., M. Allen, and J. P. Pinto, Photochemistry of the atmosphere of Titan - Comparison between model and observations, *AJS*, 55, 465–506, doi: 10.1086/190963, 1984.

ABSTRACT

Dynamics of Titan and Mars

by
Jared Bell

Chair: Bougher